Development of Essential Components for Soft Wearable Technologies

THÈSE N^{O} 7688 (2017)

PRÉSENTÉE LE 9 JUIN 2017

À LA FACULTÉ DES SCIENCES ET TECHNIQUES DE L'INGÉNIEUR
LABORATOIRE DE ROBOTIQUE RECONFIGURABLE
PROGRAMME DOCTORAL EN ROBOTIQUE, CONTRÔLE ET SYSTÈMES INTELLIGENTS

ÉCOLE POLYTECHNIQUE FÉDÉRALE DE LAUSANNE

POUR L'OBTENTION DU GRADE DE DOCTEUR ÈS SCIENCES

PAR

Amir FIROUZEH

acceptée sur proposition du jury:

Prof. A. Ijspeert, président du jury
Prof. J. Paik, directrice de thèse
Prof. R. Full , rapporteur
Prof. F. Iida, rapporteur
Prof. R. Clavel, rapporteur

ÉCOLE POLYTECHNIQUE
FÉDÉRALE DE LAUSANNE

Suisse
2017

By three methods we may learn wisdom:
by reflection, which is noblest;
by imitation, which is easiest;
and by experience, which is
the bitterest.
—Confucius

Acknowledgements

I am thankful for the many good moments I had during my PhD life at EPFL. For that, I should thank the people who have made my journey as a PhD student possible and enjoyable. First, I would like to thank my adviser Prof. Jamie Paik for giving me the chance to start my studies at EPFL and for providing support during these years. I would like to thank her for providing an environment that allowed me to explore different ideas while always feeling supported and acknowledged for my efforts, even when the results were less than satisfactory. I would like to thank her for the discussions and many feedbacks during our meetings that significantly assisted me in developing ideas during my research at RRL.

I would like to thank the members of my jury Prof. Reymond Clavel, Prof. Robert Full, Prof. Fumiya Iida, and Prof. Auke Ijspeert for their valuable suggestions and insightful comments that not only assisted me in improving this dissertation but also provided me with insightful guidelines for planning the future steps of my research.

I would like to thank the past and present colleagues at RRL. Specifically I am grateful for the support and assistance from Yi Sun, my first and only colleague at the time. I would like to thank him for making the working days of my first year at EPFL enjoyable. My special thanks to Marco Salerno who has improved my work as a researcher by providing valuable feedback during our teatime discussions. More importantly I am grateful for the friendly environment that he brought to the lab which made us closer to each other at RRL.

It is impossible for me to imagine my life in Switzerland without my friends. I need to specially thank Mohsen, Mostafa, Marco, Parastoo, Asiye, and Cate with whom I shared some of my best moments and most joyful laughs. I am also thankful for lots of good moments in Lausanne and mountains around spent with my other good friends Mehran, Samaneh, Sina, Mina, Basil, Darina, Sara, Jordi, Hadis, Mehran-Shah, Maryam, Naghmeh, Dordaneh, Behzad, Zohreh, Matt, Amy, Mohammad, Soha, and Thomas.

Last, but far from least, I would like to thank my family for their unconditional love. Maliheh, my mom, and Mohammad, my dad, have always been providing me with strong emotional support and thoughtful advice that helped me in overcoming difficult moments in my life. I am also grateful for my sister Samareh who has been one of my best friends throughout my life. I am thankful to have a family that I can turn to during the difficulties and be sure that they would be there for me and would support me in whatever way possible for them.

Lausanne, April 2017 A. Firouzeh.

Abstract

The rising demand for safe human-robot interaction in daily tasks has motivated significant research effort in the robotics field towards compliant and conformable robots, capable of replicating complex human movements in applications such as wearable rehabilitative devices and haptic interfaces. Novel manufacturing, actuation, and sensing technologies contributed significantly to this field by providing design and manufacturing frameworks for inherently compliant robots. Although promising, these technologies are still in the early stages of development and fundamental research for refining their design, improving their performance, and defining design criteria is still required for these technologies to reach their full potential.

In this thesis, some of the main challenges hindering the effective application of robotics in wearable devices are tackled. We propose the robotic origami (robogami) framework with multiple but finite degrees of freedom (DoFs) for soft wearable devices. Robogamis are low profile robots that provide conformity and compliance with their multiple DoFs driven by soft actuation methods. The finite DoFs in these robots enable better prediction and planning of their motion while highly customizable joint designs, thanks to the layer-by-layer manufacturing and the precise quasi-2D fabrication processes, allows the multiple DoFs to be embedded to achieve the required level of conformity.

To effectively actuate the multiple DoFs in robogamis, it is imperative to embed means of actuation or energy transmission into the robots body. The layer-by-layer manufacturing allows us to embed layers of functional materials into the robot's structure to achieve soft actuation methods that meet the requirements of a wearable device, i.e. the actuation band width, load capacity, and range of motion. We take up the challenge of soft actuation of individual joints and synchronized actuation of a series of joints to follow a desired trajectory or perform a specific reconfiguration by developing functional layers of smart materials to exploit their unique characteristics.

The compliance of soft robots originates from the elastic properties of the manufacturing materials. Depending on the application, materials with different levels of stiffness are used to achieve a compromise between mechanical transparency and load capacity. A wearable robot needs to cover a wide range of mechanical transparencies and load capacities to be able to fulfill different tasks, e.g. providing varying levels of support at particular stages of rehabilitation. To broaden the applications of a soft robot to meet the requirements of different tasks, it is necessary to develop a means of stiffness control for its segments or joints. By embedding layers of functional materials with controllable stiffness into robogamis, we can

develop robots that are able to change their mode of interaction and compliance depending on their task.
The inherent compliance of soft robots allows safer interactions with the environment. The compliance and multiple DoFs, however, complicate the estimation of the robot's configuration and contact forces from the model. So for a more effective interaction with the environment it is necessary to embed a network of sensing elements into the robot to observe its configuration, contact forces, and displacements at the contact points. Given the limitations on the size, shape, and the required measurement range, it is imperative to design and manufacture customized sensors. We developed under 100 μm thick sensors with an adaptable and scalable design for accurate joint angle measurement in robogamis, which are compatible with their demanding working conditions, i.e. large range of strain and temperature variation. Using the same sensing principles, we also developed thin and mechanically transparent stretch sensors that can be used in networks of sensing elements in wearable devices to measure body movements.
The main contributions of this thesis are:

- Study and development of the robogami framework as a design platform for soft robots with programmable reconfigurations and compliance.
- Design and validation of actuation solutions based on smart materials for independent actuation of robogami joints.
- Adoption of the smart materials' variable mechanical properties to adjust the stiffness of robogami joints and the overall compliance of the robot.
- Development of customized sensing methods to measure robogami joint angles and stretchable sensors based on the same principles to measure body movements.

We believe that these contributions facilitate some of the main challenges for the effective application of robogamis in wearable devices for safe and yet functional interactions with humans. The highly customizable components can also be used in design frameworks other than robogamis and other applications where compliance and conformity are required.

Keywords: Robotic origamis, layer-by-layer manufacturing, tendon-driven under-actuated robots, functional materials, adjustable stiffness, curvature sensors, stretchable sensors, soft robots.

Résumé

La demande croissante pour une interaction sûre du robot humain dans les tâches quotidiennes a motivé un effort de recherche important dans le domaine de la robotique, vers des robots conformables qui sont capables de reproduire des mouvements humains complexes dans des applications telles que des appareils de réhabilitation mettable et des interfaces haptiques. Les nouvelles technologies de fabrication, d'actionnement et de détection ont contribué de manière significative à ce domaine en fournissant des cadres de conception et de fabrication pour des robots intrinsèquement conformes. Bien que prometteur, ces technologies sont encore à leurs premiers stades de développement et la recherche de base pour affiner leur conception, améliorer leur performance, et la définition de critères de conception est toujours nécessaire pour qu'ils atteignent leur plein potentiel.

Au cours de cette thèse, nous abordons certains des principaux défis qui entravent l'application effective de la robotique dans les appareils mettable. Nous proposons le cadre robogami pour les robots conformables avec des degrés de liberté (DoFs) multiples mais finis. Robogamis sont des robots de profil fin qui fournissent la conformité avec leurs DoFs multiples induites par des méthodes d'actionnement doux. Les DoF finis de ces robots conformes nous permettent de mieux prévoir et planifier leur mouvement, tandis que la conception d'articulation hautement personnalisable, grâce à la fabrication couche-par-couche et aux processus de fabrication 2D précis, permet d'intégrer des DoF multiples pour atteindre le niveau de conformité requis.

Pour actionner efficacement de multiples DoFs de robogami, il est impératif d'intégrer des moyens d'actionnement ou de transmission d'énergie dans le corps du robot. La fabrication couche-par-couche de robogami permet d'incorporer des couches de matériaux fonctionnels dans la structure du robot pour obtenir des procédés d'actionnement doux qui répondent aux exigences des appareils mettables : vitesse d'actionnement, capacité de charge et amplitude de mouvement. Dans cette thèse, nous abordons le défi de l'actionnement doux d'articulation individuel et de l'actionnement synchronisé de séries d'articulations pour suivre une trajectoire souhaitée ou effectuer une reconfiguration spécifique en développant des couches fonctionnelles qui exploitent des caractéristiques uniques de matériaux intelligents.

La conformité des robots intrinsèquement souples provient des propriétés élastiques des matériaux constitutifs. En fonction de l'application, des matériaux avec différents niveaux de rigidité sont utilisés pour obtenir un compromis entre la transparence mécanique et la capacité de charge. Un robot portatif doit couvrir une large gamme de transparents mécaniques et de capacités de charge pour accomplir différentes tâches, p. ex. offrir un niveau de soutien variable à différents stades de la réhabilitation. Pour élargir l'application d'un

robot conformable pour répondre aux exigences de différentes tâches, il est nécessaire de développer des moyens de contrôle de rigidité pour ses segments ou ces articulations. En incorporant des couches de matériaux fonctionnels avec une rigidité contrôlable dans les robogamis, nous développons des robots qui peuvent changer leur mode d'interaction et de conformité en fonction de leur tâche.
La conformité intrinsèque des robots conformables garantit une interaction sûre avec l'environnement. La conformité et la multitude de DoFs, cependant, complique l'estimation de la configuration du robot et les forces de contact à partir du modèle. Ainsi, pour une interaction efficace avec l'environnement, il est nécessaire d'intégrer un réseau d'éléments de détection dans le robot pour observer sa configuration, les forces de contact et les déplacements aux points de contact. Étant donné les limites de la taille, de la forme et de la gamme de mesure requise, il est impératif de concevoir et de fabriquer des capteurs personnalisés. Nous avons développé des capteurs minces (au-dessous de 100 μm) avec une conception adaptable et évolutive pour une mesure précise d'angle de joint dans les robogamis qui sont compatibles avec leurs conditions de travail exigeantes, c'est-à-dire la plage de déformation et de variation de température. En utilisant les mêmes principes de détection, nous avons également développé des capteurs extensibles' minces et mécaniquement transparents qui peuvent être utilisés dans des réseaux d'éléments de détection dans des appareils mettables pour mesurer les mouvements du corps.
Les principales contributions de cette thèse sont :

- Etude et development du robogami comme un cadre de conception pour des robots conformables avec reconfiguration et conformité programmable.
- Conception et validation de solutions d'actionnement basées sur des matériaux intelligents pour l'actionnement indépendant des articulations de robogami.
- Adoption de propriétés mécaniques variables des matériaux intelligents pour le réglage de la rigidité des articulations de robogami et de la conformité globale du robot.
- Développement de méthodes de détection personnalisées pour mesurer les angles des articulations de robogami et les capteurs extensibles sur la base des mêmes principes utilisés pour mesurer les mouvements du corps.

  Nous croyons que ces contributions facilitent certains des principaux défis dans l'application efficace de robogami pour une interaction sûre et pourtant utile avec des humains dans des appareils mettable. Les composants hautement personnalisables peuvent également être utilisés dans des cadres de conception autres que les robogamis et d'autres applications où la conformité est nécessaire.

Mots clefs : Robogami, fabrication couche-par-couche, matériaux fonctionnels, conformité programmable, robots conformables

Contents

Acknowledgements i

Abstract (English/Français) iii

List of figures xi

List of tables xv

Introduction 1

1 Robogamis: Design and fabrication 9
- 1.1 Introduction . . . 9
- 1.2 Robogami Joint design . . . 11
- 1.3 Layer-by-layer manufacturing . . . 15
- 1.4 Conclusion . . . 18

2 Robogamis: Sensing solutions 19
- 2.1 Introduction . . . 20
- 2.2 Carbon particle based curvature sensors . . . 22
  - 2.2.1 Design and fabrication . . . 22
  - 2.2.2 Model and characterization . . . 25
  - 2.2.3 Comparison of carbon particle based sensors . . . 32
- 2.3 Carbon particle based stretchable sensors . . . 33
- 2.4 Metal based curvature sensor . . . 35
  - 2.4.1 Sensor design and model . . . 35
  - 2.4.2 Characterization . . . 37
- 2.5 Metal based stretchable sensor . . . 40
  - 2.5.1 Design and working Principle . . . 40
  - 2.5.2 Characterization . . . 50
- 2.6 Conclusion . . . 52

3 Robogamis: smart materials for soft actuation and compliance control 55
- 3.1 Introduction . . . 55
  - 3.1.1 Methods of soft actuation . . . 56
  - 3.1.2 Methods of compliance control . . . 57

3.2 Shape memory alloy for soft actuation of robogami joints . . . 58
3.2.1 SMA actuator model . . . 59
3.2.2 SMA actuator characterization . . . 64
3.2.3 Feedback control of a SMA actuated Robogami joint . . . 65
3.3 Shape memory polymer for stiffness control in soft robots . . . 68
3.3.1 SMP layer with embedded heater . . . 68
3.3.2 Improving shape recovery by embedding SMP in silicone rubber . . . 71
3.3.3 Glass-fiber frame for ASL . . . 74
3.3.4 Temperature feedback for controlling the stiffness of ASL . . . 77
3.4 Conclusion . . . 78

4 Robogamis: trajectory planning and compliance control 81
4.1 Introduction . . . 82
4.2 Robotic manipulator with lockable joints . . . 84
4.2.1 Joint design and actuation mechanism . . . 85
4.2.2 Sequential actuation of joints for reaching points in the workspace . . . 87
4.3 Robogamis modules with adjustable stiffness joints . . . 89
4.3.1 Model and parameter characterization of a tendon-driven robogami with adjustable stiffness joints . . . 90
4.3.2 Experimental result and model verification . . . 97
4.4 Two-fingered robogami gripper with compliance control . . . 101
4.4.1 Tendon-driven robogami finger with adjustable stiffness joints . . . 101
4.4.2 Under-actuated robogami gripper with compliance control . . . 105
4.5 Three-fingered robogami gripper with multiple grasp modes . . . 109
4.6 Conclusion . . . 113

5 Robogamis: towards wearable devices for robot-assisted facial rehabilitation 115
5.1 Introduction . . . 115
5.2 Stretchable sensors for wearable devices . . . 117
5.3 SMA actuated robogami platform for soft actuation in a wearable device for face 119
5.4 Tendon-driven robogami platform for programmable soft actuation in rehabilitative devices . . . 120
5.4.1 Compliant actuation using tendon-driven robogami . . . 121
5.5 Soft sensing and actuation for facial rehabilitation . . . 125
5.6 Conclusion . . . 126

6 Concluding remarks and future direction of research 129
6.1 Concluding remarks . . . 129
6.2 Future directions of research . . . 132

A SMA actuated robogami crawler 135
A.1 Crawler design and stepping sequence . . . 135
A.2 Crawler motion . . . 137

B SPA with adjustable stiffness layers for multi-DoF actuation **139**
B.1 Actuation concept and fabrication process 139
B.2 Actuator design and its model 141
B.3 Experimental results 143
B.3.1 Temperature gradient in SMP and its transient response 144
B.3.2 Different actuation modes of a SPA with embedded ASLs 145

Bibliography **160**

Curriculum Vitae **161**

List of Figures

1 Examples of assistive robots. 1
2 Examples of assistive robots utilizing novel methods of manufacturing, sensing, or actuation. 2
3 Robogami, a low profile platform with multiple DoFs for developing wearable devices. 3

1.1 Examples of origami robots. 10
1.2 Castellated pattern of the robogami joints. 13
1.3 Deformation of the elastic elements with motion of the robogami joints. 14
1.4 Layer-by-layer manufacturing of a SMA actuated robogami. 16
1.5 Layer-by-layer manufacturing of tendon driven robogamis. 17
1.6 Overview of the micro-machining laser system. 18

2.1 Robogami joint angle sensing solutions. 20
2.2 Stretchable sensing solutions for measuring body movement. 21
2.3 Fabrication process of the conductive silicone sensors. 23
2.4 Fabrication process of the carbon ink sensors. 24
2.5 Design of different carbon ink sensors. 24
2.6 The equivalent mechanical model for the carbon particle based sensors. 26
2.7 Transient response of a carbon ink curvature sensor. 27
2.8 Elements of the carbon based sensor model capturing the transient response. . 27
2.9 Transient response of a conductive silicone curvature sensor. 28
2.10 Elements of the model capturing the recoverable drift in the sensor response. . 30
2.11 Recoverable drift in a carbon based sensor. 30
2.12 Quasi static response of a carbon ink sensor. 31
2.13 Carbon ink stretchable sensor 34
2.14 Carbon ink stretchable sensor for measuring facial movements. 34
2.15 Schematic of the metal based curvature sensor. 36
2.16 Metal curvature sensor measurements. 37
2.17 Three major effects of temperature on the metal based sensors. 38
2.18 Corrected measurements from two sensors versus the joint angle. 39
2.19 Bending deformation of the micro-beams in the mesh structure of the stretchable sensor. 41
2.20 Twist buckling of the micro-beams in a stretched mesh sensor. 42

2.21 The twist angle as a function of stretch in the sensor. 43
2.22 Twist direction of micro-beams. 44
2.23 Fabrication process of metal based stretchable sensors 45
2.24 Effect of different parts of the sensor pattern on the electrical resistance. 46
2.25 Bending of a single micro-beam 47
2.26 Estimated electrical resistance change of the stretchable sensor. 50
2.27 Comparing the sensitivity of stretch sensors with different patterns. 51
2.28 Resistance change as a function of stretch in the sensor. 52

3.1 Comparing the energy density and the range of motion of different smart materials. 56
3.2 Comparing the work density and actuation frequency of different smart materials. 57
3.3 Roboagmi Joint with bidirectional actuation using antagonistic SMA actuators. 59
3.4 Thermal analysis of SMA actuator. 60
3.5 Working principle of SMA actuators. 62
3.6 Estimated torque of sheet SMA bending actuator. 63
3.7 Test setup for mechanical characterization of SMA actuators. 64
3.8 SMA actuator characterization result. 65
3.9 Curvature sensor characterization for feedback control of SMA actuated modules. 66
3.10 Feedback control of a SMA actuated Robogami joint. 66
3.11 Variability of elasticity modulus of SMP MM5520. 68
3.12 Fabrication process of the SMP layer with an embedded heater. 69
3.13 SMP layer residual strain after loading cycles. 70
3.14 Stiffness variability of a SMP layer with embedded heater. 70
3.15 Silicone embedded SMP with high recovery rate and repeatable response. . . . 71
3.16 Silicone embedded SMP in linear stiffness test setup. 73
3.17 Silicone embedded SMP characterization test results. 73
3.18 Fabrication process of the final ASL design 74
3.19 Elastic behavior of the final ASL design at different temperatures 75
3.20 Stiffness of the final ASL design. 76
3.21 ASL temperature versus heater's electrical resistance (quasi-static condition) . 77
3.22 Temperature estimation from the heater's electrical resistance and the thermistors (transient response) 78

4.1 Examples of robotic hands and grippers that use soft actuation methods. 82
4.2 Compromise between DoF and compliance on one side and the force magnitude and precision of the robotic hands. 83
4.3 Under-actuated manipulator with SMP joints. 85
4.4 Schematic of the under-actuated manipulator and the deformation of the SMP layers in each joint. 86
4.5 Joint stiffness variation with temperature using variable stiffness of the SMP layers. 87
4.6 Sequential activation of joints in an under-actuated manipulator. 88
4.7 Robogami joint with adjustable stiffness layer and embedded curvature senors. 89
4.8 Robogami manipulator with adjustable stiffness joints. 90

4.9 Schematic of robogami manipulator actuation. 91
4.10 Tendon friction characterization. 95
4.11 Characterizing joint stiffness correction factors. 96
4.12 Configuration control in the robogami manipulator in simultaneous actuation of all joints. 98
4.13 Compliance control of the robogami manipulator. 100
4.14 Schematic of the robogami design used in studying compliance control. 102
4.15 Compliance control of robogami's end-effector, simulation results. 103
4.16 Compliance control of the end-effector of the robogami finger, experiment results. 104
4.17 Two-fingered robogmai gripper with compliance control. 105
4.18 Power grasp using the robogami gripper. 106
4.19 Precision grasp using robogami gripper. 107
4.20 Grasp compliance control using the robogami's adjustable stiffness joints. . . . 108
4.21 Three-fingered robogami gripper with multiple grasp modes. 109
4.22 Schematic of the three-fingered robogami gripper. 110
4.23 Control scheme for determining the initial configuration and the actuation pattern. 111

5.1 Examples of sensory and rehabilitative devices for the face. 116
5.2 Stretchable sensor for measuring facial movements. 118
5.3 SMA actuated wearable robogami. 119
5.4 The conceptual design of an under-actuated robogami for facial rehabilitation. 120
5.5 Under-actuated robogami with programmable trajectory and compliance. . . . 121
5.6 Compliance control in the tendon-driven robogami, simulation results. 122
5.7 Comparison of the compliance in different directions at different stiffness settings. 123
5.8 Compliance control in the tendon-driven robogami, experimental results. . . . 124
5.9 Preliminary experiments of soft robogami actuation in contact with the face. . 125
5.10 Coupling of the soft stretchable sensor and the robogami actuation. 126

6.1 Conductive silicone pressure sensors. 133
6.2 Example of a motorized robogami gripper. 134
6.3 Conceptual design of a surgical tool based on robogami platform with adjustable compliance. 134

A.1 SMA actuated robogami Crawler. 136
A.2 Stepping sequence of the crawler. 136
A.3 Snapshots of crawler's motion. 137

B.1 Soft pneumatic actuator with a single chamber and multiple modes of operation. 140
B.2 Fabrication process of SPA with embedded SMP layers. 140
B.3 Elongation and forces produced in the SPA walls. 141
B.4 Workspace of the SPA actuator with controllable mode of operation. 143
B.5 Temperature gradient in SMP sample. 144
B.6 Thermal time response of ASL. 145

B.7 SPA motion at different temperature settings and input pressures. 146
B.8 Characterizing SPA's bending angle in different modes of actuation. 146
B.9 Characterizing SPA's length in different modes of actuation. 147

List of Tables

1.1 Tendon-driven robogami joints. 12

2.1 Performance of different types of carbon particle based sensors. 32

3.1 Comparison of different methods of stiffness control 58

4.1 Design parameters for robogami modules. 92
4.2 Design parameters for the two-fingered robogami gripper. 102
4.3 Design parameters for the three-fingered robogami gripper. 110
4.4 Different grasp modes of the three finger robogami gripper. 113

5.1 Design parameters for the robogami for soft facial actuation. 122

A.1 Crawler's joint set points for performing the stepping motion. 137

B.1 Temperature and pressure settings in different steps of characterization. 145

List of acronyms

Robogami: robotic origami.

DoF: degree of freedom.

SMA: shape memory alloy.

SMP: shape memory polymer.

ASL: adjustable stiffness layer.

CI: carbon ink.

CSC: carbon silicone composite.

SPA: soft pneumatic actuator.

Introduction

The rising demand for safe human-robot interaction in daily tasks has motivated significant research efforts in the field of robotics towards robots capable of replicating complex human movements. Researchers are targeting broad applications such as exoskeletons for increased power or stamina, as well as more specific applications such as rehabilitation, and haptic interfaces. With the ever increasing average age of the population, assistive and rehabilitative robots are expected to make a significant impact in improving daily life. Small actuation

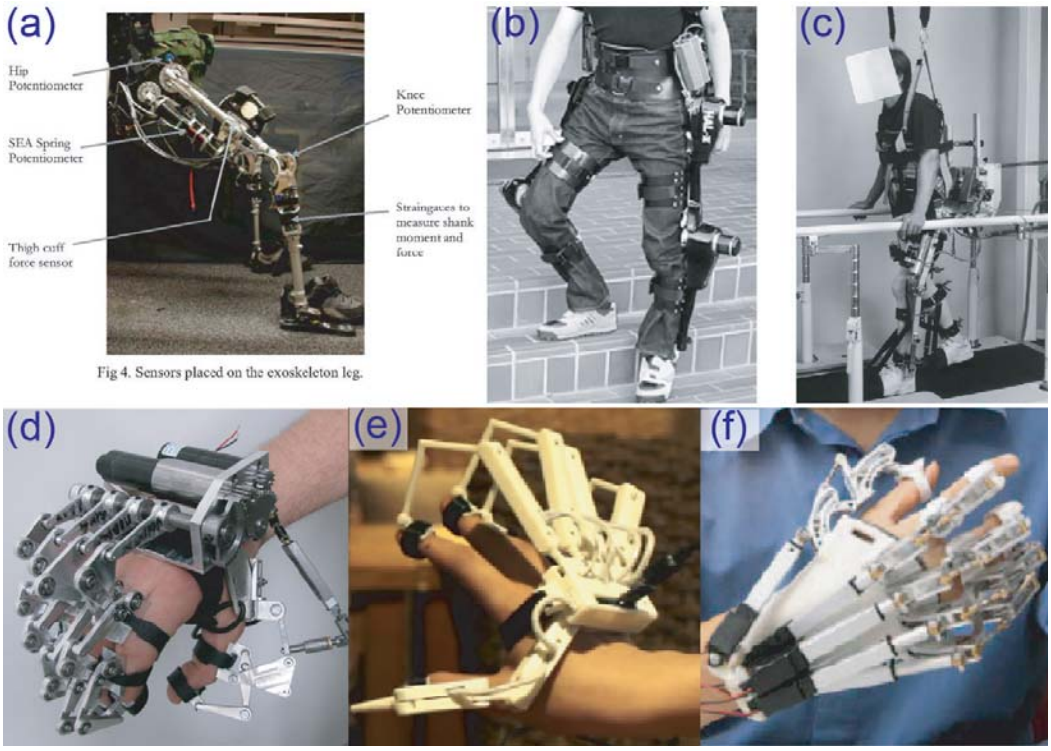

Figure 1: Examples of assistive robots. (a) Driven gait orthosis for improvement of locomotor training in paraplegic patients [1]. (b) Robot suit HAL for providing active assistance [2]. (c) Under-actuated exoskeleton for load carrying augmentation [3]. (d) Robotic hand exoskeleton for bilateral rehabilitation [4]. (e) Hand exoskeleton for virtual reality applications [5]. (f) EMG-driven exoskeleton robot for stroke rehabilitation [6]

units with high power density, novel sensing methods, miniaturized controllers, and the expanding literature on mechanisms and controllers for safe human-robot interaction has led to a surge of assistive robots for different body parts. Fig. 1 presents examples of robots with applications in rehabilitation, assistive devices for increasing power or stamina, and virtual reality. Although considerably more compact in volume compared to their earlier stationary counterparts, these devices are still bulky and cumbersome to wear. Moreover, their rigid body and limited number of degrees of freedom (DoFs) limits their capability to replicate complex human motions in all aspects.

Figure 2: Examples of assistive robots utilizing novel methods of manufacturing, sensing, or actuation. (a) Soft sensing elements for measuring lower body movements [7]. (b) Soft tendon actuation in an assistive device [8]. (c) Soft exoskeleton powered by pneumatic actuators [9]. (d) Hand exoskeleton for rehabilitation, driven by a three-layered sliding spring mechanism [10]. (e) Tendon driven hand exoskeleton that uses novel fabrication methods for fast and cheap customized manufacturing [11]. (f) Hand exoskeleton powered by soft pneumatic actuators [12]. (g) Pneumatically actuated exoskeleton [13]. (h) Music glove uses sensory data to assess the performance of patients [14]. (i) Soft sensing elements embedded in a silicone glove. [15]

In recent years, there has been a paradigm shift in the design and manufacturing of assistive devices towards making them wearable and inherently compliant. This shift has mainly been powered by the novel soft and stretchable sensing and soft actuation technologies that are replacing the conventional means of sensing and actuation. The new manufacturing processes for these sensors and actuators have also contributed to their popularity with the roboticists by making the design and fabrication of customized actuators and sensors cheap and fast, which allows for effective iterations towards design improvements. Fig. 2 presents examples of a few wearable devices utilizing these technologies for sensing and actuation.

In this research, I focus on an alternative platform for compliant robots with multiple DoFs that is inspired by the art of paper folding [16–24]. **Robotic origamis**, robogamis, are thin robots with many DoFs driven by soft methods of actuation. Compared to other design frameworks, distinctive features of robogamis are: thin body with different functional layers embedded in the structure, multiple but finite DoFs, and acute level of accuracy that is owed to the precise quasi-2D manufacturing techniques. These features make robogamis a unique platform for designing wearable devices for body parts such as the face, with its complex morphology and movements, Fig. 3. The finite DoFs in robogamis make the behavior of these robots more predictable and easier to control compared to actuation methods with entirely soft bodies. The scalable joint design and manufacturing process allow the required DoFs to be embedded in the robogami to conform to the shape of the face and follow or replicate its natural motions.

The novel designs and manufacturing processes have contributed significantly to making the production of customized robots cheap and fast. Effective application of these methods, however, relies on developing enabling technologies compatible with these novel design and manufacturing frameworks. Enabling technologies can be divided into sensing, actuation, computation, and other categories [25–27]. The goals of this thesis are to adjust the design of

(a) **(b)**

Figure 3: Robogami, a low profile platform with multiple DoFs for developing wearable devices. (a) Different functional layers are embedded in the thin structure of the robot. (b) The robot can reconfigure to the face's shape and perform different tasks, depending on the embedded components.

existing technologies, when available, and to develop new technologies, when missing, for application in the robogami framework towards developing compliant wearable devices. I will mainly focus on enabling sensing and actuation technologies. The inherent conformity and compliance of the proposed framework simplifies the computation problem at the interaction level by making the robot responsive to external loads and disturbances and in this sense allows us to partially implement the controller in the robot's hardware. The proposed technologies in this thesis are developed for application in robogamis but their adaptable and scalable designs allow application to other design frameworks of soft robots and wearable devices.

Problem statement

The goal of my PhD research was to study and develop essential robotic components towards a wearable device with multiple DoFs focusing on technologies applicable to rehabilitative devices. This specific application requires a robot that can provide large interaction forces at initial stages of therapy and then transform to a softer system with high mechanical transparency, for the whole or a part of motion, at the final stages of the rehabilitation. I focused on the following challenges to realize such a robotic device:

1- Design methodology for **low profile** robots with interactive and compliant motions.

2- Study of different sensing principles and performance validation for **reliable and compact sensing** technologies for controlling the configuration of the robot and monitoring the end effector displacement and applied forces with a minimum effect on robot's performance.

3- Design a framework based on the performance study and model of functional materials for developing adaptable and scalable methods of **soft actuation** and **compliance control**.

Robogamis offer a low profile platform for developing compliant robots. The manufacturing process of the robogamis allows us to scale the joints from few centimeters to few millimeters and also to embed different functional layers to meet the requirements of size, number of DoFs, and functionality. So far, the robogami framework has been mainly used for mobile robots and other applications where motions are rather simple and mainly blocked at the joint limit. Moreover, target forces were mostly large enough to support the robot's mass (few grams). To modify this framework for providing larger output forces and complex precise motions with inherent compliance is the first challenge, which requires modification of the actuation principle, the joint design, and the transmission mechanism. Based on the requirements of a wearable device for the face [28], we aim for a maximum loading capacity of a few Newtons with the moment arm in the 10 cm range. Novel actuation methods are therefore required to provide this load capacity and the necessary DoFs. Contingent on the the size and weight limitations of the robot, it is imperative to embed some aspects of the control and actuation systems in the robot using functional materials. This requires refining the design of the functional material layer and the auxiliary layers for its activation.

Effective and safe interaction relies on the feedback from the robot itself and the resulting forces and deformations experienced by the environment. The size, number of DoFs, and compatibility with the fabrication process limit our options for sensors and make it necessary to develop customized sensors for joint angles, overall displacement of the end effector, and for the contact forces. Therefore, a second challenge is to develop these sensors with designs and manufacturing processes compatible with robogamis. We also need to analyze and model the behavior of these sensors, and validate their performance in an integrated system with different functional layers.

Comprising materials of soft robots are chosen to achieve a desired compromise between the compliance and maximum interaction forces. In many applications, such as robot-assisted rehabilitation, however, a robot should cover a wide range of transparency and output forces depending on the task. To overcome a third challenge of developing a soft actuation method with compliance control we need to embed layers of functional materials with adjustable mechanical properties into the robogami structure. This requires a study of material properties, developing models for their behaviors, and refining their design for successful integration into robogamis.

In the next Section I present the outline of the thesis. For each Chapter my approach towards resolving the above challenges and the contributions are discussed.

Thesis outline

Chapter 1, **Robogamis: Design and fabrication**:

The robogami layer-by-layer manufacturing process and joint design are presented in this Chapter. The unique manufacturing process enables the design and fabrication of robots with multiple DoFs with desired functions embedded. I present novel tendon-driven joints with adjustable stiffness which allow us to place rotational DoFs along any direction in the plane of the robot and in the normal direction. The main contributions of Chapter 1 are:

- Introducing tendon-driven robogami joints with adjustable compliance for rotational DoFs along three orthogonal axes.
- Studying the compliance of the robogami joints and their loading capacity by analyzing the deformations of the hinge and adjustable stiffness layers.

Chapter 2, **Robogamis: Sensing solutions**:

This Chapter presents sensing solutions for measuring the robogami joint angles. Two sensing principles are considered: piezo-resistivity of carbon polymer composites and resistance variation in a metal film under strain. The first method offers lower cost, easier manufacturing of networks of sensing elements, and high sensitivity to strain. Metal sensors, on the other

hand, offer higher accuracy and the feasibility of built-in temperature compensation. I study the response of both sensors and propose models unique in their coverage of different aspects of the sensor's response.

The same sensing principles are then used in a novel stretchable sensor design that allow us to measure body movements. In these sensors a mesh structure transforms the linear elongation of the sensor into bending of micro-beams. The proposed stretchable sensors are thin (below 100 μm), mechanically transparent, and suitable for application in sensing networks to measure body movements. The working principle of the sensors, the model of their behavior, and the results of characterization experiments are presented in this Chapter. The main contributions of Chapter 2 are:

- Introducing joint angle sensors compatible with robogami's size requirements and the layer-by-layer manufacturing process.
- Introducing novel stretchable sensors, based on the same sensing principles for joint angle sensors, permitting body movement measurement.
- Studying different aspects of the sensors behavior and presenting appropriate comprehensive models.
- Validating the sensors repeatable measurements in integrated systems.

Chapter 3, **Robogamis: smart materials for soft actuation and compliance control**:

Methods of actuation and compliance control using functional materials are presented. For the individual actuation of a joint, a **shape memory alloy** (SMA) sheet actuator that is activated by a stretchable heater is proposed and its performance is characterized. A **shape memory polymer** (SMP) with significant stiffness variability around its glass transition temperature is used to control joint stiffness and compliance of the robogamis. The main contributions of Chapter 3 are:

- Studying and modeling the thermal and mechanical responses of the SMA sheet actuators and refining the design accordingly.
- Developing **adjustable stiffness layer** (ASL) with a SMP core to control the compliance of joints and segments in soft robots.
- Studying the behavior of ASL and verifying repeatable response and effective stiffness control using an embedded heater in the SMP.

Chapter 4, **Robogamis: trajectory planning and compliance control**:

The limited load capacity and slow response of SMA actuators confines their application range and necessitates another actuation method. I propose tendon-driven robogami joints as an alternate actuation method. To control the energy distribution in under-actuated robogamis, ASLs are used for modulating joints' compliance. I developed under-actuated robotic grippers with multiple fingers as a platform to study the performance and refine the design of tendon-driven robogamis with ASLs. The main contributions of Chapter 4 are:

- Developing a detailed models for under-actuated robogamis with adjustable stiffness joints.
- Studying the behavior of different sequences of joints and demonstrating soft actuation with programmable trajectory and compliance.
- Designing and manufacturing multi-fingered robogami grippers with adjustable modes of operation using material properties.

Chapter 5, **Robogamis: towards wearable devices for robot-assisted facial rehabilitation**:

The first prototype of a rehabilitative device based on the robogami platform is presented as a proof of concept for the feasibility of using robogamis for performing programmable reconfiguration with a desired level of compliance. Stretchable sensors are used for measuring facial movements with a minimum effect on its natural movements; feedback was used to drive the robogami. The main contributions of Chapter 5 are:

- Demonstrating soft actuation with programmable compliance for applying required forces to move the face.
- Confirming the feasibility of using stretchable sensors to measure facial movements with minimum effect on natural motion.

1 Robogamis: Design and fabrication

In this Chapter, we introduce the robogami platform and its layer-by-layer manufacturing process. Robogamis are low profile robots that are fabricated by integrating layers with different functions. We use accurate 2D fabrication methods to process tiny features (down to 50 μm) on each layer. The high accuracy of the manufacturing process allows us to design small robots with multiple DoFs and desired functions (sensing, actuation, compliance control) embedded. The low profile and multitude of DoFs driven by soft actuators make robogamis a desirable platform to develop wearable devices for safe human-robot interaction. In this Chapter after an overview of the state of the art, we present the robogami joint design and its layer-by-layer manufacturing process.

1.1 Introduction

Origami robots are characterized by their layer-by-layer manufacturing process, their thin profile in unfolded state, and their multiple DoFs which are defined by a folding pattern of a conformable hinge material. Fig. 1.1 (a-c) presents three examples of 3D reconfiguration of thin robotic origami sheets. In these examples the transformation is powered by the active material embedded in the joints. In Fig. 1.1 (a-b) the bending SMA sheet actuators define the joints' axis of rotation and their position. The independent actuation of the joints which is possible through significant energy density of the SMA actuators allows these robots to reconfigure to different 3D shapes. The complexity of the actuation and position control of the joints along with the limited load capacity, however, confine the application range of this family of robogamis. Fig. 1.1 (c) presents another similar actuation method for robogami

The material of this Chapter is from the following self-authored publications:
[29] **A. Firouzeh**, et al., "Sensor and actuator integrated low-profile robotic origami", IROS 2013.
[30] **A. Firouzeh** and J. Paik, "Robogami: A fully integrated low-profile robotic origami", ASME Mechanisms and Robotics 2015.
[31] **A. Firouzeh** and J. Paik, "An under-actuated origami gripper with adjustable stiffness joints for multiple grasp modes", Smart Materials and Structures 2017.

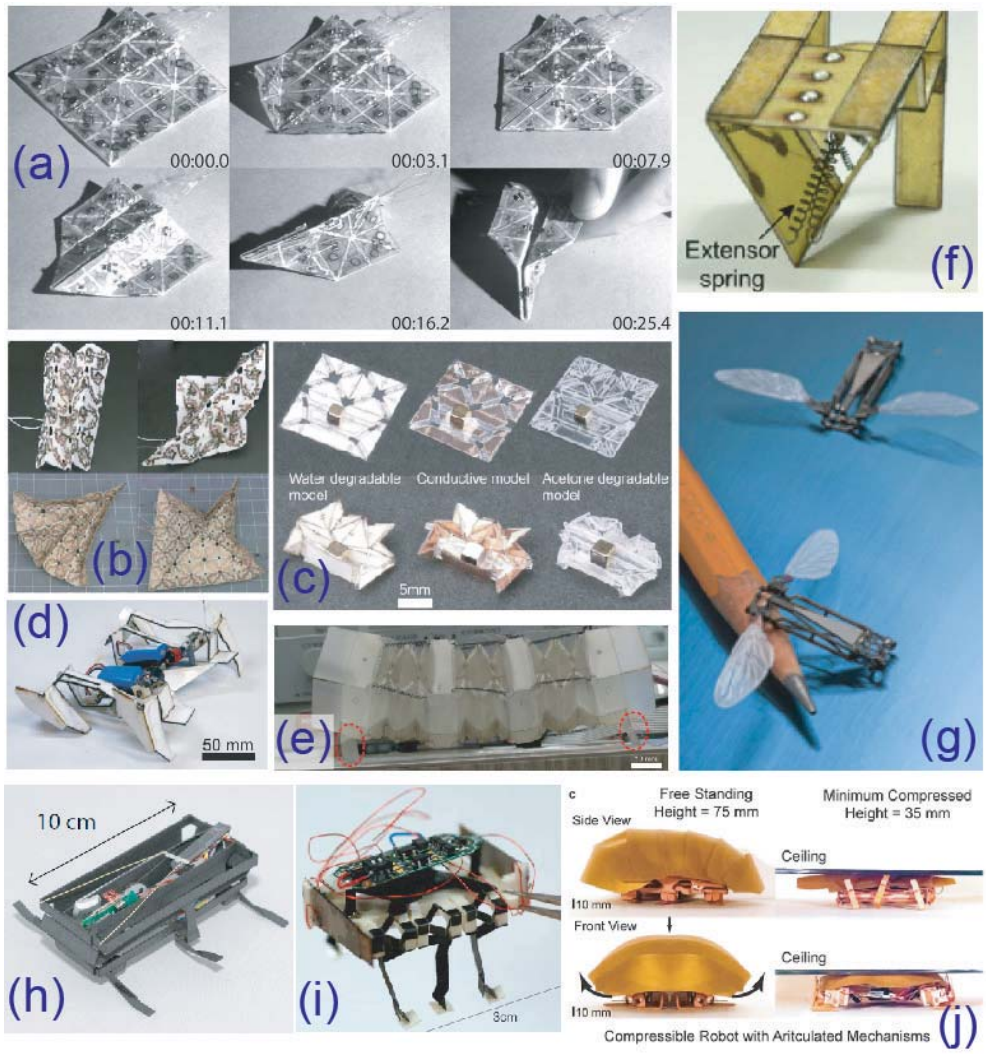

Figure 1.1: Few example of origami robots. (a,b) Robogami sheets with SMA actuated joints capable of multiple shape transformations [17, 18]. (c) Transformations of sheet robogamis powered by shrinkage of polymer layers embedded in the structure [16]. (d) Origami mechanism for transforming motor power to desired leg motion. The initial transformation of the robogami in this case is done using thermal shrinkage of an embedded polymer layer [19]. (e) Actuation of multiple origami joints, which form a spring element, using SMA coils [20]. (f) Robogami jumper [21]. (g) The scalability of the robogami stucture and the actuation method based on smart materials is well illustrated in the RoboBee [22]. (h) An example of miniaturized walking robot using robogami structure [23]. (i) Scaled down version of the same design in (h) [24]. (j) Robogamis for mimicking complex locomotion modes of insects [32].

reconfiguration: shrinkage of thermally activated polymers transforms the sheet in this example. This mode of reconfiguration is desirable in specific for initial reconfiguration of the robot from its initial flat state. The unique manufacturing technique of the robogamis which is based on processing individual layers using precise quasi-2D manufacturing techniques

and integrating them into a robotic sheet allows for precise placement of DoFs to achieve any desired transformations.

Origami structures can also be used as the underlying mechanism for directing robot's input actuation for preforming a desired motions, Fig. 1.1 (d-j). These examples highlight few important features of robogamis: the scalability, the versatility of the actuation methods, and the adaptability of design. These features along with low cost and easy manufacturing has made robogamis a desired frame for fast prototyping of robots as test platforms in different fields such as bio-inspired robotics [32, 33]. So far this framework has been mainly used in mobile robots and other applications where the motions are rather simple and mainly blocked at the joint limit. Moreover target forces were mostly large enough to support robot's mass (few grams). To use robogamis in human size applications (e.g. wearable devices), we would require different actuation methods compatible with the requirements of these applications and other functional layers for sensing the position and controlling the compliance of the joints.

We considered two types of robogami joints: the SMA actuated joints, in which the joint axis of rotation and position is defined by the shape of sheet SMA actuator, and tendon driven robogami joints in which the DoFs are defined by the folding pattern of a polyimide sheet. The manufacturing process of these robogamis are similar but their design and load capacity, hence their application, are very different. In what follows, first the design of the tendon driven joints, which is more complex compared to the SMA actuated joints, is presented and then the layer-by-layer manufacturing process and 2D fabrication processes used in this research are presented in detail.

1.2 Robogami Joint design

Robogamis are thin robotic sheets with folding joints in the plane of the robot. The DoFs in robogamis are defined by the folding pattern of a hinge material. In the case of SMA actuated robogamis the active material used in the hinge area defines the axis of rotation and also actuates the joint. In tendon driven robogamis, the joints are defined by a folding pattern that a stiff structure imposes on the polymer sheet. Here, the joint design of the latter is presented.

The first two rows in Table 1.1 presents tendon driven robogami joints of this kind, the top layer in figures of Table 1.1 are made transparent to highlight the routing of the tendon in the tiles. In these joints, we used a castellated pattern to fix the axis of rotation and to increase the lateral stability of the joints. The axis of rotation falls between the tips of the castellated structure from the two tiles and on the polyimide hinge layer, Fig. 1.2. The gap between the tips of the castellated design should be small enough to keep the axis of rotation fixed and on the polyimide layer. Still, this distance should be large enough to ensure the mechanical endurance of the polyimide hinge layer in repeated cycles of loading. In the present design, this distance was set to 50 μm which yielded robust and repeatable motion.

Table 1.1: Robogami joint designs for rotation along the 3 orthogonal axis. For the joints along x and y axis, the castellated pattern of the glass fiber layer defines the axis of rotation on the polyimide layer. For the z axis joints the design is different and the rolling motion of the two adjacent tiles defines the axis of rotation. The top layer is made transparent to depict the tendon routing.

Joint axis	Initial configuration	Joint displacement	View along the axis
y-axis	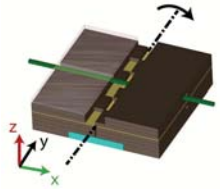	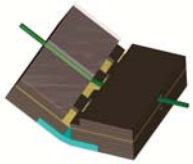	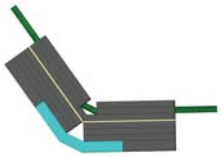
x-axis	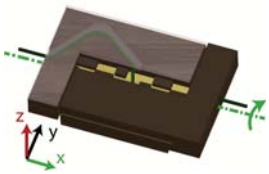	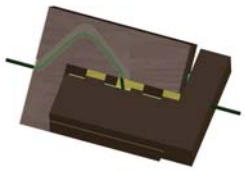	
z-axis	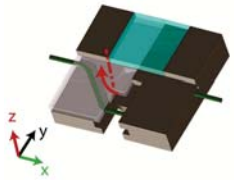		

Fig. 1.2 presents robogami joint's castellated pattern which defines the joint axis and its position limit [34]. A zoomed in view illustrates the design parameters for setting joint limits. By modulating the length, $g/2$, and the height, h, of the teeth in this design we can set the joint limits according to:

$$\theta_{JointLimit} = sin^{-1}(\frac{g}{2h}) \tag{1.1}$$

(1.1) will be used throughout the thesis for assigning desired joint limits to prevent over strain in the components comprising each joint. In this research, we mainly used robogami joints in series to form manipulators or robotic fingers. Introducing a joint design with the axis of rotation outside the plane of the robot permits simple sequence of joints to follow complex trajectories. For the rotation along the z axis, which is presented in the third row of Table 1.1, the rolling contact point between the two tiles defines the axis of rotation. The balance between the forces in the elastic element and the tendon determines the position of the joint and provides structural stability.

The compliance of these joints is determined by the stiffness of the elastic elements. In Chapter

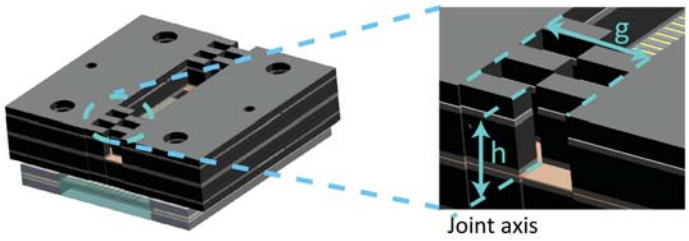

Figure 1.2: Castellated pattern of robogami joint defines the joint axis and the limit of motion. A zoomed in view illustrates the design parameters for setting joint limits.

3 we present the design of an ASL which is used to control the stiffness of the joints. Here, we study the motion of the joints and the deformation of the elastic elements to determine loading capacity, the range of motion, and the compliance of the joints. The torque in the robogami joints along x and y axis are transferred through the tension and compression of the polyimide layer and the ASL. The main failure modes for these joints are the over strain in the hinge layer and the buckling of the ASL. The calculation in this Section is done for the unit width of the hinge layer and unit distance between polyimide layer and ASL. For the designs that are studied in Chapter 4 and 5 these values are scaled according to the design parameters and are used to determine the safe loading conditions.

Given the small length of the polyimide layer between the tips of the castellated pattern on the two sides, buckling is not a failure mode for hinge layer and over strain in tension is expected to be the main failure mode which is also concordant with the test results. The hinges of the robogami are made of 0.125 mm Polyimide sheet. Considering the ultimate strength of the material (169 kPa) this layer can hold upto 21.3 N in its unit width. The maximum torque that the hinge layer can hold is $21.3wh$ $N.m$ where w is the width of the Polyimide layer and h is its distance from the ASL.

The second mode of failure is the buckling of the elastic layer under compression. In the stiff mode a thin, 500 μm, polymer layer, SMP, is the main load bearing element in the ASL. (1.2) estimates the critical buckling load for this layer.

$$F_{bcuckling} = \frac{n\pi^2 EI}{L^2} \tag{1.2}$$

Considering the modulus of elasticity of the SMP layer in the stiff state, (1.2) predicts the buckling load to be 42.8 N/mm for the unit width of the layer which is twice the maximum allowed force for the polyimide sheet. So the limit defined by the strength of the polyimide layer is the upper bound of the load bearing capacity of the joints with polyimide hinges.

For the joints along the z axis, the torque in positive direction is transferred through the contact

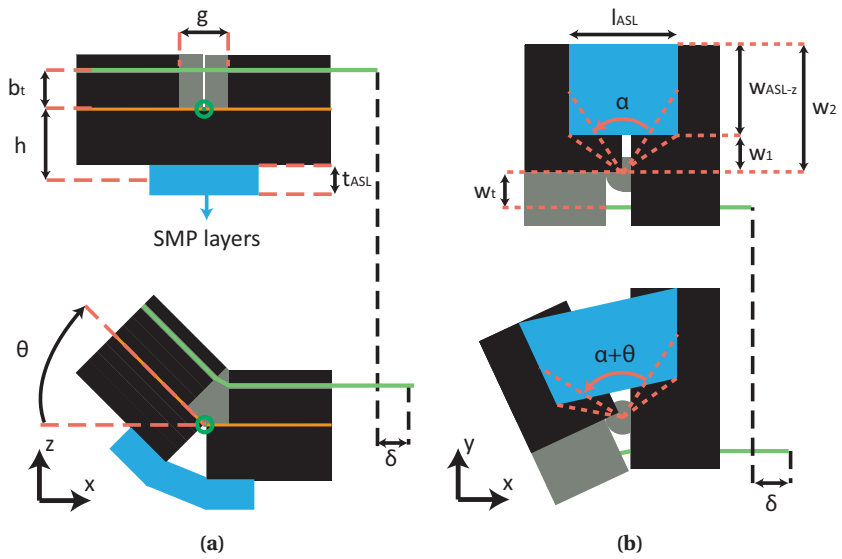

Figure 1.3: The schematic of the joint motion and deformation of ASL. (a) Robogami joints along x and y axis. (b) Robogami joint along z axis.

force and tension in the elastic layer. A more critical case for these joints is the torque in the negative direction which puts the elastic layer in compression. The buckling of the elastic layer determines the maximum torque for joints along the z axis: $1.8w^2$. In a sequence of joints usually the y axis joints bear the maximum load since the moment arm of the forces are larger for these joints. So the admissible torque for z axis joints, though smaller, is well suited for the designs studied in this research.

To estimate the compliance of DoFs, we study the deformation of the elastic layers. The study presented here provides the basis for the design of robogami joints with a desired compliance. The schematic of the joints along different axis depicting the joint motion and the design parameters are presented in Fig. 1.3. For the joints along the x and y axis, the strain along the width of the ASL is constant. The stiffness for these joints, $k_{x,y}$, is calculated as:

$$k_{x,y} = \frac{\partial M_{x,y}}{\partial \theta} = \frac{1}{l_{ASL}} \frac{\partial F_{ASL}}{\partial l_{ASL}/l_{ASL}} \frac{\partial l_{ASL}}{\partial \theta} hcos(\theta/2) + \frac{F_{ASL}}{2} hsin(\theta/2) \tag{1.3}$$

In (1.3), $M_{x,y}$ is the required bending moment at a given bending angle θ and $\frac{\partial F_{ASL}}{\partial l_{ASL}/l_{ASL}}$ represents the stiffness of the ASL, $(k_{ASL-x,y}(T))$ which is characterized in Chapter 3. For small angles around the straight configuration, $\theta = 0$, the joint stiffness is approximated as:

$$k_{x,y} = \frac{k_{ASL-x,y}}{l_{ASL}} h^2 \tag{1.4}$$

For the z axis joints, the instantaneous axis of rotation is the contact point between the two tiles. The moving axis of rotation complicates the calculation of the joint stiffness for this case. Given the small radius of the rolling, and the small goal angles around this joint, 25^o at maximum, we can simplify the problem by estimating the motion of this joint by a rotation along a fixed axis passing through the center of the cylindrical part. Given the non-uniform strain along the width of the elastic layer, we have the following relation for the required moment for rotating the joint:

$$M_z(\theta_0, \delta\theta, T) = \int_{w_1}^{w_2} \frac{k_{ASL-z}}{w_{ASL-z}} (\frac{ysin(\frac{\theta}{2})}{\frac{l_{ASL}}{2}}) cos(\theta/2) y \, \mathrm{d}y \tag{1.5}$$

For small angles around the straight configuration, the joint stiffness along the z axis is calculated as:

$$k_z = k_{ASL-z} \frac{w_2^3 - w_1^3}{3 w_{ASL-z} l_{ASL}} \tag{1.6}$$

We will use (1.4) and (1.6) to design joints along different axis to meet the stiffness requirements of different applications. In this section, we introduced the design of the robogami joints and studied its loading capacity and compliance. In a SMA actuated joint, the load capacity and joint's compliance are directly determined by the state of SMA. More on this type of joint will be presented in Chapter 3. In the next section, we introduce the layer-by-layer manufacturing process to construct these joints.

1.3 Layer-by-layer manufacturing

Robogami's unique layer-by-layer manufacturing methodology allows us to integrate different functional layers such as sensors, actuators, adjustable stiffness elements, and control circuit in thin robots, from few hundred microns to few millimeters in thickness. Once the components for a single joint is finalized, the design and manufacturing process of robogamis allow us to easily scale the design and place multiple DoFs to achieve any required reconfiguration. Fig. 1.4 and 1.5 illustrates the assembled components in SMA actuated and tendon driven robogamis, respectively. The structural material in robogamis is pre-cured glass-fiber (300 μm from Swiss-Composites Co.) or carbon-fiber (250 μm from easy-composites LTD.) layers. The processing of carbon fiber is easier and it has better mechanical properties but it is conductive which causes interference in the measurements of the curvature sensors. So in this research we mainly used glass-fiber as the structural material of the robogami. To bond different layers, we used two different methods: for coarse structures we used thermoplastic adhesive layers,

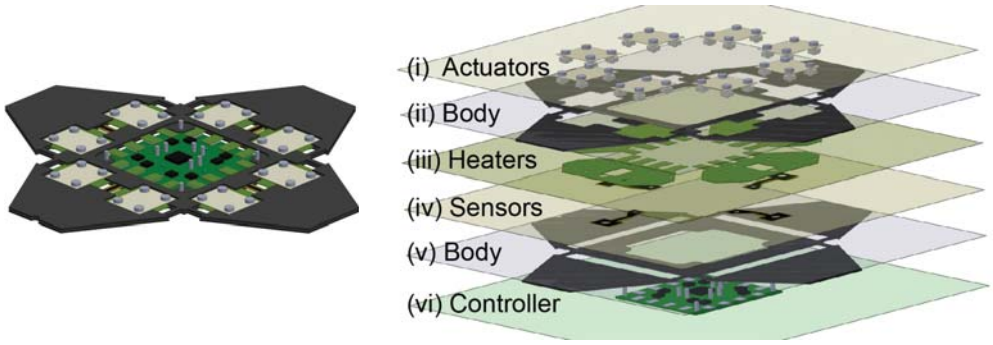

(a) (b)

Figure 1.4: Layer-by-layer manufacturing of a SMA actuated robogami. (a) Schematic of the robot. (b) The exploded view of the functional layers. Actuators are in layer (i). (ii) and (v) are glass fiber layers that make the body. (iii) and (iv) contain heaters and joint position sensors, respectively. (vi) is the controller circuit. More details about this robot are presented in Appendix A

and for finer features we used thermoset adhesive layer with polyimide packing (Pyralux film from DuPont) which allows more precise positioning and has smaller flow in the bonding process.

The DoFs in the robogami of Fig. 1.4 are defined and derived by SMA actuators which are mounted on the structure using bolts and nuts. The actuators are activated by stretchable heaters which are embedded in the structure and attached to the surface of SMA using thermally conductive adhesive. In this version of robogami, we also have curvature sensors that are embedded between the glass-fiber layers and a controller board that activates the heaters based on the sensors measurements and the programmed task.

Fig. 1.5 presents different layers comprising a tendon driven robogami with three joints: $[y, z, -y]$. The channel in the glass-fiber guides the tendon to apply forces at desired distance from the axis of rotation for each joint. The glass-fiber structure also determines the joint limits and the deformation of the ASL layers in these joins. More on the design of the ASL layer and its characteristics will be presented in Chapter 3.

To cut the patterns on different layers we used a custom-made laser micro-machining laser system which was developed by Inno6 Inc. (LAB 3550). Fig. 1.6 presents an overview of the machine and its components. LAB 3550 uses DCH-355-4 laser head from Photonics Industries Inc. which can produce adjustable power from 0 W to 4.7 W. This enables us to machine a wide variety of materials. For small patterns galvanometer-driven scanner (HurryScanII10 from ScanLab) is used to make the cuts which can machine materials with the rate of up to 2.5 m/s and within a field of 50×50 mm with accuracy of 15 μm (beam size). For larger patterns (up to 200×200 mm) the linear stage (LP 200-ST-200L from LPK with linear encoder MS30.73 from RSF Elektronik) is utilized. Cutting with stage movement will be slower; which causes a larger affected area by heat and hence less accuracy. Patterns with different size

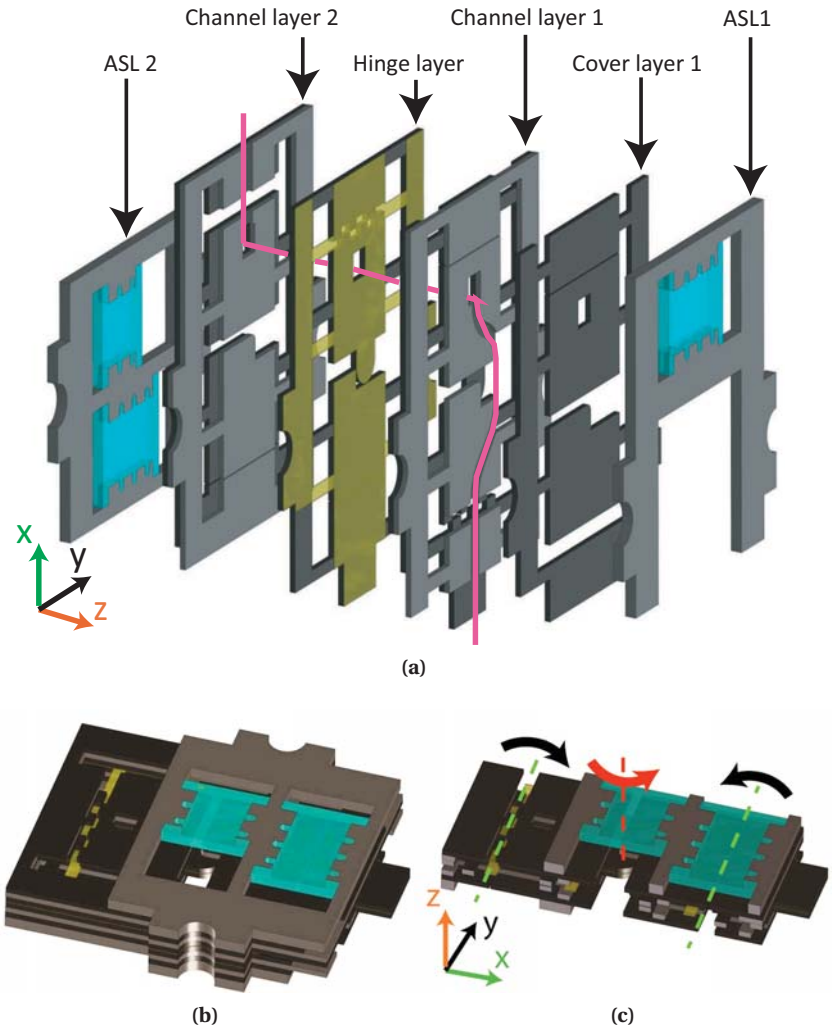

Figure 1.5: Layer-by-layer manufacturing of tendon driven robogamis. (a) Different layers are processed using accurate quasi-2D fabrication processes. These layers are aligned and bonded together using thermoset adhesive. The purple line in this figure shows the path of the tendon. (b) The layers are bonded together to from the final structure. (c) The alignment structure which keeps the joints fixed during the bonding process is cut using laser to free the joints and finally the tendon is passed through the channel.

and required accuracy can be cut by these two machining systems and their combination. Using the mico-machining center, we can engrave and cut patterns accurate as that needed for heaters (parallel lines 50 μm apart) as well as less accurate but larger patterns like the glass fiber pattern for robot's body. Two cameras with magnifications of 3.2 and 10 are installed which enables us to inspect the parts after the process and to align the work piece between different steps of processing. Moreover the cameras can be used to determine the thickness of the material and the focus point of the laser.

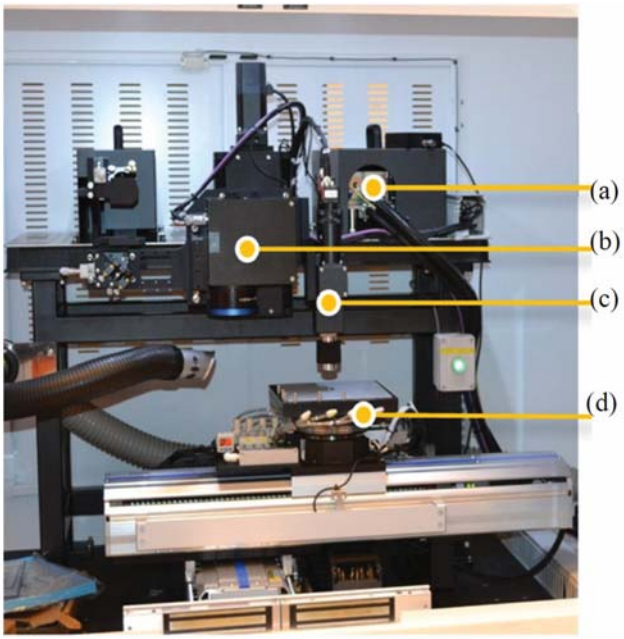

Figure 1.6: Overview of the Laser-micro machining instrument: (a) laser head, (b) scanner, (c) camera, and (d) moving stage.

1.4 Conclusion

Low profile, adaptable design, and feasibility of embedding different functional layers in the structure make robogami a desirable platform for developing wearable devices with multiple DoFs. The application of this platform, however, has mainly been limited to meso-scale mobile robots and it is imperative to revise the joint design and actuation principles to accommodate for the higher load capacity and compliance variability required in a wearable device. In this Chapter, the design of the novel tendon driven robogami joints along three orthogonal axis are presented and their load bearing capacity and compliance were estimated. More on the energy distribution between the joints of under-actuated robogamis and structure's compliance control will be studied in Chapter 3.

One of the main characteristics of robogamis is their layer-by-layer manufacturing technique which allows seamless integration of different functional layer in the structure. Two examples of integration of different layers in robogamis, one SMA actuated and the other tendon-driven, are presented in this Chapter and the 2D micro-machining process that enables the manufacturing of different layers is introduced briefly. In the next Chapters we elaborate on different functional layers in the Robogamis and study their performance in few applications.

2 Robogamis: Sensing solutions

Effective human interactions in soft wearable devices rely on feedback from the configuration of the robot and motion of the body. In this Chapter we present joint angle sensing solutions for robogamis and stretchable sensors for measuring body movements. Given the requirements on the size, the maximum strain range, and the customizability, it is imperative to develop customized sensors for measuring bending angle of robogami joints. Sensors based on two different physical principles were developed for measuring robogami joint angle: sensors based on piezo-resistive property of carbon-polymer composites and sensors based on the strain in metal films. Here, these sensing solutions are characterized and a model explaining different aspects of their behavior is presented.

The same sensing principles were also used in stretchable sensors for measuring the body movements. In the stretchable sensors, a mesh structure transforms the linear elongation of the sensor into bending deformation of series of micro-beams. we measure the electrical resistance change due to strain in the sensitive material as micro-beams bend with sensor's elongation.

Sensors based on carbon-polymer composites are easier and cheaper to fabricate. However, the accuracy and repeatably of the measurements from metal based sensors are significantly superior. In this Chapter after a brief overview of the state of the art of relevant sensing solutions, we present the design of curvature and stretchable sensors based on each of the sensing principles. For each case, we model and characterize the sensor responses. The results help us to choose the sensing principle and design sensors for different applications based on their specific requirements.

The material of this Chapter is from the following self-authored publications:
[35] **A. Firouzeh**, et al., "Soft piezoresistive sensor model and characterization with varying design parameters", Sensors and Actuators 2015.
[36] **A. Firouzeh** and J. Paik, "The Design andModeling of a Novel Resistive Stretch Sensor With Tunable Sensitivity", IEEE Sensors 2015.

2.1 Introduction

Different sensing principles are proposed in the literature for measuring robogami joint angles including: using inertial sensors Fig. 2.1 (a), measuring overall shape change through a varying characteristic of the structure such as the capacitance Fig. 2.1 (b), and measuring electrical property variation due to strain Fig. 2.1 (c, d). In this research we focus on methods that rely on electrical property change under strain for directly measuring the angle of each individual joint. The strain and deformation of the materials can be detected by measuring the resulting change in their electrical properties such as their: capacitance [38, 41–43] or resistance [40, 44–47]. The manufacturing process and the auxiliary equipment for reading resistive sensors are generally less complicated which simplifies their application in arrays of miniaturized sensing elements. We studied two sensing principles for curvature sensors: strain induced resistance change in Constantan (copper–nickel alloy with low electrical resistance sensitivity to temperature), and in carbon polymer composites. For Constantan the resistance change is mainly governed by the shape change of the metal path under strain. For the carbon based sensors, the deformation of the micro structure breaks off the conductive paths under

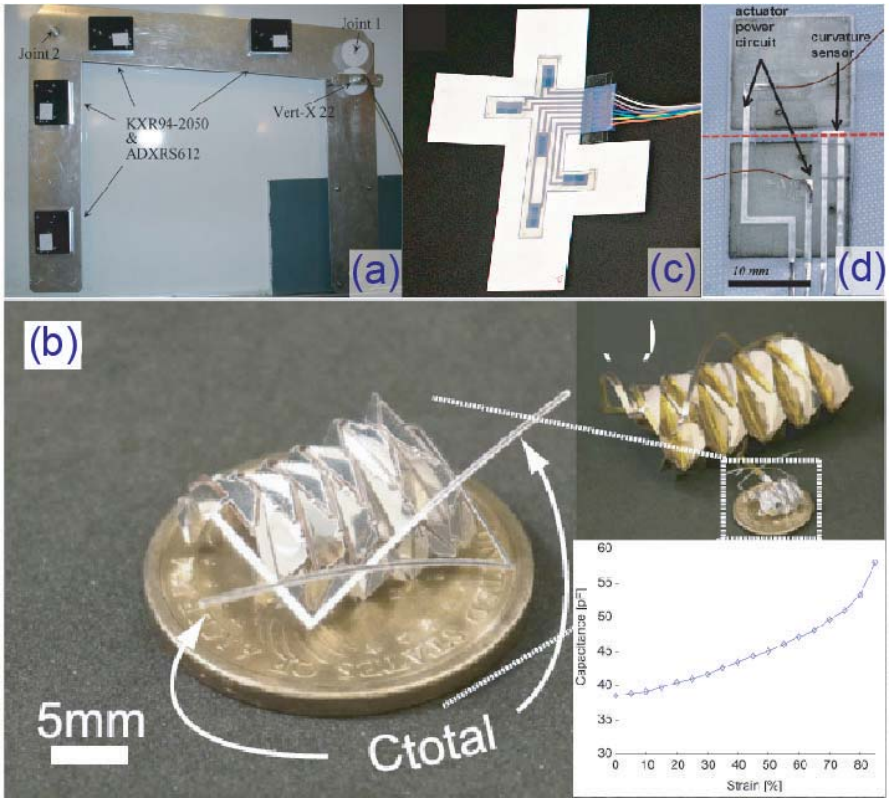

Figure 2.1: Examples of joint angle sensing solutions utilized in robogamis. (a) Inertial sensors for measuring orientation of the tiles [37]. (b) Capacitive sensing based on the relative displacement of adjacent tiles of the robogami [38]. (c) Curvature sensors based on Piezoresistivity of carbon and polymer composite [39]. (d) Liquid metal curvature sensor [40].

strain which increases the electrical resistance [48–51]. The performance of these two sensing methods are studied in detail in this Section and the advantages of each group are highlighted. The model and characterization results presented in this Chapter help with choosing the proper sensing method for different applications.

Stretchable circuitry is a necessity in soft robots for transferring signals and powering different sections. Fig. 2.2 (a-c) presents few examples of stretchable circuitry using different methods. All three methods(in plane bending [52, 57], out of plane waves [53, 58], and twist bending of micro beams in a mesh [40]) are based on transforming the elongation of the sensor into bending motion of the connected beams. Based on the powering requirements, elongation range, and compatibility with the available fabrication processes, we used the last method which is based on twist buckling and bending of micro-beams to make stretchable circuits. Changing the design parameters of the mesh structure allows us to use the same design also as stretchable heaters for activating the functional materials in the structure of the robot.

Stretchable sensors for measuring body motion is a requirement in any type of wearable device. Different methods have been proposed based on variability of electrical resistance and capacitance for measuring body movements, three examples of such methods are presented in Fig. 2.2 (d-f). In this research we adapted the same mesh structure we used for stretchable circuitry to make sensors with a desired sensitivity to stretch. This allows us to integrate the sensor layer into stretchable circuit layer. We experimented with both sensing principles we used for measuring joint angles, carbon and metal based, to develop stretch sensors. Details of the sensor design and the characterization results for the stretchable sensors are also presented in this Chapter.

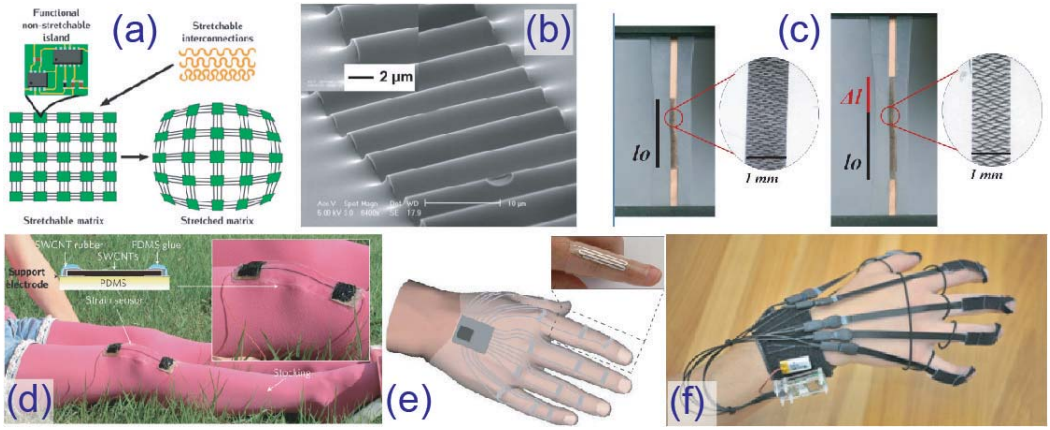

Figure 2.2: Examples of stretchable circuits and sensors. (a) Stretchable circuit based on in-plane bending motion of a metallic meander [52]. (b) Out of plane bending of a conductive path [53]. (c) Metal mesh structure resulting in out of plane twist and bending of the micro-beams [40]. (d) Piezoresistive based stretch sensor based on a carbon polymer compound [54]. (e) Liquid metal stretchable sensor [55]. (f) Capacitive sensor for measuring hand movements [56].

2.2 Carbon particle based curvature sensors

When piezoresistive sensors undergo strain, the electrical paths made by the conductive particles break down and their electrical resistance increase. The piezoresistive material consists of conductive particles in a non-conductive soft polymer matrix. One family of these sensors are made by impregnating different rubbers with carbon particles [54, 59]. This conductive paste can later be molded into a desired shape. The ease of fabrication in large arrays is one the main advantages of this type of sensor. Another family of strain sensors are based on a carbon ink deposited on polymer sheets [60]. Carbon inks contain a hard polymer as the matrix which results in better transient and more repeatable response.

To assess the feasibility of the application of these sensors in robogamis, we need a comprehensive study on potentials, drawbacks, and different parameters that affect the response of these. In this Section, we present the design, fabrication process and characterization results for conductive silicone polymer and carbon ink-based curvature sensors. These sensors are flexible, mechanically robust under large strains, scalable, cheap, and easy to fabricate in large numbers. The proposed model for the sensors is unique for its extensive characterization of these polymer-based sensors and for its systematic categorization to compare performance of sensors with different design parameters.

2.2.1 Design and fabrication

We study two families of piezoresistive sensors with different mechanical properties and possible applications: **Carbon silicone composite** (CSC) and **carbon ink** (CI) sensors. Under strain, due to relative motion of the conductive particles, that make the conductive paths, the overall electrical resistance of the sensing material changes. Although the working principle is quite similar, the appearance, mechanical properties, and fabrication process of these sensors are very different. The main advantages of the CSC sensors are their ease of fabrication and robustness in extreme loading conditions (upto 100% strain). The main advantage of the ink-based sensors is their better transient response, lower drift, and better accuracy as will be discussed. In what follows, we present the design and fabrication processes of these sensors.

Conductive Silicone Composite (CSC) Sensors

Composites of carbon black with silicone rubber have different levels of conductivity, sensitivity to strain, and mechanical properties depending on the mixture ratio, the matrix properties, and carbon particle size. Smaller particles generally result in more uniform mixture and better sensing quality. Based on this, we used carbon black with particle size of 42 nm in this research (39724, Alfa Aesar). Under strain, the conductive links in the CSC made by these particles break, causing an increase in the electrical resistance of the sensor. To study the effect of the polymer properties, we used two silicone rubbers with different mechanical properties: Ecoflex 0030 and Dragon Skin 30 (Smooth-on ™). The latter is around 10 times

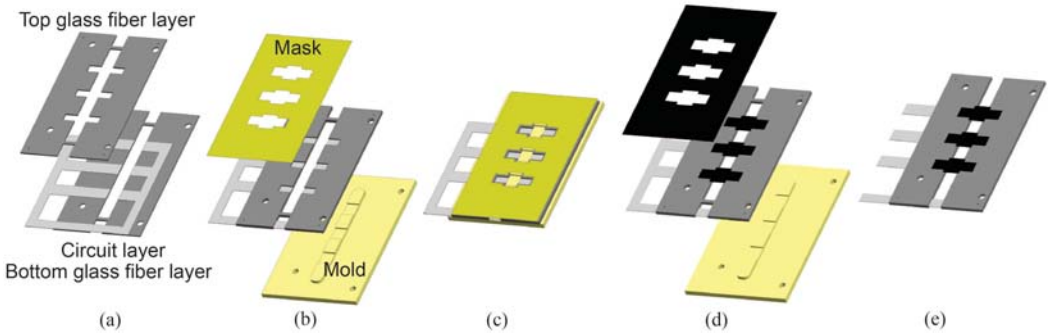

Figure 2.3: Fabrication process of the CSC sensors. (a) In the first step, the patterned pre-impregnated glass fibre and conductive fabric (which makes the circuit and the sensors electrodes) are stacked and cured in a heat press at 135°C for 30 minutes. (b,c) In the second step, the sensor base is fixed on a 3D printed mold and is covered with a mask layer. The mold makes the shape of the sensors more uniform and the mask makes cleaning and isolating the sensors easier in the subsequent step. (d) Next, the conductive polymer layer is cast and placed in the oven for curing. Finally, the module is released from the mold and the mask is lifted off. (e) In this module, we have three sensors in parallel which allows us to compare the response of three sensors in the characterization tests.

stiffer (600 kPa) than the former (69 kPa). As for the mass ratio, as suggested in [61], there is a compromise between sensitivity and conductivity. For sensors with Ecoflex matrix 5.5% and for sensors with Dragon skin matrix 7.5% carbon to silicone mass ratio give acceptable results which will be presented here. To achieve a more uniform mixture, we also added 15% mass ratio of n-Hexane solvent to reduce the viscosity of the mixture. Fig. 2.3 presents the overview of the fabrication process of CSC sensors. Here we use the robogami structure as the base for casting the conductive silicone. The fabrication process starts with laser micro-machining of the components needed for the base: pre-impregnated glass fiber layers, and conductive layer. Then, these components are stacked and cured in a heat-press to form the base for the sensors. In this design, we make three sensors on each module to study the repeatability of the fabrication process. We use a 3D printed mold and a mask as presented in Fig. 2.3 to better control the thickness and the shape of the sensors in the casting step. After casting the silicone, the module is placed in a vacuum chamber to degas the polymer. Then it is placed in an oven at 70 ^oC to cure the polymer. These steps are illustrated in Fig. 2.3.

Carbon Ink (CI) Sensors

Carbon inks are also composites of a polymer matrix and carbon particles. The matrix of the inks are significantly stiffer than the silicone rubbers that we use in CSC sensors. In general, stiffer matrix is expected to produce more repeatable results. Unlike the CSC sensors, we cannot cast the carbon inks directly for making the sensors and a substrate layer is necessary for the ink deposition. We used a Polyimide film as the substrate material based on its desirable chemical, thermal and electrical characteristics. The thickness of the polyimide substrate determines the strain in the ink layer. Based on the compromise between the sensitivity and

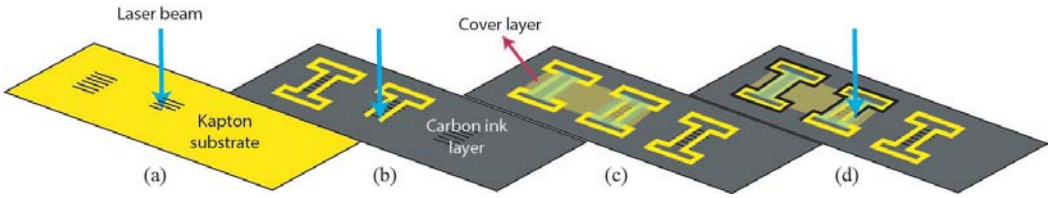

Figure 2.4: Fabrication process of the CI sensors. (a) In the first step, the surface of the polyimide sheet is engraved by UV laser. (b) Next, a layer of carbon ink is deposited on the polyimide and after curing, the anchoring points around the sensing area are cleaned by burning the carbon layer with laser. (c) In the third step, the cover layer is added. (d) Finally, the outline of the sensor is cut out and the wires are attached to the electrodes.

the accessible range of deformation, we chose 50 μm thick polyimide sheet as the substrate which gave good results in the experiments. As for the ink, different compositions were studied and based on their performance, a water based ink with micron size particles (conductive ink No. 16051, PELCO) was chosen.

The fabrication process, Fig. 2.4, starts with engraving straight parallel line on the surface of polyimide sheet with the laser up to half its thickness along the area which will make the sensitive part, the first step in Fig. 2.4. The width of the score marks is the same as the beam size of the laser which is 30 μm. These notches on the polymer layer will provide points of stress concentration and hence increases the sensitivity of the sensor. Next, a uniform layer of carbon ink is deposited on the polyimide sheet using fine glass-fiber fabric. After the ink is cured, we burn the ink on the side of the sensitive part in order to make anchoring areas for the cover layer, the second step in Fig. 2.4. The cover layer protects the ink from physical damage and also reduces the effects of change in the ambient condition, specifically the humidity.

The cover material changes the behavior of the sensor. We compared the effect of three different cover layers on the sensor's performance. The first cover layer, CI1, was a thin polyimide layer (13 μm) bonded on to the substrate and the ink layer using polyurethane

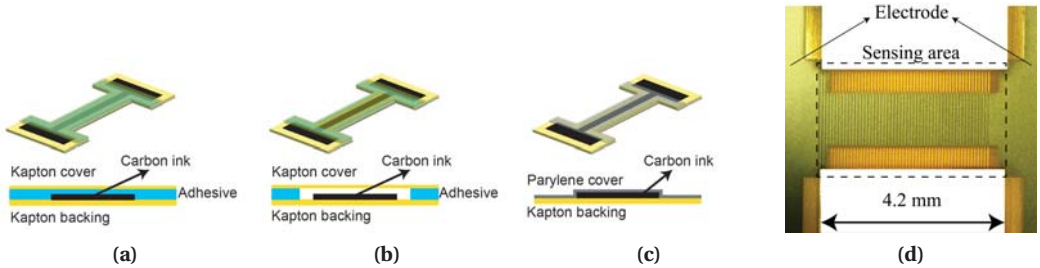

Figure 2.5: Design of different CI sensors. (a) Sensor with polyurethane and polyimide layer, CI1. (b) Sensor with polyurethane and polyimide layer, CI2. The ink and the polyurethane are not in contact in CI2. (c) Sensor with parylene coating, CI3. (d) A microscopic image showing the score marks on the substrate.

hot-melt (Fig. 2.5(a)). In another version, CI2, the same combination was used but the polyurethane layer was cut to keep it from contacting the ink layer in the sensing area (Fig. 2.5(b)). In the third design, Fig. 2.5(c), a thin parylene coating (2 μm) was used as the cover layer, CI3, which is expected to have smaller effect on the sensor reading based on its smaller thickness.

2.2.2 Model and characterization

The behavior of the carbon particle-based sensors is studied in micro-scale [48–51] and in macro-scale [61–63]. The study of the interaction of carbon particles and the polymer matrix in the micro scale is interesting for understanding the nature of different phenomena and optimizing the components of the conductive composite. In the second approach, a gray box model is used to explain the relation between the resistance and the strain. This type of modeling is more attractive for studying the bulk behavior of the sensors. Such a model is still useful in optimizing the design parameters [63] of the sensor since the elements that make up the model are representative of different components' characteristics [61]. In this research, we modeled the behavior of the sensors using the second approach.

To characterize the sensors, researchers mostly studied cyclic loading with fixed loading rate [64, 65]. Some aspects of the dynamic response of these sensors were also studied [48, 61]. Still, effects such as drift or creep [50] are not studied thoroughly. A model in macro scale [61] that explains all these effects would provides us with a set of figures of merit for comparing the performance of different sensors [66, 67].

We present a model that can explain the main aspects of the sensor response and introduce the characterization tests to determine the parameters of the model for different sensors, which we use to compare their performance. Moreover, by interpreting the physical meaning of the elements in the model, we will acquire a guideline for improving the design of the sensors. The equivalent mechanical model of Fig. 2.6 captures different aspects of the sensor behavior. In this model, the carbon particles are presented in black and the polymer matrix is presented by blue carts that are connected with a combination of dampers and springs. The movement of the particles (strain) in the equivalent model translates into the electrical resistance change of the sensor. The elements of the model are chosen to capture two main characteristics of the sensor reading: the transient response and the amplitude dependent drift in the sensor reading. This drift is referred to as the recoverable drift throughout the text. In a perfect sensor, these two effects should be negligible. But due to the inherent material characteristics, all polymer based sensors display these effects to different extents.

To characterize the sensors, we examine three different aspects of the their response. First, we study the transient response which is governed by the dynamics of the polymer matrix (presented by components with **P** label in Fig. 2.6). Next, the recoverable drift in the sensor reading is studied which is governed by the interaction between the polymer matrix and the carbon particles (modeled by the components with **CP** label in Fig. 2.6). Finally, the quasi-

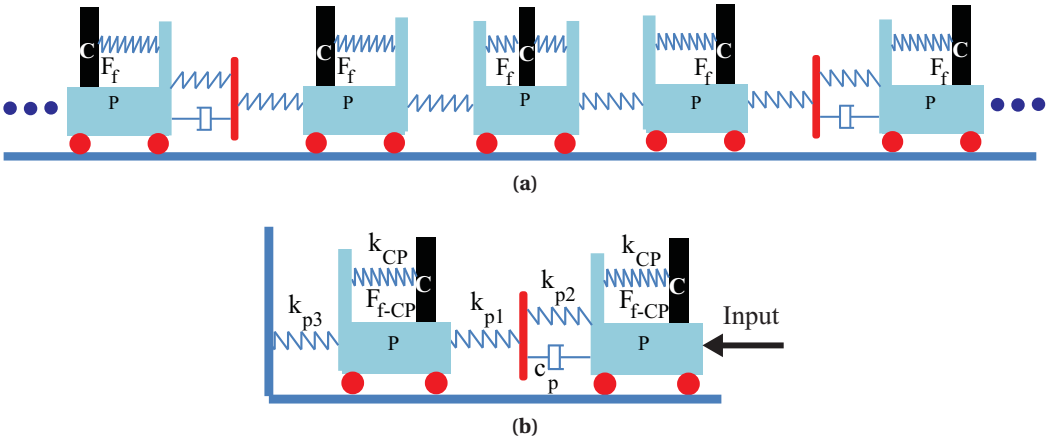

Figure 2.6: The equivalent mechanical model for the carbon particle based sensors. (a) The model proposed in this research contains more elements compared to the previously suggested models to cover different aspects of sensor behavior. (b) The simplified model where all the elements with same effect are lumped into one equivalent element. In this model, black blocks represent the carbon particles (labeled **C**) and the distance between them is translated to the resistance change of the sensor. The carts and the connecting springs and dampers represent the polymer matrix (labelled **P**). The friction force between the carbon particle and the polymer matrix and the force in the spring that is labeled **CP** are the forces between the carbon particles and the polymer matrix.

static response of the sensor will be investigated. As previously suggested in [61], the transient response of the sensors can be attributed to the polymer's visco-elasticity. The drift in the sensor reading can be attributed to the friction force between carbon particles and polymer matrix.

The study of the model suggests that the drift part of the response is only dependent on the fast movements in the matrix and not on the slow relaxation and moreover the transient response of the sensors is not dependent on the recoverable drift. So, these two parts of the model can be studied separately. In what follows, we present the test procedure for characterizing different aspects of sensors' behavior.

Transient response

The transient response of the sensors is caused by the visco-elastic behavior of the polymer. This behavior is modeled using a combination of springs and dampers. The resistance of the sensor changes due to both normal and lateral strains in the material. The elements in the model are chosen to capture closely different aspects of the transient response. Considering the normal strain as the input, the lateral deformation is the main reason for the resistance change by breaking the conductive paths.

The transient response is characterized in two steps: first, loading the sensor from relaxed (0^o) to a half closed position (90^o) with a step input (approximated by a ramp loading with 0.5 s

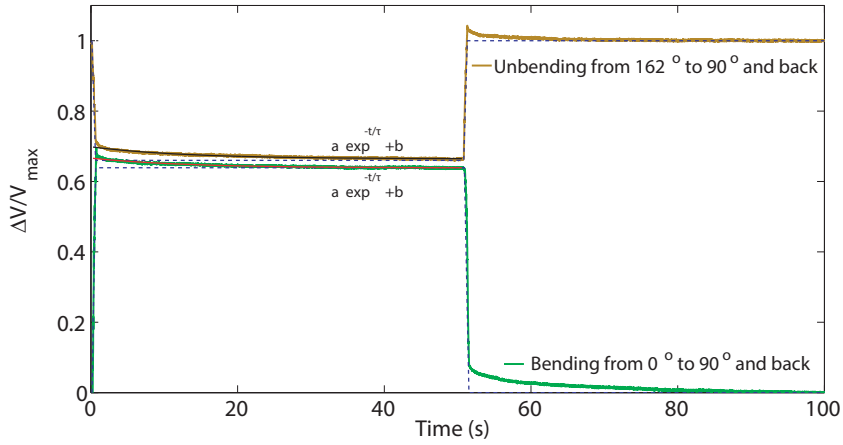

Figure 2.7: The transient response of the CI2 in moving from 0° to 90° (green line) and from 162° to 90° (brown line). Both on the rising and the falling edges the resistance decreases over time. This can be attributed to different effects such as the lateral deformation in the sensor. We model this response using the first order dynamics.

rise time); second, unloading the sensor from completely closed state (162^o for CIs and 144^o for CSCs) to (90^o). For the CSCs bending over 144^o would cause the two sides of the sensor to come in contact. Fig. 2.7 presents the response of the CI2 sensor in these two tests.

An interesting feature in the response of this sensor is that both in loading and unloading, the sensor reading decreases over time after the deformation. We use the equivalent mechanical system of Fig. 2.8 to model the transient behavior of sensors. The input deformation in this model, causes two displacements of interest which can be attributed to the volume change in the material, x (governing the particle distance in the direction of the main deformation), and the lateral displacement, u. Regardless of the direction of motion, the lateral deformation causes increase in the resistance which can be explained by the theory of destruction of conductive networks [68, 69]. The same model can also explain the resistance increase of the piezoresistive materials under the pressure. Based on this model, we present the resistance of

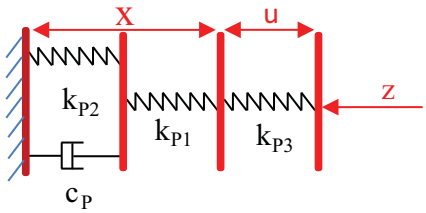

Figure 2.8: The transient response components of the sensor model. The portion with the displacement x is the standard model that captures creep and viscoelastisity in the polymers. The displacement in the third spring denotes the lateral strain in the material which causes the effective conductive paths to break. The input to the model is the displacement z and the outputs are x and u.

the sensor as:

$$R = R_1(x) + R_2(|u|) = r_1 x + r_2|u| \tag{2.1}$$

In this model, we assumed that the resistance is a linear function of the displacement. As will be seen in the quasi-static characterization of the sensor, this assumption is not true for the whole range of motion but it can be used in finding a measure of performance for the sensor around a specific point. For the displacements of interest we have:

$$\begin{aligned} X(s) &= (\frac{1}{A} + \frac{1}{B+DS})Z(s) \\ U(s) &= (\frac{A-1}{A} - \frac{1}{B+DS})Z(s) \end{aligned} \quad \rightarrow \quad \begin{aligned} x(t) &= ae^{-t/\tau} + b \\ u(t) &= -ae^{-t/\tau} + (1-b) \end{aligned} \tag{2.2}$$

Using the test results presented in Fig. 2.7, the parameters of (2.2) can be determined but we are more interested in finding a tangible measure of performance to compare different sensors. So the parameters we report for each sensor are: the time constant of the first order dynamic model (τ), and the normalized amplitude of the transient response in rising and falling edges

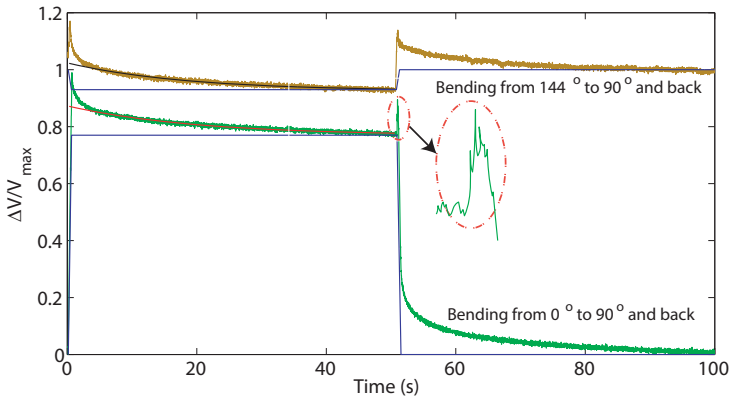

Figure 2.9: The transient response of CSC1 in moving from 0^o to 90^o and from 144^o to 90^o. The different aspect in the dynamic response of this sensor compared with the CI sensors (Fig. 2.7) is the initial increase in the resistance regardless of the direction of deformation. This point is emphasized in the plot by zooming in on the initial pick on the falling edge.

(a_{r_n} and a_{f_n} respectively) which are defined as:

$$a_{r_n}(\%) = \frac{a_r}{a_s} \; and \; a_{f_n}(\%) = \frac{a_f}{a_s} \tag{2.3}$$

According to (2.3), the normalization should be carried out using the steady state amplitude of the resistance change but because of the non-linearity in the behavior of the sensor, the amplitude of the transient response is not necessarily dependent on the step size. So to have comparable values, for both the rising and falling edges, we used the resistance change of the sensor as it bends from 0^o to 90^o for normalizing the readings.

Conductive silicone with soft matrix (such as the compound we used for CSC1) exhibit a behavior different from what is presented in Fig. 2.7. For sensors using such materials, we observe an initial increase in the sensor reading as it moves back to the relaxed state as shown in Fig. 2.9. In CSCs with soft matrix, the damping effects are highly dominant, which causes large initial deformation in k_2 (attributed to large lateral motion) and hence an initial increase in the resistance. The same characterization tests were performed on all sensors and the results will be compared in Section 2.2.3.

Recoverable drift

For most polymer sensors, due to the inherent matrix characteristics, drift in the sensor reading over time is inevitable. Though being neglected in many researches, this effect is one of the biggest drawbacks of the polymer based sensors. One part of this drift is caused by the degradation of the sensor and is irreversible. The quasi-static experiments confirms that this effect is negligible. On the other hand, there is a reversible and significant drift in the sensor reading dependent on its loading history. The frictional force between the carbon particles and the polymer matrix is added to the model to capture this behavior. Fig. 2.10 presents a part of the general model, we proposed in Fig. 2.6, that explains the recoverable drift in the sensors. The parameters of this model are the mass of the carbon particles, the friction force, and the spring constant.

In cycles with large bending angles, the positive work done by the spring and the friction in the first half of the cycle (Fig. 2.10 (a) to 2.10 (b)) is greater than the positive work when the polymer matrix goes back to the relaxed initial state (Fig. 2.10 (b) to 2.10 (c)). This will cause an offset in the position of the carbon particles after a high amplitude loading cycle (Fig. 2.10(c)). When the sensor is later loaded with smaller amplitudes (Fig. 2.10(d)), the residue of the spring force would cause smaller positive work when the polymer gets stretched compared to the positive work when it shrinks back to its initial state. This will cause the particles to spring back to their initial state in the matrix in the repeated cycles (Fig. 2.10(e)). While the drift appears after the first couple of cycles with large amplitudes (after the first two cycles, the

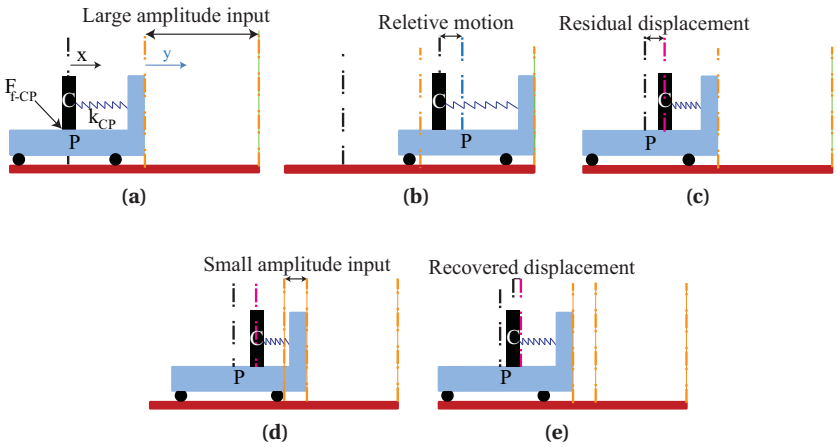

Figure 2.10: The portion of the model that represents the interaction between the carbon particles and the polymer matrix. The components in this part of the model were chosen to yield the same drift behavior as is observed in the sensor reading. (a) Initial state. (b) Deforming the sensor with large amplitude. (c) Polymer matrix returns to its initial state but carbon particles maintain some residual displacement. (d) Deforming sensor with small amplitude. Because of the pre-strain in the spring, the carbon particle's displacement is small. (e) Polymer matrix returns to its initial state after a small amplitude deformation and the carbon particles recover some part of the drift in their position.

sensor readings would be similar for the rest of the cycles with high amplitude), the relocation of the particles to their initial state is a very slow process and many cycles of loading with small amplitudes are necessary to relieve the residual strain in the sensor, Fig. 2.11.

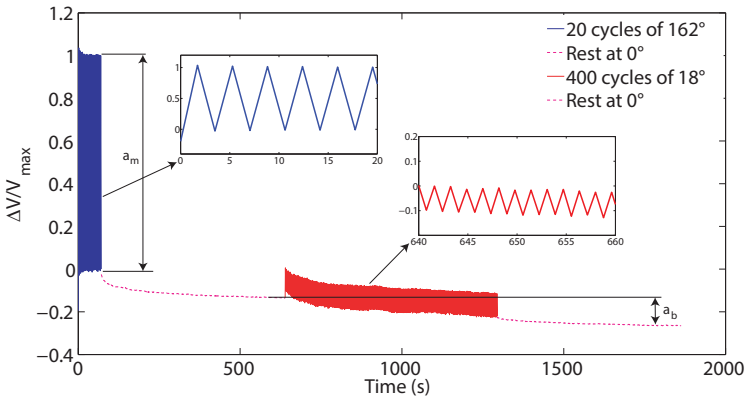

Figure 2.11: Recoverable drift in CI2. In this experiment, the sensor was loaded to the maximum bending angle (162^o) for 20 cycles which causes the drift in the reading. After that, the sensor was kept in the relaxed state so the transient response vanishes. Then in 400 cycles of 18^o, the recoverable drift was relieved and the sensor is held steady again for the transient response to vanish. The voltage difference between the two steady state readings is the measure that we use for comparing different carbon based sensors.

Finding all of the parameters in the model requires extensive testing including loading with different rates. Here, we only report the normalized recoverable drift in the sensor reading for one loading speed which provides a measure of performance for comparing different sensors:

$$ab_n(\%) = \frac{a_b}{a_m} \tag{2.4}$$

The characterization test for this part begins with loading the sensor with the maximum bending angle, 162^o, for 20 cycles. Then the sensor is left at its relaxed state so that the transient response fades. Next, the sensor is loaded with smaller amplitude, 18^o, for 400 cycles to relieve the residual strain. In these repeated cycles the drift in the sensor reading is recovered little by little. In the final step of the test, the sensor is again left at rest to reach its steady state. Fig. 2.11 presents the result of these tests for CI2. a_b in this figure presents the value we refer to as the recoverable drift in the sensor response.

Quasi-static response

To study the repeatability of the sensor measurements, we loaded the sensors in 18^o increments between unfolded and folded states for 50 cycles and calculated the variance of the voltage reading in repeated cycles. We use the mean of the variance for all points to compare the quasi static performance of different sensors in repeated cycles ($\overline{\sigma_V}$). The measurements from the first cycle are different from all the following readings. This is caused by the slow transient behavior of the sensor which results in slightly higher readings from the second cycle on. In this Section, we are concerned with the repeatability of the sensor measurements. So we put aside the first cycle and calculate the variance based on the data from the remaining

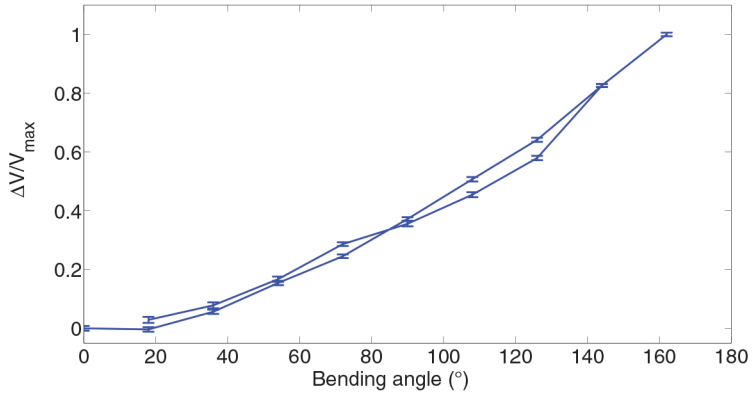

Figure 2.12: Quasi static response of CI1 in 50 cycles with 18^o step increments. The mean cycle and the variance are presented. The variance is a measure of the repeatability of the readings and the robustness of the sensors.

cycles. To give comparable numbers for different sensors, we normalized the error with the amplitude of the mean cycle. Fig. 2.12 presents the result of this test for CI1.

The coherence of the data presents a measure of the repeatability of the readings and the robustness of the sensors. The accuracy of the sensor estimation also depends on its sensitivity (the slope in Fig. 2.12). To study the accuracy of the sensors, a more detailed quasi-static test with increments of 1.8^o was performed and a curve was fit to the data to find the correlation between the bending angle and the voltage reading from the sensor. The difference between the prediction of the fitted function and the actual bending angle provides a measure of accuracy of the sensor around each bending angle. We use the mean of the standard deviations for all test point ($\overline{\sigma_\theta}$) as a measure to compare the accuracy of the sensors.

Another measure of the sensor performance is the width of its hysteresis loop. We present the maximum normalized width of the hysteresis loop which is the difference between the voltage on the rising edge and falling edge over the voltage amplitude of the whole cycle:

$$w_{Hys._n}(\theta) = \frac{|V_{rising}(\theta) - V_{fallin}(\theta)|_{max}}{V_{max} - V_{min}} \tag{2.5}$$

The parameters introduced here are used in the next Section to compare different aspects of the response of carbon particle based sensors.

2.2.3 Comparison of carbon particle based sensors

In this Section, we compare the response of carbon based piezo-resistive sensors using the figures of merit defined in the previous Section. Table 2.1 compares the three aspects of the sensor response: transient response, drift, and quasi static response. Based on the model we expect better transient response from compounds with stiffer polymers and more dominant elastic behavior. A stiffer matrix also reduces the recoverable drift in the sensor since the conductive particles would follow the polymer matrix more closely. The comparison between the values in Table 2.1 confirms these predictions.

The CI sensors have stiffer polymer and hence better characteristics compared to CSC sensors.

Table 2.1: Comparing the performance of different types of carbon particle based sensors.

	Transient response			Drift	Quasi-static response test		
Sensor type	τ(s)	a_{r_n}(%)	a_{f_n}(%)	ab_n(%)	$\overline{\sigma_V}$ (%)	$\overline{\sigma_\theta}$ (°)	$W_{Hys._n}$(%)
CSC1	19.24	13.8	13	28.37	2.37	5.98	25.57
CSC2	12.5	9.0	10.9	15.76	2.48	2.65	17.33
CI1	17.1	10.7	23.5	39	0.75	2.67	8.2
CI2	12.78	4.4	5.3	12.95	0.55	1.05	2.9
CI3	14.22	5.2	5.6	11.42	0.67	0.89	4.2

Among the ink based sensors, CI1 is an exception and it has the worst transient response based on the value of a_{f_n} and a_{r_n} presented in Table 2.1. Also, its recoverable drift amplitude is quite substantial. In this sensor, the conductive ink is in direct contact with the polyurethane layer and it is partially transferred onto this layer in the laminattion process. While the sensor is under strain the polyurethane layer moves with respect to the polyimide layer which breaks the conductive paths. The anchoring points added in the fabrication process reduces this relative motion and significantly improves the result but it does not solve the problem entirely. The other two packaging techniques used (in CI2 and CI3) do not have the same problem and give significantly better results, Table 2.1.

In the quasi-static tests, the repeatability of the measured data for the ink based sensors ($\overline{\sigma_V}$) is significantly better, Table 2.1. This is mainly caused by the drift in the CSC sensors over time. Also, the shape of the CSC sensors are rather unconstrained compared to CI sensors that have a stiff polyimide backing. The accuracy of the sensor readings is not only a function of the repeatability of the measurements but also the sensitivity in different regions. In general, CI sensors have more uniform sensitivity in their whole range of motion. This partly comes from their smaller hysteresis loop ($W_{Hys._n}$) which makes the insensitive zones smaller. Better sensitivity and repeatability result in more accurate readings for CI compared to CSC sensors.

According to Table 2.1, CI sensors have better characteristics in all three aspects studied in this research. The figures of merit presented in this table will guide us in choosing the proper sensing method based on the application requirements. The main advantage of the sensors introduced in this Section is their ease of fabrication which makes it possible to design network of them for monitoring the configuration of robogamis. These sensors were successfully used in robogami joints for following a repeated loading cycle with a fixed amplitude at a rather slow rate (more details in Appendix A). The application of the sensors presented in this Section is, however, limited by their slow transient response and the drift in their reading. Later in this Chapter we introduce curvature sensors based on metal film-polyimide laminates which provides more repeatable and reliable response but at the cost of increased manufacturing complexity and cost.

2.3 Carbon particle based stretchable sensors

Among the curvature sensors we studied in the previous Section, ink sensors with polyimide backing had the best response. We used the same sensing principle in a stretchable sensor for measuring facial movements. The sensor is fabricated by cutting a mesh pattern similar to the one presented in Fig. 2.13a through a polyimide sheet covered with carbon ink. The mesh structure makes a series of micro-beams that bend and allow significant displacements at the two ends of the sensor. Fig. 2.13b presents a stretchable sensor based on this design. Similar to the curvature sensors, this senor is coated with parylene for protecting the ink layer. Fig. 2.13c presents the characterization result of 3 stretchable sensors in 20 cycles.

Similar to piezo-resistive curvature sensors, the main advantage of carbon based stretchable

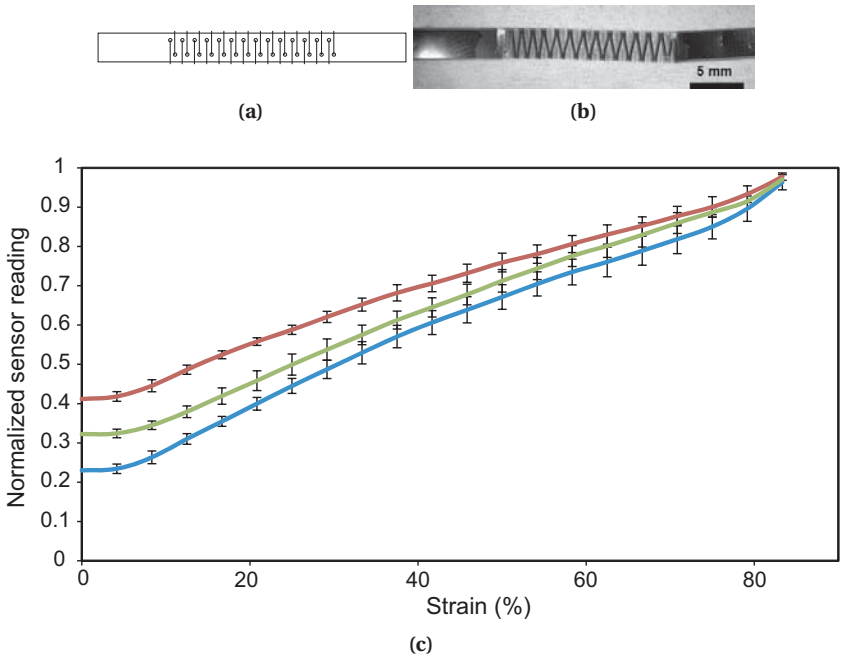

Figure 2.13: Carbon ink stretchable sensor. (a,b) The overall design of carbon ink stretchable sensor. (c) The response of 3 sensors at 80% elongation in 20 loading cycles.

Figure 2.14: A network of stretchable sensors are designed to measure facial movements.

sensors is the ease of design and fabrication of networks of sensing elements. Fig. 2.14 presents an example of a network of seven sensors designed to measure facial movements to detect facial gestures. Given the limited accuracy and repeatability and significant dependence on the ambient condition, refined measurement of the facial movements is not feasible using these sensors. Later in this Chapter, we introduce a stretchable sensor based on metal films for applications requiring more precise measurements.

2.4 Metal based curvature sensor

The main advantages of the conductive polymer sensors are their ease of fabrication, low cost, and high sensitivity to strain, which simplifies considerably the data acquisition hardware. However, the high sensitivity to the ambient condition and instability of the matrix in repeated cycles of loading, inherent to the polymers, restrict the applications of these sensors. In this Section we present a sensor with higher accuracy for robogamis that uses electrical resistance change caused by strain in a metal film as the sensing principle.

2.4.1 Sensor design and model

The customized curvature sensors presented in this Section functions based on the resistance change of a metal path under strain [70, 71]. To induce unidirectional strain in the metal layer under bending deformation, we used a laminate of metal and polyimide. To increase the resistance change of the sensor, a serpentine path was etched in the metal layer. The schematic of the sensor is presented in Fig. 2.15a. Constantan was chosen as the metal layer based on the low sensitivity of its electrical resistance to temperature change.

The axis of rotation in the robogami joints are determined either by the folding pattern of the polyimide or by the shape of the actuators (in the case of SMA actuated joints). By fixing the curvature sensors on both sides of the robogami joint, it is forced to follow deformations that are dictated by tile motions. This can cause large strains in the sensor and for the metal sensors this would result in plastic deformation. To prevent this, the sensor is fixed at one end and is free to slide in and out of the adjacent tile while following its bending angle, Fig. 2.15b. Allowing this sliding motion reduces the maximum strain in the metal layer and prevents plastic deformation and failure of the sensors.

To reduce the maximum strain for a given bending angle, and maximizing the elastic range of deformation, thin metal and Polyimide layers were used in the laminate, 10 μm and 50 μm respectively. For this laminate, the neutral plane falls 2.3 μm above the metal and Polyimide interface which puts the metal layer (as presented in Fig. 2.15c) partly in tension and partly in compression under bending loads. Ideally using a thinner metal layer for having the entire Constantan volume in either tension or compression is preferable (we used 10 μm Constantan layer based on the availability). Considering the gauge factor of 2.0 for Constantan, the

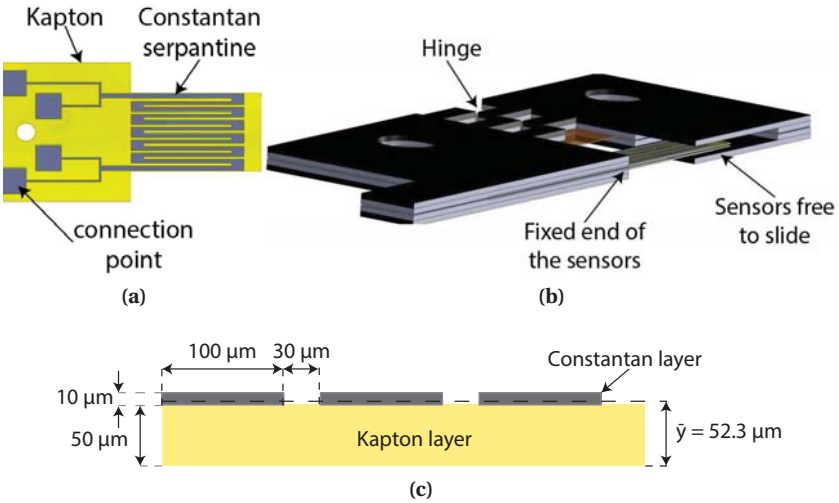

Figure 2.15: Low profile metal based curvature sensor for robogami structures. (a) The schematic of the sensor which comprises a Constantan serpentine (10 μm thick) laminated on thick Polyimide (50 μm). When the sensor is bent, the metal layer mainly undergoes tension or compression, depending on the bending direction. This loading condition results in increase or decrease in the overall resistance of the sensor. (b) The overview of the assembly of two sensors in a robogami joint. The sensors are fixed on one tile and are free to slide in and out of the second tile. (c) Schematic of a curvature sensor cross-section.

resistance change is given by the following equation:

$$\Delta R = 2R\bar{\epsilon} \tag{2.6}$$

In (2.6), ΔR is the overall resistance of the sensor, and $\bar{\epsilon}$ is the average strain in the metal layer. Considering a simple bending, the strain in the metal layer is calculated as:

$$\epsilon = \frac{(y-\bar{y})}{\rho},\ \rho = \frac{l_{sensor}}{\theta} \tag{2.7}$$

In (2.7), $y-\bar{y}$ is the distance from the neutral plane and ρ is the radius of curvature. l_{sensor} is the length of the sensor and θ is the bending angle. Given the dimensions that are presented in Fig. 2.15c, the average strain in the metal layer is calculated as:

$$\bar{\epsilon} = 3.8 \times 10^{-4}\theta \tag{2.8}$$

According to (2.6) and (2.8), the expected sensitivity, $\delta R/R$, is 7.6×10^{-4}/rad. Because of the low sensitivity, we need to use precise electronics and 4-point measurement for avoiding inaccuracies related to contact and wiring resistances.

2.4.2 Characterization

In this Section, we present the characterization results for the metal curvature sensors. The actuation and compliance control methods that we use in robogamis are thermally activated. So we expect significant temperature variation in the sensors. Although Constantan has a low sensitivity to temperature variation, given the wide temperature range, the thermal effects are not negligible. To illustrate the temperature dependence of the electrical resistance, we tested a sample with rising temperature. The results, Fig. 2.16a, confirm significant thermal effects. To account for these effects, we placed two sensors with the same pattern back to back which puts the metal layers in opposite loading conditions. Given the thin profile of the two sensors, we expect them to have similar thermal conditions. So the resistance change due to the temperature rise in the sensors would have the same value while the resistance change due to the bending motion would have opposite values. Subtracting the resistance of the two sensors is expected to cancel out the effect of the temperature on resistance and adding the sensor readings is expected to cancel out the strain effect, Fig. 2.16.

We define the joint angle, I_θ, and temperature, I_{Temp}, indicators as:

$$I_\theta = R_1 - R_2 \tag{2.9}$$

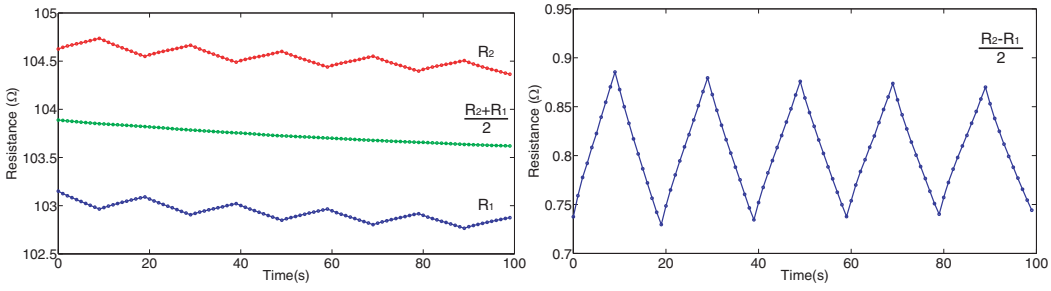

Figure 2.16: Sensor measurements and joint angle and temperature indicators. (a) The raw sensor readings show significant variation with both time (due to varying temperature) and strain. Adding the readings of the two sensors cancels out the strain effect on the resistance. (b) subtracting the sensor readings cancels partially the temperature effect. Although the range of motion remains the same, $[-50^o\ 50^o]$, the amplitude of the joint angle indicator decreases at higher temperatures and further treatment of the data is required for accurate joint angle estimation.

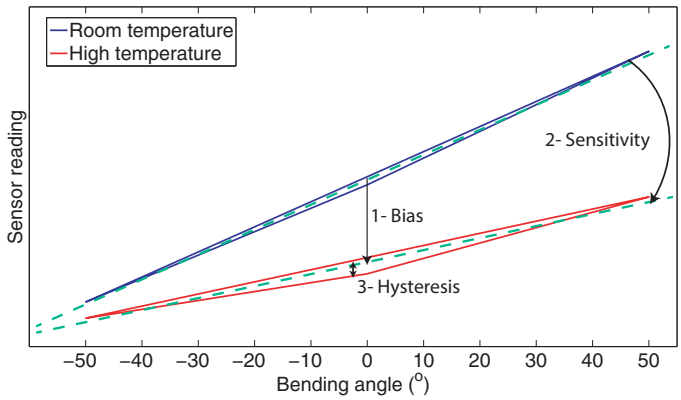

Figure 2.17: Three major effects of temperature on the sensor measurement. 1) The negative bias in the reading (caused by the negative electrical resistance-temperature coefficient of Constantan). 2) The decrease in the sensitivity of the sensor. 3) The increase in the hysteresis loop width. This figure is an schematic representation of the sensor reading and the effects are not to the scale.

$$I_{Temp} = \frac{R_1 + R_2}{2} \tag{2.10}$$

Fig. 2.16 presents the raw sensor readings, temperature, and joint angle indicators. Ideally we expected the joint angle indicator to be independent of the temperature. The test results, however, suggests that the temperature change affects the resistance in three different ways: 1- adding a bias to the sensor reading which is compensated in the joint angle indicator, 2- changing the sensitivity, and 3- increasing the hysteresis in the sensor reading. These three effects are presented in the exaggerated schematic of Fig. 2.17. The overall resistance of each sensor can be written as:

$$R_{sensor} = b(Temp) + K_\theta(Temp)\theta \pm hys(Temp) \tag{2.11}$$

In (2.11), $b(Temp)$ is the bias in the sensor reading, K_θ is the sensitivity of the sensor which as discussed is a function of the temperature, and $hys(Temp)$ represents the hysteresis. Subtracting the resistance of the two sensors cancels out the bias in the temperature reading but it does not compensate for the sensitivity change and the hysteresis. So the joint angle indicator has the following form:

$$I_\theta = R_1 - R_2 = 2k\cdot(Temp)\theta \pm 2hys(Temp) \tag{2.12}$$

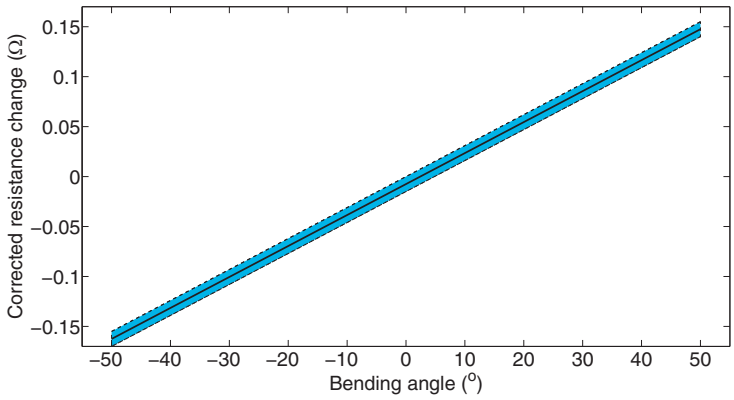

Figure 2.18: Corrected measurements from two sensors versus the joint angle. The bias caused by temperature variation is compensated by subtracting the resistance of the two sensors. The reading was also corrected to account for the change in the sensitivity due to the temperature variation. The sensor is tested in 25 loading cycles with different amplitudes. The results are fairly repeatable and linear and an envelope of $\pm 2.4^o$ contains the data from all the loading cycles.

The sensitivity change which is a function of the temperature can be accounted for based on the temperature of the sensors. We estimate the temperature of the two sensors using the temperature indicator, I_{Temp}. We approximated the change of the sensitivity, K_θ, with a linear function of the temperature. To characterize the rate of sensitivity change, we tested the sensors in its maximum range of motion with increasing temperature. We used the results to determine K_θ as a function of I_{Temp}. The last term in (2.12) can not be compensated easily. However, the temperature indicator can provide a measure of how prominent the hysteresis effect is. In the characterization tests, the hysteresis in the sensor reading was negligible.

To study the repeatability of the sensor readings, it was tested with different maximum amplitudes $(10, 20, 30, 40, and 50^o)$ with 10^o steps. The tests were repeated 5 times for each maximum amplitude. The sensor was characterized in varying thermal conditions. The thermal effects are compensated using the measurement from the two complementary sensors to make the response compatible with the sensor reading at the room temperature. Fig. 2.18 presents the characterization test results. The sensor response is fairly linear with sensitivity of 8.5×10^{-4}/rad which is higher than the estimated value. The difference can be attributed to variation in the thickness of the metal layer and its gauge factor. The sensor response is fairly repeatable and an envelope of $\pm$ 2.4° contains the data from all the tests.

Compared to carbon based sensors, the sensors presented in this Section are significantly more accurate and stable. The metal based sensors are a better choice for the robogami applications requiring accurate configuration feedback.

2.5 Metal based stretchable sensor

In Section 2.3, we presented carbon based elongation sensors based on a stretchable mesh pattern. Given the significantly better response of metal based curvature sensors in comparison to carbon based sensors, we decided to adopt the design of the carbon ink mesh sensors and develop a stretchable sensor based on the strain in a metal film laminated on polyimide sheet. In this Section, the design of the metal mesh sensor, a model to predict its behavior, and the results of its characterization tests are presented.

2.5.1 Design and working Principle

In the mesh pattern introduced for the carbon based stretchable sensors, the bending motion of the beam puts the ink layer partly in tension and partly in compression. The resistance of carbon ink increases both under tension and compression. So stretching the mesh structure resulted in resistance increase for these sensors. For the metal mesh sensor, however, the resistance of sections in compression decreases and we expect no resistance change in a design with symmetric pattern. By modulating the track width, however, we can make stretch sensors with either increasing or decreasing resistance. This is specifically of interest since we can cancel out the thermal effects on the sensor reading by using a sensor with positive and a sensor with negative sensitivity in parallel. Here, the design and the working principle of a metal based stretchable sensor is presented in detail.

The mesh pattern that is proposed for stretchable sensor, Fig. 2.19, was previously used as stretchable heaters and circuit. The pattern for the heater is insensitive to strain given the fact that the metal layer is partly in tension and partly in compression. To make the mesh sensitive to stretch, we modified the metal track profiles to have different contributions to the electrical resistance in sections with positive and negative strain. Effective modulation of the metal track profile requires understanding of the relation between the stretch and the strain distribution in the metal layer. Fig. 2.19 (a-c) present a sensor as it stretches. The mesh pattern transforms the linear displacement into bending deformation of the micro-beams. This enables us to reach a large linear deformation without exceeding the maximum elastic strain in each micro-beam. Fig. 2.19 (c) and (a) also present a side view of the few first and couple of middle section columns, respectively. Under strain, the micro-beams twist out of plane and bend about the axis with the lowest moment of inertia. As presented in Fig. 2.19 (c), this twist occurs in the first few columns and from the third column on, the twist angle stays approximately the same and the bending motion is the dominant mode of deformation.

In Fig. 2.19a, the sections marked by + are in tension and the sections marked by - are in compression. The number of micro-beams and hence the length of the conductive tracks in tension and compression are equal. In the sensor pattern, we modulate the width of the metal tracks in one half (either in the sections with metal layer in tension or in compression) to produce narrower metal tracks with a larger electrical resistance. In the sensor, the parts with narrow and wide tracks have opposite loading conditions and because of higher initial

resistance of the part with narrow tracks, the resistance change of this part dominates the overall resistance change of the sensor. Fig. 2.19 presents an example of a sensor with a narrower track in the beams under compression resulting in negative sensitivity. The radius of curvature and the strain in the metal tracks change along the micro-beams. In order to maintain the overall resistance of the sensor as low as possible, the metal tracks in the sections of the sensor without substantial curvature are designed to have the same wide cross-section as the parts in tension. So the narrow metal track in each beam is shorter than the wide metal track. This design reduces the overall resistance of the sensor without much influence on the resistance change and in effect increases the ratio of the resistance change to the initial resistance.

The twist buckling which occurs in the first few columns of the sensor is a phenomenon

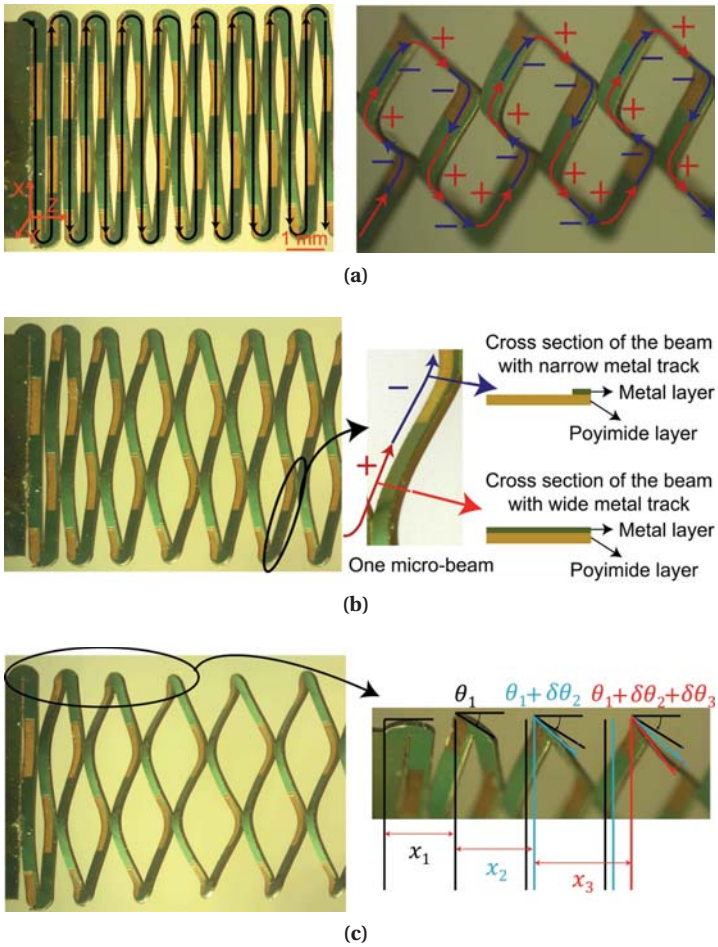

Figure 2.19: Bending deformation of the micro-beams in the mesh structure of the stretchable sensor. (a) The electrical path and the sign of the resistance change are illustrated in this figure. (b) One micro-beam and different metal profile in sections in tension and compression. (c) The twist buckling motion of the micro-beams is developed in the first few columns of the sensor.

in which a beam under bending load twists out of plane and bends about an axis with a lower moment of inertia. The twist angle is determined for the beam to have the minimum deformation energy. Apart from the first few columns, for the main body of the sensor the dominant deformation is bending along the micro-beams. This bending motion for one micro-beam is presented in Fig. 2.19b. Fig. 2.19c presents the twist which occurs in the first few columns. Given the larger number of the beams with dominant bending motion, they have the main influence over the twist angle and resistance change in the sensor. Therefore, we model the behavior of the sensor through studying the deformation only in these beams. To find the relation between the bending deflection of each micro-beam and the stretch, we need to know the twist angle. Since we only consider bending about the minimum moment of inertia axis, we can estimate the twist angle using geometrical relations. we expect this estimate to be accurate since the maximum moment of inertia is 2000 times larger. Based on the boundary conditions for each micro-beam, we can estimate the twist angle as:

$$\begin{aligned} 2\delta_z &= 2\delta\sin\theta = D + b(1-\cos\theta) \\ 2\delta_y &= 2\delta\cos\theta = b\sin\theta \end{aligned} \qquad \frac{\tan\theta\sin\theta}{D+b(1-\cos\theta)} = \frac{1}{b} \tag{2.13}$$

In (2.13), δ, δz, and δy are the deflection of the beam and its components along z and y directions respectively which are depicted in Fig. 2.20. Here, b is the width of each micro-beam and θ is the twist angle of the beams. For D, the contribution of each micro-beam to the overall stretch, we have:

$$D = \frac{\triangle x}{N_{columns}} \tag{2.14}$$

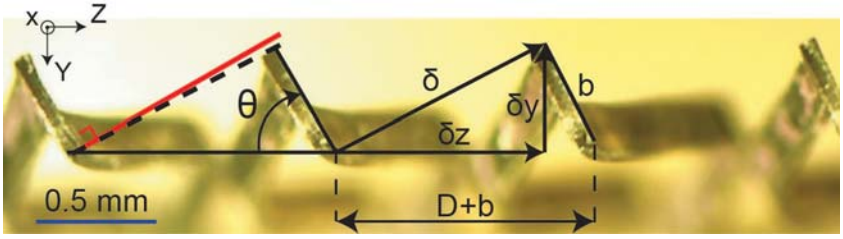

Figure 2.20: Twist angle, θ, in a stretched sensor (sensor view along x axis). To measure this angle as a function of elongation, the sensor was mounted on a linear stage and stretched in 1 mm steps under a microscope. The small angle between the dashed black and the solid red lines in this figure is caused by the secondary bending about the axis of maximum moment of inertia, I_{max}, which is neglected in this study.

where $\triangle x$ is the overall stretch of the sensor and $N_{columns}$ is the number of columns along the sensor. Fig. 2.21 presents the estimated and the measured twist angle as a function of contribution of each micro-beam to the elongation (D). To measure the twist angle, we placed the sensor on a micro stage and studied its deformation under a microscope in 1 mm steps.

The deformations considered in (2.13) are not the only possible deformations to satisfy the boundary conditions but these deformations are the most energy efficient and bending about the other axis would require more energy. The estimated value from the model and the measured twist angles match closely, Fig. 2.21. The small discrepancy can be attributed to small bending about the I_{max} axis. This secondary bending causes the small angle between the dashed black and the red lines in Fig. 2.20. Also as presented in Fig. 2.19c, the few first columns have a smaller contribution to the elongation which means that the deflection in the beams in the middle section is slightly underestimated by (2.14).

The twist direction is determined by the pattern of the metal layer. For the pattern presented in Fig. 2.19, the sensor deforms so that the narrow metal tracks would always be in compression and the sensor's resistance decreases as it stretches. For the symmetric sections with a wide metal track, the twist can happen on either side and it is the parts with narrow metal tracks that determine the twist direction. Fig. 2.22 presents a schematic of a micro-beam with a patterned metal layer. It is attached to the left columns on two ends and to the column on the right in the middle. As the sensor is stretched, the micro-beams can twist about x axis in both positive and negative directions. If it twists in the positive direction, the moment of inertia of the bending axis (I_{yy}) increases. As a result this damps the out of plane twist motion. On the other hand, if the beam twists in the negative direction of x axis (Fig. 2.22b) I_{yy} decreases, which allows bending deformations requiring less energy. So the micro-beams with the pattern presented in Fig. 2.19 always twist in the direction that puts the narrow metal tracks in compression and the wide metal tracks in tension. So a sensor with this pattern has negative sensitivity to elongation. By etching the metal on the opposite side (mirrored

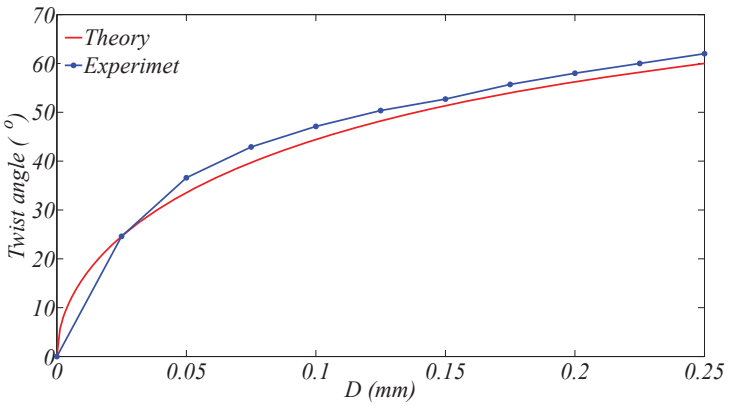

Figure 2.21: The twist angle as a function of the contribution of each micro-beam to the elongation from theory and experiment.

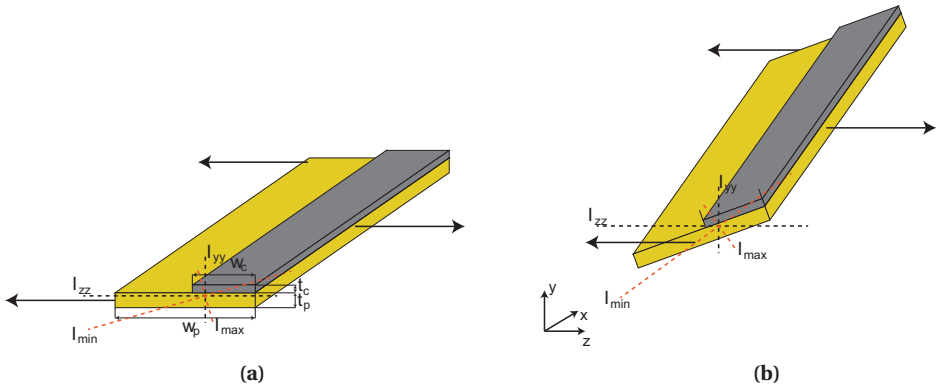

Figure 2.22: Twist direction of micro-beams. this deformation occurs to reduce the moment of inertia about the bending axis. The twist direction determines whether the metal layer would be in tension or in compression. For a beam without pattern in the metal layer, the twist can happen in either directions. In a patterned beam, the twist always happens in a direction that results in a smaller I_{yy}. This selective twist happens since the axis of minimum moment of inertia is slightly tilted due to the asymmetric pattern in the metal layer.

about the y axis), we will have the opposite twist direction leading to positive sensitivity to elongation.

To fabricate the stretch sensors, we engrave, machine and chemically process the surface of a Constantan-polyimide laminate, 5 μm Constantan film (CU040200, Goodfellow) and 50 μm Pyralux film (LF0110, Dupont). The surface of Constantan layer is covered with etch resist. After curing the resist layer, the sensor pattern is cut through this layer to expose the metal layer (see Fig. 2.23a). Engraving the surface in the first step of fabrication is not uniform mainly because of the uneven surface of the sample. This results in a non-uniform wet etching process. Therefore, to ensure that all tracks remain connected, we keep the minimum track width in the engraving process. In our experiments, the minimum reproducible track size was determined to be 90 μm; used in the sensor design here. After engraving the sensor pattern in the resist layer, the mesh pattern is cut through all layers (see Fig. 2.23b) and the outline of the sensor is cut. In the next step, the metal layer in the exposed parts is etched in ferric chloride solution (see Fig. 2.23c). This step of the process is very sensitive and over-etching damages the tracks. On the other hand, if the metal in the exposed parts is not removed completely, it causes irregularity in sensor reading under strain. After this step, the resist on the electrode parts are cleared and wires are connected to the electrodes using conductive epoxy (CW2460 from Chemtronics).

The sensor consists of two patterns: a cut-through mesh and a profile pattern in the metal layer. The stretchable mesh pattern, Fig. 2.24a, transforms the elongation into bending of the micro-beams and allows large displacements without surpassing material's elastic loading range. The pattern in the metal layer consists of two parts, a serpentine path, Fig. 2.24b, and an asymmetric pattern, Fig. 2.24c, that selectively makes narrower metal tracks in the sections

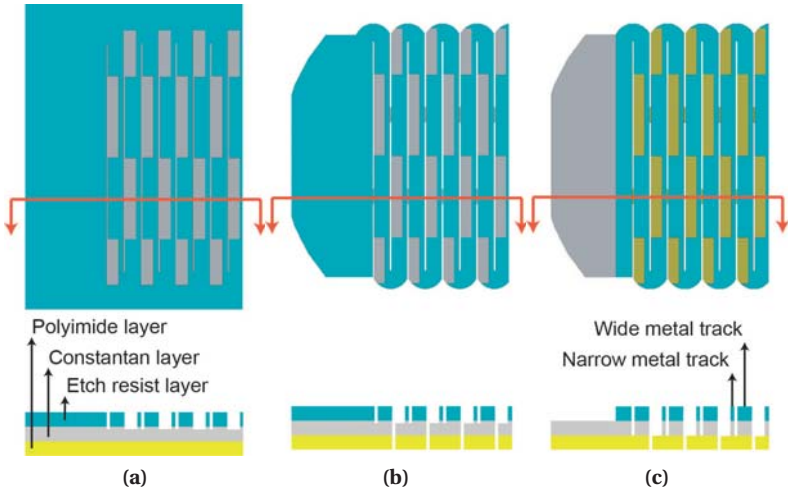

Figure 2.23: Fabrication process of metal based stretchable sensors. (a) Exposing the metal layer in the desired areas. (b) Micro-machining the mesh pattern and the outline of the sensor. (c) Etching the metal in the exposed areas to create the desired pattern in the metal layer.

under tension or compression. The role of the serpentine path is to increase the resistance of the sensor and its variation under strain.

The mesh pattern, Fig. 2.24a, has low electrical resistance and sensitivity to stretch and can be used as stretchable tracks for power and signal transmission. Etching the metal along the serpentine pattern on the same mesh pattern produces a resistor with a high resistance but a low sensitivity to strain, Fig. 2.24b, that is used as a voltage divider resistance for reading the sensors and canceling out the thermal effects. To make the pattern of Fig. 2.24b sensitive to strain, the metal tracks in tension or compression are selectively exposed and etched to become narrower (hence having a higher contribution to the final resistance change). This leaves us with the asymmetric pattern of Fig. 2.24c with narrower metal tracks in compression and negative sensitivity to stretch. To have the maximum range of stretch, it is imperative to choose the minimum thickness for the sensor to reduce the strain in the micro-beams. The sensor is made of a laminate of Constantan on polyimide. For the samples used to refine the design and those used to study the electrical properties of different patterns, we used 10 μm Constantan film. For the final prototype, we used 5 μm Constantan film. The sensor design is based on the laminate using thinner Constantan film. We chose the thickness of the polyimide layer to place the neutral plane somewhere in the polyimide to have the whole metal layer in each cross-section in tension or compression. Fig. 2.22 presents a schematic of the beam's cross-section and the relative position of the metal layer and neutral plane. Considering simple bending, to place the neutral plane at the intersection of the Constantan and polyimide, the ratio of the thickness of the two layers should satisfy the following relation:

$$(ES)_{Constantan} = (ES)_{polyimide} \rightarrow k^2 = \frac{E_{Constantan}}{E_{Polyimide}} \tag{2.15}$$

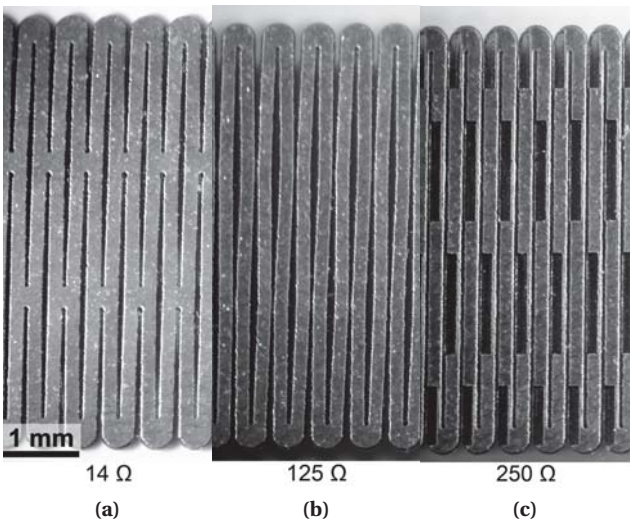

Figure 2.24: Effect of different parts of the sensor pattern on the electrical resistance. (a) The mesh structure with very low resistance can be used as a circuit to make the electrical connections between different parts. (b) The serpentine path which has a large electrical resistance (10 times the mesh structure) but low sensitivity to stretch (given its symmetric electrical path) can be used as a voltage divider for reading the sensors and compensating the thermal effects. (c) Finally the complete pattern which selectively increases the contribution of sections in compression. Thickness of the Constantan film used to check the electrical properties of different designs was 10 μm. The resistance is reported for 80 columns of micro-beams.

In (2.15), S is the first moment of area, E is the modulus of elasticity, and k is the ratio of the thickness of the polyimide to Constantan. Based on (2.15), the thickness of the polyimide layer for 5 μm Constantan film should be 40 μm. Based on the availability, we used Pyralux LF0110 composed of 25 μm polyimide and 25 μm acrylic adhesive layer as the substrate for laminating Constantan. Here, we approximate the properties of the adhesive layer by polyimide properties and model the laminate as a film composed of 5 μm Constantan and 50 μm polyimide. In this laminate, the neutral plane will be in the polyimide layer and 1.2 μm below the intersection with the metal layer.

If the metal layer undergoes a large strain above its elastic range, sensor's reading starts to drift in repeated cycles due to the plastic deformation in the metal layer. Accordingly, the maximum range of stretch in the sensor is dependent on the strain in the laminate as the micro-beams bend. Neglecting the first few columns, where the twist motion happens, we study the strain in each micro-beam considering simple bending under concentrated load at one end. Fig. 2.25 presents the loading condition on each micro-beam. The maximum deflection in each beam is limited by the minimum allowed radius of curvature, ρ_{min}, which

is governed by the maximum elastic strain, ϵ_{max}:

$$\rho_{min} = \frac{y}{\epsilon_{max}} \tag{2.16}$$

In (2.16), y is the distance from the neutral plane. The maximum elastic strain is dependent on the properties of each layer. Considering the loading condition introduced in Fig. 2.25, we have the following relation governing the beam's deflection:

$$\delta_{max} = \frac{(l_{mesh}/4)^2}{3\rho_{min}} \tag{2.17}$$

For a desired range of stretch, one can choose the design parameters (l_{mesh}, b, and the number of columns) to keep the radius of curvature above ρ_{min}. The mechanical properties of the laminate used in the sensors is dependent on the properties of each individual layer and is also influenced by the fabrication processes such as heat press lamination and laser micro machining. We determine the allowed range of motion using experimental data for the specific design presented in here. Using the experimental data and (2.17) one can estimate the maximum allowed strain in the laminate which will be used as a guideline for designing sensors with a desired range of elongation.

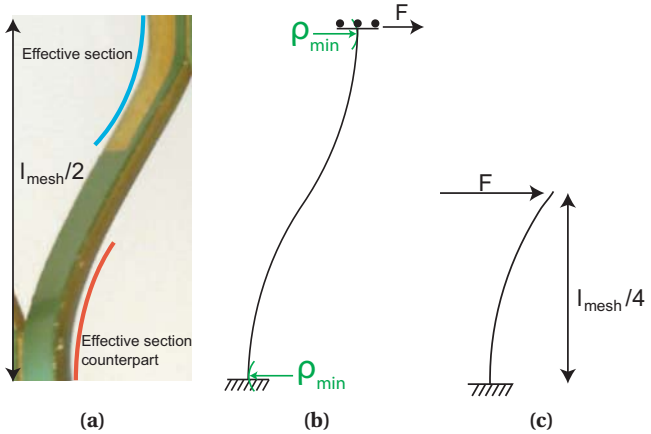

Figure 2.25: Bending deformation in one of the micro-beams that makes up the mesh structure (as presented in Fig. 2.19). (a) The section with narrow metal track and effective resistance change and its counter part with wide metal track are highlighted in this figure. (b) The schematic of the equivalent loading condition. (c) Based on the symmetry in the beam, we can study the bending deformation in half of beam's length.

The study of the deformations of the micro-beams and the strain in the metal layer can also be used to estimate the sensitivity of the sensor to elongation. The resistance change in the stretched sensor originates from the strain in the metal layer. Considering the gauge factor of 2 for Constantan, the resistance change, δR, in the effective part and in its counter part, Fig. 2.25a, is estimated using the mean strain in the beam:

$$\delta R = 2R\bar{\bar{\epsilon}} \tag{2.18}$$

where R is the electrical resistance of the corresponding portions of the micro-beam and $\bar{\bar{\epsilon}}$ is the mean strain in the metal layer. To evaluate the mean strain, we use the following equation for strain, ϵ, in each cross-section:

$$\epsilon = \frac{y}{C}\epsilon_m \tag{2.19}$$

where C is the distance of the outer layer of the metal to the neutral plane. ϵ_m is the minimum or the maximum strain in the metal layer for a beam in compression or in tension, respectively. Integrating the above equation gives us the following relation for the average strain in each cross-section ($\bar{\epsilon}_{section}$):

$$\bar{\epsilon}_{section} = \frac{1}{t_c}\frac{(t_c+y_c)^2 - y_c^2}{2(t_c+y_c)}\epsilon_m \tag{2.20}$$

where y_C and t_C are the distance of the Constantan-polyimide intersection from the neutral plane and the thickness of the Constantan layer respectively. y_c in (2.20) is different for the sections with narrow and wide metal tracks and is equal to 5.3 μm and 1.2 μm, respectively. In this study we neglected the initial tilt of the minimum inertia axis in sections with narrow metal track (see Fig. 2.22). Considering the ratio of the width of the micro-beam and the thickness of the Constantan layer this tilt angle is small and neglecting it would not affect the result significantly.

As described, we estimated the deformation of each micro-beam as a beam in simple bending and under concentrated load at one end. For this loading condition, the curvature, $1/\rho$, changes linearly along the beam between zero and the maximum curvature, $1/\rho_{min}$, (given the linear distribution of the moment along the beam). So in average, the strain along the whole length would be the mean of the strain of the beginning and the end of each part. Combining (2.17), (2.18), and (2.20) will give the following expression for the resistance change of the effective section and its counterpart in each micro-beam. These are highlighted in Fig.

2.25a.

$$\delta R = 2R\bar{\bar{\epsilon}} = 2R\frac{1}{2t_c}\frac{(t_c+y_c)^2 - y_c^2}{2(t_c+y_c)}\frac{3C}{(l_{mesh}/4)^2}\delta(1+\frac{\delta l}{l_{mesh}/4}) \tag{2.21}$$

The term $^{\delta l}/_{l_{mesh}/4}$ accounts for the difference between the length of the part in tension and compression. The value for the present design is 0.15. y_c and R in this equation are different for effective section with narrow metal track and its counterpart with wide cross-section. The overall resistance change in the sensor, $\triangle R$, is the sum of the resistance change in the effective sections in compression, δR_C, and their counterpart in tension, δR_T:

$$\triangle R = \delta R_T + \delta R_C \tag{2.22}$$

The strain in the material and the resistance change depend on the sensor's design parameters. For the experimental studies, we used a design with parameters determined based on the experience and limitations dictated by the fabrication process. The slit size in the mesh pattern, l_{mesh}, in the case study is 3.45 mm. In this pattern, the beam width is 250 μm, the track size in the wide section is 230 μm and in the narrow section is 90 μm. The metal track width is smaller than the designed value because of the metal removal from under the protective layer in the wet etching process. So the resistance of the sensors are larger than the resistance expected from the track's design parameters. In order to evaluate R_T and R_C, we fabricated one sample with the asymmetric pattern and the other with only the serpentine pattern and measured their resistances. We found the resistance of the effective part in compression and its counterpart in tension to be 210 Ω and 660 Ω, respectively. Using these values along with (2.21) and (2.22), we can estimate the resistance change in the sensor. (2.21) suggests a linear relation between resistance and deflection of the micro-beams. The only non-linearity arises from the relation between the sensor's stretch and the deflection in the micro-beams as suggested in (2.13). This is specifically important in small deflections where the rate of the twist angle change is significant.

Fig. 2.26 presents the estimated resistance change as a function of sensor's stretch. The response of the sensor over 1 mm stretch can be closely estimated by a linear function with R^2 of 0.992. As will be discussed in the next Section, due to the residual deformation in the mesh structure, in the experiments the measurements will be in the linear part of this plot. The slope of the line fitted to this part is $-0.22\ ^{\Omega}/_{mm}$.

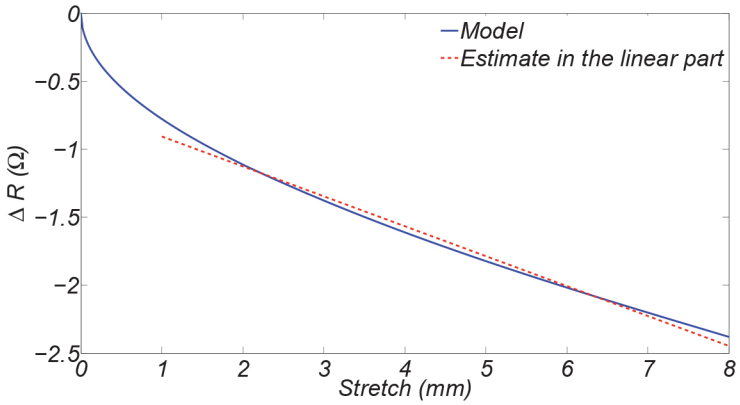

Figure 2.26: Estimated resistance change as a function of sensor elongation. Aside from the first 1 mm of stretch, the response is quite linear (the slope is $-0.22\ ^{\Omega}/_{mm}$). We have calculated the resistance change for a sample with 20 mm sensing length equivalent to 80 columns of micro-beams so the result would be comparable with the experimental results.

2.5.2 Characterization

In this Section, we investigate the quasi-static response of the metal stretchable sensor in detail and examine the effect of loading rate on the its response. To study the quasi-static response, we first compare the sensitivity of a sample with the complete pattern including the asymmetric pattern in the metal layer, similar to Fig. 2.24c, and a sample with the same mesh and serpentine patterns but without the asymmetric pattern in the metal layer, similar to Fig. 2.24b. The goal is to confirm the working principle of the sensor and to study the possibility of using the sample with the symmetric pattern as voltage divider resistance. The sensors fabricated for studying the pattern are made out of laminate with 10 μm thick Constantan. The resistance of the symmetric sample is 125 Ω. Etching the metal layer in the desired areas increases the resistance to 250 Ω. The difference between the two is the effective resistance of the sensor. Fig. 2.27 presents the measurements from these two samples when stretched in 500 μm increments up to 2.5 mm and back. The meshed length of both samples is 20 mm.

As expected, the resistance of the sample with the complete pattern decreases under load. The results confirms repeatable measurements in 50 cycles. Although the overall resistance change is not high compared to the initial resistance of the sensor, the repeatable measurements with mean standard deviation of 1.7% confirms a good accuracy. For the sample with the symmetric pattern, we expected no resistance change under strain but among the three samples tested, the resistance always increased with stretch in the sensor. This rules out to some extent the random uneven wet etching of the metal sections in tension and compression as the reason for the positive sensitivity. It seems that the reason for this is the uneven gauge factor of Constantan in tension and compression, which is also reported for the commercial film strain gauges. We have tested the same samples up to 3.5 mm stretch but since the readings started to drift in repeated cycles (indicating overloading of the metal layer), we presented the result

of the experiment with 2.5 mm stretch which corresponds to 12.5 % increase in the sensor length.

One way to increase the sensitivity of the sensors without surpassing the maximum allowed strain or limiting the maximum elongation in the sensor is using thinner Constantan layer in the laminate. This increases the average magnitude of the strain in the metal layer (2.21) by placing the neutral plane further away from the metal layer and inside the polyimide. Making the laminate thinner also increases the allowed range of motion of the sensor. We fabricated a sensor with 5 μm Constantan and the same polymer layer (25 μm polyimide and 25 μm adhesive). Fig. 2.28 presents the result of the quasi static tests on this sensor. We tested the sensor with different maximum stretch amplitudes with 500 μm increments. The goal is to establish the maximum allowed elongation for the sample and to ensure that the sensor reading is repeatable in different loading amplitudes. We tested the sensor in 20 cycles for each amplitude. The mean cycle for each test is presented in Fig. 2.28 which illustrates the repeatability of the sensor measurements. At 4 mm stretch, the sensor reading at zero deviates from its initial value, which corresponds to the plastic deformation in the sensor. By increasing the pre-strain in the sensor, we could use it in a wider range but for the present design parameters, 4 mm (the start of the plastic deformation) is advisable as the allowed range of elongation (equivalent to 20 % of the sensor length). To design sensors for a specific application, one can use this maximum deformation along equations 2.13 - 2.17.

Contrary to the initial expectation from the model, Fig. 2.28, the response of the sensor is almost linear in its entire range of deformation. This discrepancy is due to the unrecoverable

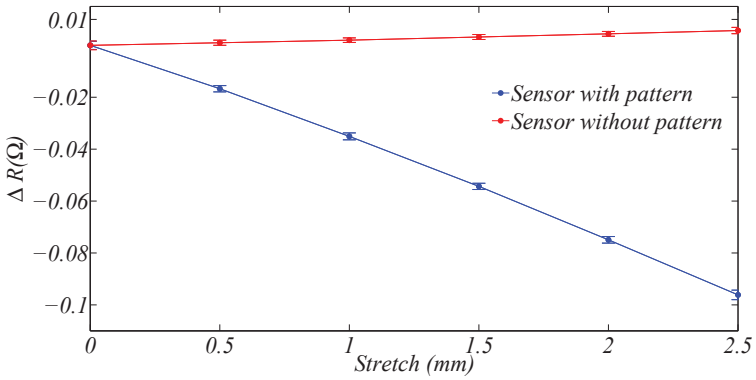

Figure 2.27: Comparing the sensitivity of stretch sensors with different patterns. The result of 50 stretch cycles for a sample with the complete pattern and a sample with just the serpentine and mesh patterns. The active length of both samples is 20 mm. As expected, the resistance of the sample with complete pattern decreases under strain and shows high sensitivity to strain and a good repeatability with mean standard deviation of 1.7%, of the whole range of resistance change, in 50 loading cycles. For the control sample without the asymmetric pattern, we expected no resistance change, but the tests on symmetric samples repeatedly showed a small increase in the resistance under strain. The resistances of the sample with full pattern and the control sample were 250 and 125 Ω, respectively.

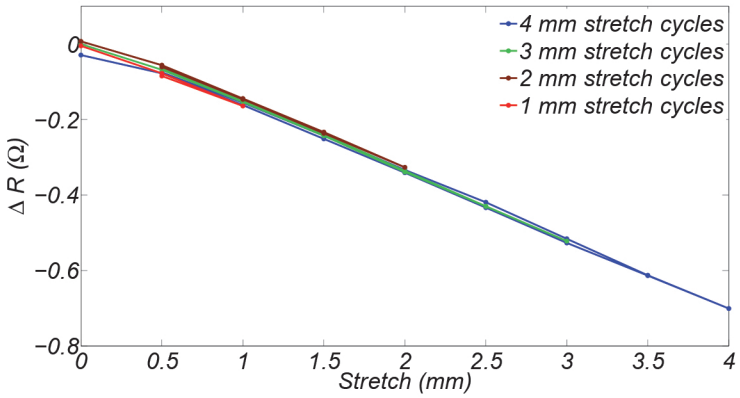

Figure 2.28: Resistance change as a function of stretch in the sensor. The plot presents the average of 20 cycles with four amplitude of loading $1-4\ mm$. For the present design, stretch up to $4\ mm$, 20 % of the length, causes no damage and plastic deformation in the sensor. The response of the sensor can be estimated by a line with the slope of $-0.18\ ^{\Omega}/_{mm}$. The maximum hysteresis loop width is 2 % (0.014 Ω) of the maximum resistance change and is of the same order of magnitude as the standard deviation.

twist in the sensor. After stretching the sensor for the first cycle, part of the twist angle and deformation in the sensor will not be recovered. This residual strain shifts the response of the sensor to the linear part of Fig. 2.26. We should point out that the sensor was conditioned with few cycles of medium amplitude prior to the experiments. The slope of the resistance change in Fig. 2.28 is $-0.18\ ^{\Omega}/_{mm}$. This is comparable but smaller than the estimated theoretical value ($-0.22\ ^{\Omega}/_{mm}$). One reason for this is the different gauge factor for the metal in tension and compression which was mentioned as the reason for the resistance increase in the symmetric sample in Fig. 2.27.

In this Section, we introduced a novel sensing concept based on the strain in metal film for measuring stretch. Being thin and complaint, this sensing method can be used in different emerging soft and wearable robots. The possibility to control the sensitivity by modulating the profile of the metal layer, enables us to produce stretchable surfaces with integrated sensing elements and circuitry out of a low profile Constantan-polyimide laminate. In Chapter 5, we use this concept in a sensor with two gauges in parallel with opposite sensitivity to measure facial movements.

2.6 Conclusion

In this Chapter, we studied position sensors based on two different sensing principles for robogami joints: piezo-resistive sensors based on carbon particle compounds, and strain sensors based on thin metal films. Depending on the application and the required accuracy, different sensor designs from each group might be used. In general carbon based sensors are cheaper and easier to manufacture. Slow transient response, high sensitivity to ambient conditions, and drift in their measurements, however, limit the application of these sensors.

The metal based curvature sensors are significantly more accurate. Unlike the piezo-resistive sensors' resistance, which increases under both tension and compression, the resistance change in metal sensors depends on the strain sign. This allowed us to design sensors that can more effectively cancel out the thermal effects on the sensor measurement.

The curvature sensors provide feedback from robogami's configuration in a wearable device. For effective interaction with humans, we also require to measure body movements. In this research we proposed thin, stretchable, and mechanically transparent sensors for measuring body movements. These sensors are designed based on the same sensing principles that were used in the curvature sensors. A mesh pattern transforms the elongation in the sensor into bending of a series of micro-beams connected in series. Similar to the curvature sensors, the carbon based stretchable sensors are easier and cheaper to fabricate and their high sensitivity to strain simplifies the required hardware for measuring their resistance change. For applications requiring higher accuracy, metal based stretchable sensors perform better. These sensors can be designed to have positive, negative, or no sensitivity to elongation, which allows us to design a network of sensors with built in temperature compensation.

The sensing solutions presented in this Chapter are unique for their thin profile, adaptability of design, and compatibility with robogamis' manufacturing process. Combination of these sensing elements in a wearable device can provide the necessary feedback for effective interaction with the subject. In Chapter 4, we present application examples of the sensing methods for robogami joints and in Chapter 5, we study the application of metal based stretchable sensors measuring facial movements.

3 Robogamis: smart materials for soft actuation and compliance control

Functional materials with adjustable mechanical properties have applications in robot's structure to provide actuation, compliance control and other functions. adaptable manufacturing, inherent compliance, and ease of integration and activation are among the main advantages of using functional materials. One of the application fields that can greatly benefit from these smart materials are the wearable devices with strict restrictions on inherent compliance, required DoFs, and size limits. In this Chapter, we introduce actuation and compliance control methods for robogami platform. we present a method for independent actuation of joints using thermally activated SMA. Also a method for compliance control using thermally activated SMP is presented. Both of these methods are well adapted to the manufacturing process of the robogamis. SMA and SMP can be embedded in a robogami as one of the functional layers. In this Chapter, the design, manufacturing process, and performance analysis of SMA and SMP layers are presented.

3.1 Introduction

Augmenting functional materials in the structure of robots allow us to target new applications that were previously inaccessible due to the requirements on size and interactivity. The functional materials also simplify the hardware required to actuate and control robots and

The material of this Chapter is from the following self-authored publications:
[29] **A. Firouzeh**, et al., "Sensor and actuator integrated low-profile robotic origami", IROS 2013.
[30] **A. Firouzeh** and J. Paik, "Robogami: A fully integrated low-profile robotic origami", ASME Mechanisms and Robotics 2015.
[31] **A. Firouzeh** and J. K. Paik, "An under-actuated origami gripper with adjustable stiffness joints for multiple grasp modes", Smart Materials and Structures 2017.
[72] **A. Firouzeh**, et al., "Soft pneumatic actuator with adjustable stiffness layers formulti-dof actuation", IROS 2015.
[73] **A. Firouzeh**, et al., "An under actuated robotic arm with adjustable stiffness shape memory polymer joints", ICRA 2015.
[74] **A. Firouzeh** and J. Paik, "Stiffness control in under-actuated robotic origamis with shape memory polymer", TRO 2017.

in effect reduce the cost and complexity of manufacturing and operation. In this Section, an overview of different methods for actuation and compliance control are compared and the most appropriate ones are highlighted based on the compatibility with the manufacturing process and the requirements from a wearable device.

3.1.1 Methods of soft actuation

Functional materials with different working principles are utilized to actuate DoF in robots. In general these methods of actuation are characterized by the inherent compliance, simplicity of auxiliary equipment, scalability, and adaptability of the design. Most of these methods, however, lack in one or few of the actuation characteristics (band width, work density and range of motion) which limits their application. Fig. 3.1 compares the actuation range (strain) and the work density of few options among the smart materials. Actuator's work density is the main limiting factor in miniaturizing independently actuated DoFs. SMA actuators offer significantly larger work density compared to all other smart materials. The range of strain recovery of SMA is also favorable. Moreover, in applications requiring larger strain range, SMA actuators in coil [21] or other spring forms [75] can be used to acquire the right balance between output force and displacement.

Based on the low profile and compatibility with the manufacturing process, we chose SMA sheet actuators for driving robogami joints. High work density and design adaptability allow for easy miniaturization and design of thin robogamis with multiple DoFs. We use SMA actuators in the bending mode to directly drive the adjacent tiles in the robogami, as suggested previously by Paik, et. al. [77].

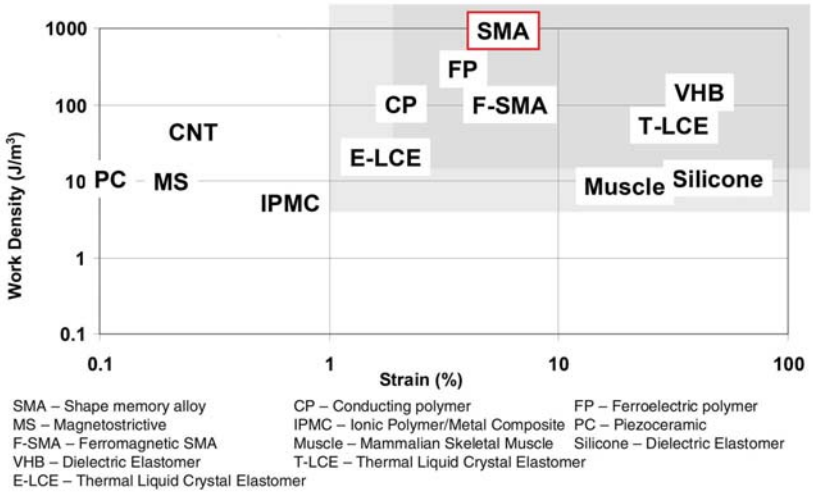

Figure 3.1: Comparison between the work density and the stain of different soft actuation methods based on smart materials. SMA actuators offer significantly larger work density which makes them a desirable method of actuation in small scale robotics. The figure is adopted from [76].

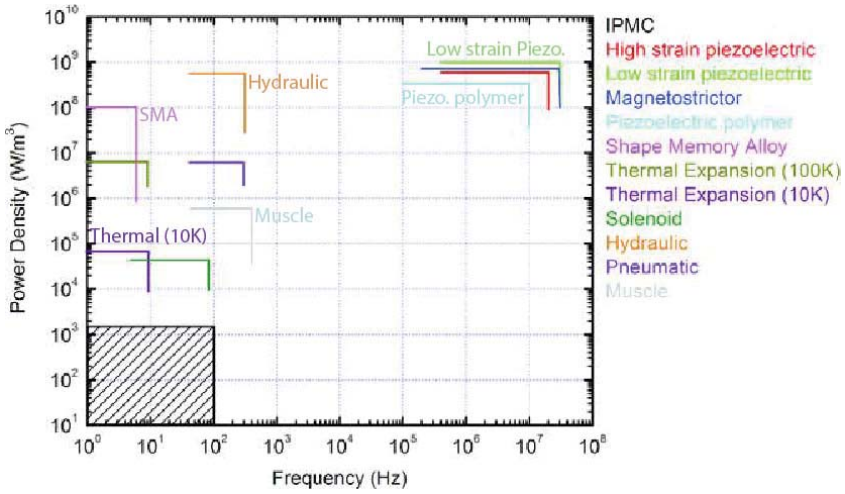

Figure 3.2: Comparison between the work density and the frequency of different soft actuation methods based on smart materials. This figure highlights the most important shortcoming of actuators with thermal activation which is their slow response. The figure is adopted from [78].

SMA actuators provide significant blocked torque and large range of motion. The main obstacles for using SMA actuator is its slow response. Fig. 3.2 compares the frequency range of a selection of smart materials. Thermally activated systems are inherently slow. The response time can be improved by integrating a cooling system such as a Peltier module. Nonetheless, the response time remains as one of the limiting factors for using SMA actuators.

In this Chapter, we introduce a bidirectional actuation scheme using antagonistic SMA bending actuators for driving robogami joints. Depending on the required range of motion and loading capacity, the design parameters of the actuator (thickness, width, and the length of the active section) are determined. A model to study the behavior of SMA actuators and corresponding characterization results provide a design guideline for SMA sheet actuators.

Miniaturizing the SMA actuators and the robogami joints enables us to design systems with more DoFs but at the cost of reduced loading capacity. In a wearable device, many of DoFs are utilized for initial reconfiguration and only few would be actively used to apply a desired force or displacement. This motivates the design of a locking method for robogami joints resulting in higher loading capacity. Moreover locking the joints after initial reconfiguration simplifies the control problem and reduces the energy consumption of the system (considering that the locking method would not consume energy). Joints with adjustable stiffness can be used to achieve the desired locking and more as will be discussed next.

3.1.2 Methods of compliance control

Compliance of inherently soft robots originates from the elastic properties of the comprising materials. Based on the application, materials with different levels of stiffness are used to

Table 3.1: Comparison between methods of stiffness control based on different physical principles. Some entries in the table are taken from [97]. For many of the methods, depending on the design, higher stiffness variability could be achieved. Nonetheless, this table provides an approximation of the performance of different methods.

Reference | Method or material	Stiffness variability	Additional info.
Shape memory alloy [98]		
55-NiTiNOL	$E_{hot}/E_{cold} \approx 4$	82-38 °C
Shape memory polymer [98]		
Polyurethane	$E_{cold}/E_{hot} \approx 100$	below and above 55 °C
Low melting point alloys [99]		
In rubber	$E_{cold}/E_{hot} \approx 25$	below and above 47 °C
Jamming through vacuum [92]		
Granular jamming	$E_{stiff}/E_{soft} \approx 5.3$	applying vacuum pressure °C

achieve a compromise between mechanical transparency and load capacity. To broaden the application of inherently compliant robots, to meet the requirements of different tasks, it is necessary to develop means of stiffness control for its segments or joints. By embedding elements with adjustable stiffness, we develop robots that can change their mode of interaction and compliance depending on their task.

Different methods for directly embedding the compliance in the robot's hardware have been proposed [79–82]. Many of these rely on conventional means of actuation and mechanisms [83–85]. In this research, we are interested in methods that rely on material properties based on their scalability and versatility of design.The elastic modulus variability in polymers [72, 73, 86–90], Jamming [91–93], and phase change in wax [94] and metals [95, 96] are among the different methods [97] that use material properties for controlling the stiffness of the structure. Table 3.1 presents examples of few methods of stiffness control.

Among the methods listed in Table 3.1, SMP is the most desirable based on its high ratio of stiffness variability around its glass transition temperature, its low cost, and easy processing. More detailed comparisons between stiffness control methods in the literature [100] confirms the aforementioned advantages of SMP for stiffness control. Moreover, a locking mechanism based on SMP does not consume energy in the locked state. As mentioned before, this is a significant advantage in a wearable device since many of DoFs are only used for the initial reconfiguration. In this Chapter, we present few different designs of SMP based ASLs and their characterization results. ASL can be augmented as one of the functional layers in the robogami structure for controlling the reconfiguration, number of DoFs, and the overall compliance of the structure as will be discussed in more detail in the next Chapter.

3.2 Shape memory alloy for soft actuation of robogami joints

High energy density of SMA actuators [75,101,102] make them a desirable choice for small scale robots. Low profile, design versatility, compatibility with the layer-by-layer manufacturing of

robogamis, and the quasi-2D fabrication processes make these actuators a good candidate for driving the joints of robogamis with multiple DoFs [18, 77, 103]. In this Section, we study bending SMA actuators for bidirectional actuation of robogami joints using two antagonistic actuators as presented in Fig. 3.3. In this design, one of the actuators has its annealed shape in folded state and the other has unfolded annealed shape. Here, we study the time response of SMA actuators, their loading capacity, and feasibility of robogami joint's position control using SMA actuators and carbon ink sensors.

3.2.1 SMA actuator model

In this Section we present the thermal and mechanical model of sheet SMA bending actuators. The thermal model provides us with guidelines to design effective heating elements and allows us to estimate the required heating power to activate SMA actuators. By studying the temperature distribution, we design heaters to reduce the temperature gradient in the active part of the actuator for preventing overheating and for achieving faster response. To determine the dimensions of the SMA actuator based on a desired range of motion or a blocked torque, we need to model and characterize the mechanical behavior of the actuator. The proposed mechanical model explains the behavior of the robogmai joints with antagonistic SMA bending actuators.

Thermal model

The response time of the SMA actuator mainly depends on its thermal transient response. Different parameters such as heater design, boundary condition, and the heating energy input influence this transient response. In this Section, we study the case in which the heaters are

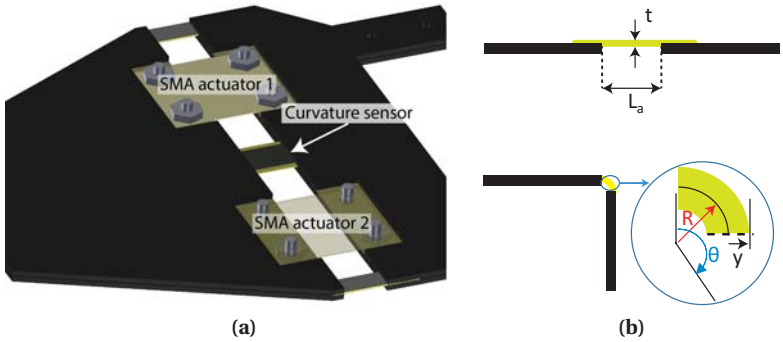

Figure 3.3: Robogami joint with antagonistic bending actuators. (a) One of the actuators has its annealed shape in folded state while the other has unfolded annealed shape. By activating each of the two, we can transform between the folded and unfolded states. One of the actuators is made transparent to show the heating elements embedded inside the tiles. (b) Schematic of the joint actuation depicting deformation of the SMA actuator and its design parameters. In the side views, the tiles are shown in black and the yellow parts represent the actuators.

placed inside the tile areas as presented in Fig. 3.3. Neglecting the radiation, the governing equation is written as:

$$\rho C\dot{T} + \triangle u\dot{Z} = q_{contact} + q_{convection} + \gamma(T)\triangle T \tag{3.1}$$

In (3.1), $\rho, C, \triangle u, \gamma$ are density, thermal capacity, latent heat of phase transition, and thermal conductivity coefficient respectively. The heat transfer between SMA and its surrounding is via natural convection ($q_{convection}$) and contact with other solid surfaces ($q_{contact}$). Here we assumed zero thermal resistance for contact between different layers. As presented in this equation, the input heat to each element (right hand terms of the (3.1)) affects two parameters. One is the temperature, T, and the other one is the mass of material in Austenite phase, Z.

For other components such as glass-fiber, heater, bolts, and nuts; the governing equation

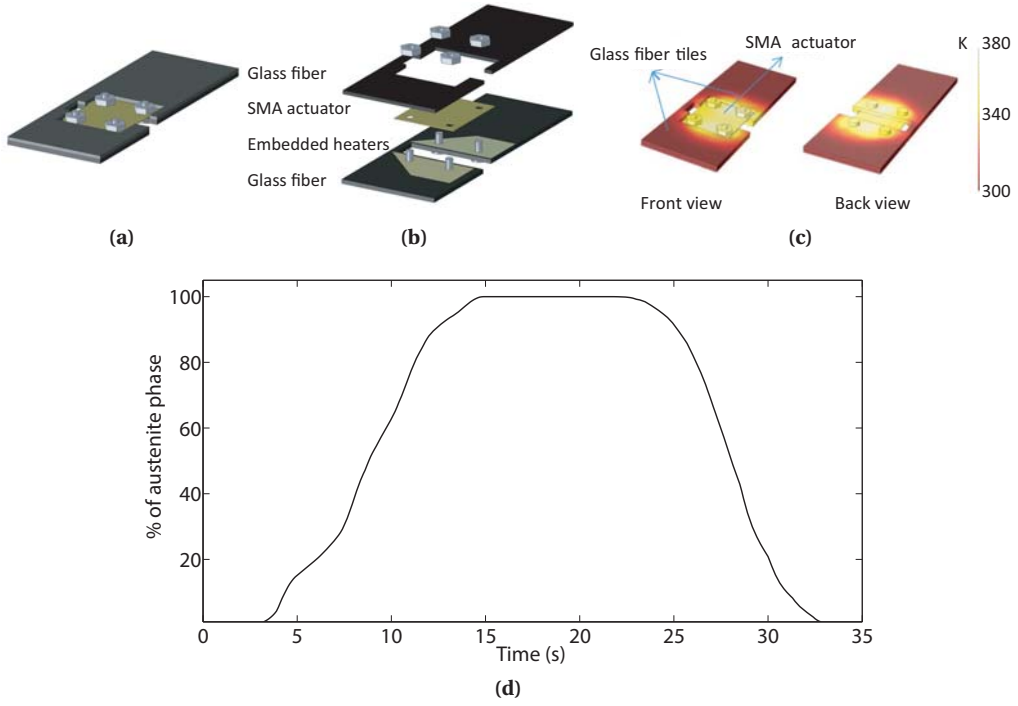

Figure 3.4: Thermal analysis of an SMA bending actuator. (a) SMA actuated robogami joint. (b) Different layers in the joint. (c) The temperature gradient in the actuator and the tiles, corresponding to the instance that all SMA material has transformed to Austenite phase. (d) SMA phase transition versus time. The response time in heating is much slower than expected which is due to the thermal dissipation to the tiles which are in direct contact with the heaters in this design. The heating power is 1.8 W and actuator dimensions (thickness, overall length, and the width) are: 0.1 mm, 11 mm, and 9 mm respectively.

is the same as (3.1) without the latent phase transition heat and temperature dependency of thermal conductivity (the thermal properties of SMA significantly change with the phase transition).

For SMA thermal characteristics, we used the material properties provided by the manufacturer [104]. Fig. 3.4 shows the result of this thermal analysis in which the input heating power was to 1.8 W, the same power is later used in the experiments. Given the location of the heaters, there is a significant power dissipation into the glass-fiber. Initially, based on the lower thermal conductivity of glass-fiber (20 times less than that of the SMA) we expected it to be insulating and to have little influence on the transient thermal response of the system. But as can be seen in Fig. 3.4c, temperature rise in this layer is substantial. The phase transition in the SMA actuator versus time (Fig. 3.4d) shows that nearly 15 s is needed for complete transition of material into Austenite phase. In this plot, the slope change during heating is caused by the latent heat of phase transition and change in the thermal properties of SMA in different phases.

In the blocked force experiment with the same heating power, 1.8 W, it takes around 15 s for actuators to generate maximum torque which is in agreement with the simulation results. The transient response is considerably slower than the expected time response for the actuator. Through the simulation we can confirm that the main reason is the placement of the heaters inside the tile area. To improve the actuator response time, in later versions of SMA actuated robogamis, we designed stretchable heaters which are bonded directly to the SMA actuators in the active region using double sided thermal adhesive. Relocating the heaters, improved the time response significantly (the actuation time was reduced to 2-3 seconds). This also alleviated the rate of the memory loss in the actuators, due to more uniform temperature distribution. The stretchable heaters are similar to the ones embedded in the SMP layer and more on their fabrication process is presented later in this Chapter.

Mechanical model

SMA actuators work based on the temperature controlled transition between the soft Martensite and the stiff Austenite phases. At low temperatures, the crystal structure allows for large strains in the martensite phase. When heated, the crystal structure transforms into Austenite form which has a larger modulus of elasticity. Deforming this crystal structure and transforming it back to the Martensite phase requires larger force. So at higher temperature, the actuator moves to its original memory shape and applies forces if its deformation is blocked, Fig. 3.5 presents an overview of working principle of SMA actuators. In the proposed design for the bidirectional actuation of the robogami joints, the two actuators have different annealed shape (memory shape). Activation of each SMA actuator produces enough force to deform the other actuator at low temperature, in Martensite phase. In this Section, we model the behavior of the SMA bending actuators and estimate the blocked torque that the actuators can generate at different bending angles and the range of motion of a joint with antagonistic SMA actuators. Assuming a simple bending beam model, a uniform radius of curvature along the actuators,

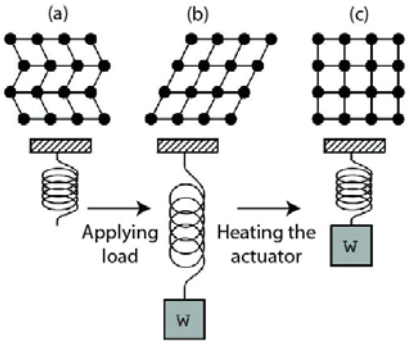

Figure 3.5: Working principle of SMA actuators. (a) SMA actuator at low temperature in Martensite state. (b) The crystal structure allows for large deformation at low temperature. (c) At high temperatures, SMA actuator goes back to Austenite state and applies force to move the load. The figure is adopted from [105]

and neglecting the twist in the tiles, (3.2) yields the following relation for the torque (T) in each actuator.

$$T = \int_{-t/2}^{-t/2} y\sigma w dy,\ \epsilon = \frac{y}{R} = \frac{y\theta}{L_a}\ and\ \sigma = F(\epsilon, Temp) \tag{3.2}$$

In (3.2), t and w are thickness and width of actuator. ϵ and σ are strain and stress, y is the distance from the neutral plane, R is the radius of curvature, L_a is the length of the actuator and θ is the bending angle. Fig. 3.3 presents the design parameters of the SMA actuator. To evaluate this equation, stress-strain data $F(\epsilon, temp)$ is required. Here, we used data from [106]. $F(\epsilon, temp)$ is dependent on many factors such as annealing process, number of actuation cycles and grain structure of the metal, which are different from case to case. So using the data from [106], will not give us accurate numbers for the torque, but it provides an estimation which highlights the important design parameters and the overall behavior of SMA actuators in antagonistic arrangement. Fig. 3.6 presents the torque generated by the active SMA actuator and the torque that is needed to deform the passive actuator as a function of the bending angle based on (3.2).

In Fig. 3.6, there are three lines for the blocked torque of each actuator. They correspond to the torque that the active actuator (in Austenite phase) generates, the torque that is needed to deform the inactive actuator (in Martensite phase) and the elastic relaxation in the passive actuator around the equilibrium point when it is unloaded. The intersections of the lines corresponding to the Austenite phase of one actuator and the Martensite phase of the other determines the equilibrium angle of the joint. When the heater of the active actuator is deactivated, the actuator cools down and the torque line drops to the Martensite phase line. The torque in the passive actuator also drops along the unloading line till a new equilibrium point is reached.

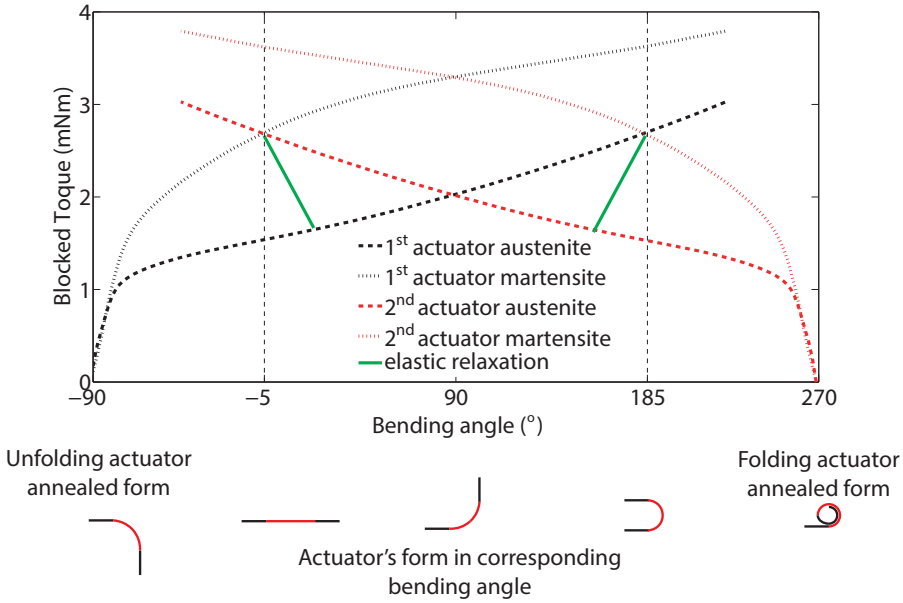

Figure 3.6: Blocked torque in folding and unfolding actuators and the equilibrium angles. Blocked torque of the unfolding actuator is presented by black lines which is zero at -90^o, it corresponds to the memory shape of the actuator. The schematics in this figure presents the corresponding shape of actuators in each bending angle. Based on the temperature of the actuators (the phase of the material), each bending angle corresponds to two values: one for active (heated) and one for passive (cold) actuator. For folding actuator (red lines), the memory shape (zero torque point) is at 270^o and its trend is similar as before. There are two equilibrium points that correspond to the intersection of the blocked torque of an active (heated) actuator with the other actuator in inactive (cold) state. After reaching the equilibrium point and cutting off the current, the equilibrium point starts to shift along the green lines (elastic relaxation of the passively deformed actuator) till reaching the new equilibrium where both actuators are cold. The dimensions of the active part of the actuator (thickness, active length, and the width) are: 0.1 mm, 4.5 mm, and 9 mm, respectively.

The range of motion for a joint with bidirectional actuation is determined by the length of the actuator. According to the model, for 0.1 mm SMA, 4.5 mm long actuators will give a range of motion slightly higher than 180^o (Fig. 3.6). Here, we have chosen the annealed position of the actuators in a way to get the equilibrium points at unfolded and folded states, 0^o and 180^o. In the model, we assumed 8% as the maximum allowed strain for the material. In the remainder of this Section, we study the performance of the actuators in experiments and more accurately investigate the accessible range of motion in a joint with bidirectional actuation. The design of the actuators (their dimensions and annealed shapes) are based on the result of the theoretical study presented here.

3.2.2 SMA actuator characterization

To verify the behavior of SMA actuators and to estimate the range of motion, its blocked torque at different joint angles was characterized. Fig. 3.7 illustrates a schematic of the blocked force test setup. The rotating base in this setup allows us to measure the blocked forces in different bending angles. One side of the actuator is fixed on the rotating base while the other side's motion is blocked by a load cell. The arm on the load cell side is designed to be long (five times the active length of the actuator) in order to get a more uniform moment in the actuator throughout its length.

The range of motion of the actuators in antagonistic arrangement is smaller than the bending angle of the annealed shape of each actuator. This is caused by the opposing force needed for deforming the second actuator, in the Martensite state. When activated without any opposing force, SMA actuators have a high fidelity to their memory shape in repeated cycles. Blocking the deformation of the actuator, however, changes their memory shape in repeated cycles of actuation. Many factors such as the temperature gradient, the actuation time, and the blocked shape contribute to the memory shape variation over time. These two factors limit the range of motion of the bidirectional robogami joints driven by SMA actuators. So the final annealed shape should account for a larger deformation than the goal angles. Here, the folding actuator was annealed in cylinder shape with diameter close to 1.5 mm, Fig. 3.8a. For the unfolding actuator, the annealed shape was a half cylinder with the radius of curvature close to 3 mm, Fig. 3.8b. These annealed shapes produce large enough bending angles to enable repeated motion in the range of $40^o - 140^o$. This range of motion was determined based on the requirements in the crawling motion of a meso-scale robot, Appendix A.

Activating the actuator and blocking its motion, results in decreasing blocked force output in repeated cycles, due to the memory shape change. To be conservative with the estimation of the blocked torque of the actuators, we activated them in the maximum deformation and

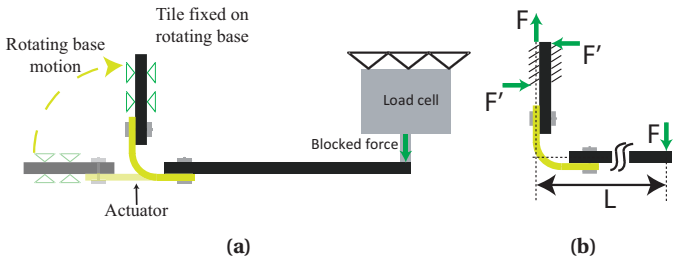

Figure 3.7: Schematic of the test setup for measuring blocked torque of SMA bending actuators in their whole range of motion. (a) The actuator is fixed to the rotating base on one side and is in contact with the load cell on the other side. The tile in contact with the load cell is longer (its length is 5 times the length of the active part of the actuator) in order to get a more uniform moment throughout the actuator. (b) Free body diagram depicting the force measured by the load cell and its moment arm. We report FL as the blocked torque of the actuator in different bending angles.

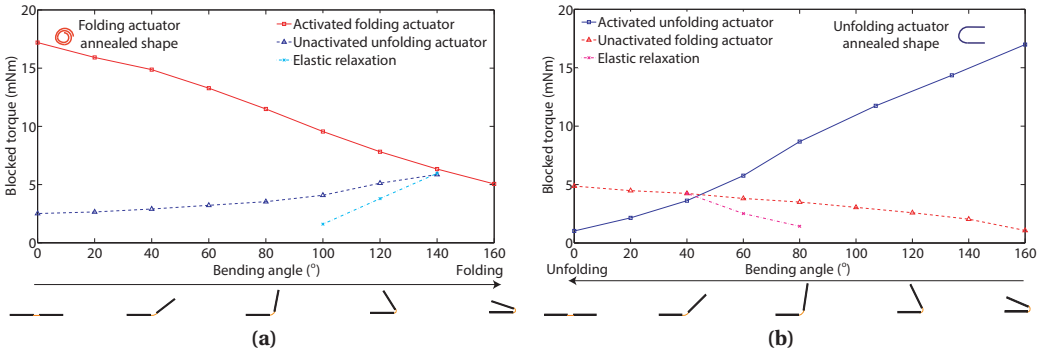

Figure 3.8: Results of the blocked torque tests which corresponds to the theoretical study presented in Fig. 3.6. (a) Torque generated by the actuators in motion toward 180^o (the folded state) with the folding actuator activated and passive unfolding actuator. (b) Torque generated by the actuators in motion toward 0^o (the unfolded state) with the unfolding actuator activated and passive folding actuator. The elastic relaxation in both plots corresponds to unloading of the passive actuator which happens when the current to the active actuator is cut off and it starts to cool down and its blocked torque decreases.

step by step relaxed the strain. This gives a conservative estimate because in the antagonistic arrangement under a large strain, the opposing force of the other actuator, and hence memory loss, is much smaller. Fig. 3.8 presents the results of the characterization test for folding and unfolding actuators. The blue lines present the torque in the unfolding actuator with the annealed shape of a half cylinder in the active region and the red lines represent the torque in the folding actuator with the annealed shape of a complete cylinder. This figure also presents the elastic relaxation of the inactivated actuator around its equilibrium point. The small slope of this elastic relaxation implies that when the driving actuator starts to cool down, there will be a rather large relaxation and change in the position. This makes the feedback control for robogami modules a necessity. To keep the SMA actuated robogami joints in the desired position, we need to activate the actuators and control the temperature constantly.

The conservative characterization of the blocked torque predicts around 100^o range of motion for the robogami joint with bidirectional SMA actuation, Fig. 3.8. This is enough for many applications. If a larger range of motion is required, one could use a thinner or longer actuators. According to (3.2), both of these decrease the strain level for a given bending angle. In the next section, we use the SMA actuators to control the position of a single joint using feedback from an embedded curvature sensor.

3.2.3 Feedback control of a SMA actuated Robogami joint

In this Section, we study the feedback controlled motion of a robogami joint. We used carbon ink sensors presented in the previous Section (CI3) for measuring the joint angle and an on-off controller to drive the joints to a desired position. First, we present the characterization results for the curvature sensor and later study the results of the position control. Fig. 3.9 presents

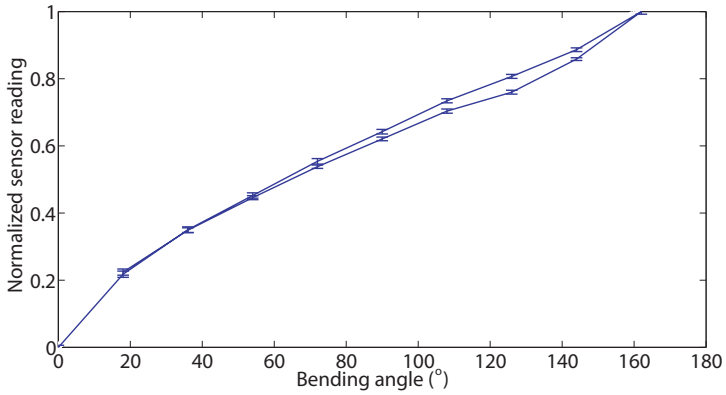

Figure 3.9: Mean value and standard deviation for normalized readings of a carbon sensor versus the bending angle in 50 cycles. The results show good repeatability and a small hysteresis loop.

the sensor reading at different bending angles. For this test, we mounted the module with the embedded sensor onto a motorized stage and tested the sensor with 18^o increments between folded and unfolded states. Sensor readings shows repeatable response and rather small standard deviation in 50 cycles. At each sampling point, the mean of 50 measurements (with 100 Hz sampling rate) is recorded as sensor reading. The average standard deviations for this sensor in this specific loading condition is 1.1^o (as presented in the previous Chapter, the loading condition significantly affects the sensor accuracy).

In the characterization tests, we deformed the sensors in pure bending. In the case of bidirectional actuation using SMA actuators, the axis is defined by the shape of the actuator and can vary based on the loading condition. Moreover we observed a small twist in the folding area that is caused by offset between the the application point of the forces from the two actuators. To study the feasibility of position control using the proposed arrangement of actuators and sensor we tested repeatability of reaching three goal angles: 60^o , 90^o , and 120^o in five cycles, Fig. 3.10. The average of the standard deviations for these three angles was 1.4^o which shows an acceptable repeatability for this specific actuation sequence.

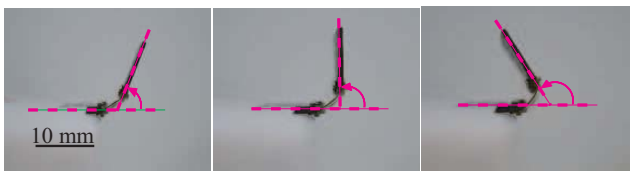

Figure 3.10: Feedback control of a SMA actuated Robogami joint for reaching three goal angles: 60^o (a), 90^o (b), and 120^o (c). The joint was actuated to reach these three goal angles one after the other for five cycles. The controller can position the tiles in the desired angles using the sensor feedback.

In this Section, we studied SMA actuated robogami joints. Given their high energy density and their compatibility with the layer by layer manufacturing, SMA bending actuator is a good option for driving multiple DoFs in robogamis. In Appendix A, we briefly present the motion of a meso-scale crawler robot that uses SMA actuators.

To produce a desired reconfiguration in a wearable device, a synchronized motion of multiple joints are required in contrast to position control of an individual joint. The thermal activation of SMA actuators and their relaxation around the equilibrium point complicate precise control required for such a task. In the next Chapter, we introduce an alternative compliant actuation method based on synchronized actuation of multiple robogami joints with adjustable stiffness using an embedded tendon. In the next Section, the adjustable stiffness layers that allow us to control the stiffness of robogami joints are introduced and characterized.

3.3 Shape memory polymer for stiffness control in soft robots

In this Section, we introduce a method for controlling the stiffness of robogami joints based on the variable stiffness of SMP around its glass transition temperature. In the following subsections different iteration that has lead to the final design of the ASLs are presented and the improvements made at each step are discussed. Like other thermoplastics SMPs show significant stiffness variability around their glass transition temperature. Moreover, The high recovery rate in these polymers helps preventing residual strain in repeated cycles of loading. Fig. 3.11 presents the elastic modulus variability of SMP that we used in this research (MM5520, SMP Technologies). According to the manufacturer, the modulus of elasticity changes from 2150 MPa in glassy to 2.1 MPa in the rubbery region.

3.3.1 SMP layer with embedded heater

In the first design, we study the feasibility of stiffness control of different segments of a SMP layer using an embedded heater. At this stage, the shape recovery solely relies on memory effect of SMP. Using external heaters, as done in [88, 108], does not allow independent activation of the ASLs and embedding heaters is necessary to activate different SMP segments independently. Here we used the stretchable mesh structure previously introduced as stretchable circuit, Chapter 2, as heaters. The stretchable heater layer is made form Inconel, Ni-Cr alloy, polyimide laminate (20 μm Inconel and 50 μm Polyimide) through laser ablation and chemical etching. Fig. 3.12 presents an overview of the fabrication process of the heater and the process for embedding it inside SMP. The gaps on the sides of the heater, Fig. 3.12g, are added to prevent delamination and to ensure that the embedded heater would move with the SMP layer. After preparing the heater, wires are connected to its terminals and it is pressed between 2 layers of SMP (each 300 ± 50 μm thick) in a heat press at 160 ^oC, Fig. 3.12e. The outer frame of the heater is designed to prevent deformation during this process. We used two

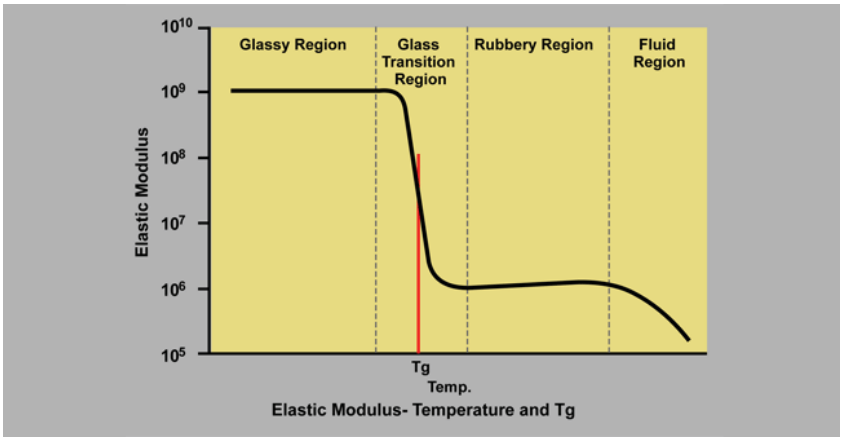

Figure 3.11: Variability of elasticity modulus of SMP MM5520, from the manufacturer's website [107].

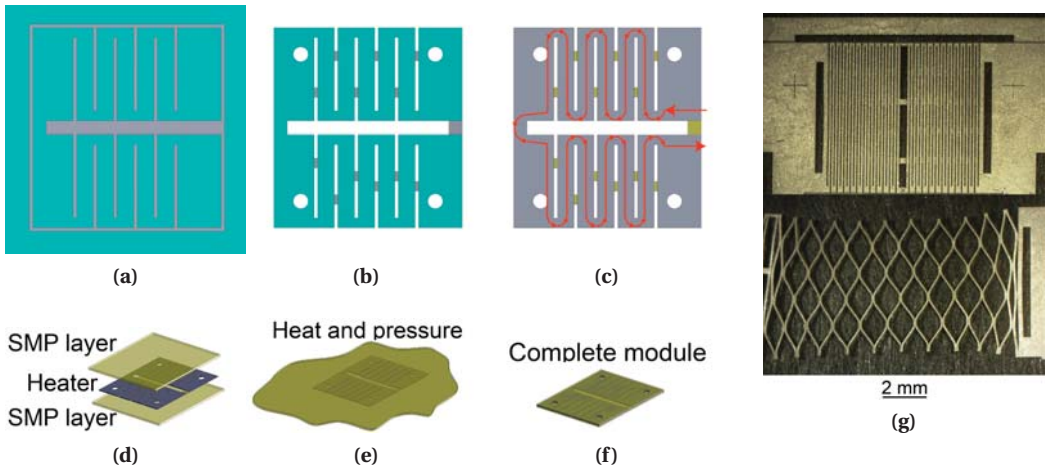

Figure 3.12: Fabrication process of the SMP layer with embedded heater. For clarity, the dimensions in the schematics are not to scale. (a) A serpentine path, which makes the heating element, is cut through the etchant resist layer. (b) The stretchable pattern and the outline of the heater is cut through all layers. (c) The Inconel in the exposed areas is etched and the etchant resist is cleaned. The red line shows the conductive path of the heater. (d) The heater is sandwiched between 2 SMP layers. (e) High temperature and pressure form the SMP layers around the heater. (f) The outline of the module is cut and its ready for assembly. (g) The fabricated heater in its initial and stretched states.

spacers, each 500 μm thick, to control the overall thickness of the SMP layer. After integration, the outline and the mounting holes are cut, Fig. 3.12f.

Stiffness adjustment of a SMP layer with embedded heater

Mechanical properties of SMP including its recoverable range of deformation, the stress-strain characteristics and its dependence on the temperature have already been studied in detail [109]. The test conditions in these studies are usually very well controlled and external heating elements ensure a uniform temperature distribution throughout the sample. In an actual application, however, there will be a considerable temperature gradient. So, the characterization tests are necessary for understanding the behavior of a SMP layer that is activated using an embedded heater. We tested SMP samples in a C42 universal testing system from MTS Systems, Fig. 3.13, and used a thermal camera, FLIR A35, to monitor the temperature of the sample and to regulate the heating power accordingly. The heating power was set to achieve the mean temperature of 80 °C on the SMP layer to ensure that it has surpassed the glass transition temperature. To characterize the stiffness in different initial deformations, we deformed the SMP layer while it was in rubbery state (high temperature) and performed the tensile tests around different initial displacements in glassy and rubbery states. After each loading cycle, the memory effect of the SMP layer drives it back toward its initial shape. However, in the range of strains tested here, up to 60%, the sample does not completely recover its initial shape. The residual strain at zero displacement causes the SMP layer to buckle, Fig.

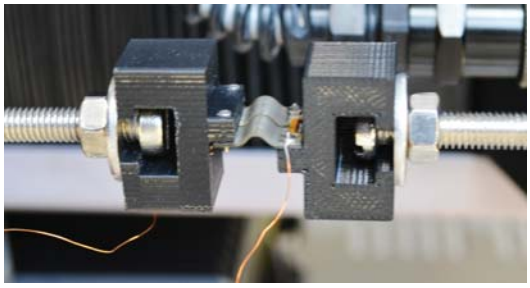

Figure 3.13: SMP layer after loading cycles at zero displacement. The buckled shape caused by the residual strain changes the loading condition in the hard state to bending which results in much smaller stiffness compared to the stiffness of a straight layer.

3.13 shows the sample after the characterization tests at zero displacement. This residual strain affects the response of SMP significantly. Most of the unrecoverable deformation happens in the first cycle of loading. In Fig. 3.14, the test results for a sample after 10 cycles of loading, when the layer has reached a rather stable state, is presented. We characterized the stiffness modules in two states: at room temperature; and at 80 ^oC. We characterized the elastic behavior in tension and compression. The stiffness of the layer is a functions of the the initial shape and temperature.

In the experiments, the SMP layer is in the buckled state for most of the measurement points, shaded part of the graph represents the section with buckled SMP layer. The buckled shape in positive displacements, till 1 mm , is due to the residual strain in the SMP layer. In points with

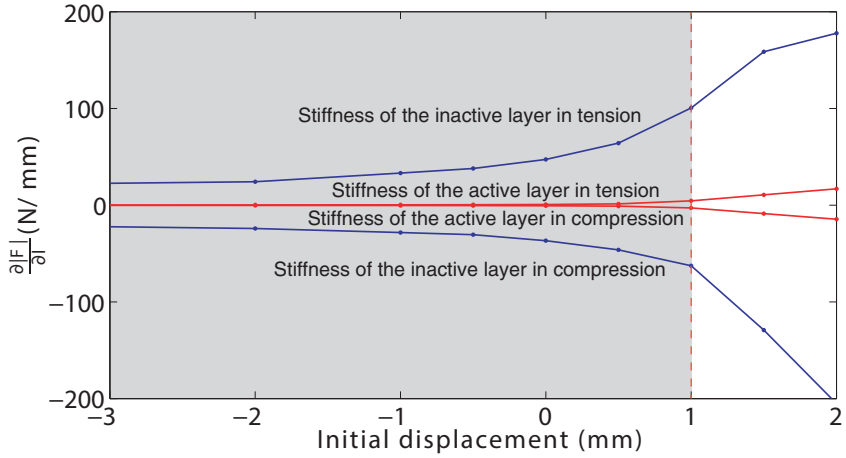

Figure 3.14: Linear stiffness of SMP layer in different initial deformations. This plot presents the stiffness of a SMP layer with embedded heater in tension and compression in inactive and active states. The stiffness changes significantly when the polymer enters the rubbery state. Using this, we can control the compliance of joints and segments in soft Robots. The stiffness in compression is presented with negative sign. The shaded area represents the measurement points with buckled SMP layer that result in a lower stiffness compared to the rest of the measurement points.

initial buckled shape, the displacement causes bending in the SMP layer which requires much less energy compared to stretching or compressing the layer in its plane. In this region, the stiffness of the layer both in compression and tension is lower compared to the points where SMP layer is straight. The significant variation in the stiffness between cold and hot states confirms the feasibility of using SMP as the variable stiffness layer for compliance control in soft robots. The variation of the stiffness depending on the initial position, however, complicates the compliance estimation and control. This can be partially resolved by designing structures that put SMP solely in tensile loading. But even in such loading conditions, the residual strain still causes problems. In the next Sections, we present improved design of ASLs that provide a higher recovery rate and a more repeatable response.

3.3.2 Improving shape recovery by embedding SMP in silicone rubber

To improve the shape recovery, we embedded the SMP layer in an elastic polymer. In this Section, we study the compatibility of the SMP with the polymer and characterize the stiffness change of the composite. At this stage we decided to test this solution in an application at a larger scale which allows us to observe and resolve the design flaws more easily. To this end, we designed a soft pneumatic actuator, SPA, that uses the SMP for modulating the stiffness of the chamber walls. The study of the motion of the SPA is presented in Appendix B. Here, we present the design and fabrication process of the test sample used in the characterization experiments and report the stiffness variability of silicone embedded SMP.

The design of the heater and the process for embedding it in the SMP layer is similar to the process presented in the previous Section. In the heater presented in Fig. 3.15, a mesh pattern that is cut through all layers provides the stretchability. As presented in Fig. 3.15, the heating area is slightly longer than the stretchable area. The unstretchable heating sections result in a more uniform temperature distribution along the stretchable section of heater and hence the active length of the SMP layer. We use three thermistors (SMD 0402 from Vishay) in this sample for measuring the temperature and controlling the heating power accordingly. After

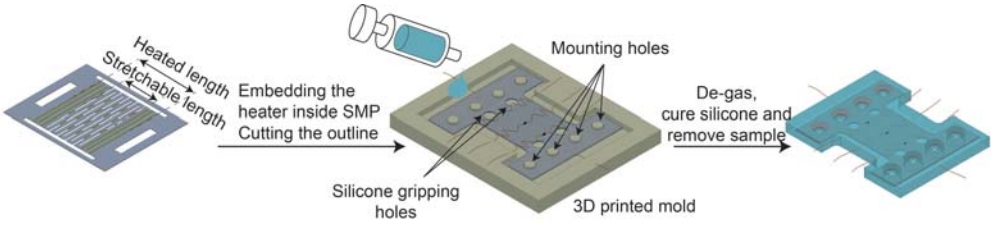

Figure 3.15: Fabrication process of the ASL sample. The process starts with the fabrication of the heater. It is composed of a serpentine path that makes the heater and a stretchable mesh pattern. After the heater is fabricated using laser ablation and wet etching, it is embedded in SMP. In this design we used three thermistors to control the temperature of the SMP layer. The SMP layer is embedded in silicone rubber using the mold in the final step of fabrication. For clarity, the dimensions in the schematics are not to scale.

attaching the thermistors, the SMP layer is placed in a mold and is embedded in a silicone rubber layer.

There are two openings on each side of the SMP layer in Fig. 3.15. This is in addition to the holes for clamping the sample to the setup. These openings are designed to make silicone connections inside the SMP layer in the integration process. The adhesion between SMP and silicone is very weak and the silicone columns that are made during the integration process exchange forces between the SMP layer and the enveloping rubber layer. The cross-section of the columns should be large enough to prevent shearing failure:

$$\frac{F}{2\frac{\pi d^2}{4}} < S_{sp}/n_s \tag{3.3}$$

In (3.3), F is the force needed for deforming the SMP sample, d is the diameter of the silicone column in SMP, and S_{sp} is the ultimate shear strength of the silicone rubber which according to the distortion energy theory equals to $\frac{S_p}{\sqrt{3}}$, where S_p is the ultimate strength of the silicone rubber. Finally, n_s is the safety factor. The column should also resist against bearing:

$$\frac{F}{2t_{SMP}d} < S_p/n_s \tag{3.4}$$

In (3.4), t_{SMP} is the thickness of the SMP layer, 500 μm. Based on the initial test on a SMP sample, the required force to stretch the active sample (at high temperature) to twice its initial length is around 8 N. A strain of 100 % is more than the expected work range in this study. Based on (3.3) and (3.4), the openings in the SMP layer were designed to be 4 mm in diameter which gives us a safety factor of 1.6.

Stiffness adjustment of a silicone embedded SMP layer

To characterize the stress-strain relation of the ASL in different temperatures, we used a setup that automatically performs a series of characterization tests in different temperatures and elongation ranges. Fig. 3.16 presents the test setup with a sample mounted. The temperature is monitored and a proper input voltage is applied, to an embedded heater in the material for keeping the desired temperature during the tests. The deformation is applied using a spindle drive from Maxon motors with 10 μm accuracy. The force is measured with a Nano 17 force sensor with 3 mN accuracy.

Fig. 3.17 illustrates the characterization test results for a silicone sample, and for an ASL sample in active (in high temperature) and inactive (in low temperature) states. The temperature used

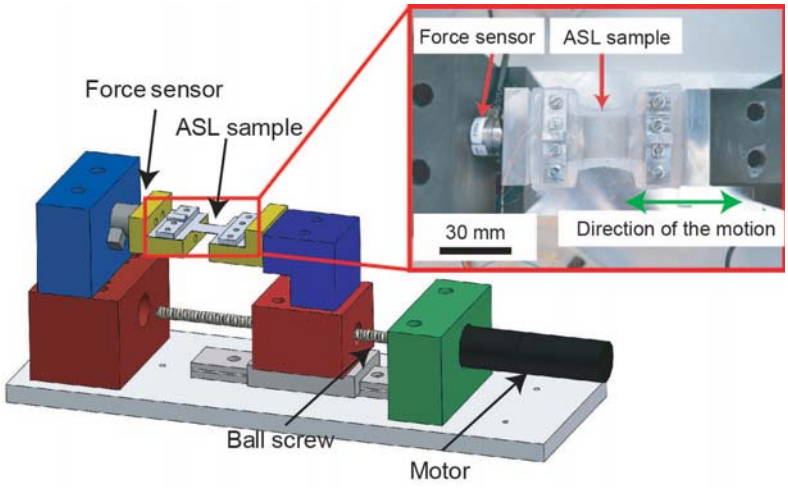

Figure 3.16: Stress-strain test setup. The temperature of ASL strip is controlled through feedback from the thermistors using an embedded heater. The linear stage applies a series of programmed deformations at different temperatures while the load cell records the applied forces.

in active tests was 110 ^oC. We set the temperature so high to ensure that the whole SMP layer surpasses the glass transition temperature. In the characterization of the ASL, we first cycled the inactive sample 50 times, then cycled the activated sample 500 times and finally loaded it 10 times in active and inactive states (the test results presented in the figure are for the final ten cycles).

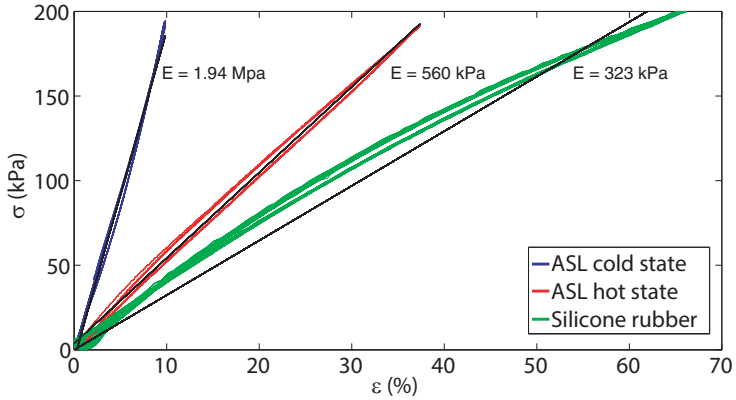

Figure 3.17: Result of the characterization tests on a silicone rubber sample and an ASL in active and inactive states. The ASL is composed of SMP and heaters (500 μm thick) that is embedded in 4 mm thick layer of Dragon skin 30, from Smooth-on. The results suggest 4 times decrease in stiffness after the glass transition of SMP. The stress strain behavior of silicone and ASL are approximated by a linear function.

The test results confirm repeatable deformation of ASL in more than 500 cycles and almost 4 times drop in its stiffness in active state. The ratio of stiffness in active and inactive states can be controlled by using silicone rubbers with different modulus of elasticity and also by adjusting the relative thickness of the SMP and silicone layers. Here, we have chosen a very hard polymer and designed the ASL to have a rather thick silicone layer to maximize the strain recovery of the SMP layer. An important feature of the characterization test results is its linearity (especially for the complete ASL sample).

The proposed design in this Section resolved the problem of residual strain to a good extent. The stiffness variability however is only 4 times, which is lower than the expected variation. Also in the first 500 cycles there is still a significant residual stain, around 20%. Relative motion between the SMP layer and the silicone rubber and difficulties in anchoring ASL onto the test setup (due to the compliance of the silicone rubber) are among the reasons for under performance of the current design. In the next Section, the design of ASL is improved by adding a glass-fiber frame that provides better anchoring points. The thickness of the silicone rubber is also reduced to half to increase the stiffness variability of the sample.

3.3.3 Glass-fiber frame for ASL

The stiffness variation reported in the previous Section, was lower than the expected stiffness change. The stiffness of the ASL in the stiff mode was under estimated due to the deformation

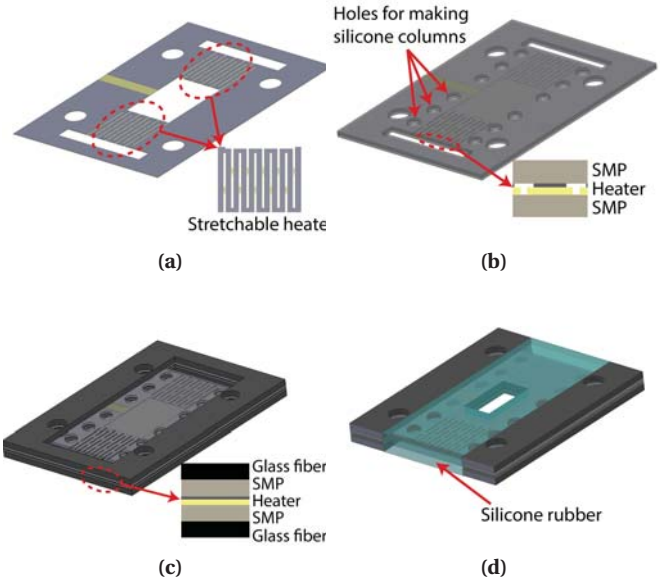

Figure 3.18: Overview of the fabrication process of the ASL with glass-fiber frame. (a) The schematic of the stretchable heater layer. (b) The heater is embedded in SMP. (c) The SMP layer in the glassfiber frame. (d) The final module with silicone rubber enveloping the SMP layer.

of the silicone layer in the anchoring area and the relative motion of the SMP and silicone rubber. To resolve this issues, a glass-fiber frame was added to the design of the ASL. The overall design and the fabrication process of the ASL with glass-fiber frame is presented in Fig. 3.18. The first two steps for embedding the heater in the SMP layer are the same as before, Fig. 3.18a and 3.18b. In the third step, the SMP layer is embedded in a glass-fiber frame, Fig. 3.18c. The glass-fiber layers act both as the frame for attaching the ASLs to the robogami joints and also as a mold for casting the silicone layer. Fig. 3.18d presents the final form of the ASL which is easily glued onto the robogami using the anchoring points at the two ends. We also decreased the overall thickness of the ASL layer from 4 mm to 2 mm with the same thickness for SMP, 500 μm. Decreasing the thickness of the silicone is also expected to increase the stiffness variability of the sample.

Stiffness adjustment of the final ASL design

In this design of ASL, we removed the thermistors and used the heater's electrical resistance to estimate and control the temperature of SMP. This facilitates the manufacturing process by reducing the components. Moreover, heater's electrical resistance correlates with the average temperature of the SMP layer which provides a closer estimation of the layer's stiffness. The stiffness of the ASL was characterized at different temperatures (30 ^oC to 110 ^oC with 10 ^oC increments). At each temperature, the sample was loaded three times up to 2.5 mm, corresponding to 60% strain, or 15 N, the limit for the force sensor, whichever occurs first. Fig. 3.19 presents elastic behavior of the ASL layer at different temperatures. The overshoot in the force at lower temperatures and in strain at higher temperatures are due to the acceleration limits of the test setup which results in stretching the sample beyond the set points. At low temperatures (30 $^oC - 50$ ^oC) the ASL is stiff and its elastic behavior is rather linear. At higher

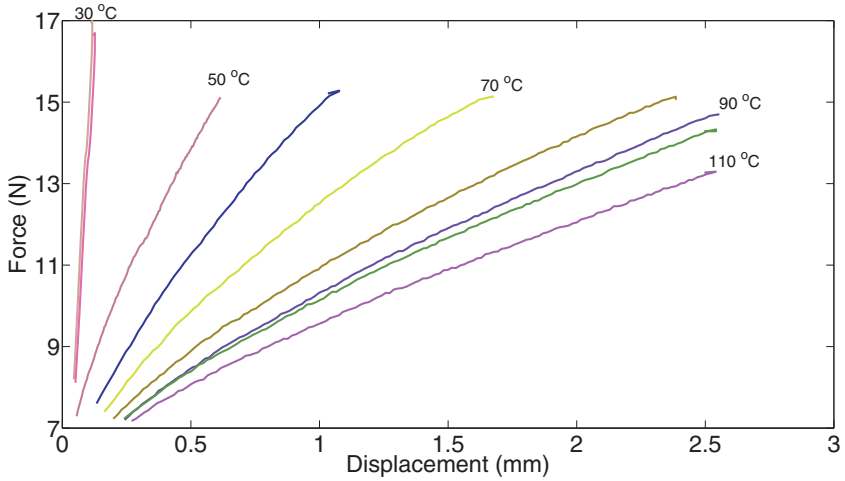

Figure 3.19: Elastic behavior of the ASL at different temperatures. We estimated this behavior with a linear function. The sample dimensions ($w \times l \times t_{total}, t_{SMP}$) are: $7 \times 4 \times 1.6, 0.5$ mm.

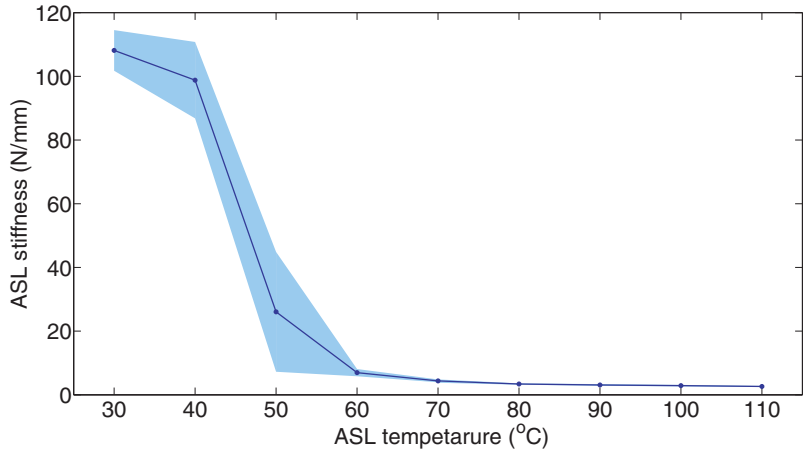

Figure 3.20: Stiffness of the ASL layer as a function of its temperature. The shaded area represents the standard deviation of the data points.

temperatures ($80\ ^oC - 110\ ^oC$) ASL becomes more compliant. The elastic behavior at these temperatures can also be estimated by a linear function. Due to the temperature gradient, varying thermal boundary condition with strain, and a high temperature sensitivity of the elasticity modulus, the behavior of the sample is quite nonlinear in the mid temperature range ($50\ ^oC - 80\ ^oC$). Moreover, at these temperatures the behavior of the ASL is characterized by significant visco-elastic effect. So large deformations of ASL in these temperatures are not recommended.

We approximated the elastic behavior of the ASL with a linear function at each temperature and reported the slope as the stiffness of the sample. This stiffness will be used in the next Chapter for studying the energy distribution in under-actuated robogamis with adjustable stiffness joints. Fig. 3.20 presents the average stiffness and the standard deviation at each measurement point, 12 tests per point (two sets of tests on two samples with three measurements per temperature setting in each set).

The SMP that we used in the ASLs has the glass transition temperature at $55\ ^oC$. In calibrating the temperature sensors using the thermal camera, we used the temperature of silicone surface which is lower than the temperature of the SMP layer. This is the reason for the abrupt stiffness change between $40\ ^oC$ and $50\ ^oC$ in Fig. 3.20 instead of the expected sharp drop between $50\ ^oC$ and $60\ ^oC$.

Due to the variation in the sample thickness, there is a discrepancy between the silicone surface temperature, used in calibration, and the effective temperature of the SMP layer for each sample. Moreover, we observed that the heater's resistance of the same sample can have a small drift over time which leads to errors in the temperature set point even for the same sample in different cycles of loading. The inaccuracies in controlling the temperature along with the high stiffness sensitivity to temperature variations around the glass transition point

lead to a large standard deviation around the transition temperature. This problem can be alleviated in future by using polymers with more gradual modulus of elasticity change with temperature.

According to Fig. 3.20, the stiffness of the ASL changes more than 40 times in the entire temperature range. The stiffness drops more than 15 times between 30 ^oC and 60 ^oC. Although the rate of the stiffness change with temperature is considerably lower at temperatures higher than 60 ^oC, this region is still useful for controlling joint stiffness and stable configuration of robogamis.

3.3.4 Temperature feedback for controlling the stiffness of ASL

At different stages of research, we used different methods for setting the temperature of ASL. In the most basic case, the heating power was set based on the measurements of a thermal camera. Later we used measurements of a thermistor in contact with SMP layer. Eventually, we used the electrical resistance of the heater to estimate the temperature of the ASL. This method has three important advantages: there is no need for added components, the estimated temperature will be an approximation of the average temperature (compared to the point measurement using thermistors), and the response time is faster which results in more accurate estimation in transient conditions. In this Section, we present the characterization result of the heater's electrical resistance at different temperatures.

We studied the relation between the electrical resistance of the heater and the temperature of SMP surface at different set-points using a thermal camera. The test results, presented in Fig.

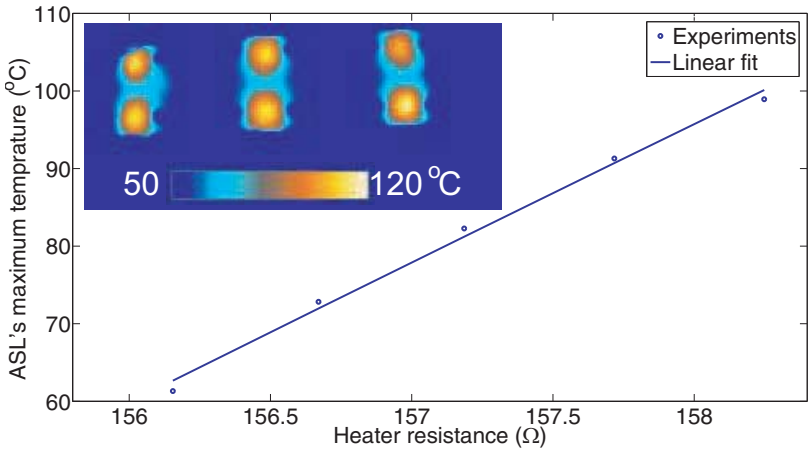

Figure 3.21: ASL temperature vs. heater's electrical resistance. The resistance has a linear correlation with the temperature. In calibrating the reading from the heater, we used the maximum temperature at each ASL. The photo from the thermal camera illustrates the temperature gradient on the ASL surface. The maximum temperature of all three samples in this photo is around 110 ^oC and the average temperature of each ASL is around 95 ^oC.

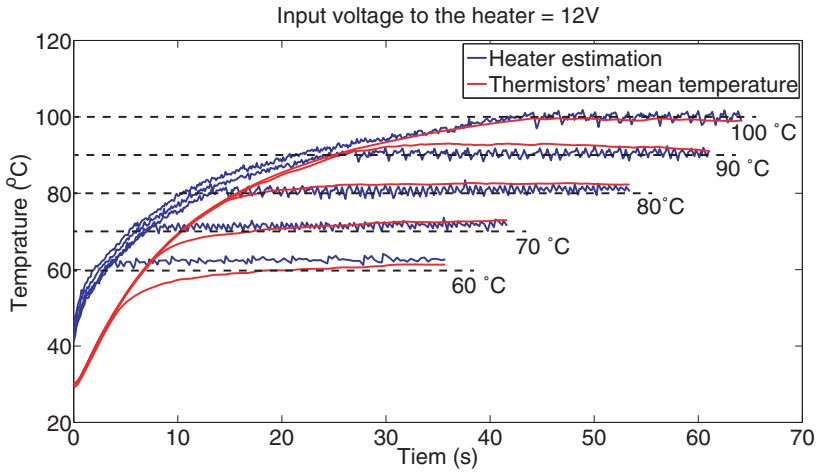

Figure 3.22: Temperature estimation from the heater's electrical resistance and the thermistors as the temperature of SMP reaches different set-points.

3.21, show a linear relation between the resistance of the heater and the temperature of the ASL, with R^2 of 0.99. We should point out that for each heater, we have a slightly different sensitivity due to small fabrication differences. We calibrate the temperature sensitivity of each heater using the thermal camera measurement by setting the desired temperature to the maximum set point (110 ^oC) and varying the sensitivity factor till reaching similar estimation for the temperature from the thermal camera and the heater. There is a considerable temperature gradient in the ASL (as presented in Fig. 3.22) and we used the maximum temperature reading from the thermal camera in characterization and calibration of the heaters.

Fig. 3.22 presents the transient thermal response of ASL as it reaches different temperature set-points. Temperature estimation from the heater's electrical resistance is compared with the average measurement from two thermistors in contact with the surface of SMP and embedded in silicone rubber. The heater's electrical resistance in this experiment is calibrated using the thermistor's measurement and is used as the feedback in an on-off controller. The experiment confirms the feasibility of using heater's electrical resistance for controlling the temperature of the SMP layer. Note that the different initial temperature is caused by the sudden increase in the temperature of the heater at the every beginning of the experiment as electrical current starts flowing. Another important aspect of the heater response is its faster response time compared to the thermistors, more visible at lower temperature settings, which highlights one of the advantages of using this method for closing the temperature loop.

3.4 Conclusion

In this Chapter, we studied functional materials for actuation of robogami joints and controlling their compliance. The high work density of the sheet SMA actuators along with the compatibility with the layer-by-layer manufacturing of robogamis make these actuators an

attractive option for independently driving the robogami joints to perform a complex reconfiguration. Given the level of conformity required in wearable devices, this soft actuation method can be utilized in driving multiple DoFs of robogamis to conform to the shape of the body and follow its motion or apply forces and displacements. In a wearable device after the initial reconfiguration, many of DoFs would be required to keep their position. Implementing a method of stiffness control in the joints simplifies this task and after reaching the desired configuration, the joint can be locked in place by increasing its stiffness. This facilitates the control problem and can potentially increase the load capacity of the robot. To this end we proposed a compliance control method based on stiffness variability of SMP around its glass transition. By embedding ASLs with SMP core in the robogami structure, we can keep the position of the joints without energy consumption. This method of stiffness control also allows us to control the overall compliance of a wearable device and the magnitude of the contact forces it applies.

The slow response of SMA actuators complicates the synchronized actuation of multiple joints for precise motions. In the next Chapter another actuation method is proposed which can be used in conjunction with SMA actuators where synchronized motion of multiple joints is required. In this method actuation from a single source drives multiple tendon-driven robogami joints.The energy distribution between the joints is determined by the stiffness assigned to each joint using the embedded ASLs. Integrating materials with adjustable stiffness allow us to design soft robots with adjustable compliance and mode of operation for different applications including wearable devices.

4 Robogamis: trajectory planning and compliance control

Robogami's unique manufacturing method allows us to implement multiple DoFs in a confined space. In many applications, synchronized motion of these DoFs is required for performing a task. By controlling the joint stiffness in tendon-driven robogamis, we can activate different actuation patterns and perform a desired reconfiguration using a single source of actuation. To control the joint stiffness, we embed ASLs as one of the functional layers in the robogami joints. The inherent softness of tendon-driven robogamis, originating from the redundant and under-actuated DoFs, provides a soft method of actuation. The embedded ASLs enable us to control the trajectory and the compliance of this soft actuation. In this Chapter, different aspects of the under-actuated tendon driven robots with adjustable stiffness joints are elaborated.

We used under-actuated manipulators and grippers as a platform to study the reconfiguration of tendon-driven robogamis with adjustable stiffness layers. These applications have similar geometrical features and are tested under similar loading conditions and range of motions expected in a wearable device. The trajectory planning and control problem in these systems, however, are far simpler than the expected ones for a wearable device which facilitates the detection of design flaws and the development of models and control schemes. The application of robogamis in soft robotic hands and grippers can also be of interest on its own. Robotic gripper is one of the first applications of soft robotics that entered the commercial market

The material of this Chapter is from the following self-authored publications:
[31] **A. Firouzeh** and J. Paik, "An under-actuated origami gripper with adjustable stiffness joints for multiple grasp modes", Smart Materials and Structures 2017.
[72] **A. Firouzeh**, et al., "Soft pneumatic actuator with adjustable stiffness layers formulti-dof actuation", IROS 2015.
[73] **A. Firouzeh**, et al., "An under actuated robotic arm with adjustable stiffness shape memory polymer joints", ICRA 2015.
[74] **A. Firouzeh** and J. Paik, "Stiffness control in under-actuated robotic origamis with shape memory polymer", TRO 2017.
[110] **A. Firouzeh** and J. Paik, "Grasp mode and compliance control of an under-actuated origami gripper using adjustable stiffness joints", T-Mech 2017.

as a competitive product and we believe that the proposed robogami design with adjustable grasp mode and compliance contributes to solving some of the current challenges in this field. In the next Section, a brief overview of soft robotic hand and grippers is presented and the advantages of the soft actuation using tendon-driven robogamis with compliance control are highlighted. Next, different aspects of the design, the model, and the control are presented through few examples of tendon-driven robogamis.

4.1 Introduction

The self-adaptability of soft actuators enables them to conform to the shape of the objects and the environment in contact without the need for complex controller or actuation pattern. Robotic hands and grippers are among the applications that can greatly benefit from this

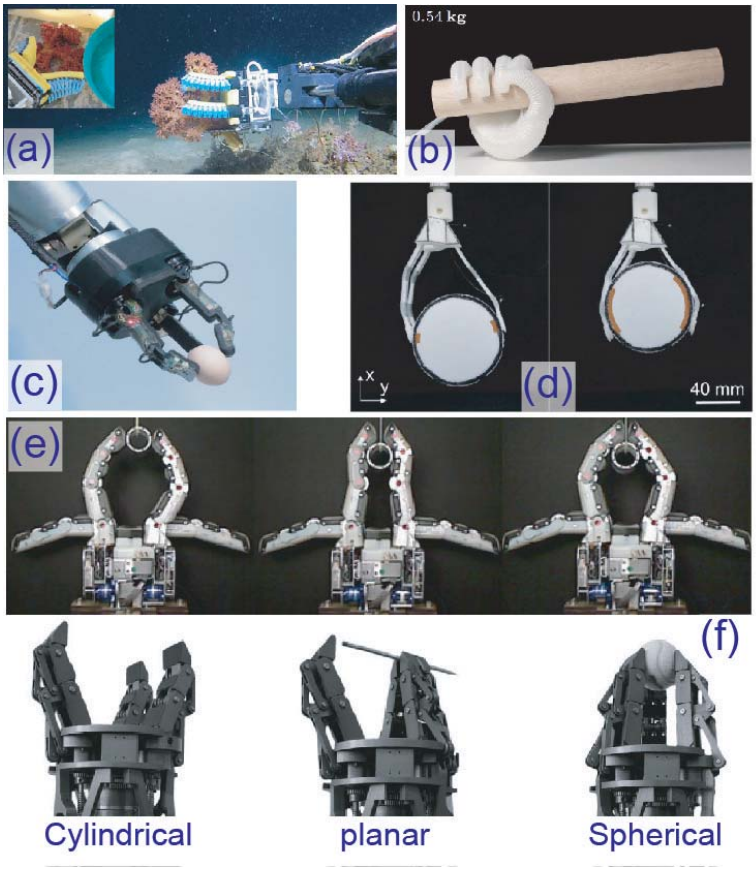

Figure 4.1: Examples of robotic grippers using different soft actuation principles. (a,b) present two robotic grippers using pneumatic soft actuators, [111] and [112]. (c) an under-actuated soft gripper with tendon-driven fingers [113]. (d) Tendon driven fingers actuated by SMA wired [95]. (e) Using lockable joints for controlling the grasp mode in an under-actuated gripper [114]. (f) Different grasp modes of a gripper with adjustable initial configuration [115].

feature of soft actuation methods. Many examples of robotic hands and grippers using different soft actuation principles have been studied in the literature, Fig. 4.1 summarizes some of these. The first two examples illustrate the application of SPAs in robotic grippers. The soft body of the actuator provides infinite DoFs that allows the distribution of the input actuation, pressurized air, according to the shape of the object. Tendon-driven under-actuated fingers are also used as a method of soft actuation in robotic hands, Fig. 4.1 (c)-(e) present few examples of robotic grippers using this method of actuation. The redundant under-actuated DoFs in these grippers provide inherent mechanical softness. Compared to the pneumatic actuators, the finite DoFs in tendon driven grippers makes it easier to model and control the behavior of these soft grippers.

As presented in Fig. 4.2, there is a compromise between the number of DoFs and compliance on one side and the force magnitude and precision of grasp on the other. This compromise between the compliance and force has started to gain attention as one of the limiting factors for applications of soft methods of actuation for producing large forces [116]. A soft actuation method with adjustable stiffness allows us to assign a proper compliance based on the task. This is specifically important in application of soft robots dealing with different tasks and load requirements, such as robotic hand and grippers. Engaging different set of joints in under-actuated grippers is one way of changing the grasp and interaction mode of the gripper. Fig. 4.1 (e) present an example of a gripper that uses electrostatic locking for achieving the mode transition. Other methods of mode transition through mechanism design [117, 118], variable transmission ratio [119, 120], lockable joints [121, 122], and adjustable joint compliance [84] were suggested in the literature. In hands with more than two fingers, the initial configuration of the fingers can also change the grasp mode and the interaction forces of the gripper, Fig. 4.1.

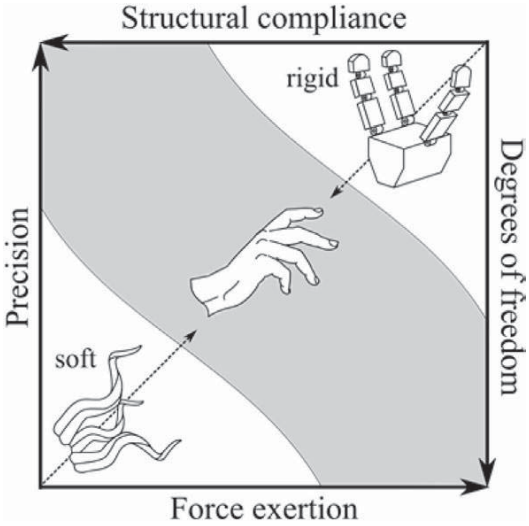

Figure 4.2: Compromise between DoF and compliance on one side and the force magnitude and precision of the robotic hands. The figure is adopted from [123].

In this Chapter, we target a versatile light-weight robogami gripper with compliance control. The ASL embedded in tendon-driven robogami joints of the gripper allows us to control the stiffness of each joint and hence the actuation pattern and the overall compliance of the gripper. Compared to the other methods, the proposed design has the following advantages

- Continuous control over the joint stiffness resulting in precise control over the grasp mode and compliance of the gripper.
- Adjustable initial configuration of the gripper without requiring any additional actuators.
- Scalable and adaptable design relying on material properties for stiffness control.
- Low cost and easy fabrication of complex sequence of joints.

We present the under-actuated robogami fingers and their application in robotic grippers. The resulting technologies and design methodology will contribute specifically to the field of soft grasp and manipulation but is also transferable to other application fields of soft robotics such as human-robot interaction. We start by studying the motion and compliance of a single finger and later in this Chapter will study grippers with two and three fingers. In the gripper with two fingers, the main goal is to demonstrate the compliance of the fingers. In the gripper with three fingers, the main objective is to utilize DoFs in different directions to achieve different initial configurations and grasp modes.

4.2 Robotic manipulator with lockable joints

As the first step toward an under-actuated robogami with adjustable stiffness joints, we designed a manipulator with redundant DoFs and lockable 3D printed joints, (Fig. 4.3), to investigate the feasibility of mode transition using stiffness variability of SMP. The design was made with interchangeable joints to allow more freedom in the initial stages of research. The manipulator has four DoFs that are normally locked in place by two thin, 500 μm, SMP layers. These layers are placed at a distance from the axis of rotation, 2 mm, to increase the moment of inertia and hence the load bearing capacity of the joint. The joints are activated using the stretchable heaters embedded inside the SMP layers. Two stepper motors pull and release the tendons for actuating the activated joints.

To activate a single DoF, the temperature of the SMP layers in that joint are increased using the embedded heaters. In the experiments on the current prototype, power transmission to a single joint was studied. Reaching different points in the workspace by activating the joints in sequence is demonstrated using this prototype. An algorithm was developed to find the configuration of the finger with minimum active joints for reaching different points [1].

[1]The algorithm design and implementation was carried out in collaboration with LASA/EPFL and is not elaborated in this thesis, the details are published in [73]

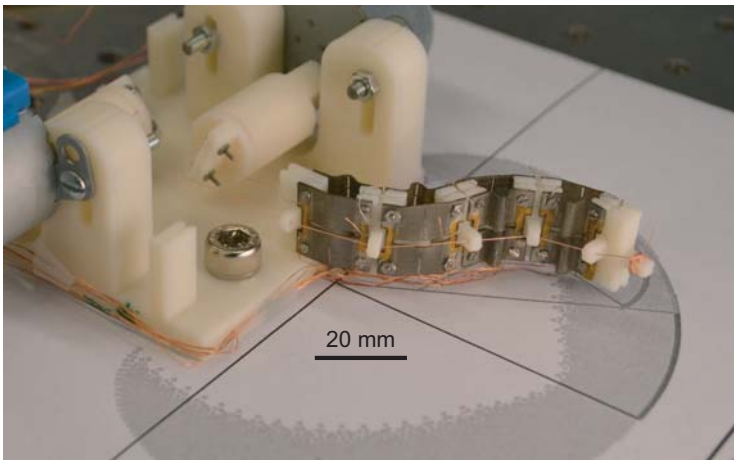

Figure 4.3: Under-actuated manipulator with SMP joints. The tendons that run along the manipulator actuate the joints according to their stiffness.

4.2.1 Joint design and actuation mechanism

In this Section, we present the joint design and estimate its stiffness at different temperatures. Fig. 4.4 presents the schematic of the manipulator and the actuation of its second joint. To actuate a joint, the tendon on its compression side is pulled by the motor and the otehr tendon is released. The SMP layer in compression buckles under load and the layer in tension stretches. The deformation of the SMP layers in each joint determines the joint stiffness. The zoomed in view in Fig. 4.4 presents a more detailed schematic of the joint and deformations of the SMP layers. The moment in each joint is calculated as:

$$M(\theta_0, \delta\theta, T) = F_t(\theta_0, \delta\theta, T)\frac{t_s}{2} + F_c(\theta_0, \delta\theta, T)\frac{t_s}{2} \tag{4.1}$$

In (4.1), $M(\theta_0, \delta\theta, T)$ is the moment required for changing the joint angle, $\delta\theta$, around its initial state, θ_0. $F_t(\theta_0, \delta\theta, T)$ and $F_c(\theta_0, \delta\theta, T)$ are the forces in SMP layers in tension and compression, respectively. These variables are dependent on the initial position of the joint, θ_0, and the temperature of the SMP layers, T. In this study, we considered joint properties at room temperature and 80 ^oC which are bellow and above the transition temperature, respectively. t_s is the distance between the joint axis and the mid section of SMP layer, Fig. 4.4a. Neglecting the bending motion, we assumed the force in the SMP layers to be a function of their length change. To evaluate these forces, we use (4.2) and (4.3) to calculate the length of the SMP layers as functions of the joint angle.

$$L_{pt} = L_{p0} + \frac{(t_s)}{2}\theta \tag{4.2}$$

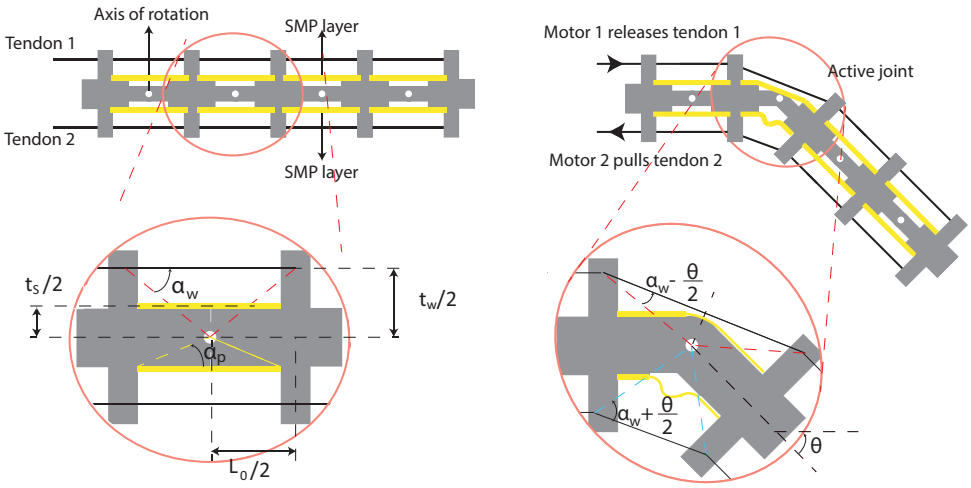

(a) **(b)**

Figure 4.4: Actuation of a joint in an under actuated robotic manipulator. a) Tendons are driven by two stepper motors and can actuate each of the 4 folding areas based on their stiffness. b) By activating the second fold while keeping the rest of the folding areas stiff, we are able to direct the actuation to the desired joint. The zoomed in view presents the details of the joint design. Each joint consists of a revolute joints and 2 SMP layers. In the folded state, the layer in compression collapses (buckles) and the layer in tension stretches.

Under compression, the SMP layer buckles and the displacement would cause the buckled arms of the SMP layer to bend. Nonetheless, the force in this layer is a function of the displacement of the two ends that are anchored on the tiles. This displacement is calculated as:

$$L_{pc} = L_{p0}\frac{\cos(\alpha_p + \theta/2)}{\cos(\alpha_p)} \tag{4.3}$$

In (4.2) and (4.3), L_{pt} and L_{pc} are the length of the polymer layers in tension and compression, respectively. L_{pt} is different from anchoring point distance since the deformation of the layer is confined by the joint shape as presented in Fig. 4.4b. The joint stiffness is calculated by differentiating (4.1) with respect to the joint angle:

$$\begin{aligned} K_{bend} &= \frac{\partial M}{\partial \theta} \\ &= \frac{\partial F_t}{\partial L_{pt}}\frac{\partial L_{pt}}{\partial \theta}\frac{t_s}{2} + \frac{\partial F_c}{\partial L_{pc}}\frac{\partial L_{pc}}{\partial \theta}\frac{t_s}{2} \end{aligned} \tag{4.4}$$

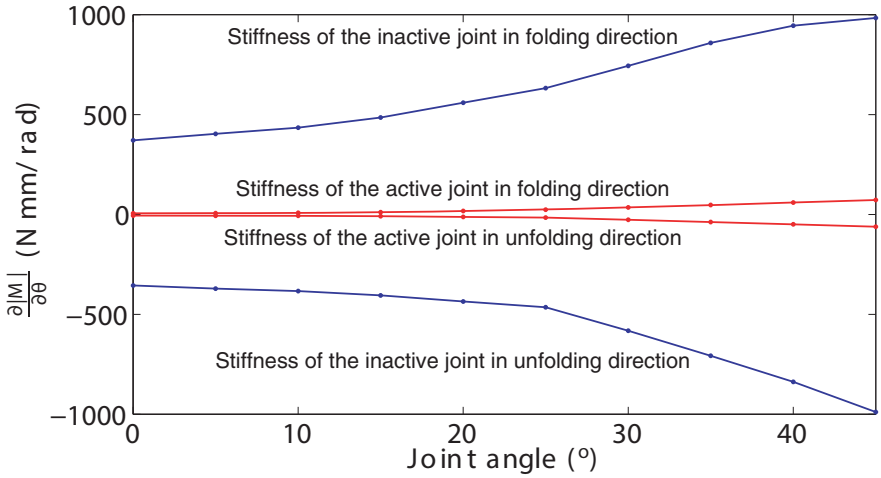

Figure 4.5: Joint stiffness in active and inactive states as a function of joint angle. The significant stiffness change between active and inactive states allows us to actuate desired joints while locking the rest of DoFs.

Using (4.2) - (4.4) and the elastic behavior of the SMP (characterized in the Chapter 3), we can estimate the stiffness of the joints at different bending angles and temperatures, Fig. 4.5. The considerable stiffness change between the locked and active states allows us to actuate any desired joint while locking the rest of the joints in position. The variation in the joint stiffness at different angles is caused by the residual strain in the SMP layer. This significant variation is undesirable and complicates the control problem. In the next prototype, we use the silicone embedded SMP layers with higher recovery rate to improve the shape recovery and hence acquiring a more uniform joint stiffness at different angles.

4.2.2 Sequential actuation of joints for reaching points in the workspace

Fig. 4.6 depicts the actuation sequence of the arm to reach a point in the workspace. In each step, the SMP layers of the active joint are heated to make the joint complaint. Fifteen seconds was allocated between the steps for the activation of the new joint and cooling down of the previous one. (4.5) and (4.6) were used in this experiment to estimate the required tendon displacement and the motor rotation for reaching different configurations.

$$L_{t-1} = L_{w0}\frac{\cos(\alpha_w - \theta/2)}{\cos(\alpha_w)} \tag{4.5}$$

$$L_{t-2} = L_{t0}\frac{\cos(\alpha_w + \theta/2)}{\cos(\alpha_w)} \tag{4.6}$$

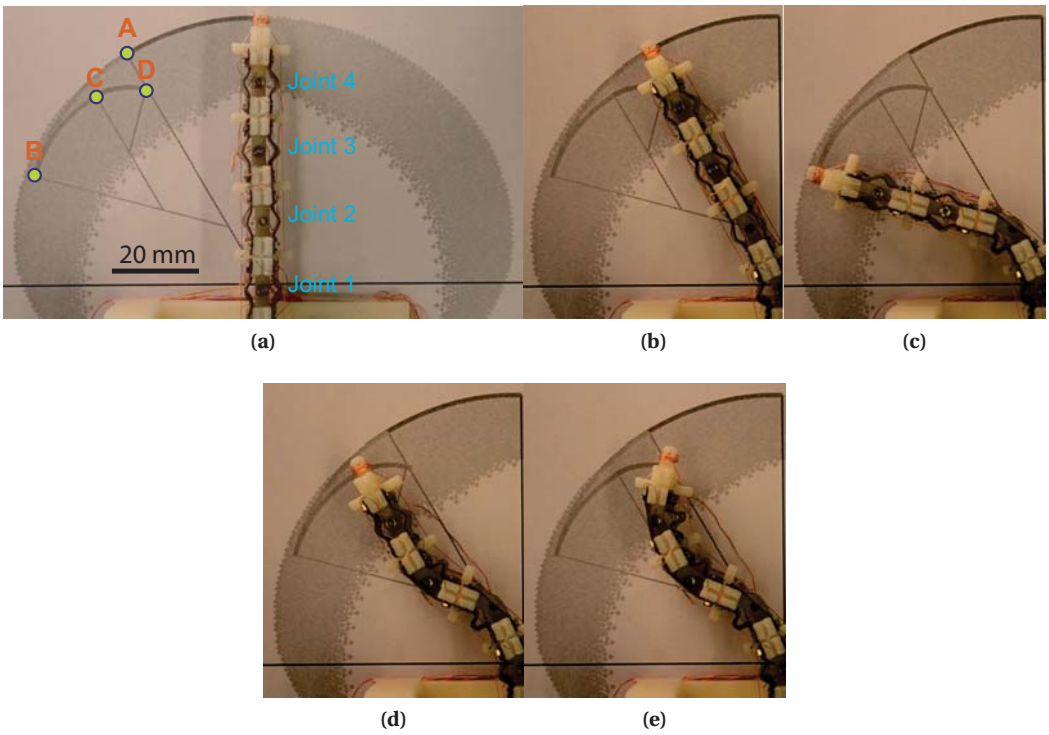

Figure 4.6: Sequential activation of joints in an under-actuated manipulator. The shadowed area in the background shows the work space of the arm (considering 45^o joint limit). (a) The goal position is $[-26\ 44]\ mm$ which is accessible by moving the joints to the following angles $[30^o\ 45^o\ -45^o\ -45^o]$. A, B, C, and D present the desired tip position at the end of each step. (b), (c), (d), (e) Shows first, second, third and forth joints reaching their desired configurations.

In this Section the variability of the elasticity modulus of SMP was used for adjusting the stiffness of the joints in an under-actuated robot. We estimated the joint stiffness at different bending angles and temperatures which verified the possibility of locking in position and activating the joints using material properties. We verified the feasibility of the stiffness adjustment by sequential activation and actuation of the joints in an under-actuated manipulator for reaching different points in the workspace. The current study revealed two design flaws: the residual strain of the SMP, which significantly reduces the joint stiffness; the buckling of the SMP layer in compression, which makes the contribution of the SMP layer in compression to joint's stiffness negligible. In the next Section, we present the robogami version of the manipulator, which resolves these design flaws.

4.3 Robogamis modules with adjustable stiffness joints

The 3D printed under-actuated manipulator of Section 4.2 confirmed the feasibility of joint stiffness adjustment using elasticity modulus variability of SMP around its glass transition temperature. In this Section, we study the integration of the ASLs in tendon-driven robogami joints. Similar to the previous prototype, we use a modular design to have the option of changing joints in case of malfunction and experimenting with different arrangements of DoFs, Fig. 4.7. The ASLs that are used in the robogami joints comprise of a stretchable heater, SMP, silicone rubber, and a glass fiber frame. The higher shape recovery of these ASLs compared to SMP layer along with the robust anchoring points, provided by the glass-fiber frame, allow reliable adjustment of the joint stiffness. In the experiments of this Section the electrical resistance of the heater is used to estimate the temperature and to control the joint stiffness. Here, we demonstrate gradual stiffness control in contrast to joint locking and unlocking which was presented in the previous Section. We also embedded curvature sensors as one of the functional layers in the robogami modules. The joint angle feedback is necessary in under-actuated robogamis for adjusting the control parameters: temperatures of the ASLs, and tendon displacement.

We designed the robogami joint, Fig. 4.7, to have one directional motion in 0^o to 45^o range and placed the ASL only in the tension side of the joint, ASL layer on the compression side buckles and would not contribute to the joint stiffness. We assembled three modules to form the simple manipulator of Fig. 4.8 and studied the simultaneous actuation of the joints at different stiffness settings. In this design, we used polyimide tendon which was integrated in

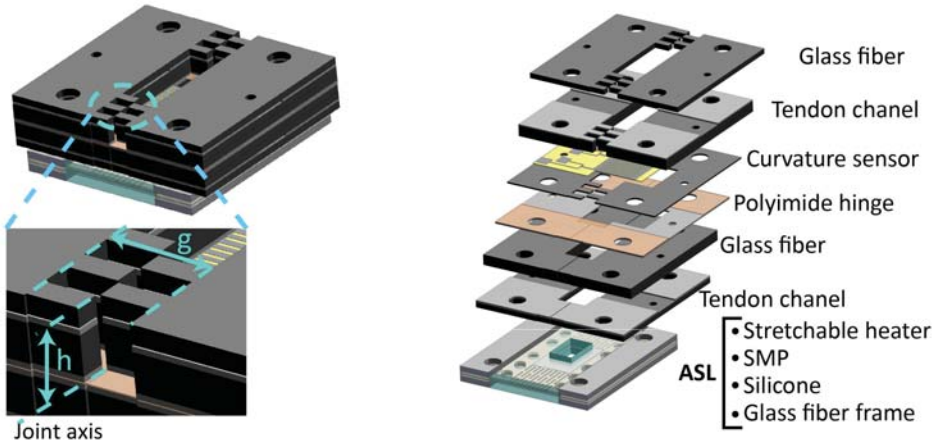

(a) **(b)**

Figure 4.7: Robogami joints with adjustable stiffness. (a) Each joint is designed as a stand alone module. The castellated pattern in the module places the axis of rotation on the polyimide sheet and at a constant distance from the ASL. (b) Different functional layers are integrated using the layer by layer manufacturing process to make each module.

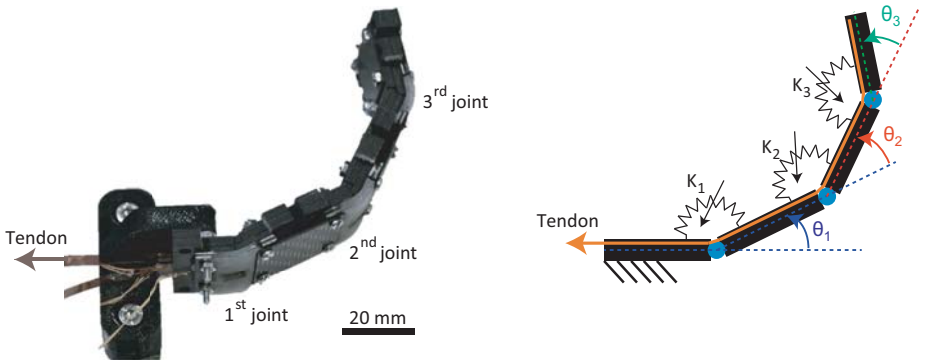

(a) (b)

Figure 4.8: Robogami manipulator with adjustable stiffness joints. (a) The finger consists of three joints with adjustable stiffness and a tendon that drives the joints. (b) Schematic of the finger depicting the joint positions, θ_i, and their adjustable stiffness, K_i.

the robot during the fabrication. These tendons are thin (125 μm) and wide (5 mm) and can transfer up to 105 N force. There are two tendons running through the channels on both sides of the hinge layer but we use only the tendon on the compression side for actuation and rely on the ASL recovery force for the return motion.

4.3.1 Model and parameter characterization of a tendon-driven robogami with adjustable stiffness joints

The stable configuration of the under-actuated robogami and its compliance are determined by the joints' stiffness. The stiffness of the robogami joints are adjusted through controlling the temperature of the ASLs, Fig. 4.8. In this Section, we model the behavior of the robogami which helps us in designing robots with compliance control for various applications. We begin by finding the ratio between the input force and the torque transmitted to each joint. This is the inverse of the ratio between the rate of tendon displacement and the rate of the joint angle variation. According to Fig. 4.9, the contribution of each joint to the displacement of the tendon is calculated as:

$$X_i = g - \sqrt{{X_{i_x}}^2 + {X_{i_y}}^2} \tag{4.7}$$

In (4.7), X_i is the contribution of the i^{th} joint to the tendon displacement. X_{i_x} and X_{i_y} are the components of X_i, depicted in Fig. 4.9, which are calculated as:

$$X_{i_x} = g/2(1+\cos\theta_i) - b\sin\theta_i \tag{4.8}$$

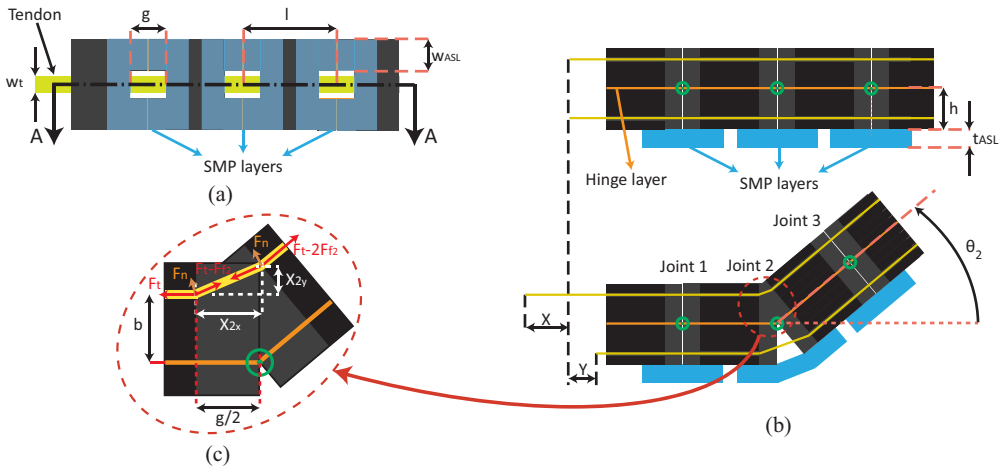

Figure 4.9: Schematic of the finger presenting the design parameters and the actuation of the second joint. (a) The top view. (b) The side view of the cross section A-A depicted in Fig. 4.9(a). The schematic of the finger with its second joint at an angle θ is presented to highlight tendon displacement and elongation of ASL. (c) The point of interaction between the tendon and the glass fiber layer is magnified to show the contact forces that result in frictional losses.

$$X_{i_y} = g/2(\sin\theta_i) + b\cos\theta_i - b \tag{4.9}$$

The geometrical parameters in (4.8), (4.9), and the following equations are depicted in Fig. 4.9 and their values are presented in Table 4.1. Using (4.7)-(4.9), the relation between the joint angular speed and the rate of tendon displacement is calculated as:

$$dX_i = \frac{X_{i_x} b + X_{i_y} \dfrac{g}{2}}{\sqrt{{X_{i_x}}^2 + {X_{i_y}}^2}} d\theta_i \tag{4.10}$$

The displacement X, from (4.7), corresponds to the effective displacement that results in the configuration change. The input displacement, however, is the sum of this effective displacement and the tendon elongation due to the tensile load. So for the total input displacement, X_{total}, we have:

$$X_{total} = \sum_{i=1}^{n} X_i + \sum_{i=1}^{n} \frac{F_t - \sum_{j=1}^{i-1} 2F_{f_j}}{k_{t_i}} \tag{4.11}$$

Table 4.1: Design parameters for robogami modules. The thickness of different layers in this table can vary up to 10%. This is caused by the difficulties in controlling the thickness of different layers in the composite.

Parameters	Value (mm)	Description
l	34	Phalanx length
g	4	Gap size in the middle part
w_{ASL}	7	ASL width in the active part
l_{ASL}	4	ASL length in the active part
w_t	6	Tendon width
t_{ASL}	2	ASL thickness
t_{SMP}	0.5	SMP layer thickness
h	2.4	ASL distance from the axis of rotation
h_{tot}	6.8	The overall height of the module
b	2	Tendon distance from the axis of rotation

The first term in (4.11) accounts for the effective displacement and the second term for the elongation of the tendon. k_{t_i} in this equation is the stiffness of a section of the tendon between joints $i-1$ and i. Here we considered the decrease in the tendon force, F_t, from the base to the tip due to the friction forces at each joint, F_{f_j}, and calculated the elongation for each segment between the joints separately. There are two contact points per joint, Fig. 4.9 (c). We considered the friction force for both contact points to be equal. This force, which depends on the tendon force and the joint angle, is calculated as:

$$F_{f_i} = \mu_f F_{n_i} + C_{f_i} F_t = (\mu_f 2 \sin(\theta_i/4) + C_{f_i}) F_t \tag{4.12}$$

In (4.12), μ_f is the friction coefficient and F_{n_i} is the normal contact force between the tendon and its channel. The second term in this equation accounts for the friction forces due to the misalignment in the tendon channel and is independent of the joint angle.

To study the stable configurations of the finger at different joint stiffness settings, the kineto-static analysis of under-actuated fingers presented by Birglen and Gosselin [115] is adopted and modified to account for the energy storage in the ASL and the friction losses. Equating the input work and the work done by the finger on the environment and the stored energies in the ASLs, we have:

$${F_t}^T \dot{X} = \sum_{i=1}^{n} \xi_i \circ \zeta_i + W_{ASL} \tag{4.13}$$

In (4.13), the left side is the input work minus the friction losses. The elements of F_t are

the tension in the tendon at each joint and the elements of $\dot{X}$ are the rate of the tendon displacement caused by the motion of each joint. The first term on the right side of this equation is the reciprocal product of the screws corresponding to the twist, ξ_i, and the wrench, ζ_i, at the contact point on each phalanx. The second term on the right, W_{ASL}, corresponds to the work done for deforming the ASLs. For the contact point with the object, we neglected the friction forces and only considered the normal forces. So the work done by the contact forces is calculated as:

$$\sum_{i=1}^{n} \xi_i \circ \zeta_i = f^T J\dot{\theta} = f^T \begin{bmatrix} d_{11} & 0 & ... & 0 \\ d_{12} & d_{22} & ... & 0 \\ . & . & . & . \\ d_{1n} & d_{2n} & ... & d_{nn} \end{bmatrix} \dot{\theta} \tag{4.14}$$

In (4.14), f is the vector of the contact forces, d_{ij} is the distance of the i^{th} joint from the contact force vector applied to the j^{th} phalanx, and $\dot{\theta}$ is the vector of the joints' rotational speed. The tendon force at each joint, elements of F_t in (4.13), is calculated by subtracting from the input tension all the friction forces from the base to that joint:

$$\boldsymbol{F_t}^T = \begin{bmatrix} F_{t_0} - F_{f_1} & F_{t_0} - F_{f_2} - 2F_{f_1} & F_{t_0} - F_{f_3} - 2\sum_{i=1}^{2}(F_{f_i}) & ... \end{bmatrix} \tag{4.15}$$

The rate of the tendon displacement, $\dot{X}$ in (4.13), has the following relation with the angular velocities of the joints:

$$\dot{X} = T\dot{\theta} = \begin{bmatrix} \frac{\partial X_1}{\partial \theta_1} & 0 & ... & 0 \\ 0 & \frac{\partial X_2}{\partial \theta_2} & ... & 0 \\ . & . & . & . \\ 0 & 0 & ... & \frac{\partial X_n}{\partial \theta_n} \end{bmatrix} \dot{\theta} \tag{4.16}$$

$\frac{\partial X_i}{\partial \theta_i}$ in this equation is the transmission ratio between the input and the i^{th} joint. This is calculated from (4.10) which corresponds to the relation between the tendon displacement rate and the angular velocity of a desired joint when all the other joints are locked in position.

The stored energy in the ASL, W_{ASL}, is found as:

$$W_{ASL} = {F_{ASL}}^T \dot{\triangle} = (K_{ASL}\triangle)^T \dot{\triangle} \tag{4.17}$$

In (4.17), $\triangle$ and F_{ASL} represent the elongation and the force of the ASLs. K_{ASL} in this equation is the matrix of the joint stiffness which has the following form:

$$K_{ASL} = \begin{bmatrix} C_{k_1}F_{k_{ASL}}(T_1) & 0 & ... & 0 \\ 0 & C_{k_2}F_{k_{ASL}}(T_2) & ... & 0 \\ . & . & . & . \\ 0 & 0 & ... & C_{k_n}F_{k_{ASL}}(T_n) \end{bmatrix} \tag{4.18}$$

In (4.18), $F_{k_{ASL}}(T)$ is the ASL stiffness which is a function of its temperature. This function is determined using the tensile characterization test results presented in the previous chapter. $F_{k_{ASL}}(T)$ provides the trend of the stiffness change with temperature. Due to the variation between different ASL samples and robogami modules (mainly the variation in the thickness of the layers), we expect some variation in the stiffness of the joints which is accounted for, in (4.18), by the correction factors (C_{k_i}). The ASL elongation, Δ, is a function of the joint angle and is calculated as:

$$\triangle = 2(h + \frac{t_{ASL}}{2}) \sin\frac{\theta}{2} \tag{4.19}$$

Replacing the stored energy in the ALSs in (4.13) yields the following set of equations that correlate the tension in the tendon with the joint angles, their stiffness and the contact forces:

$${F_t}^T T = f^T J + ((h + \frac{t_{ASL}}{2})^2 (K_{ASL}\sin\theta)^T) \tag{4.20}$$

(4.20) determines the configuration of the robogami for a given joints' stiffness and tendon tension. This set of equations and (4.11) are used to evaluate the tendon displacement. To use this model for predicting the behavior of the under-actuated robogami, we need to determine the missing parameters in the model: the tendon stiffness, the friction forces, and the correction factors for the joint stiffness, C_{k_i}.

There are two sources of friction loss in the robogami finger: 1- the friction between the castellated features of the adjacent tiles, 2- the friction between the tendon and its channel.

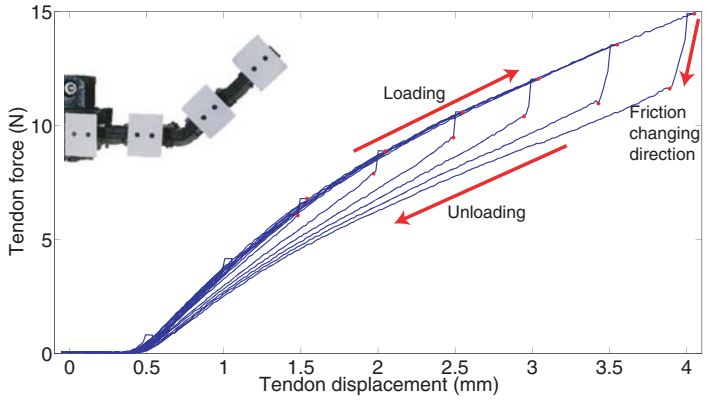

Figure 4.10: Tension in the tendon as a function of its displacement. We test each joint in the finger individually at the maximum temperature in order to characterize the friction force. The sudden drop in the tendon tension when the direction of motion is reversed corresponds to the change in the direction of friction force between the tendon and the glass fiber channel. The corresponding bending angle for each displacement is found from the video of the tests. A snapshot of the video corresponding to the characterization test for the second joint is presented in this figure. The markers on each phalanx are to facilitate the video processing.

The first source of friction is independent of the force in the tendon and based on the tests on a sample without the ASL, is negligible. The second source of friction is significant and is accounted for in the model as presented in (4.12). The magnitude of this force depends on the joint angle and the tendon tension. To study this force and to find the friction coefficient for each joint, we activated one ASL in the finger at 110 ^oC and left the other two ASLs at room temperature. After reaching the thermal equilibrium, we applied tendon displacements in the range of $0-4$ mm with 0.5 mm increments. As presented in Fig. 4.10, when the direction of the motion reverses, there is a sudden drop in the tendon tension. This drop is caused by the friction force changing direction. Due to the elasticity of the tendon, this drop is not completely vertical. The slope of this change depends on the tendon length and it varies for different joints. The drop in tensile force (ΔF_t) is due to the accumulated friction forces from the base to the active joint and is calculated as:

$$\Delta F_t = 2[F_t(\mu_f 2\sin(\theta_i/4) + \sum_{j=1}^{i} C_{f_j})] \tag{4.21}$$

The friction force changes direction when the direction of the motion reverses. So the drop in the tendon tension is twice that of the friction force which is accounted for by the factor of two in (4.21). Based on the characterization results, the parameters of the friction force were found as 0.23 for μ_f and 0.01, 0.011, and 0.014 for C_{f_1}, C_{f_2}, and C_{f_3} respectively. To find these parameters, the joint angles corresponding to each displacement were determined from the video processing.

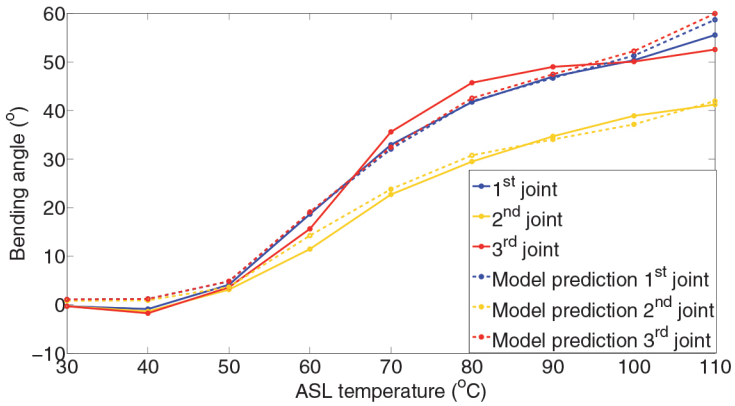

Figure 4.11: Characterizing joint stiffness correction factors. The bending angle for the three modules at different temperature settings with 15 N tenon tension (each module was tested separately). The model was corrected based on the experimental results by applying a correction factor to the ASL stiffness (C_{k_i}) that accounts for the variation of different layer's thickness.

The second set of parameters to be determined is the correction factors for the joint stiffness. In the model, we use the stiffness-temperature correlation presented in Fig. 3.20 ($F_{k_{ASL}}(T)$) to determine the stiffness of the joints at different temperatures. The correction factor for the stiffness of the ASL (C_{k_i}) which is introduced in (4.18) accounts for the differences between the ASLs and the height of the modules. To find the correction factors, each joint of the finger was tested individually at different temperature settings (from 30 ^oC to 110 ^oC with 10 ^oC increments). At each temperature, the tendon was pulled until 15 N, the force sensor loading limit. Fig. 4.11 presents the maximum bending angle at each temperature setting. The first and the third joints in the finger have similar behavior but the second joint bends less for the same tendon force, which indicates that the second joint is stiffer than the other two joints. Based on the test results we found the following correction factors: 1.14, 1.48, and 1.12 for the first, the second, and the third joints, respectively.

The elongation of the tendon under tensile load is not negligible and is accounted for in the model, (4.11). To evaluate the stiffness of the tendon, we used the force displacement relation in the test with all ASLs at 30 ^oC. The results confirmed linear elastic behavior for the tendon with the stiffness coefficient of 10.7 N/mm for the full length of the tendon, 142 mm. We use this to calculate the stiffness of the segments of the tendon between each two joints, k_{t_i}, which is used in (4.11).

The model presented in this Section allows us to study the behavior of different arrangements of joints in robogami in the design process and to control the stiffness of the joints in the prototype for achieving desired behavior. In the next Section, we verify the model by comparing simulation predictions with the results of free motion and blocked force experiments.

4.3.2 Experimental result and model verification

In this Section, we verify the model using a tendon-driven robogami with three modules. In the first part, we study the free displacement of the robogami at different stiffness settings. In this study, we also compare the curvature sensor estimation and the actual configuration of the robogami. Next, the compliance of the manipulator's end-effector at different stiffness settings is characterized in blocked force experiments.

Configuration control in free motion

The stable configuration of the robogami finger can be controlled by assigning proper stiffness to the joints. Here, we compare the model prediction and the sensor estimation with the actual configuration of the finger at different temperature settings for the ASLs. In total 15 temperature settings were tested. Fig. 4.12a presents three examples of these experiments. In each experiment, the tendon was pulled up to 15 N, the force sensor loading limit, or 4.5 mm displacement, resulting in motions within the joint limits (whichever happened first). We started the tests with the ASL of all joints at 110 ^oC. The configuration of the finger at this temperature setting is presented in the first plot of Fig. 4.12a. At each temperature setting the finger was actuated twice. The return motion to the straight configuration as the tendon is released after each actuation is powered by the elastic force of the ASLs. With the same stiffness setting (i.e. all the ASLs at the same temperature) the model predicts a decrease in the joint angles from the base to the tip, which is confirmed by the results of the first experiment. This is due to the friction force between the tendon and its channel. Next, we decreased the temperature of the base joint to 40 ^oC with 10 ^oC increments. Reducing the temperature of the first joint results in a smaller bending angle for this joint and larger angles for the other two joints (with the same tendon displacement). The second case in Fig. 4.12a shows an intermediate step, with the first joint at 60 ^oC and the other two at 110 ^oC, which illustrates the decrease in the bending angle of the first joint and increase in the angles of the other two.

After the temperature of the first joint was decreased from 110 ^oC to 40 ^oC, the tests were continued by decreasing the temperature of the middle joint to 40 ^oC with 10 ^oC increments. As expected, the second joint angle decreases as it becomes stiffer at lower temperatures. The third case in Fig. 4.12a shows the test result for one of the settings with the first joint at 40 ^oC and the second and third joints at 80 ^oC and 110 ^oC, respectively. Fig. 4.12a also presents the comparison between the sensor estimation (dashed line) and the actual phalanx angle (solid line). The curvature sensors are able to estimate the configuration of the finger with high accuracy. The RMS error between the estimated and the actual joint angles at the maximum deformation for the three joints in the 15 tests with different temperature settings (2 repetitions for each test) was 1.8^o, which guarantees reliable feedback from the embedded sensors.

The model predictions for the configuration of the robogami finger were also compared to the actual configuration of the finger in the 15 tests. The model is able to predict the trend in the

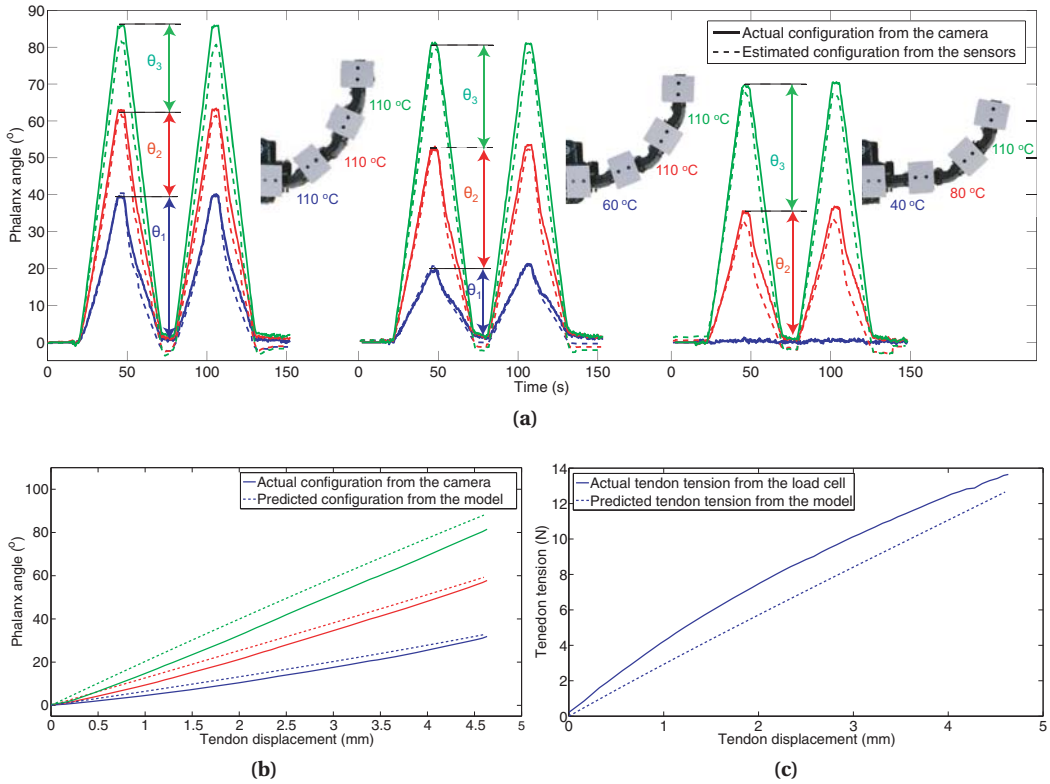

Figure 4.12: Configuration control in the robogami manipulator in simultaneous actuation of all joints. (a) The angles of the three phalanges of the finger from their initial position at different temperature settings, the results of three experiments from the overall 15 tests are presented. The dashed lines represent the curvature sensors' measurements and the solid lines are from video processing. The joint angles (the difference between the angles of two adjacent phalanges) are marked in the plot. The configuration of the finger for each temperature setting with the temperature corresponding to each joint is also presented in this figure. (b) Model prediction for each of the three phalanges and their actual position. The temperature set points in this case are 80 ^oC for the 1^{st} joint and 110 ^oC for the 2^{nd} and 3^{rd} joints. (c) Tendon tension predicted by the model and the actual tension. The temperature set points are the same as part (b).

configuration change at different temperatures. Fig. 4.12b presents the comparison between the model prediction and the actual configuration for one example. The RMS error between the model prediction and the actual joint angle for the 15 tests is 4.6^o .

Fig. 4.12c compares the tension in the tendon with the predicted value from the model which shows around 7% error at the maximum load. The trend for the force displacement relation predicted by the model is rather linear since we have adopted a linear model for the elastic behavior of the ASL. However, the actual force displacement relation is nonlinear. To have a better prediction in the future we need to use a more accurate model for the elastic behavior of the ASL.

The test results confirmed the feasibility of the configuration control by modulating the

temperature of the SMP layers. The model is able to predict the configuration of the finger at different temperature settings and can be used to assign the temperature of the ASLs in the joints to reach a desired configuration. The errors caused by model inaccuracies can be corrected by adjusting the control command for the tendon displacement and ASL temperature set points using the curvature sensors' feedback.

Robogami compliance control

We can control the overall stiffness of the finger by modulating the stiffness of its joints. Using this feature, we can operate it in its *soft mode* in sensitive environments with limited applied contact forces and in its *stiff mode*, for handling heavy loads or performing precise motions. Here, we study the motion of the under-actuated finger with different joint stiffness as it conforms to the shape of a fixed object and apply contact forces. We considered three different cases. In the first case, all three joints are activated at 110 ^oC and the finger is in its softest state. Next, all the joints are activated at 55 ^oC. We expect the ratio of the stiffness of the joints and hence the motions of the finger to be similar in these two cases, with the only difference being the contact force magnitudes. Finally we study the case where the first two joints are fixed in position and only the tip joint is moving. In this mode of operation, the initial deformation puts the tip phalanx at the desired position and orientation. By activating only one joint in this state, we expect larger forces compared to the other two cases.

Fig. 4.13a-4.13c present the simulation results for the finger in the three cases. We considered one contact point per phalanx. We placed the contact point at 2 mm distance from the tip when the finger initially conforms to the object. We study the forces that the robogami applies before the deformations in the first and second joints cause the third phalanx to lose contact with the force sensor.

For the first and the second cases, as the tendon is pulled, the finger conforms to the shape of the object, starts applying force to the force sensors, and finally loses its contact with the tip force sensor. The configurations of the finger in the first two cases, Fig. 4.13a-4.13b, are very similar. The estimated maximum contact force from simulation, however, changes from 0.23 N to 0.7 N by increasing the stiffness of the finger. In the third case the finger is initially actuated in its soft mode to conform to the shape of the object and then the first and second joints are locked in this position. The third joint is the only active joint and as demonstrated by the simulation results, Fig. 4.13c, the maximum force before the finger loses its contact at the tip increased to 0.95 N.

To verify the simulation results, a 3D printed stand with one-directional force sensors (FSS015WNGX, Honeywell) in the same orientation was fabricated and the same scenarios of simulation were replicated. Snapshots from the experiment corresponding to the first temperature setting, Fig. 4.13d-4.13f, illustrate the initial contact and the retracting motion of the tip. The maximum contact forces for the three cases were measured: 0.17, 0.32, and 0.75 N, respectively. While the measured forces confirm the trend observed in the simulation, their values are smaller in

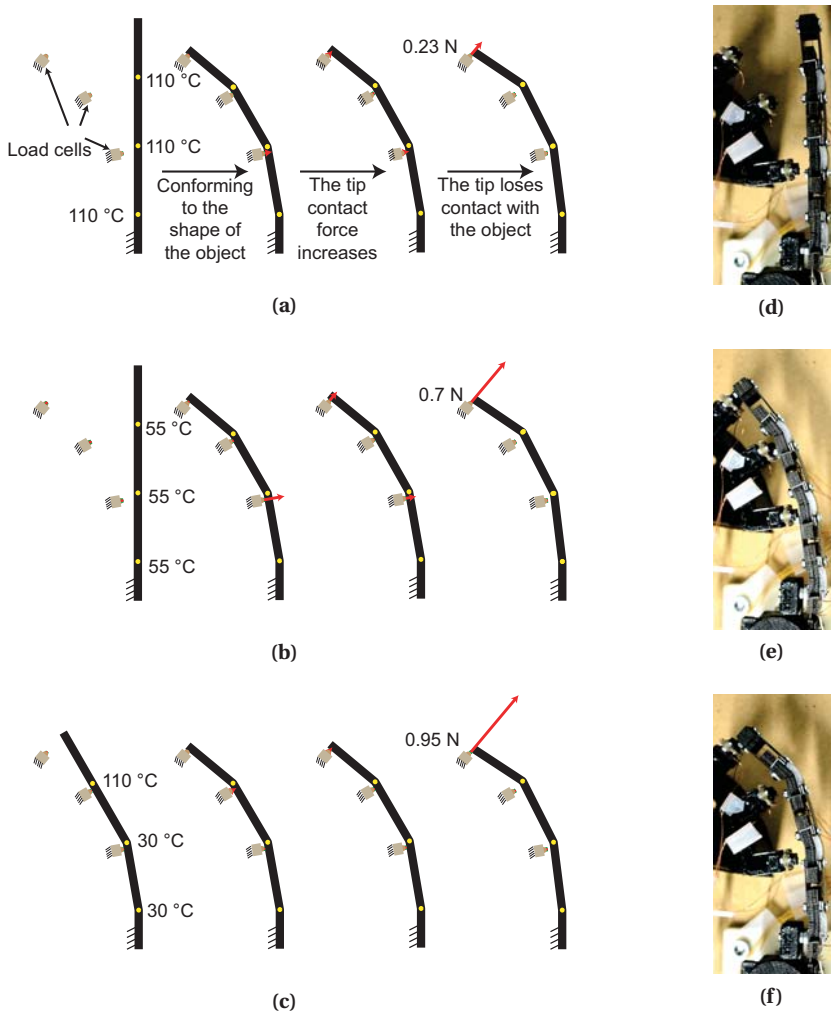

Figure 4.13: The contact force study. (a)-(c) The simulation results for the contact forces between the finger and the object at different stiffness settings. (a) In this case the temperature of all joints is set to the maximum, 110 ^oC, and the finger is in its softest state. By pulling the tendon, the finger conforms to the shape of the object and starts applying contact force. Increasing the tendon displacement increases the contact force at the tip and finally causes the finger to deform at the first and second joints which results in losing contact at the tip. (b) In this case the temperature of all joints is set to 55 ^oC. The motion of the finger in this case is similar to the previous case but the contact forces are larger. (c) In the third case only the third joint is activated. The other two joint angles are set to put the last phalanx at a desired position and orientation. The maximum contact force in this case is larger since the first and second joints are stiffer compared to the other two cases. (d)-(f) Snapshots from the contact force experiment with all the joints at 110 ^oC. (e) The robogami conform to the shape of the object. (f) Increasing the tendon tension results in the retracting motion of the finger which causes the tip to lose contact with the force sensor.

comparison. This difference is caused by the combination of positioning errors for the object and the deformation in the force sensors' 3D printed stand.

Controlling the overall compliance of an under-actuated system allows us to adjust the magnitude of the maximum contact force for safe interaction, which depends on the application. In the remainder of this chapter, we focused mainly on application of robogami as a soft and programmable actuation platform with compliance control in under-actuated grippers.

4.4 Two-fingered robogami gripper with compliance control

One of the main motivations for using robogami structures is the ease of miniaturization and feasibility of packing multiple DoFs in a confined space with minimal structural complexity in the hardware, thus in the manufacturing. In the previous Section, we refined the joint design and the manufacturing process of the robogami modules. Here, we present a robogami with eight joints that is manufactured in one piece to highlight the ease of extension of the concept to more complex structures. Using this prototype, we also present the concept of soft actuation with compliance control in robogamis with adjustable stiffness joints. We use two robogami fingers with a similar design in a gripper and demonstrate its task versatility in soft and stiff modes by assigning model-based stiffness settings for performing different grasp modes.

4.4.1 Tendon-driven robogami finger with adjustable stiffness joints

Fig. 4.14 illustrates the schematic of the robogami studied in this Section. All joints in this robogami have parallel axis of rotation and the motion of the robot is limited to the plane which simplifies the analysis and experiment design for studying the soft actuation with compliance control. The first and the last joints in this design are actuated in the opposite direction compared to the rest of the joints. The range of motions of these two joints are set to $[-45^o\ 0^o]$ and for the rest of the joints, joints 2-6, the range of motions are set to $[0^o\ 45^o]$. In general activating more joints makes the structure more compliant. The activation of the first or the last joint, however, has more significant influence on the compliance which originates from their opposite direction of actuation. This allows us to switch between different modes to achieve either higher forces or more adaptable and compliant actuation. We assigned a smaller tendon distance from the joint axis for the first and the eighth joints to use more effectively the soft mode of these joints by limiting their displacement in the free motion of the finger. The design parameters for this finger are presented in table 5.1.

We use a model similar to the one presented in the previous Section, (4.20), to study the behavior of the robogami. Here, we are concerned with the contact forces at the end-effector.

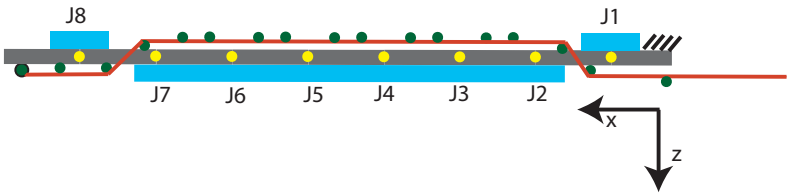

Figure 4.14: Overview of the robogami design with high compliance variability. The tendon path depicts how it changes side around the neutral plane to actuate joints in different directions. The ASL is placed on the opposite side of the tendon in all joints to be on the tension side.

So the force matrix, f^T, and the Jacobian matrix, J, are rewritten as:

$$J = \begin{bmatrix} \sum_{j=1}^{n} l_j sin(\sum_{i=1}^{j} \theta i) & \sum_{j=2}^{n} l_j sin(\sum_{i=1}^{j} \theta i) & ... & l_n sin(\sum_{i=1}^{n} \theta_i) \\ \sum_{j=1}^{n} l_j \cos(\sum_{i=1}^{j} \theta i) & \sum_{j=2}^{n} l_j \cos(\sum_{i=1}^{j} \theta i) & ... & l_n \cos(\sum_{i=1}^{n} \theta_i) \\ 1 & 1 & ... & 1 \end{bmatrix} \tag{4.22}$$

$$f^T = \begin{bmatrix} F_x, F_z, M_y \end{bmatrix} \tag{4.23}$$

J correlates the Cartesian and the rotational velocities of the end-effector to the rotational velocity of the joints. The elements of f are the components of the contact force in x and z directions and the moment in y direction.

We use model to study the effect of joint stiffness on the reconfiguration of the finger and the compliance of the end-effector. The activation of different joints changes the free motion trajectory of the end-effector. The compliance of the finger for each trajectory can be controlled through the joints stiffness. Joints 1 and 8 of the robogami finger, with their opposite direction of actuation, influence the compliance of the finger significantly. Here, we study the effect of

Table 4.2: Design parameters for the two-fingered robogami gripper.

Parameters	Value (mm)	Description
l_{pn}	8.2	the length of 2^{nd}-6^{th} and 8^{th} Phalanges
l_{pl}	11.4	the length of 1^{st} and 7^{th} Phalanges
g	4	Gap size in the middle part
w_{ASL}	14	ASL width in the active part
l_{ASL}	4	ASL length in the active part
t_{ASL}	2	ASL thickness
h	3.25	ASL (mid-layer) distance from the axis of rotation
b_1	3.5	Tendon distance from the axis of rotation for joints $2-7$
b_2	-2.5	Tendon distance from the axis of rotation for joints 1 and 8

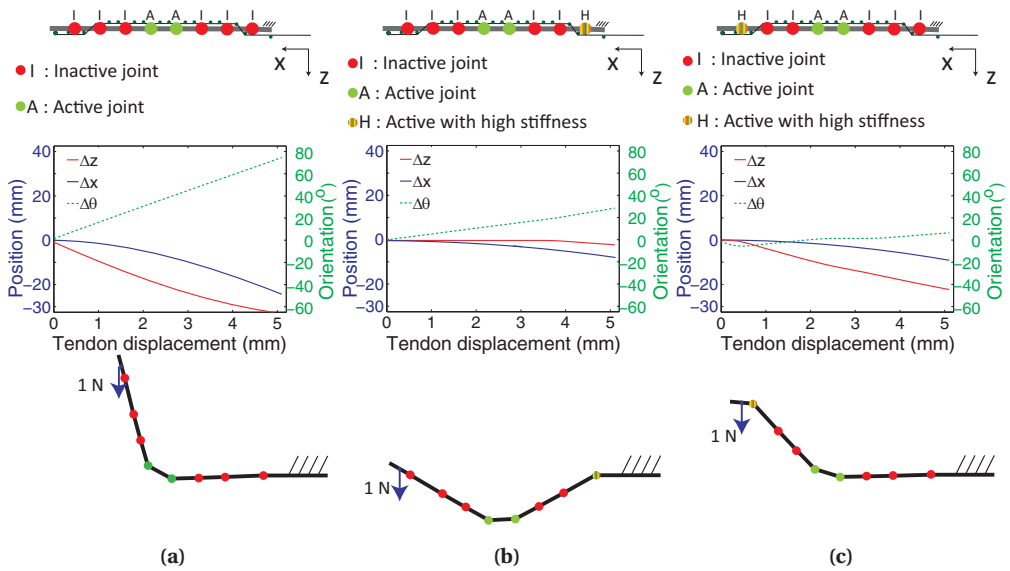

Figure 4.15: Displacement of the end-effector with three different stiffness settings under 1 N load in z direction. (a) In the first case, joints 4 and 5 are at high temperature (110 ^oC) and all the other joints are at room temperature. (b) In the second case, the first joint is activated at a lower temperature (65 ^oC). Given the higher stiffness of the joint and its smaller actuation moment, the free displacement of the finger is similar to the previous case. The trajectory of the end-effector under load, however, is significantly different. (c) In the third case, the eighth joint is activated at 65 ^oC. The activation of this joint also does not considerably change the free displacement but the rotational compliance of the end-effector is remarkably increased compared to the first case.

activation of these joints. For each simulation, we report the trajectory of the end-effector and the final configuration of the finger which is estimated by the model. To verify the simulation results we tested the finger with the same stiffness setting and contact load and compared the final configuration of the finger with the simulated configuration.

The motion of the robogami finger under load in z direction is simulated with three different stiffness settings, Fig. 4.15a-4.15c. In simulation, the contact force increases with the motion of the end-effector in the z direction at the rate of 50 N/mm and is saturated at 1 N. The linear compliance of the end-effector in z direction and its rotational compliance are dependent on the stiffness assigned to different joints. The first simulation, Fig. 4.15a, is the reference to verify the effect of activation of the first and the last joints. In this case, joints four and five are active at their most compliant state, 110 ^oC. For this setting, the motion of the finger is not effected by the load and it is characterized by high linear stiffness for the end-effector in z direction and high rotational stiffness. Activating the first joint makes the finger considerably more compliant in the z direction, Fig. 4.15b. In this case, the first joint is activated at 65 ^oC and the setting for the other joints is similar to the previous case. The activation of the first joint at this temperature does not significantly affect the free displacement of the finger. However, the trajectory of the end-effector changes considerably under load and the position

(a) (b) (c)

Figure 4.16: Configuration of robogami under load with different stiffness settings. The overall behavior follows the one predicted in simulation. The main reasons for discrepancy are: the neglected effect of the tendon friction with its channel; and the slight differences between different joints and ASLs.

of the end-effector in z direction stays without much change during the actuation. Note that actuating the first joint in the opposite direction is more effective for changing the compliance of the finger compared to having a passive joint. The increased tendon tension amplifies the moment applied to the first joint by the contact force and makes the finger more responsive, compliant, to the contact forces. In order to limit the deformation of the base joint in free displacement, to have similar free motion, the tendon is placed closer to the neutral plane for the first joint and this joint is activated with a lower temperature, higher stiffness, compared to the rest of active joints. This design for the tendon distance and temperature setting for the first joint, results in similar free motion trajectories for the first two cases of Fig. 4.15. The compliance of the end-effector, however, is significantly different for these two cases which results in different trajectories and final configuration under load.

The activation of the last joint also affects the compliance of the end-effector as presented in Fig. 4.15c. Given the small distance between this joint and the end-effector, the compliance in z direction does not change much in this case. The rotational compliance of the last link, however, significantly changes when this joint is activated. As was the case for the first joint, activation of the last joint at 65 ^oC does not affect the trajectory of the free motion. Under load, however, the orientation of the last link remains almost constant. By increasing the lateral and rotational compliance, the manipulator becomes self-adaptive in these directions to an assigned degree. This is desirable for safe interaction with sensitive environment. Compared to a fully actuated system, this approach is superior since it requires much less computation and control effort and only high level control on the joint stiffness and the overall behavior is required.

To verify the simulation results, we tested the robogami finger with the similar settings used in the simulations, Fig. 4.16a-4.16c. In the experiments the duty cycle for the heaters were set based on the readings from a thermal camera for reaching the desired temperature at each joint. The tendon displacement corresponding to the displacement used in the simulation is applied using an electric motor, Dynamixel MX-28. The final configuration of the finger with different temperature settings are presented in Fig. 4.15 for comparison. The overall behavior is similar to the one predicted by simulation. The main discrepancy reasons are: the slight

differences between different joints and ASLs; and the neglected tendon friction in simulation (in this study we considered constant tendon tension for all joints).

In this Section, we demonstrated the compliance control of a robogami finger in different directions through joint stiffness adjustment. In the next Section we demonstrate the grasp versatility of a gripper with two fingers similar to the one studied here.

4.4.2 Under-actuated robogami gripper with compliance control

Tendon-driven robogamis provides a platform for designing compliant robots. The compliance in these robots originate from their under-actuated and redundant DoFs. Here, we study the application of tendon-driven robogamis in a gripper. The conformity of such a gripper allows it to orient its contact points to apply forces in a proper direction for a robust grasp. By implementing the adjustable stiffness joints such a gripper can perform different grasp modes based on the assigned stiffness setting. The design of the gripper with two fingers is presented in Fig. 4.17. The actuation from the slider is divided between the two fingers through the tendon and the pulley. The tendon displacement drives different joints in the robogami according to their stiffness. In the schematic of the gripper, Fig. 4.17b, the active and inactive, soft and stiff, joints are marked. In this Section, we demonstrate two different grasp modes: **power grasp** and **precision grasp**. For power grasp the object is enveloped by the fingers and is secured between the fingers and the palm of the gripper. In the precision grasp, the object is secured between the finger tips. These two modes of grasp require the activation of different joints. In each mode, the compliance of the fingers can also be adjusted by setting different levels of joint stiffness. In the last part of this Section, we compare the grasp of a soft object in two different modes to showcase the effect of the activation of the first joint on the finger's compliance.

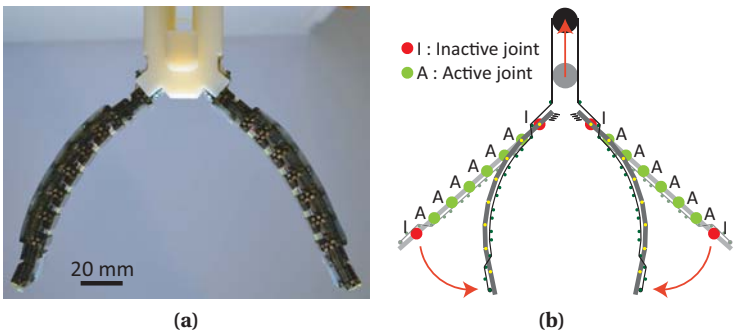

Figure 4.17: Overview of two-fingered robogami Gripper. The gripper consists of two fingers similar to the one of Fig. 4.14. (a) A single input actuates both fingers through a pulley. (b) The schematic of the gripper and its motion with the setting for power grasp. The green and red dots represent the active and inactive joints, respectively.

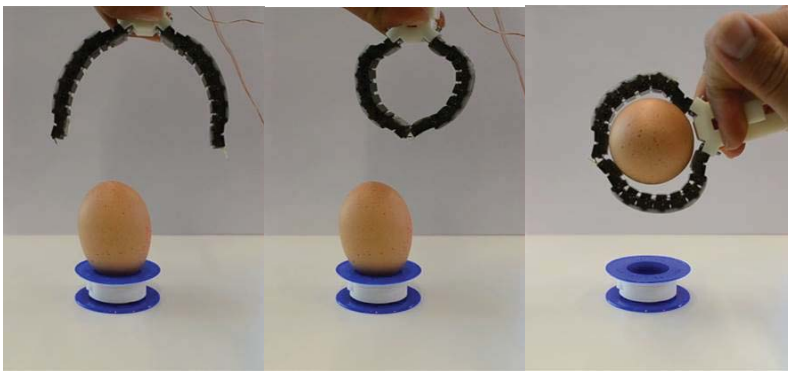

(a) (b) (c)

Figure 4.18: *Power grasp* mode. In this mode all joints except for J1 and J8 are active. (a) Initial state. (b) Free motion. (c) Grasp of an egg. The redundant DoF of the fingers in this mode of operation allows the last link to orient itself for applying the contact force at the proper direction for a stable grasp.

Power grasp

In the *power grasp* mode, the gripper secures the object between the fingers and the base. To perform the power grasp, joints 2-7 are activated at their most compliant state. The schematic of Fig. 4.17b presents the stiffness assignment and the actuation overview. The redundant DoFs of the fingers and the inherent softness of the under-actuated gripper, allow the last link of each finger to adapt its orientation to apply forces in the the proper direction for a robust grasp of the object as presented in Fig. 4.18. For larger objects, the fingers compliance allow them to conform to the shape of the object and envelope it. For the smaller object, like an egg, the self-adaptability of the last link illustrates the conformity of the gripper and the softness of the grasp.

Precision grasp

The second grasp mode of the gripper we study is the *precision grasp* of small objects between the finger tips. In this case, large displacement and small orientation change at the tip are required. So, joints 2 and 3 are activated for performing the precision grasp, the first schematic of Fig. 4.19d. The orientation of the end-effector for grasping small objects has to be adjusted based on the contact force and the size of the object. One approach is to reconfigure and lock the tip joint of the finger in the proper orientation based on the object. Here we use a different approach and activate the tip joint at a lower temperature (65 ^oC) to increase the rotational compliance of the end-effector. The schematics of Fig. 4.19d present how the activation of the last joint helps with the self-adaptability of the last link's orientation. Fig. 4.19a - 4.19c presents the free displacement and the grasping of a 5 CHF coin ($t = 2.4\ mm$, $\phi = 31.5\ mm$, $m = 13.2\ g$). We should point out that the compliance setting for the tip is a delicate task since excessive rotational compliance can diminish the grasp stability.

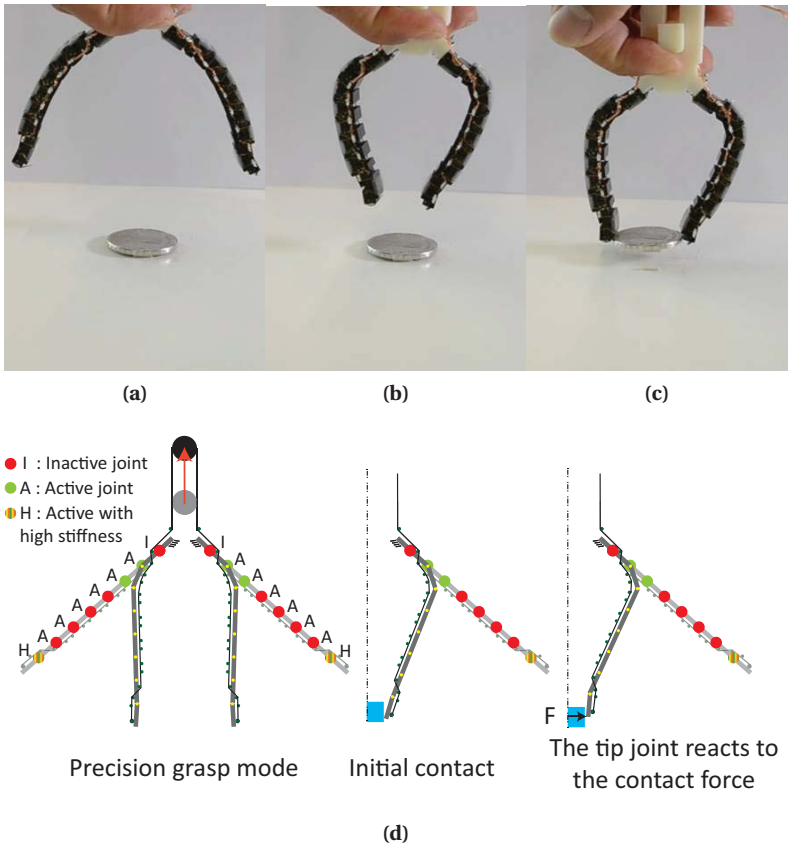

Figure 4.19: *Precision grasp* mode. Only three DoFs are active in this mode which results in less compliant and more controlled motion of the end-effector. (a) Initial state. (b) Free motion. (c) Grasp of a 5 chf coin(31.5 mm in diameter and 13.2 g in mass). (d) To facilitate the precision grasp, the eighth joint is also activated at 65 ^oC. This increases the rotational compliance of the end-effector which improves the orientation self-adaptability of the last link.

Grasp compliance

The compliance of the robogami fingers can be adjusted by changing the stiffness of the active joints and also by activating additional joints. In the present design, the activation of the first joint significantly increases the compliance of the finger. The increased compliance is desired in grasping soft and delicate objects since the contact forces are limited in this mode without the need for any feedback control. To illustrate this, we compare the grasp of a foam with two different compliance settings. In the stiff mode, joints 2-7 are active. For the soft mode, we activate the same joints, 2-7, and to increase the compliance, we also activate the first joint but at higher stiffness, 65 ^oC. The schematics of Fig. 4.20a illustrates the temperature setting and the motion of the gripper with these two compliance settings. The free motion of the gripper in these two modes are similar, Fig. 4.20c, but when the gripper comes in contact with an object the increased tendon tension along with the moment from the contact forces push

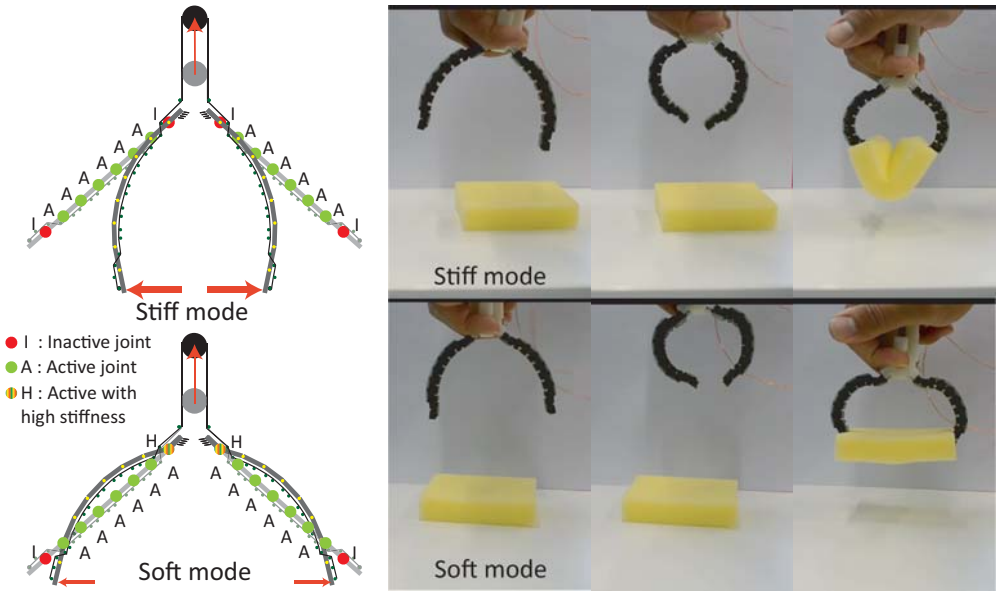

Figure 4.20: Grasp compliance control using the robogami's adjustable stiffness joints. (a) Activation of the first joint considerably increases the lateral compliance of the fingers which is desirable for handling soft and sensitive objects. In grasp with the soft setting, the force that the end-effector can apply is limited. To contrast the behavior of the gripper in soft and stiff modes, the grasp of a soft foam is studied. (b) Initial state. (c) Free motion. (d) Grasp of a foam. With the stiff setting, the gripper can apply large enough forces to deform the foam but with the soft setting the contact force is limited and the end-effector does not deform the foam. Given the higher stiffness of the base joint and its lower actuation moment, the free motion of the gripper in similar in both settings.

back the first joint. This results in limited contact force and hence inherently soft performance as presented in Fig. 4.20d. In the grasp with stiff setting, the end-effector applies large enough forces to deform the foam. However, with the soft grasp setting, the contact force is limited and applying more input displacement causes the contact points to come closer to the base but their distance and hence the applied force to the foam does not change considerably.

In this Section, we presented a robogami with multiple joints and demonstrated soft actuation with compliance control. The prototype highlighted the ease of design and manufacturing of robogamis with multiple joints in confined space. We used fishing wire (Fireline from Berkley-Fishing with 53 kg load limit) as tendon in the current design which simplified the routing of the tendon. The gripper design presented here illustrated the feasibility of driving two robogamis and multiple points of actuation using a single source. This can be used in applications where synchronized motion of multiple points of actuation is required. The motion of the robogami presented in this Section was confined to 2D trajectories. In the next Section, other arrangements of DoFs capable of following 3D trajectories are presented. We also examine the feasibility of driving more points of actuation using a single source in the prototype of the next Section.

4.5 Three-fingered robogami gripper with multiple grasp modes

The robogamis studied so far all had DoF with parallel axis and could cover a desired workspace in a plane. By using other types of robogami joints, presented in Chapter 1, more complex reconfiguration and trajectories can be produced. In this Section, we use different arrangements of these joints in fingers of a robogami gripper. The design allows us to actuate the gripper from completely flat state into different configurations for performing various grasp modes, Fig. 4.21. Note that the 3D motion of the robogamis in this study are utilized for initial reconfiguration and afterwards motions similar to the one studied in the previous Section produces the main actuation. Generalizing the same model for producing 3D trajectories with adjustable compliance in different directions is possible and will be studied in future.

The details of the joint design and their fabrication are presented in Chapter 1. Design parameters for the joints in different directions are chosen so that all joints would have the same stiffness in the initial state, Table 4.3. Fig. 4.22 presents the schematic of the actuation system and the sequence of the DoFs in fingers of the gripper. The input sliding motion drives four tendons using a seesaw and pulley mechanism. The deformation of each joint depends on the stiffness assigned to that joint and all the rest of the joints.

The first two joints in each finger are used for changing the initial configuration of the gripper and the main grasping motion is performed by the last three y axis joints of each finger. The first y axis joint in each fingers has the opposite actuation direction compared to all the rest of the y axis joints. This allows the fingers to start from entirely flat state, Fig. 4.21a, and transform to the cylindrical grasping mode, Fig. 4.21b. For the two side fingers, we added a rotational DoF along the x axis. This allows us to orient these fingers for grasping objects with different shapes in the spherical grasp mode, Fig. 4.21c. For the middle finger we added a DoF along the z axis. Using this DoF, we can move the tip of the middle finger to face one of the side fingers, Fig. 4.21d. This mode of operation is preferred for handling small objects using only two fingers.

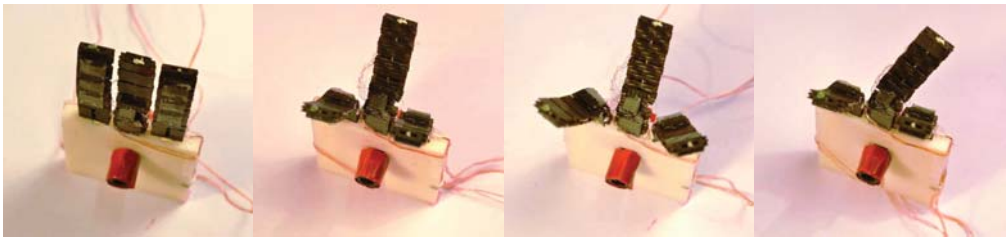

(a) **(b)** **(c)** **(d)**

Figure 4.21: Three-fingered robogami gripper multiple grasp modes. (a) The fingers start from completely flat state. (b) Cylindrical grasp mode: in this mode all of the active joints have parallel axis of rotation. (c) Spherical grasp mode: in this mode we orient the side fingers of the gripper depending on the shape of the object. (d) Two fingers pinching grasp: in this mode we orient the middle finger to face with one of the side fingers for handling small objects.

Table 4.3: Design parameters for the three-fingered robogami gripper.

Parameters	Value (mm)	Description
l	8.8	Tile length
g	1.4	Gap size between the tiles
$w_{ASL-x,y}$	7	ASL width for the x and y joints
w_{ASL-z}	4.4	ASL width for the z joints
w_1	0.6	ASL distance from the z axis
w_t	2.6	Tendon distance from the z axis
l_{ASL}	4	ASL length in the active part
t_{ASL}	1.6	ASL thickness
h	2.4	ASL distance from the x and y axis
b	1.1	Tendon distance from the x and y axis

The joint stiffness and the state of the locked joints depends on the desired motion from each finger. Here, we propose an algorithm to determine the initial configuration of the gripper and the stiffness of active DoFs depending on the contact points on the object and the desired contact forces. The goal here is to establish an approach for effectively using the DoFs of each finger and their adjustable compliance for grasping objects with different sizes and shapes. Depending on the stiffness setting for the joints, the under-actuated gripper has some degree of self adaptability and exact control over the stiffness or positioning of the gripper's base

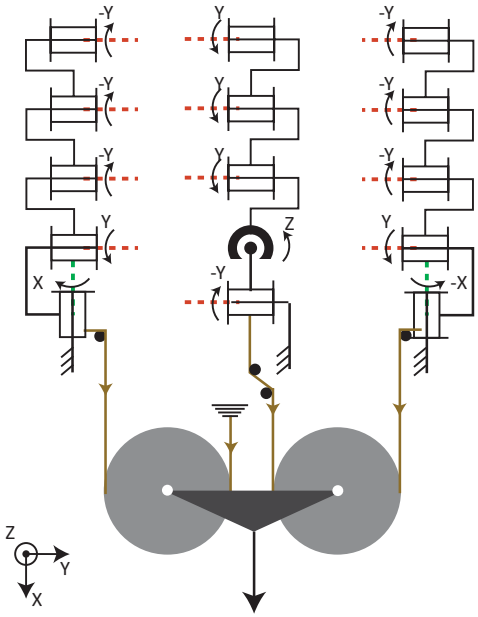

Figure 4.22: Schematic of the actuation mechanism and the DoFs in each finger. The input force is divided through the seesaw mechanism and the pulleys between the three finger. Neglecting the friction, the tendon tension in each finger is equal to a quarter of the input force. The displacement of the tendons in each finger will be dependent on the joint stiffness assignment.

would not be necessary. However, the study of the inverse kinematics and stiffness setting for the joints, through kinetostatic model for each finger, provide a general framework for setting the initial configuration of the gripper and the joint stiffness.

The overview of the grasping algorithm is presented in Fig. 4.23. Here, we consider only one point of contact for each finger. In an iterative process, we find the relative position for the object and the gripper in which we can choose points of contact on the surface that yields feasible configurations for the fingers. To simplify the problem, we considered only positions of the object along a fixed axis, step 1 in Fig. 4.23. The forward kinematics for the position and orientation of the last link of each finger are presented in (4.24) and (4.25).

$$\begin{bmatrix} p \\ 1 \end{bmatrix} = e^{\hat{\xi}_1\theta_1} e^{\hat{\xi}_2\theta_2} e^{\hat{\xi}_3\theta_3} e^{\hat{\xi}_4\theta_4} e^{\hat{\xi}_5\theta_5} \begin{bmatrix} p_0 \\ 1 \end{bmatrix} \tag{4.24}$$

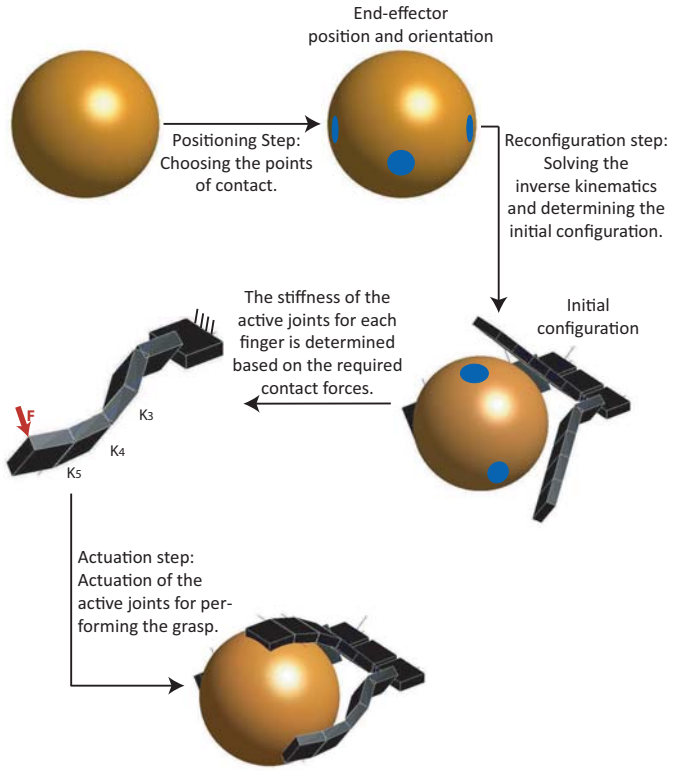

Figure 4.23: Control scheme for determining the initial configuration and the actuation pattern. Based on the shape of the object, the points of contact are chosen and the feasibility of the grasp is confirmed in an iterative process. Based on the position and the orientation of the contact points the inverse kinematics for each finger is solved. Finally, based on the desired contact force and the configuration of the finger the stiffness of each joint is assigned by solving the equilibrium equations for each finger.

$$\begin{bmatrix} n \\ 0 \end{bmatrix} = e^{\hat{\xi}_1\theta_1} e^{\hat{\xi}_2\theta_2} e^{\hat{\xi}_3\theta_3} e^{\hat{\xi}_4\theta_4} e^{\hat{\xi}_5\theta_5} \begin{bmatrix} n_0 \\ 0 \end{bmatrix} \tag{4.25}$$

In (4.24) and (4.25), $\hat{\xi}_i$ is the 4×4 matrix representation of the twist corresponding to the i^{th} joint and θ_i represents the joint angle. $e^{\hat{\xi}_i\theta_i}$ calculates the homogeneous transformation corresponding to the motion of each joint. In (4.24), p_0 and p are the initial and final positions of the contact point on the last phalanx. In (4.25), n_0 and n represents the initial and the final normal to the last phalanx which corresponds to the direction of the force applied to the object. For a given position and orientation, we numerically solve these equations to find the appropriate configuration for each finger. Since there is the possibility of multiple solutions, other optimization goals, such as equal joint angles for all active joints, can be considered to choose the best among the possible solutions.

The first two joints in each finger are utilized for reconfiguration of the gripper from its flat state into one of the initial grasp states presented in Fig. 4.21c. We refer to this step as reconfiguration step. The last three joints in each finger are the active joints that perform the grasping in the actuation step. The input displacement from the tendon is divided between these joints depending on their stiffness settings.

In order to showcase the feasibility of the different grasp modes, we prototyped a manually actuated gripper based on the proposed design. As mentioned, using the model for determining the initial configuration and the joints stiffness requires more detailed studies including motorizing the gripper and incorporating sensors. These remain as topics for the future research. Here, we present few basic grasp modes that utilize different DoFs in each finger. The initial reconfiguration is done based on the shape of the object. For the actuation step, the last three joints in each finger are activated at their maximum compliance. Table 4.4 presents the initial configuration, the free motion and the object grasp in three basic modes: cylindrical grasp, spherical grasp, and two finger grasp.

In this Section, we presented the design of a gripper with robogami fingers and studied a control scheme for assigning the initial reconfiguration and active joints' stiffness for grasping different objects. Applying the proposed control scheme requires further studies. The underactuation of multiple fingers, as presented in the prototype of this Section, allows us to distribute the input energy between few points of actuation. In practice the friction forces complicates the transmission in these systems and further study into designing a more efficient transmission between the input and the actuation tendon of each finger would be necessary.

Table 4.4: Three grasp modes which illustrate the use of joints along the three axis of rotation.

Grasp mode	Initial configuration	Free displacement	Grasping the object
Cylindrical	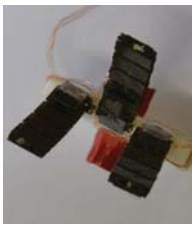		
Spherical	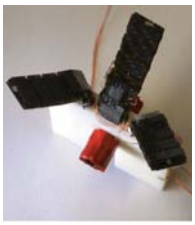		
Pinching	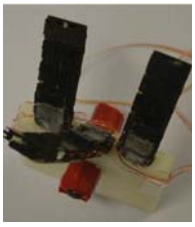		

4.6 Conclusion

In this Chapter, we utilized SMP layers for controlling joint stiffness in under-actuated robots with multiple DoFs. Depending on the stiffness setting, different synergies are activated resulting in different motions and interaction forces. The inherent softness of the actuation method, which originates from the multiple and redundant DoFs, allows safe interaction with the environment without the need for a complex control scheme. The simplicity of the actuation hardware along with the scalable stiffness control method, which is based on material properties, facilitate designing and manufacturing of robots with multiple DoFs in confined space. The adjustable stiffness of the joints in such a robot enables us to change the power transmission to different joints and to control the compliance of the robot depending on the task.

To determine the important design parameters and correct the design flaws, we started by studying the behavior of two under-actuated manipulators with modular design. The interchangeable modules allowed us to consider different sequence of joints and to change the joints in case of failure in the early stage of the research. Using these manipulators, we confirmed the feasibility of configuration and compliance control using elastic modulus variability of SMP. The detailed model developed for these manipulators assists us in designing tendon-driven robogamis for performing different reconfiguration with a desired level of compliance.

After refining the design and verifying the model, we investigated the design scalability and monolithic fabrication of joints in under-actuated robogamis with more complex joint sequences. We used soft grippers as a platform to demonstrate the potentials of the proposed tendon-driven robogami joints with adjustable stiffness. The robogami grippers have similar geometrical features and were tested under similar loading conditions and range of motions expected in a wearable device. The trajectory planning and control problem in these systems, however, are far simpler than the expected ones for a wearable device. Through these prototypes, we refined different functional layers for effective integration in robogami joints of future generation of wearable devices.

We investigated different aspects of the design in two gripper prototypes. The first gripper with two fingers was designed to mainly highlight the self-adaptability of the fingers with redundant DoFs and their compliance control through joint stiffness adjustment. The second prototype was designed to illustrate the feasibility of complex 3D reconfiguration and simultaneous actuation of multiple fingers using one input.

The results of this Chapter enable us to design robogamis for different applications and to control the joint stiffness for performing different tasks. In the the next Chapter, we investigate soft actuation using a tendon-driven robogami as a first step towards developing a soft wearable robot for facial rehabilitation.

5 Robogamis: towards wearable devices for robot-assisted facial rehabilitation

Novel stretchable sensors and soft actuators allow more compact wearable robots that are easier to wear and safer for human interaction. The new manufacturing processes for these sensors and actuators have also contributed to their popularity as they make the design and fabrication of customized actuators and sensors cheap and fast, which allows effective iterations towards design improvements. In this Chapter, we study the applicability of soft actuation and sensing methods that we proposed in the previous Chapters for next generation wearable devices. The proposed technologies are specifically appealing for complex and less explored fields of complex robot-assisted rehabilitation tasks such as facial neuromuscular reeducation. The complexity of motions, the required DoFs, and the geometrical constraints are the main obstacles for implementing the existing technologies in this application. In the next Section, a brief overview of the current actuation and sensing methods used in facial devices are presented. Our main focus is on facial assistive devices for helping with rehabilitation of facial palsy. We implement the actuation and sensing methods suggested in the previous Chapters for preliminary feasibility studies.

5.1 Introduction

The inherent softness, low cost manufacturing of customized robots, versatility of the design, and ease of control (given the self-adaptability of the robot) are among the main advantages of using novel sensing and actuation technologies in field of robot-assisted rehabilitation [7–15, 28, 125–128]. In applications targeting wearable devices for large limbs (arm, legs, fingers) with defined joints and limited DoFs, these novel technologies are in competition with conventional methods of sensing and actuation. Here, we aim for a wearable device for the face, where multitude of DoFs, complexity of motions, safety, and strict requirements on the

The material of this Chapter is from the following self-authored publications:
[124] A. Firouzeh and J. Paik, "Soft actuation and sensing toward a wearable device for robot assisted facial rehabilitation", IROS 2017.

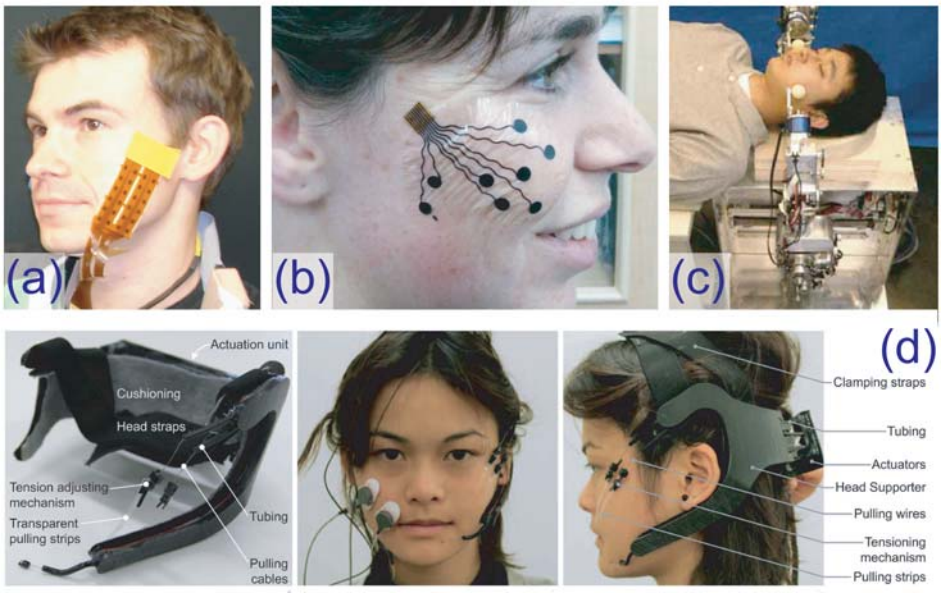

Figure 5.1: Examples of sensory and rehabilitative devices for the face. (a) Arrays of EMG sensors for measuring facial muscle movements for application in silent speech [129].(b) A compliant array of sensing elements for measuring facial muscle movements [130]. (c) A robotic system for massage therapy [131]. (d) A wearable rehabilitative device driven by soft actuation of SMA wires [126].

size and conformity of the robots necessitate the application of novel sensing and actuation methods. Fig. 5.1 presents a few examples of wearable and stationary devices for the face with different functions. Wearable EMG sensors for silent speech and facial gesture recognition, Fig. 5.1 (a,b), are two examples of wearable devices with sensory functions. A wearable device based on SMA actuated robogami can effectively be used for placing electrodes in contact with the face for these applications. The active platform can reconfigure to provide good quality measurements from the sensing elements, embedded as one of robogami's functional layers.

Examples of different sensing methods for measuring facial muscle activities and facial movements are more abundant compared to active robotic devices. Fig. 5.1 (c,d) presents two examples of robots developed for massage therapy and synchronized motion of the paralyzed side of the face in patients with facial palsy, respectively. Facial neuro-motor disorder can be caused by infections, accidents, strokes or tumors. The most common cause for facial paralysis is Bell's palsy which affects 20 people out of 100,000 of the population annually [132]. Physiotherapy is often prescribed as a treatment for facial palsy and studies suggest its effectiveness along with other methods of mime therapy [133]. Often the disability affects one side of the face and the goal in rehabilitation is to restore the motion of the paralyzed side [134]. The compliant sensing and actuation methods introduced in the previous Chapters can be utilized in a wearable device for robot-assisted rehabilitation. Such a robot will provide a desired level of assistance for regaining synchronized and symmetric motion. Also, the repeatability of the robot's motion and the feedback data on the recovery rate make it possible to perform

organized studies on the effectiveness of the treatment which is a subject of ongoing research in the rehabilitation field [126].

Here, we use the model and design framework of stretchable sensors and soft actuation methods, developed in the previous Chapters, in prototyping a preliminary example of a facial rehabilitative device. By studying this prototype and its interaction with the face, we validate the applicability of the enabling technologies for measuring facial movements and applying soft actuation with programmable trajectory and compliance. The proposed soft sensing methods allows us to directly measure the displacement of points of interest on the face, rather than translating muscle activation patterns into the facial movements [28, 126], which is expected to simplify the calibration and data analysis steps. This sensing methods can also provide complimentary data alongside EMG readings. As for the proposed actuation method, a robogami platform with multiple DoFs can theoretically produce more complex trajectories for recreating natural face movements compared to other available methods such as direct actuation with tendons [28, 126].

5.2 Stretchable sensors for wearable devices

Mechanical transparency, large range of motion, customizability, and reliable readings despite the variation in ambient conditions, e.g. temperature, are the main requirements of sensing technology for a wearable device. The method that we use to measure facial movements is based on the electrical resistance variation of a metal path laminated on a polymer sheet. A pattern that is cut through the composite produces a stretchable mesh structure. The large range of motion; up to 40%, mechanical transparency, and thin profile (under 100 μm) of this sensing technology make it a desirable choice for measuring displacement of points of interest on the face. Moreover, the control over sensitivity allows us to use gauges with opposite sensitivities for measuring displacement and to cancel out the electrical resistance variation due to the change in ambient conditions.

A network of soft sensors on the unaffected side of the face can measure the displacement of selected points with a minimal effect on natural motion. The sensor reading is then used to actuate a robogami with multiple points of contact with the face to restore the same motion on the affected side of the face.

Fig. 5.2, presents the design of a stretchable sensor consisting of two gauges with opposite sensitivities, which allows built-in temperature compensation. The differential reading of these two gauges, which is insensitive to temperature variations, is transferred to the terminal of the sensor using a stretchable pattern with no sensitivity to elongation. When stretched, the micro beams that construct the mesh structure in each gauge twist out of plane and bend. This motion requires less energy compared to the in-plane bending deformation since the bending happens around the axis with the minimum moment of inertia. The twist direction of the micro beams determines the sections in tension and compression and hence the resistance change of the sensor. This twist direction for the mesh structure with symmetric metal layer ,

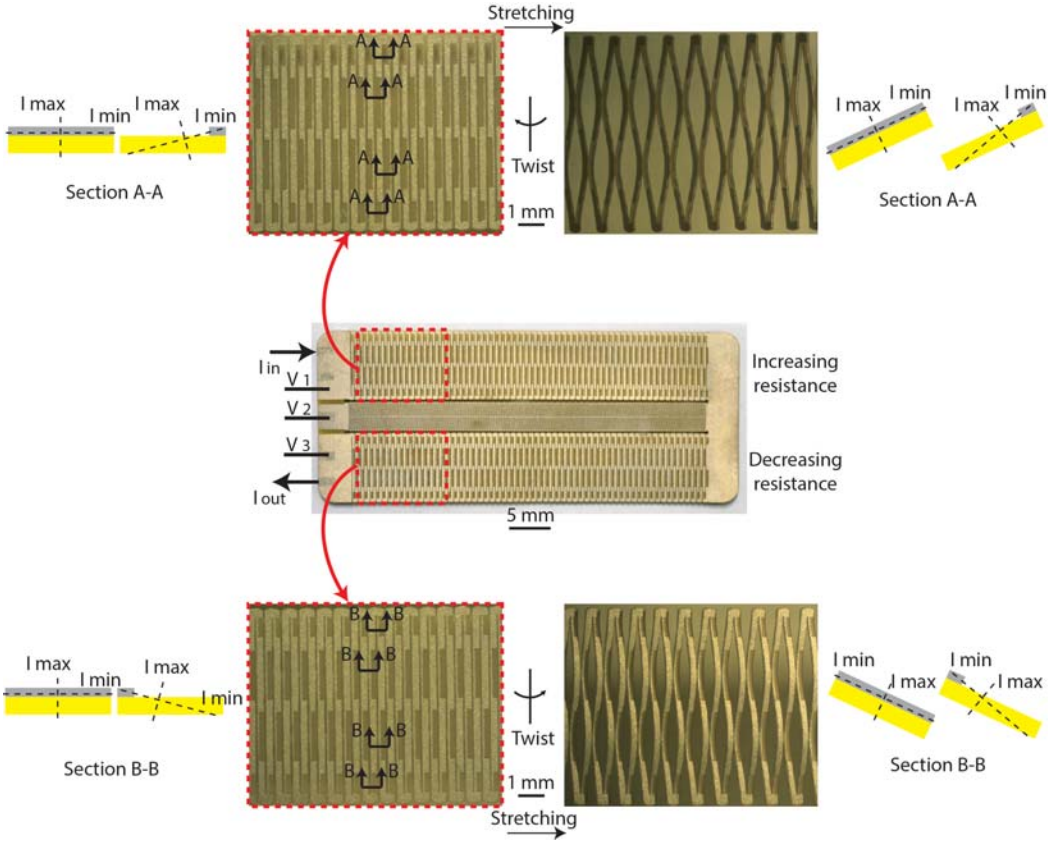

Figure 5.2: Stretchable sensor for measuring facial movements. The sensor has three sections with : positive, negative and no sensitivity to elongation. By controlling the twist direction and modulating the width of the electrical path, we can control the resistance change when the sensor is stretched. In the current design the two sensitive parts have opposite twist directions and sensitivity to stretch. This allows us to compensate resistance change due to temperature variation. The middle section has almost constant resistance under stretch and is used to read the voltage of the intersection of the two gauges.

similar to the middle part, is random. For the parts with asymmetric metal pattern, however, the twist direction is not random and always happens from the flat state towards the axis of minimum inertia as presented in Fig. 5.2. So in the proposed design, the micro beams of the top gauge always twist in the direction that puts the narrow metal section in tension, resulting in positive sensitivity to elongation, and the micro-beams of the bottom gauge twist in the opposite direction, resulting in negative sensitivity to elongation.

The sensing method presented here can be used in a network of sensing elements for wearable devices. The thin profile of the sensors and their high mechanical transparency make them specifically appealing for demanding applications such as measuring facial movements. PCB manufacturing methods can be adopted for cheap and low cost fabrication of the proposed stretchable sensors. Highly adaptable design, thin profile, and mechanical transparency are

among the main advantages of this sensing solution. In the next Section, we illustrate the feasibility of using a single sensor, similar to the one presented in Fig. 5.2, for measuring the relative displacement of two points on the face.

5.3 SMA actuated robogami platform for soft actuation in a wearable device for face

The first conceptual design for a wearable rehabilitative device was based on a robogami platform with SMA actuated joints. The prototype presented in Fig. 5.3 was manufactured to study the feasibility of the design. This robogami with independent soft actuation of the joints is ideal for conforming to the shape of a complex surface. However, it has significant drawbacks for application in rehabilitative devices.

The main issue we encountered in the prototype of the conceptual design was the complexity of the actuation of the joints. In a device with multiple joints in series, we require synchronized motion of certain joints for performing a desired reconfiguration. Given the slow response time of SMA actuators, performing such a task would require a complex control scheme and sensory data. Even with a controller to produce the desired trajectory, the contact forces that an SMA actuated robogami can provide are rather limited. The multitude of DoFs in the present design comes at the price of smaller actuation torque available at each joint, which reduces the load capacity of the robogami. These limitations make SMA actuated robogamis ill-suited for the main actuation in a rehabilitative device. However, this platform with added ASL layers is well suited for conforming to the shape of complex surfaces and can be used effectively for performing the initial reconfiguration of the device. It can also be used as a platform for placing elements such as EMG sensors and electro-stimulation electrodes in contact with desired points on the face.

(a) (b)

Figure 5.3: SMA actuated wearable robogami. (a) The conceptual design of a SMA actuated wearable device based on a robogami platform. (b) The prototype of a SMA actuated robogami. The prototype was manufactured to study the feasibility of the initial conceptual design with SMA actuated joints.

Given the need for synchronized actuation of multiple joints rather than independent actuation of every single joint in a rehabilitative device, the under-actuated robogami platform is a more viable solution, providing a higher load capacity. In the next Section, we study tendon-driven robogamis for soft actuation with programmable trajectory and compliance.

5.4 Tendon-driven robogami platform for programmable soft actuation in rehabilitative devices

Tendon-driven systems are desirable for applications with demanding geometrical constraints where smart materials cannot meet the actuation requirements, i.e. band width, range of motion, and load capacity. We propose an under-actuated robogami platform for soft actuation applicable to rehabilitative devices. In this approach, we use a single input to drive multiple DoFs and points of actuation to achieve synchronized motions. Under-actuated robogamis can generate complex trajectories with adjustable compliance in different directions.

Fig. 5.4 presents an early conceptual design for the robogami with 3 points of actuation. The joints with adjustable stiffness allow us to distribute the input energy from a single source between the different fingers and the joints in each finger in order to produce desired trajectories for the multiple points of actuation on the face. Based on the desired motion, a sequence of joints for producing a 3D trajectory can be designed. The joint stiffness control also allows us to control the compliance of the end-effector of each finger along different directions. This soft actuation method with compliance control can be utilized in rehabilitation where

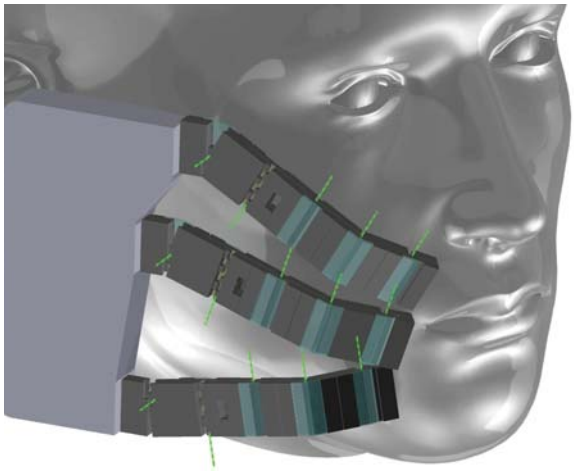

Figure 5.4: The conceptual design of an under-actuated robogami for facial rehabilitation. The power distribution between the joints, hence the reconfiguration of the fingers, is determined by the stiffness assigned to each joint. The initial reconfiguration of the fingers is performed using the first joint for rotation along the normal direction to the plane of robogami and the fourth joint for coming into contact with the face. After the initial reconfiguration, these joints are locked in place and the other joints are activated for applying displacements with a desired level of compliance.

synchronized motion of multiple points of actuation and many joints are required for training certain muscle groups. The multiple DoFs of Robogamis allow for initial reconfiguration and activation of different actuation patterns for adapting to the needs of each patient and the requirements of the specific training. In this Section, we study the motion of a single sequence of joints which is presented in Fig. 5.5. This is a simple robogami with only five joints. We use this design to demonstrate the initial reconfiguration and soft actuation with adjustable compliance.

5.4.1 Compliant actuation using tendon-driven robogami

Tendon-driven robogamis with their redundant DoFs and adjustable stiffness provide soft actuation with programmable trajectory and compliance. This makes robogamis an attractive platform to develop a low profile wearable device for robot-assisted rehabilitation in which the compliance level and the trajectory of the actuation points are adjusted according to the training and the severity of the patient's condition.

In this Section, we study the compliance control of the end-effector of a simple robogami with 5 joints, presented in Fig. 5.5a. We use the first joint of this robot to adjust the main direction of actuation. Using the other DoFs, we apply force and displacement along the main direction of actuation and control the compliance in the lateral direction. The schematic of Fig. 5.5b presents the tendon routing, the joint axis position, and the ASLs. Upon activation, the opposing direction of actuation for the second joint results in significant increase in the lateral compliance of the end-effector. In this Section, we model and simulate the motion of the last four joints of the robogami and illustrate the compliance control of the end-effector in the lateral direction. We also verify the simulation results in experiment and demonstrate the soft actuation with high lateral compliance and self-adaptability.

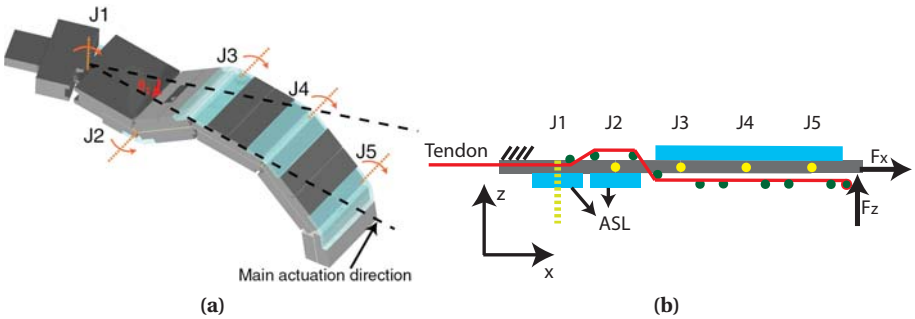

Figure 5.5: Under-actuated robogami with programmable trajectory and compliance. (a) The first joint allows us to orient the remaining links along the desired direction and the rest of the joints are activated at the proper temperature so that the end-effector follows a desired trajectory. (b) The schematic of the robogami illustrating the tendon routing. The opposing direction of motion and actuation for second joint enables us to significantly change the lateral compliance of the end-effector.

Table 5.1: Design parameters for the robogami for soft facial actuation.

Parameters	Value	Description
l_1	8.2 mm	J_1 and J_2 distance
l_{2-4}	15.6 mm	J_i and J_{i+1} distance
l_5	12.8 mm	Contact and J_5 distance
k_{ASL}	$108.0-2.6\ N/mm$	ASL stiffness [74]
h_1	$-3.25\ mm$	ASL distance from the axis J_2
h_{3-5}	3.25 mm	ASL distance from the axis $J3-5$
b_2	$-2.5\ mm$	Tendon moment arm J_2
b_{3-5}	3.5 mm	Tendon moment arm J_{3-5}

Model and simulation

The trajectory of the end-effector in the tendon-driven robogami and the compliance of the robot are determined by the joints' stiffness. Here, we study the 2D motion of the end-effector of the robogami of Fig. 5.5 resulting from the actuation of J2-J5. The design parameters for the robogami are presented in Table 5.1. The contact forces at the end-effector depends on the tendon tension, the configuration of the robogami, and the stiffness setting of the joints. To determine the stable configuration and the contact forces of the robogami at a given joints

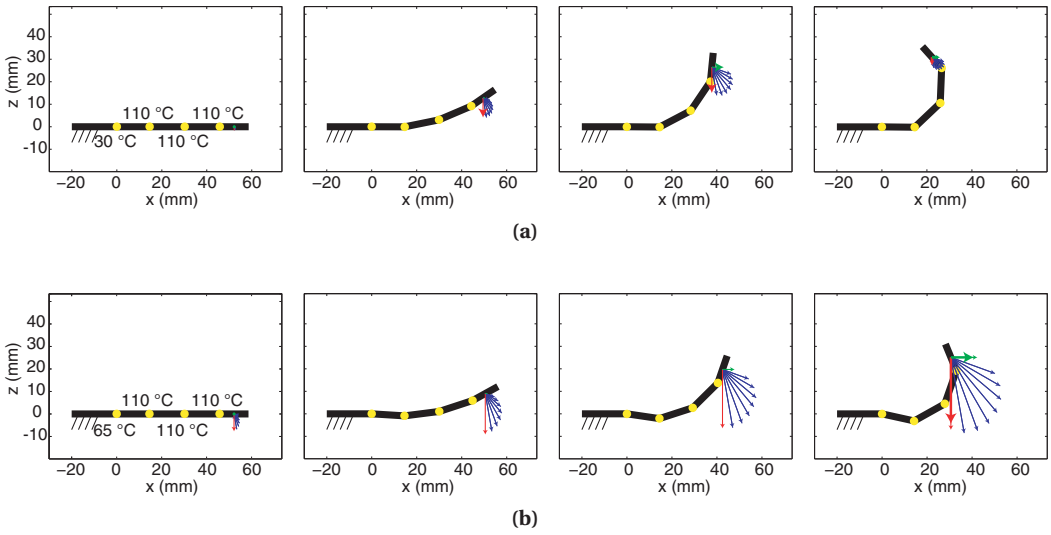

Figure 5.6: Compliance of the end-effector along different directions. The vectors represent the projection of the end-effector's displacement along the direction of the force. For each direction, 1.5 N was applied at the end-effector. As expected the compliance is dependent on the configuration of the finger. For each stiffness setting, the compliance is reported in four configurations. (a) In the first case, the robogami has small compliance in different directions. (b) Activating J2 increases the compliance significantly. The present design has a larger compliance in the lateral direction, the design is based on the requirement for the rehabilitative device. The thicker arrows in the last plot represent the experimental results for comparison.

stiffness setting and tendon tension, we used the same model and equations presented in Chapter 4.

Fig. 5.6 presents the stable configuration of the robogami at different tendon displacements. The arrows at the end-effector represent its displacement along the direction of 1.5 N contact force which provide a measure of the compliance in different directions. In the first case, Fig. 5.6a, J2 is at room temperature and the stiffness of J3-J5 are set to the lowest, 110 ^oC. In the second case, Fig. 5.6b, the second joint is also activated but with a higher stiffness, 65 ^oC. The higher stiffness setting for J2 along with the smaller moment arm of the tendon from the axis of rotation results in similar configurations in free displacement in both cases. The compliance of the end-effector in the two cases, however, are significantly different. Activation of J2 makes the robogami considerably softer in the lateral direction. Note that in the first case, the joints reach their limit, 45^o, at higher tendon displacement which reduces the compliance of the robogami.

Fig. 5.7 presents the compliance along the two main directions of interest, the main actuation direction and the lateral direction. Note that the sudden changes in the slope of the plots in Fig. 5.7 is caused by the joints reaching their limits. For a device similar to Fig. 5.4, we would like to have low compliance in the actuation direction. In this direction, the contact force is determined mainly by the tendon tension. Some degree of compliance in the lateral direction is required, however, so that the robot can self-adjust the lateral position of the contact point. The proposed design, allows us to control the lateral compliance without affecting considerably the compliance of the robot in the main actuation direction as presented in Fig. 5.7. The free motion trajectory of the end-effector in both cases are similar. The self-

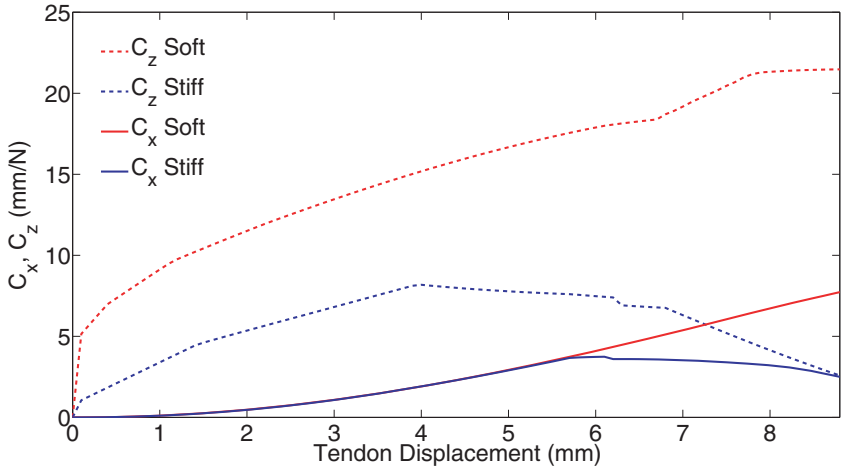

Figure 5.7: Comparison of the compliance in different directions at different stiffness settings. The compliance of the end-effector in the main direction of actuation, x, is comparable in both cases but the lateral compliance, along z, is significantly higher in the second case. The low compliance along x direction is desirable since it allows us to apply large forces in this direction. The high compliance in z direction allows the end-effector to auto-adjust its position.

adjustment of the end-effector in the lateral direction, however, is more significant in the second case. The proper compliance of the robogami depends on the required contact forces, the mechanical properties of the object in contact, and the configuration of the robot. Once the desired compliance is determined, the model presented here is used to assign the joints' stiffness.

Experimental verification

To verify the simulation results, we tested the compliance along the main actuation direction and the lateral direction. We used 160 g mass to apply the load. Fig. 5.8a-5.8d presents the free motion of the robogami and its configuration under load. We tested the robogami with the same stiffness settings as the ones used in Fig. 5.6. As predicted in the simulation, the free motion trajectory of the end-effector in both cases are similar. In the first case, the configuration change under load is rather small, around 2 mm in each direction. The trend

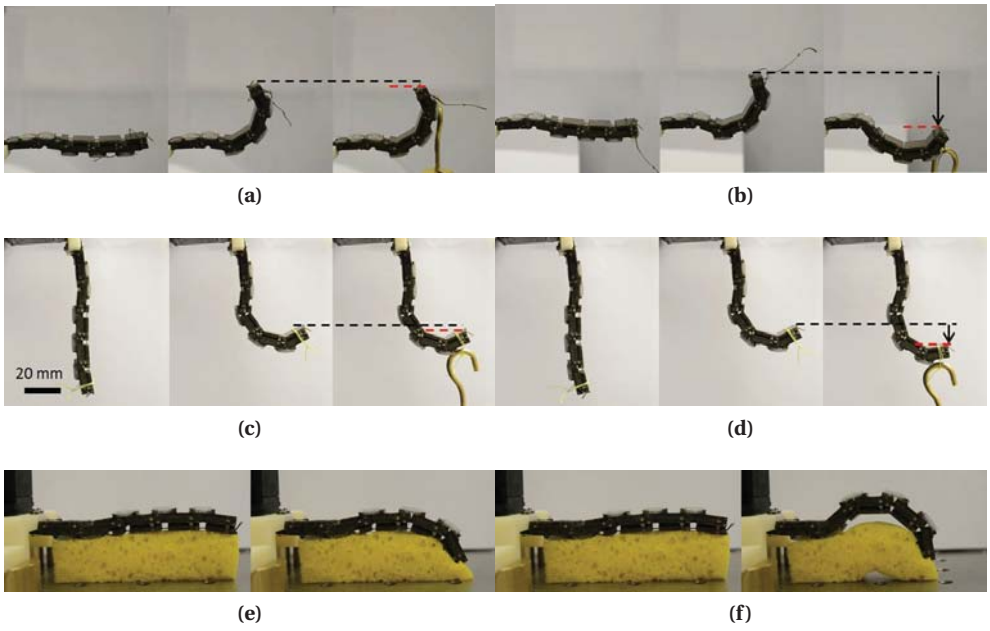

Figure 5.8: Compliance control in the tendon-driven robogami. To verify the simulation results, we compared the configuration of the robogami at different stiffness settings and loading conditions. We considered loading along the main direction of actuation and the lateral direction. (a,c) In the stiff mode, the end-effector has low compliance in both directions. (b) In the soft mode, the end-effector is significantly more compliant in the lateral direction. (d) The compliance along the direction of the finger also increases but not to the same extent as the lateral compliance. (e) In the stiff mode, the robogami has low self-adjustment capability. This limits the motion of the robot in the presence of constraints. (f) Increasing the lateral compliance of the robogami, by activating J2, allows the end-effector to auto adjust its lateral position and increases the range of motion in the presence of the constraint.

of the compliance change in the second case, where J2 is activated, is also similar to the simulation prediction. The lateral compliance increases significantly and the end-effector moves 29 mm in the direction of the force, compared to 32 mm from simulation. In the direction of actuation, the compliance is much lower and under load, the end-effector moves 10 mm in the direction of force, compared to 11 mm from simulation.

To highlight the importance of the lateral compliance and self-adjustment, we tested the robogami in contact with a soft object, a piece of foam. The objective here is to move the foam along the main actuation direction. The first case in Fig. 5.8e, presents the actuation result when only the last three joints are active, low compliance mode. The lateral constraint prevents the large displacement in this mode. As discussed before, activating J2 at 65 ^oC does not change the free motion trajectory of the finger but it makes the robogami significantly more compliant in the lateral direction. In this mode, Fig. 5.6b, the end-effector auto adjusts its lateral position and the robogami can apply larger displacement. Note that if the compliance is increased too much, the robogami would move along the foam without applying any contact force or displacement to the foam. The proper compliance setting depends on the mechanical properties of the object in contact and the required contact forces.

Tendon-driven robogamis provide soft actuation with programmable trajectory and compliance. In Section 5.5, we study the feasibility of using this early prototype for applying force in a desired direction. The self-adjustment of the end-effector in this actuation method, simplifies the control problem and the hardware required for the actuation.

5.5 Soft sensing and actuation for facial rehabilitation

In this Section, we present the result of some preliminary tests to illustrate the applicability of the actuation and sensing methods in facial assistive devices. Fig. 5.9a presents the initial reconfiguration of a simple robogami for orienting the main actuation along a desired direction. Fig. 5.9b presents soft actuation of the face along this direction. In this experiment, the fist joint is locked in place and the other four joints are activated with the same setting as the one

(a) **(b)**

Figure 5.9: Preliminary experiments using a single robogami finger. (a) Performing the initial reconfiguration. (b) Soft actuation on the face.

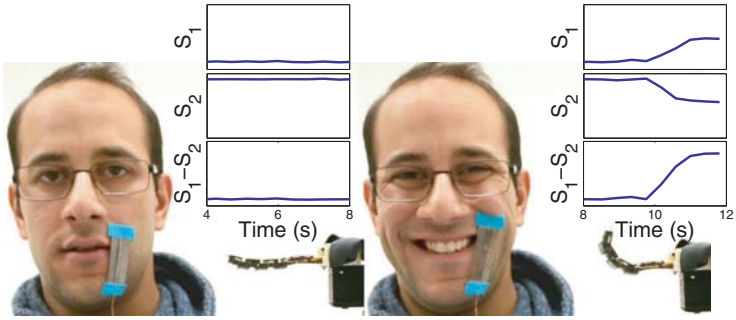

Figure 5.10: Coupling of the soft stretchable sensor and the robogami actuation. The sensor measures the displacement of the point of interest on the face and the robogami finger is actuated accordingly. The readings from the two stretchable sensors and the subtracted value are also presented in the figure.

used in Fig. 5.8f. Multiple points of actuation with a more complex sequence of joints, capable of following 3D trajectories and compliance setting in other directions, will be studied in the future for recreating natural motions of the face.

To demonstrate the mechanical transparency and the feasibility of measuring the facial movements, we placed a sensor to detect and measure the displacement of a point of interest for the smiling motion. We used the sensor reading to drive the robogami as presented in Fig. 5.10. In the future, a network of similar sensors could be used to detect the motion on the healthy side of the face and drive the rehabilitative device on the paralyzed side.

5.6 Conclusion

The emerging soft actuation and sensing methods are transforming the hardware used in robot-assisted rehabilitation from stationary and bulky systems to wearable and portable robots. The inherent safety, ease of control, and customizability of the novel methods of actuation can be used in less studied and complex tasks such as rehabilitation of the face. In this Chapter, we presented soft actuation and sensing methods with low profile and adaptable design that meet the requirements of wearable assistive devices. For the actuation, we considered two methods: robogami with SMA bending actuators, and tendon-driven robogami with thermally controlled adjustable stiffness joints. The SMA actuated robogami is capable of complex shape transformations by independent actuation of each joint in the robogami. In applications where synchronized motion of many joints is required, methods of simultaneous under-actuation of series of joints using a single energy source can provide larger load capacity and also facilitate the control problem. This motivated the study on the second actuation method that is based on tendon-driven robogamis with trajectory and compliance control. The central actuation, powered by an electric motor, provides significant loading capacity with fast response that makes this platform a more suitable option for a rehabilitative robot. The compliance of the end-effector in this method of actuation can be controlled along different directions. So a tendon-driven robogami with proper design and stiffness assignment can be used for applying

force and displacement along a trajectory, the main actuation trajectory, while maintaining a desired level of compliance in other directions. Multiple points of actuation in robogamis can be driven using a single source to achieve a synchronized motion. The inherent softness, the ease of actuation, and the low profile of the tendon-driven robogamis make this family of soft robots an attractive choice for light-weight wearable assistive devices with multiple DoFs.

To measure the movements of the face we used metal mesh stretchable sensors. The accuracy, thin profile, high mechanical transparency, and controllable sensitivity make metal mesh sensors ideal for designing a network of sensing elements for measuring facial movements. By coupling gauges with positive and negative sensitivity, we can cancel out the effect of ambient conditions on the sensor reading for more accurate estimation of the motion. We briefly studied the applicability of the sensing methods by measuring the relative displacement of two points on the face when smiling and demonstrated the feasibility of using the soft actuation method for applying large enough forces to make comparable motions.

In this chapter, we validated the model and design criteria for stretchable sensors and tendon-driven robogamis by prototyping an early example of wearable components for measuring facial movements and applying soft actuation with programmable trajectory and compliance. The next steps of the research include the study of the motion of the face to design the required trajectories for rehabilitation and characterizing the mechanical properties of the facial muscles to estimate the required forces. Using these and the proposed model and design frameworks for different components, a robogami platform with the proper number of actuation points and joint sequences will be designed to reproduce the desired trajectories and contact forces.

6 Concluding remarks and future direction of research

This PhD thesis is a collection of efforts in addressing crucial and essential functional components of wearable and interactive robotic technologies. The importance of this thesis lies in creating this collective work toward a comprehensive robotic solution. Many emerging robotic fields rely on new manufacturing, actuation, and sensing methods to achieve levels of safe and effective interaction with sensitive environments that was previously inaccessible. These novel methods require careful examination of the fundamental technologies to best define their potentials, drawbacks, and design criteria. However, making such effort is arduous and is often overlooked due to the lack of global understanding of the challenges facing the design, fabrication and control of multi-DoF systems. It was my goal to build a groundwork for the enabling technologies; the presented work categorizes the state-of-the-art solutions of diverse "soft" technologies while pushing the limits of the existing solutions by introducing their immediate applications on a wearable robot platform, robogamis. In my concluding remarks, I present a summary of the scientific and practical achievements of this thesis and provide guidelines for their effective future applications.

6.1 Concluding remarks

The novel layer-by-layer manufacturing of robogamis allows precise positioning of multiple DoFs in thin robotic sheets applicable to a few hundred microns to a few millimeters-sized robots. This scalable and adaptable design and manufacturing results in cheap and fast fabrication of customized robots. The inherent compliance of the robogami, originating from its multitude of DoFs driven by soft actuators, make it a desirable platform for design and development of wearable devices. The prevailing application of robogamis was in the field of meso-scale mobile robots where cheap and easy manufacturing was utilized for fast and effective iterations on robot designs. Applying this framework to the field of wearable robots required modifications of the joint design and actuation principles to provide the required loading capacity as well as development of sensing solutions to meet the particular requirements of a robot interacting with a human. For loading requirements, based on reported values for wearable devices, Newton range loads with moment arm in the ten centimeter range

was considered. The design parameters can of course be adjusted to specific applications but the range of forces and moments provide the general design guidelines for the joint structure and actuation principle.

The first design concept we developed for wearable robogami was based on previous research on SMA actuated robogami joints. The loading capacity of these joints is directly determined by the bending moment of the actuators, embedded in each joint. For SMA actuators with a centimeter width scale, the output moment was characterized to 15 mNm range. This is an order of magnitude smaller than the desired loading capacity, in the farthest joint from the force application point. The active joints, however, are not necessarily the farthest from the force application point. This motivated research towards developing a locking mechanism to increase the loading capacity of joints after performing the initial transformation. This effort led to the design of robogami joints with controllable compliance based on the adjustable stiffness of SMP layers embedded in the structure. We confirmed in experiments up to 240 mNm load capacity, 3 N at 80 mm distance from the joint, for robogami joints with adjustable stiffness, 14 mm in width, in their locked state. This loading capacity is compatible with the design goals.

SMA actuators provide independent actuation of joints in robogamis. In many applications including potential rehabilitative devices synchronized actuation of multiple joints is required. Independent actuation of joints in such a case would be unnecessary and result in a limited load capacity and control complexity. According to this an alternative actuation method of tendon-driven robogamis with adjustable stiffness joints was proposed in this thesis. In this platform, all joints are actuated via a single source of actuation. The energy distribution between DoFs is controlled by adjusting their stiffness. The ASL design was modified in a few steps to reach the final design providing more than 40 times stiffness variation in repeated loading cycles, 108.0 N/mm at room temperature to 2.6 N/mm at 110 ^oC for a sample size ($w \times l \times t_{total}$, t_{SMP}): $7 \times 4 \times 1.6,\ 0.5$. In the final design, the electrical resistance variation of the embedded heater in the SMP was utilized as feedback to control the temperature, hence the stiffness of the ASL.

To control the configuration of robogamis it is necessary to embed joint angle sensors in the tiles. The requirements on the size and range of motion, along with the demanding working conditions of robogamis (the significant temperature variation) compelled us to design and develop customized sensors for robogami joints. Sensors based on two physical principles, piezo-resistivity of carbon polymer composites and metal film resistance variation under strain, were developed and embedded in robogami joints. Carbon-based sensors provide fast and cheap manufacturing but their accuracy and repeatability of measurements are not as good as metal based sensors, which were characterized with an error band of $\pm 2.4^o$ containing data from 25 loading cycles with different amplitudes (with the maximum of $\pm 50^o$). Based on the same physical principles, I developed stretchable sensors for measuring body movements in wearable devices. In the proposed stretchable sensors, a mesh structure transforms the linear displacement of the sensor into the bending of micro-beams. The proposed design

for the metal based stretchable sensors allows for sensitivity adjustment. Using this feature, networks of sensing elements with integrated temperature compensation can be designed. The repeatable response, with a standard deviation of 2% in 80 loading cycles of different amplitudes, and high mechanical transparency guarantees accurate measurements with minimum effect on the natural body movements for a wearable device.

A manipulator with three joints and a single source of actuation was designed and manufactured to study the energy distribution in under-actuated robogamis. Joint stiffness was adjusted to control the configuration of the manipulator in the synchronized actuation of joints. The accuracy of the model and joint position sensors was confirmed with an average RMS error of 4.6^o and 1.8^o, receptively, for measurement points in 30 experiments at different stiffness settings. In a wearable device with multiple joints and points of actuation, the model will be used for assigning proper joint stiffness to reach a desired configuration and sensor readings will allow fine tuning of temperature assignment and tendon displacement. Multi-fingered robogami grippers were then used as platforms to further study reconfiguration of robogamis with multiple points of actuation. The robogami grippers have similar geometrical features and were tested under similar loading conditions and range of motions expected for a wearable device, but trajectory planning and control problems in these systems are far simpler than those expected for human interaction. Through these prototypes, the designs of the different functional layers were refined for effective integration into robogami joints.

As an early feasibility study of the proposed technologies for wearable devices, a stretchable sensor with two parallel gauges with opposite sensitivity, for temperature compensation, was designed and fabricated for measuring the distance between two points of interest on the face. The measurements were used to assign tendon displacement in a robogami with adjustable trajectory and compliance. The stretchable sensor can be used to measure facial movements with minimal effect on the natural motion. The trajectory of the robogami, which consists of a series of five joints, can be controlled by initial reconfiguration and activation of a select group of joints. Moreover, in tendon-driven robogamis with multiple and redundant DoFs, the compliance of the robot in different directions can be adjusted by the stiffness assigned to the joints. By changing the compliance, a desired degree of self-adjustment in different directions can be assigned to the robot. The robogami with a proper lateral compliance, self-adjustment, produces enough force and deformation to move the face along a desired trajectory while accommodating for lateral movements.

In this thesis, I focused on developing the enabling technologies required for a low profile wearable robogami for robot-assisted rehabilitation. For each component, I studied the general requirements and chose the proper physical principle accordingly. Then the behavior of the component was characterized and modeled. Based on the performance of the components and the requirements of the task, a design methodology for each component was developed and in the case of tendon-driven actuation, a control scheme was proposed according to the developed actuation model. The knowledge produced and the design framework for the components were used to develop different robogami devices. These design principles are

transferable to other design platforms for human-robot interaction as well as other fields requiring soft methods of actuation and sensing.

6.2 Future directions of research

In this thesis, I focused on developing enabling technologies, integrating them into functioning robogami joints, and utilizing the joints in robots for different applications. The future steps in this research can be divided in similar categories: component, integration, and application levels. In what follows, I briefly mention the ongoing and envisioned research in each of these areas.

Component level

One of the main advantages of using polymers for adjusting mechanical properties is the possibility of fine tuning material properties [135]. Currently, one of the challenges in fine stiffness control is the sharp variation in mechanical properties of the SMP around its glass transition temperature. An influential future step in component level research would be to collaborate with material scientists to engineer SMPs with more gradual transitions.

Another important future step at this level is a more detailed characterization of the proposed technologies which would help in their translation to other applications. One interesting example would be use of soft elements with adjustable mechanical properties in bio-inspired robots [136, 137], which requires a detailed characterization of materials' dynamic behavior and visco-elastic effects. Elements with adjustable mechanical properties would allow bio-mechanic researchers to study the effect of different segments' compliance on the behavior of robots and to control the stiffness of segments for achieving optimum response.

One of the limiting factors in activation of SMP and SMA layers in robogamis is the significant temperature gradient that diminishes the performance of these functional layers. Ongoing research effort in the lab is focusing on utilizing conductive carbon-polymer composites as stretchable heaters that would reduce production time and cost and provide a more uniform temperature distribution.

Integration level

One of the features of the layer-by-layer manufacturing of robogamis is the potential to embed additional functional layers in the robot's structure. This can be challenging due to the size requirement and the demanding working conditions of robogamis, e.g strain level and temperature variations. In what follows we mention the ongoing and future steps in integrating additional functions in robogami joints.

The piezo-resistivity of carbon-silicone compound can be utilized for manufacturing pressure

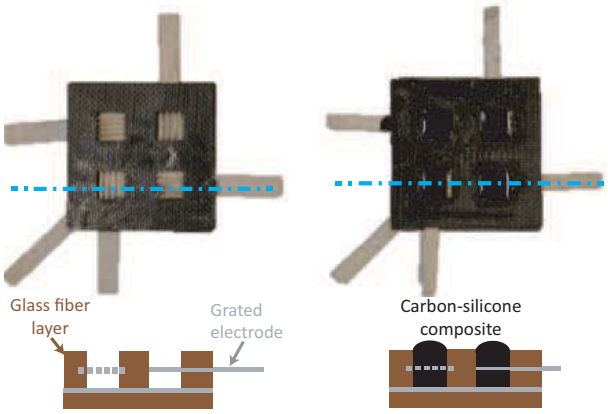

Figure 6.1: Conductive silicone pressure sensors. (a) The base for the sensor is fabricated by laminating conductive fabric and glass-fiber layers. (b) The grated electrode allows casting of conductive silicone between the fabric layers.

and force sensors as presented in Fig. 6.1. Durability, ease of manufacturing networks of sensing elements, and high sensitivity to strain are among the main advantages of these sensors that can provide important information on the tiles in contact with the environment and the magnitude of forces. Effective integration of these sensors and their required connections in each tile is a subject for the further studies.

One of the main challenges of increasing the number of DoFs in robogamis is the required connections to each joint for activation of ASLs and gathering sensory data. Integrating a low level controller as one of the functional layers in the tile area can simplify the communication and the required connections for power and signal transmission significantly. Designing robogami modules with integrated control circuit is a necessary step towards the effective application of this platform in demanding applications such as rehabilitation. This would require design and implementation of small circuits to replace the current bulky hardware including: digital multi-meters, data acquisition cards, and amplifying circuits.

Applications level

The most immediate future step of this project would be the design and manufacture of a motorized robotic hand with multiple fingers for adjustable grasp and interaction modes. Fig. 6.2 presents early result of an ongoing project towards such a motorized robogami gripper. Adaptable robotic grippers are a subject of interest in the soft robotics community and is one of the first applications of these robots entering the market. We believe that addition of compliance control would make a significant impact on their range of possible applications.

The compact design of the under-actuated robogamis with adjustable compliance is attractive

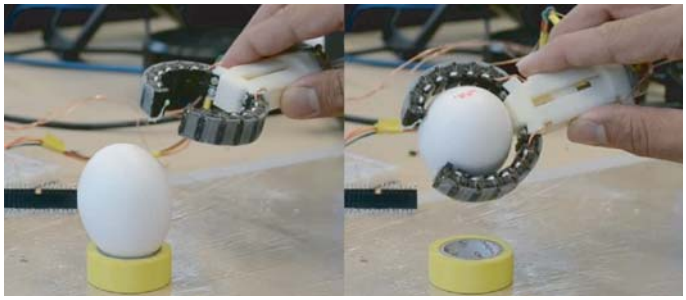

Figure 6.2: Example of a motorized robogami gripper.

for applications where multiple DoFs in a confined space is required. One such application is in minimally invasive surgery. Based on the results of this thesis, a conceptual design of a retractor for minimally invasive surgery was developed, Fig. 6.3. The multiple DoFs and conformity of the tool in soft state allows the surgeon to safely insert the tool and envelope organ of interest for relocation. Next, the retractor stem is transformed to stiff mode for keeping the organ in the desired position while the tip of the tool can be active for providing additional functions and hence decreasing the required number of entry ports.

Rehabilitative wearable devices as the main motivation for this thesis and the most demanding application for the proposed technologies would also be pursued. Rehabilitation of limbs with fewer DoFs and more defined joints and motions, such as fingers, would be a good starting point. An attractive approach would be integrating the proposed technologies into the existing devices [12, 127, 128] to demonstrate their potential and to refine their design. The next step would be to manufacture fully integrated wearable devices based on the robogami platform for more intricate tasks such as robot-assisted facial rehabilitation.

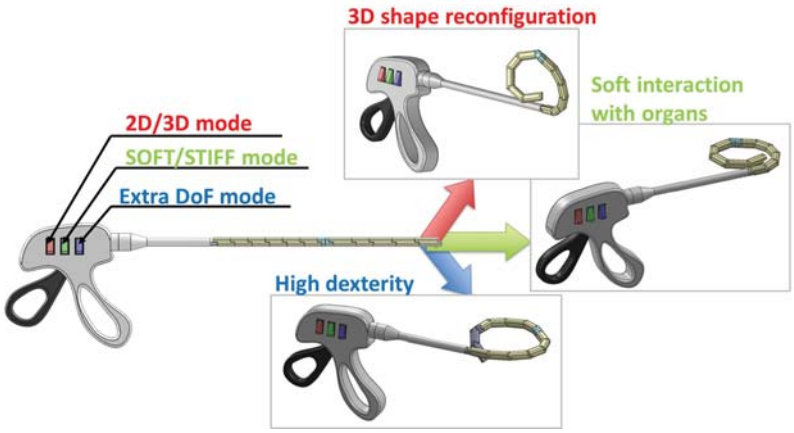

Figure 6.3: Conceptual design of a surgical tool based on robogami platform with adjustable compliance (design by Dr. Marco Salerno for research collaboration with an industrial partner).

A SMA actuated robogami crawler

In this Appendix, we present the design and locomotion of a crawler robot that uses SMA actuated robogami joints. Embedded curvature sensors are used to control the position of the joints for performing the desired stepping motion. This robot is used as a platform to study and to improve the design of different layers: actuators, heaters, sensors, and controller. We studied different versions of the crawler with conductive silicone sensors, carbon ink sensors, and metal curvature sensors. Also the design of the heater was improved from the first prototype that used heaters embedded inside the tiles to later versions that used stretchable heaters in contact with the active part of the actuators. The controller circuit was also modified in different versions to be compatible with the sensors and actuators. Here, we present the motion of a version using carbon ink sensors and stretchable heaters.

A.1 Crawler design and stepping sequence

Intelligent robotic systems that can react to un-programmed tasks and unforeseen environmental changes require augmented softness. Low-profile robogamis address intrinsic (material-wise) and extrinsic (mechanism-wise) softness with their multi DoF body driven by soft actuators. The unique hardware of the robogami and its sub-millimeter thick construction enable diverse transformations as those achievable by the paper Origami. Fig. A.1 shows the first fully integrated version that has all the essential components including its controller within a thin sheet. Construction of this robot is possible via precise, repeatable, and low cost planar fabrication methods often reserved for micro scale fabrications. In this research, we aim at expanding the capabilities of robogamis by embedding bi-directional actuation, sensing, and control circuit. To assess the performance of the proposed sensors and actuators, we report on the performance of these components in a four-legged Crawler robot presented

The material of this Chapter is from the following self-authored publications:
[30] **A. Firouzeh** and J. Paik "Robogami: A fully integrated low-profile robotic origami", ASME Mechanisms and Robotics 2015.

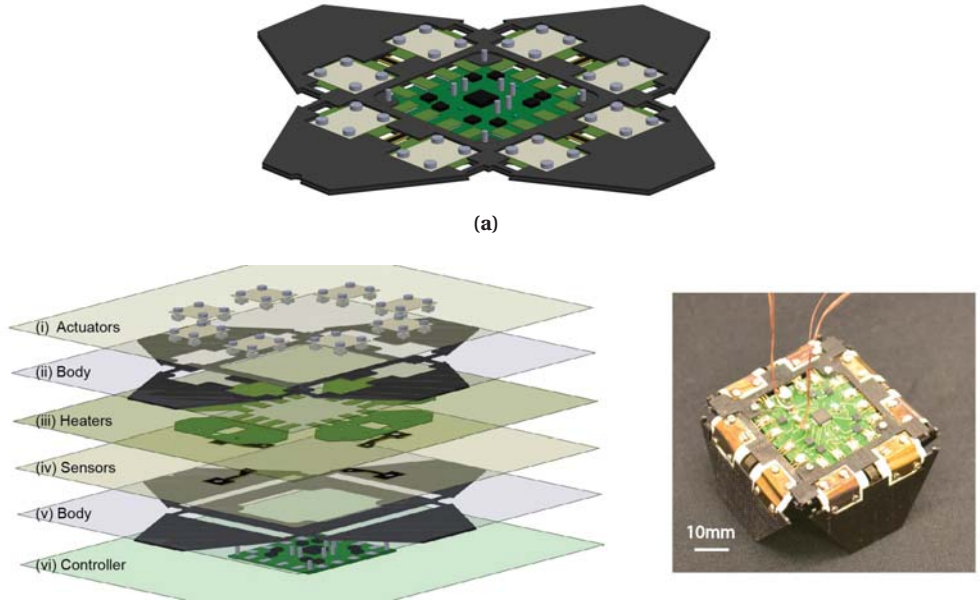

Figure A.1: SMA actuated robogami Crawler. (a) Schematic of assembled robot. (b) Exploded view of the functional layers. Actuators are in layer (i), (ii) and (v) are glass fiber layers that make the body. Layer (iii) contains the heaters and layer (iv) contains the sensors. Layer (vi) is the controller circuit. (c) The final prototype.

in Fig. A.1.

Fig. A.2 presents the stepping sequence of the robogami crawler. There are four phases in the Crawler locomotion as presented in Table A.1. The angles in this table are those between the legs and the center tile. Bold entries in the table indicate legs that bear the weight of the robot in each phase while the other two legs have no contact with the surface and can move without

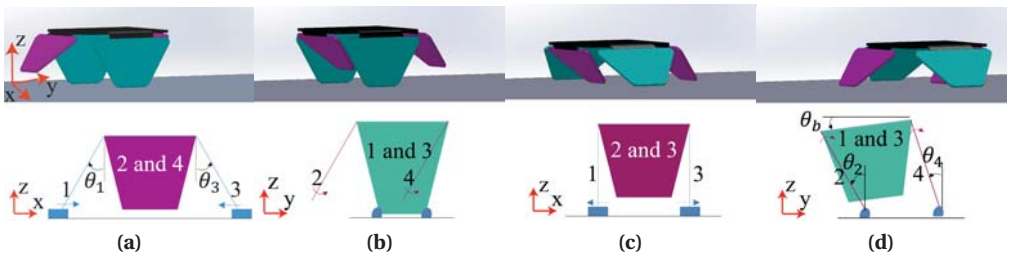

Figure A.2: Stepping sequence of the crawler. A Schematic of the goal configuration for the robot in each phase and the equivalent mechanisms for different phases of locomotion. (a-d) Represent the phases number 1-4 introduced in Table A.1. The 2D schematic in (a) and (c) are the view of the robot along the locomotion direction (y axis) which presents the motion of active legs in these two phases (leg 1-3). The 2D schematic in (b) and (d) show the view of the robot from the side (along x axis in negative direction) to present the motion of active legs in these two phases (leg 2-4).

Table A.1: Crawler's joint set points for performing the stepping motion. The bold entries indicate the legs in contact with the ground.

	Phase 1	Phase 2	Phase 3	Phase 4
Leg # 1	$\mathbf{90^o}$	$\mathbf{90^o}$	45^o	45^o
Leg # 2	135^o	45^o	$\mathbf{45^o}$	$\mathbf{135^o}$
Leg # 3	$\mathbf{90^o}$	$\mathbf{90^o}$	45^o	45^o
Leg # 4	45^o	135^o	$\mathbf{135^o}$	$\mathbf{45^o}$

any contact force. In phase 1, legs 1 and 3 lift the robot up so in the second phase, legs 2 and 4 can move forward without touching the ground. Next, in phase 3, legs 1 and 3 open so legs 2 and 4 touch the ground. Finally, in phase 4, actuators on leg 2 and 4 push the body forward.

A.2 Crawler motion

In this Section, the results of the experiment on the robot are presented. The controller decides the goal angles for each leg based on the Robot's locomotion phase and using the feedback from the sensors, determines when the goal configuration is achieved and switches to the next phase. In each phase, based on the actual and desired goal angles, an on-off controller activates the actuators to reach the desired angle. Due to the fluctuation around the equilibrium point in each leg, reaching the goal angle on all legs might not happen at once.

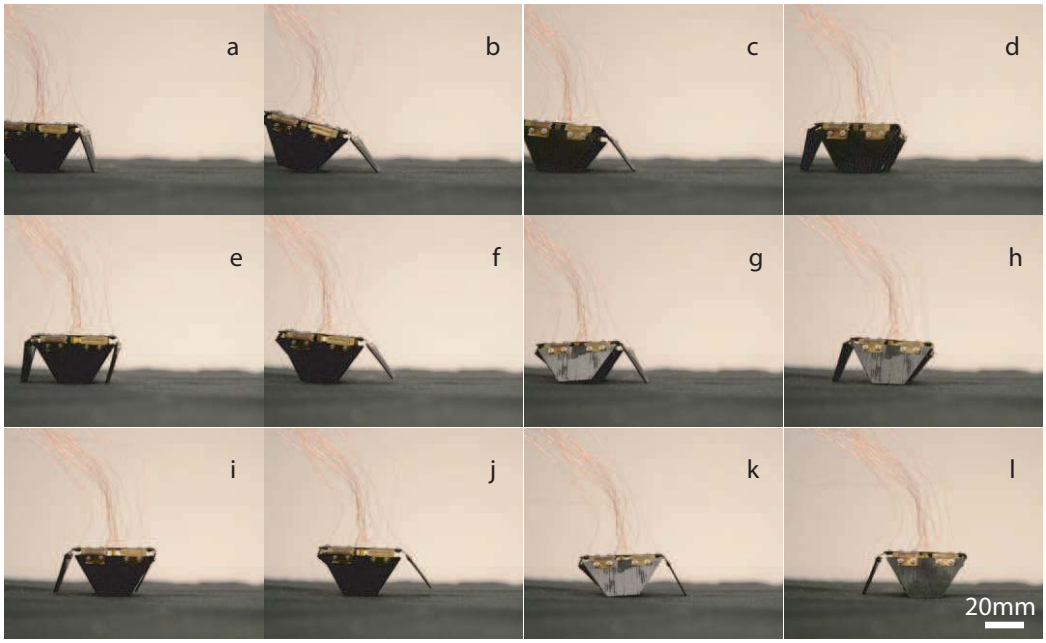

Figure A.3: Snapshots of crawler's motion. (e,i) Phase 1. (b,f,j) Phase 2. (c,g,k) Phase 3. (d,h,l) phase 4.

Each phase is considered complete if all legs have reached their goal once from the beginning of that phase. It is worth mentioning that in our experience running the robot in open-loop by assigning fix timing for stepping was not successful and the feedback data is necessary for successful locomotion. The main reason is that the stiffness and thermal conditions of the actuators would never be the same in two consecutive cycles. Fig. A.3 presents series of the snapshots taken from the Crawler as it moves three steps.

The series of the snapshots of Fig. A.3 indicates that the bidirectional folds activated by the SMA actuators, the feedback from carbon ink sensors, the controller and the overall design of the robogami are all effective. Also, the controller circuit successfully closes the loop using the sensor reading and generates the appropriate command.

B SPA with adjustable stiffness layers for multi-DoF actuation

Compliance control method presented in this thesis is applicable to other fields of soft robotics. In the process of refining the design of the adjustable stiffness layer, we used a pneumatic actuator as a platform for comparing the performance of different designs and to resolve the design flaws. In this Appendix, the design of a SPA which used adjustable stiffness walls for activating different modes of actuation is presented and its performance is characterized.

B.1 Actuation concept and fabrication process

SPAs are manufactured from soft materials and are inherently compliant. Customizability, light weight, and low cost and fast manufacturing make SPAs an attractive alternative to conventional methods of actuation in different applications such as wearable rehabilitative devices and search and rescue robots. In applications that require a high compliance for safety and a fluid interactivity, the SPAs' material-based softness returns an inherent compliance. The complexity of miniaturization and addition of DoFs in a single actuator are among the challenges that limit the application range of SPAs. We present a novel design and manufacturing method for a SPA with different modes of actuation using ASLs. Unlike conventional SPA designs where one independent chamber is needed for each mode of actuation, in this design a single chamber drives three different modes of actuation, which are activated by changing the elastic properties of the chamber walls. Using customized stretchable heaters and thermistors we controlled the temperature and the stiffness of ASLs in increments, which allows us to broaden significantly the workspace of a SPA with a single chamber. The actuation concept is presented presented in Fig. B.1. The actuation mode can be decided by controlling the stiffness of the chamber walls. By adjusting the stiffness of the walls, this actuator with a single chamber can deform in three major modes (bending in opposite sides and elongation).

The material of this Chapter is from the following self-authored publications:
[72] **A. Firouzeh**, et al., "Soft pneumatic actuator with adjustable stiffness layers formulti-dof actuation", IROS 2015..

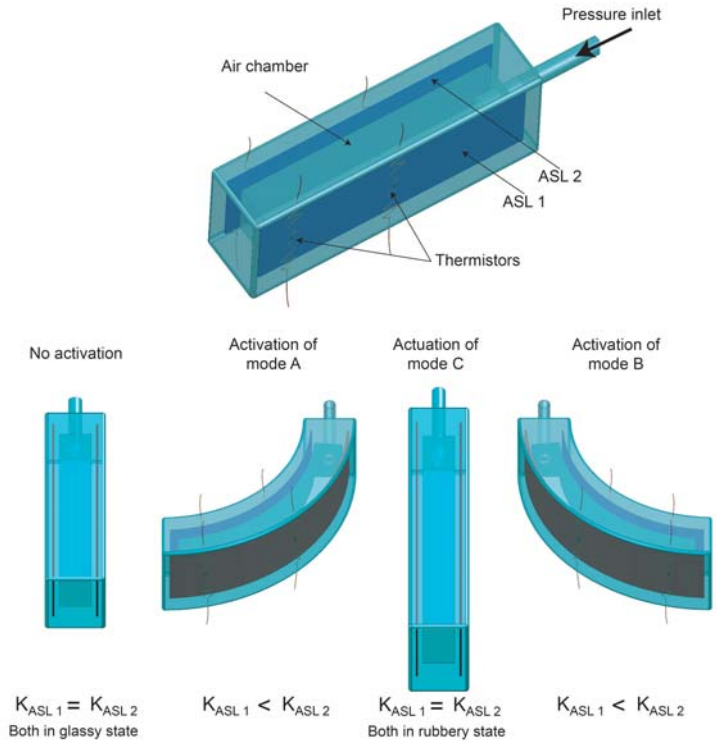

Figure B.1: SPA with a single chamber and multiple modes of operation. Depending on the stiffness setting, the actuator moves in 3 different modes: bending toward the opposite directions (mode A and B), and elongation (mode C). Different modes are activated by controlling the stiffness of the two ASLs (K_{ASL}).

The ASLs in this design are composed of SMP embedded in silicone rubber.

The fabrication of a SPA with embedded ASLs starts with embedding stretchable heaters in SMP, explained in detail in Chapter 3. Two thermistors are attached to each SMP layer to provide temperature feedback. The SPA is composed of two half sections that make the

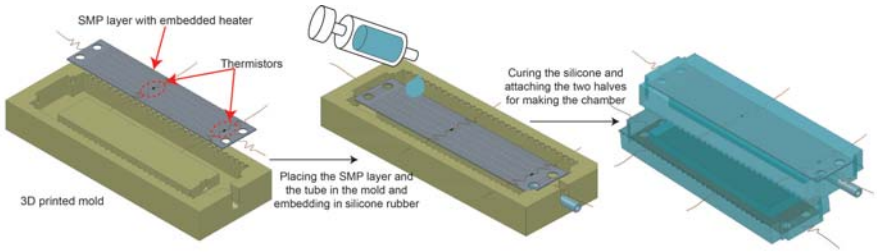

Figure B.2: Fabrication process of SPA with embedded SMP layers. The fabrication starts with making two halves of the actuator with embedded ASL. After curing the silicone, the two parts are glued together with silicone adhesive and a thread is wrapped around the actuator to confine its lateral inflation under pressure.

chamber as presented in Fig. B.2. The holders in the mold keep the SMP layer in the proper distance from the chamber wall to prevent leakages in the actuators. After the two halves are cured, they are attached together using silicone adhesive. Finally, we wrap a thread around the actuator using the teeth marks, left by the features designed in the mold, as the guide. The thread confines the lateral expansion of the SPA.

B.2 Actuator design and its model

Actuator design parameters are determined using the characterization test results (Chapter 3) and the requirement to achieve 90 ° angle in actuation in mode A and B, Fig. B.1. We consider the maximum strain applied in the characterization test (36%) as the maximum allowed strain in the ASL. Fig. B.3 presents a schematic of the actuator as it bends. Considering a uniform radius of curvature throughout the length, we have the following relation for the strain in the ASLs (ϵ_h and ϵ_c), the bending angle (θ), and the length and height of the chamber ($l_{chamber}$ and $h_{chamber}$):

$$(\epsilon_h - \epsilon_c) l_{chamber} = h_{chamber} \theta_{goal} \tag{B.1}$$

Based on (B.1), smaller the chamber height, shorter its length needs to be for reaching a goal angle while staying in the ASL's allowed strain range. On the other hand, a chamber with smaller height generates smaller blocked force (since the cross section area is smaller). Since

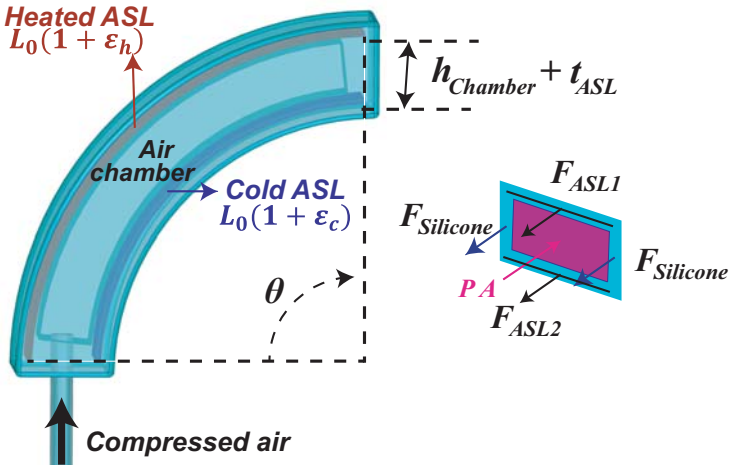

Figure B.3: Schematic of a SPA actuator with embedded ASLs. The figure shows the actuator in the deformed state and its design parameters. Also, forces applied to the cross section of the actuator are presented. In free deformation of the actuator, the force generated by the compressed air is transformed to stress and hence strain in the chamber walls. Different stiffness (controlled by temperature) determines the strain in different walls of the chamber and hence the overall deformation.

we do not have any requirement on the blocked torque of the actuator in this design, the height of the chamber remains an open parameter.

Based on the previous experience, we often put the sum of the wall thickness on the two sides of the chamber as the lower limit on the chamber height. We confirmed through experiments that to have a leak-free chamber, the wall thickness should be more than 4 mm. Based on these, we designed the chamber height to be 9.5 mm which places the SMP layers 12.5 mm apart, given the thickness and placement of the SMP layers in ASL. For a chamber of this size and given the maximum allowed strain in the ASL, the minimum chamber length for reaching the desired range of motion is calculated according to (B.1) to be 73 mm.

The width of the chamber is also dependent on the required blocked force and in this research remains an open parameter. The only limitation on the chamber width is that it should be smaller than the width of the SMP layer. We used the same width for the SMP layer as used in the characterization tests (20 mm). Through experiments, we confirmed that making the chamber 2 mm slimmer on each side prevents leaks (that makes the overall width of the chamber 16 mm).

Fig. B.3 presents the forces in a cross section of the actuator. Here, we estimate the pressure needed for generating the desired deformation, given the chamber size and ASL stiffness. In an actuator with free displacement, the force generated by the compressed air is entirely spent on deformation of the chamber walls.

$$PA_{Ch} = F_{ASL1} + F_{ASL2} + F_{Silicone} \tag{B.2}$$

Based on (B.2) and the characterization results presented in Chapter 3, the pressure required for reaching the maximum deformation angle is estimated to be 330 kPa. We should point out that the contribution of the thread that is wrapped around the actuator and the lateral expansion of the actuator has been neglected in this study.

The workspace of a normal SPA is limited to a 1 D trajectory. In the case of the actuator introduced here, the workspace covers three major lines corresponding to: activation of each individual ASL (bending in mode A and B) and activation of the both ASLs (elongation in mode C). Moreover, by incremental control of the temperature (hence the stiffness difference between the two ASLs), deformation in the intermediary modes between the three major activation modes is possible (a combination of bending and elongation in the actuator). Fig. B.4 presents the estimated workspace of the actuator based on the following relation between the length of each ASL (L_{ASL1}), the bending angle (θ), and the curvature radius (ρ) of the actuator:

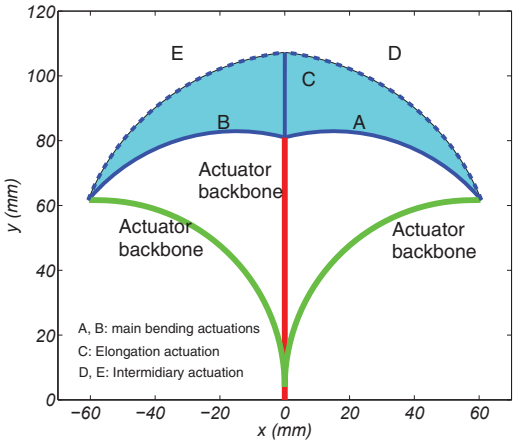

Figure B.4: Workspace of the SPA actuator with controllable mode of operation. The red line represents the initial state of the actuator, the green lines represent actuator as it bends to the side. The shaded area represents the overall workspace of the actuator. the solid blue lines represent the 3 major activation modes (bending to the opposite sides and elongation). The dashed lines present the intermediary activation modes.

$$\theta = \frac{L_{ASL1} - L_{ASL2}}{h_{chamber}}$$
$$\rho = \frac{(L_{ASL1} + L_{ASL2})/2}{\theta} \tag{B.3}$$

In Fig. B.4, the three solid blue lines present the main modes of actuation: bending toward sides and elongation. When compressed air flows into the chamber of an actuator with one ASL in soft and the other one in completely stiff state, the actuator bends along line A or B (depending on which ASL is activated) according to the input pressure. By activating the cold ASL partially, the actuator elongates and bends at the same time. The dashed lines (D and E) in Fig. B.4 present the possible tip points when SPA is actuated at maximum pressure and the inactive ASL is heated incrementally to completely active state. In this figure, line C corresponds to the workspace of the SPA with both ASLs in active state which causes elongation in the actuator. Theoretically, with a controlled and uniform temperature throughout the SMP layer, all the points in the shaded area of Fig. B.4 can be accessed.

B.3 Experimental results

In this section, the result of the performance tests on the SPA with ASL are presented in two parts. First, we study the effectiveness of the temperature control and temperature distribution in the SMP layer and then, the results of actuating SPA in different modes are presented.

B.3.1 Temperature gradient in SMP and its transient response

One of the critical aspects in thermally activated polymeric materials is the heat distribution. Nonuniform temperature distribution results in mixed behaviors such as plastic deformation and over-strain in segments of the SMP layer causing unrecoverable strain. As presented in Fig. B.5, there is a considerable temperature gradient for the sample with the present heater design. To study the temperature distribution, two thermistors in contact with each SMP layer were embedded in the actuator. The use of the sensors at the border, is useful for ensuring that the rubbery state is reached all over the SMP layer. Moreover, studying the temperature distribution using multiple embedded sensors helps with heater design for having a more uniform temperature distribution. A temperature gradient of 20 ^{o}C was observed and taken into account for defining the target temperature of the central part for the tests on the SPA in order to ensure complete transition into rubbery state everywhere in the SMP layer.

The feedback from the thermistors allows us to close the loop for maintaining a desired temperature. Adding feedback has the advantage of compensating any change in the ambient temperature or heat exchange rate. Moreover, a simple proportional-integrative (PI) controller, reduces the rise time considerably. Fig. B.6 presents a comparison between the temperature transient response of a SMP layer for two cases: first when a fixed voltage needed to maintain a certain steady state temperature is applied to the heater, and second when a PI controller with feedback from thermistors controls heater's driving voltage. The results clearly shows the advantage of using the feedback control by reducing the rise time from around 120 s to around 5 s. This figure also presents the transient temperature of a SMP layer embedded in silicone. Embedding the SMP layer in silicone increases the rise time considerably (from 5 to 20 s), given the higher energy required for heating up the silicone in contact with the SMP layer. We

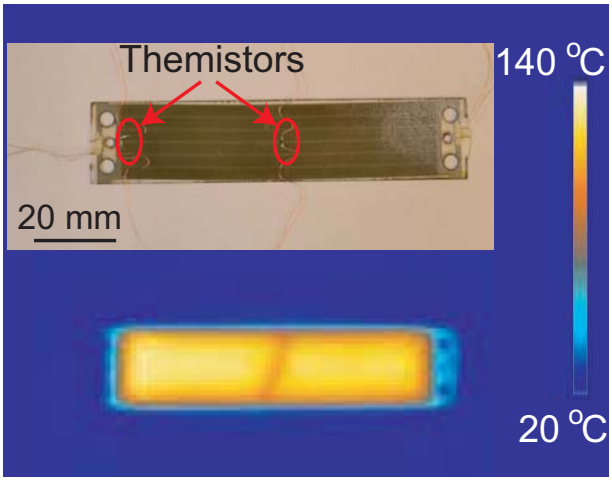

Figure B.5: Thermistors' position on the SMP layer and temperature distribution on the SMP surface. The thermal image shows considerable temperature gradient in the SMP layer. To ensure that the whole material has entered the rubbery state, we need to put the set temperature higher than the glass transition temperature.

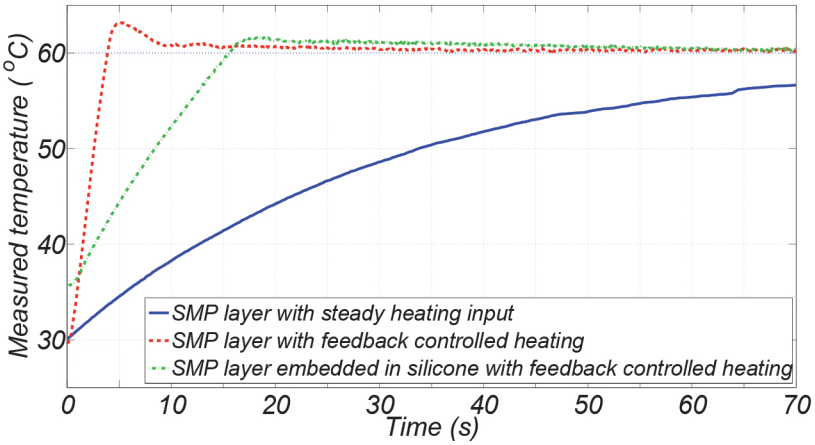

Figure B.6: Thermal time response of ASL. Temperature of the SMP layer for 3 experiments: SMP layer with and without feedback, and SMP layer embedded in silicone with temperature feedback. Using a PI controller with the temperature feedback reduces the rise time from 120 second to around 5 seconds for the SMP sample outside the silicone. Embedding the sample in silicone increases the rise time since more energy is required to heat up the silicone in contact with SMP.

confirmed through experiments that embedding the SMP layer in silicone does not affect the accuracy of the temperature control and precise (with standard deviation of less than 0.5 ^oC) and accurate (with less than 1 ^oC steady error) operating temperature was achieved which guarantees a fine control of the SMP temperature and its stiffness. This is important since it enables us to activate SPA in intermediary modes.

B.3.2 Different actuation modes of a SPA with embedded ASLs

To study the performance of the SPA with embedded ASLs, we tested the actuator under different thermal conditions with different input pressures. The goal is to determine the

Table B.1: Test conditions to characterize the main modes of operation and the borders of the workspace. The pressure increased in 40 kPa increments from 100 kPa to 300 kPa to characterize the main modes of operation (A, B, and C). For intermediary modes, the pressure was set to the maximum and the temperature was increased in 10 ^oC steps from 40 ^oC to 70 ^oC (E). The last test is applying pressure to the inactive actuator.

Actuation mode	$T_L(^oC)$	$T_R(^oC)$	$P(kPa)$
A	110	30	100-300
B	30	110	100-300
C	110	110	100-300
E	40-70	110	300
F	30	30	100-300

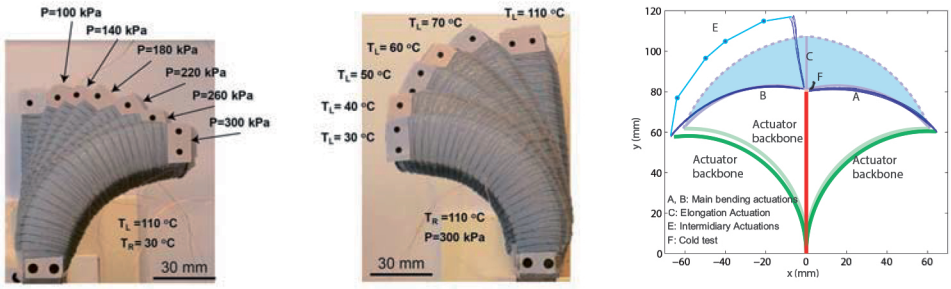

(a) (b) (c)

Figure B.7: SPA motion at different temperature settings and input pressures. (a) Actuation of SPA with one ASL activated (at 110 ^oC) and the second one inactive causes bending in the actuator with bending angle being a function of the input pressure. (b) Actuating the SPA at maximum pressure with one ASL active, causes pure bending. As we gradually increase the temperature of the second ASL, the actuator starts to elongate. (c) The workspace of the actuator covers an area similar to the expected workspace, a faded view of the estimated workspace is overlapped for comparison. In high pressures, due to the lateral expansion of the actuator which increases the force generated by the compressed air, the length is longer than expected which causes the discrepancy between the experimental and estimated workspaces. This effect is more noticeable when both ASLs are active (lines C and E) (c).

workspace of the actuator and to compare it with the estimated workspace. Table B.1 presents the test conditions used in actuator characterization. These tests are designed to determine the borders of the workspace. The maximum pressure in these tests was determined by increasing the input pressure in bending mode (mode A and B) till reaching 90^o angle (the goal in the design section). The required pressure for this deformation was 300 kPa which is lower than the expected pressure from Section B.2. The pressure in the design section was

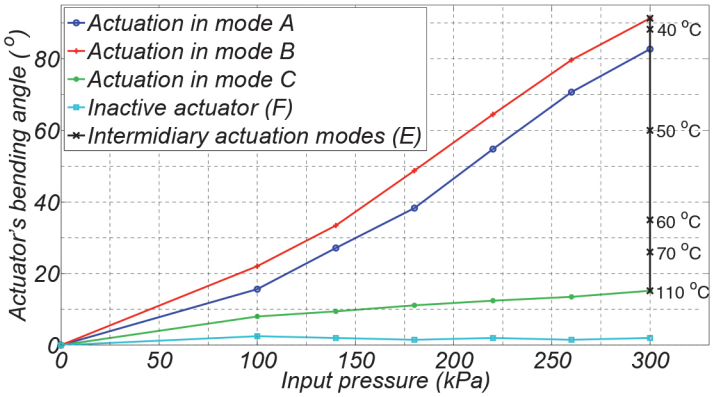

Figure B.8: Characterizing SPA's bending angle in different modes of actuation. The small difference between the bending angles for the two sides is caused by small differences in geometry of the two halves of the actuator caused by fabrication errors such as differences in the thickness of the SMP layers.

overestimated due to neglecting the lateral expansion of the chamber.

Fig. B.7a presents the overlapped snapshots taken from actuator in mode A. in this test, the input pressure changes from 100 kPa to 300 kPa in 40 kPa increments while the temperature is fixed at 110 ^oC and 30 ^oC for the left and the right ASLs, respectively. Fig. B.7b presents the snapshots from intermediary modes of operation (E) in which the pressure is fixed at 300 kPa, the temperature of the right ASL is fixed at 110 ^oC, and the temperature of the left ASL changes from 30 ^oC to 70 ^oC in 10 ^oC increments. Using a tracker software, we determined the overall workspace of the actuator from these tests (Fig. B.7c). The shape of the workspace is as expected (Fig. B.4), but compared to the estimated workspace, the actuator is longer. This is more significant in higher pressures and specifically in tests where both ASLs are active (lines C and E). In the elongation test (C), the actuator length increases 52% of the chamber length. This is substantially higher than the expected 36%. This extra increase in length can be attributed to the lateral expansion of the actuator which increases the force from the compressed air and hence the strain and elongation in the chamber walls. This is also the reason of the increasing slope of the angle and length graphs at higher pressures (Fig. B.8, B.9). Based on the rather linear stress-strain behavior of the materials (Fig. 3.17), we expected a linear relation for bending angle and length of the actuator versus the input pressure. But as the pressure increases, so does the area of the chamber which causes nonlinear relation between the force exerted to the chamber walls and the input pressure. The thread that wraps around the actuator confines the lateral expansion considerably but the chamber still expands.

Ideally, we expected the actuation in mode A and B to give identical result. But because of the discrepancies in the manufacturing (such as the variation in the thickness of the SMP layers), the results of actuation in these two modes are asymmetric. This is also the reason for small bending angles in actuation in mode C. Such issues can be accounted for in future by adjusting the activation temperature of the two ASLs.

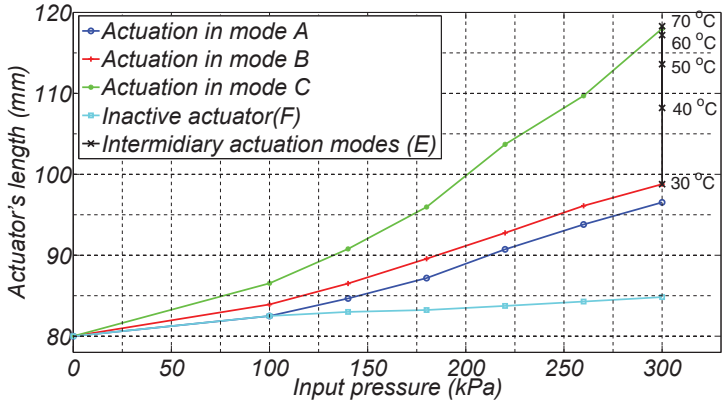

Figure B.9: Characterizing SPA's length in different modes of actuation. The length of the actuator in different modes of activation shows increasing rate of change as the pressure increases (e). The reason is the lateral expansion of the chamber which amplifies the effect of the pressure increase.

Bibliography

[1] G. Colombo, M. Wirz, and V. Dietz, "Driven gait orthosis for improvement of locomotor training in paraplegic patients." *Spinal cord*, vol. 39, no. 5, 2001.

[2] T. Hayashi, H. Kawamoto, and Y. Sankai, "Control method of robot suit hal working as operator's muscle using biological and dynamical information," in *2005 IEEE/RSJ International Conference on Intelligent Robots and Systems*, Aug 2005, pp. 3063–3068.

[3] C. J. Walsh, K. Pasch, and H. Herr, "An autonomous, underactuated exoskeleton for load-carrying augmentation," in *2006 IEEE/RSJ International Conference on Intelligent Robots and Systems*, Oct 2006, pp. 1410–1415.

[4] D. Leonardis, M. Barsotti, C. Loconsole, M. Solazzi, M. Troncossi, C. Mazzotti, V. P. Castelli, C. Procopio, G. Lamola, C. Chisari, M. Bergamasco, and A. Frisoli, "An emg-controlled robotic hand exoskeleton for bilateral rehabilitation," *IEEE Transactions on Haptics*, vol. 8, no. 2, pp. 140–151, April 2015.

[5] X. Gu, Y. Zhang, W. Sun, Y. Bian, D. Zhou, and P. O. Kristensson, "Dexmo: An inexpensive and lightweight mechanical exoskeleton for motion capture and force feedback in vr," in *Proceedings of the 2016 CHI Conference on Human Factors in Computing Systems*, ser. CHI '16. New York, NY, USA: ACM, 2016, pp. 1991–1995.

[6] N. S. K. Ho, K. Y. Tong, X. L. Hu, K. L. Fung, X. J. Wei, W. Rong, and E. A. Susanto, "An emg-driven exoskeleton hand robotic training device on chronic stroke subjects: Task training system for stroke rehabilitation," in *2011 IEEE International Conference on Rehabilitation Robotics*, June 2011, pp. 1–5.

[7] Y. Mengüç, Y.-L. Park, H. Pei, D. Vogt, P. M. Aubin, E. Winchell, L. Fluke, L. Stirling, R. J. Wood, and C. J. Walsh, "Wearable soft sensing suit for human gait measurement," *The International Journal of Robotics Research*, vol. 33, no. 14, pp. 1748–1764, 2014.

[8] B. T. Quinlivan, S. Lee, P. Malcolm, D. M. Rossi, M. Grimmer, C. Siviy, N. Karavas, D. Wagner, A. Asbeck, I. Galiana, and C. J. Walsh, "Assistance magnitude versus metabolic cost reductions for a tethered multiarticular soft exosuit," *Science Robotics*, vol. 2, no. 2, 2017.

[9] M. Wehner, B. Quinlivan, P. M. Aubin, E. Martinez-Villalpando, M. Baumann, L. Stirling, K. Holt, R. Wood, and C. Walsh, "A lightweight soft exosuit for gait assistance," in *2013 IEEE International Conference on Robotics and Automation*, May 2013, pp. 3362–3369.

[10] J. Arata, K. Ohmoto, R. Gassert, O. Lambercy, H. Fujimoto, and I. Wada, "A new hand exoskeleton device for rehabilitation using a three-layered sliding spring mechanism," in *2013 IEEE International Conference on Robotics and Automation*, May 2013, pp. 3902–3907.

[11] B. B. Kang, H. Lee, H. In, U. Jeong, J. Chung, and K. J. Cho, "Development of a polymer-based tendon-driven wearable robotic hand," in *2016 IEEE International Conference on Robotics and Automation*, May 2016, pp. 3750–3755.

[12] P. Polygerinos, Z. Wang, K. C. Galloway, R. J. Wood, and C. J. Walsh, "Soft robotic glove for combined assistance and at-home rehabilitation," *Robotics and Autonomous Systems*, vol. 73, pp. 135 – 143, 2015, wearable Robotics.

[13] "Festohand, human machine cooperation," 2012. [Online]. Available: https://www.festo.com/net/SupportPortal/Files/156734/Brosch_FC_ExoHand_EN_lo_L.pdf

[14] N. Friedman, V. Chan, D. Zondervan, M. Bachman, and D. J. Reinkensmeyer, "MusicGlove: Motivating and quantifying hand movement rehabilitation by using functional grips to play music," in *2011 Annual International Conference of the IEEE Engineering in Medicine and Biology Society*, Aug 2011, pp. 2359–2363.

[15] J. T. Muth, D. M. Vogt, R. L. Truby, Y. Mengüç, D. B. Kolesky, R. J. Wood, and J. A. Lewis, "Embedded 3d printing of strain sensors within highly stretchable elastomers," *Advanced Materials*, vol. 26, no. 36, pp. 6307–6312, 2014.

[16] S. Miyashita, S. Guitron, M. Ludersdorfer, C. R. Sung, and D. Rus, "An untethered miniature origami robot that self-folds, walks, swims, and degrades," in *2015 IEEE International Conference on Robotics and Automation*, May 2015, pp. 1490–1496.

[17] J. K. Paik, A. Byoungkwon, D. Rus, and R. J. Wood, "Robotic origamis: Self-morphing modular robot," in *ICMC*, no. IEEE, 2012.

[18] B. An and D. Rus, "Programming and controlling self-folding robots," in *2012 IEEE International Conference on Robotics and Automation*, May 2012, pp. 3299–3306.

[19] S. Felton, M. Tolley, E. Demaine, D. Rus, and R. Wood, "A method for building self-folding machines," *Science*, vol. 345, no. 6197, pp. 644–646, 2014.

[20] C. D. Onal, R. J. Wood, and D. Rus, "Towards printable robotics: Origami-inspired planar fabrication of three-dimensional mechanisms," in *2011 IEEE International Conference on Robotics and Automation*, May 2011, pp. 4608–4613.

[21] J. s. Koh, S. p. Jung, R. J. Wood, and K. j. Cho, "A jumping robotic insect based on a torque reversal catapult mechanism," in *2013 IEEE/RSJ International Conference on Intelligent Robots and Systems*, Nov 2013, pp. 3796–3801.

[22] R. J. Wood, "The challenge of manufacturing between macro and micro," *American Scientist*, vol. 102, no. 2, p. 124, 2014.

[23] P. Birkmeyer, K. Peterson, and R. S. Fearing, "Dash: A dynamic 16g hexapedal robot," in *2009 IEEE/RSJ International Conference on Intelligent Robots and Systems*, Oct 2009, pp. 2683–2689.

[24] R. J. Wood, S. Avadhanula, R. Sahai, E. Steltz, and R. S. Fearing, "Microrobot design using fiber reinforced composites," *Journal of Mechanical Design*, vol. 130, no. 5, pp. 052 304–052 304–11, 2008.

[25] R. Pfeifer, M. Lungarella, and F. Iida, "The challenges ahead for bio-inspired 'soft' robotics," *Communications of the ACM*, vol. 55, no. 11, pp. 76–87, Nov. 2012.

[26] F. Iida and C. Laschi, "Soft robotics: Challenges and perspectives," *Procedia Computer Science*, vol. 7, pp. 99 – 102, 2011, proceedings of the 2nd European Future Technologies Conference and Exhibition 2011.

[27] "Soft active materials for actuation, sensing, and electronics," Ph.D. dissertation, Harvard, Boston, 2012.

[28] D. Jayatilake, A. Gruebler, and K. Suzuki, "An Analysis of Facial Morphology for the Robot Assisted Smile Recovery," in *2008 4th International Conference on Information and Automation for Sustainability*, Dec 2008, pp. 395–400.

[29] A. Firouzeh, Y. Sun, H. Lee, and J. Paik, "Sensor and actuator integrated low-profile robotic origami," in *2013 IEEE/RSJ International Conference on Intelligent Robots and Systems*, Nov 2013, pp. 4937–4944.

[30] A. Firouzeh and J. Paik, "Robogami: A fully integrated low-profile robotic origami," *Journal of Mechanisms and Robotics*, vol. 7, no. 2, pp. 021 009–021 009–8, 2015.

[31] A. Firouzeh and J. k. Paik, "An under-actuated origami gripper with adjustable stiffness joints for multiple grasp modes," *Smart Materials and Structures*, 2017. [Online]. Available: http://iopscience.iop.org/10.1088/1361-665X/aa67fd

[32] K. Jayaram and R. J. Full, "Cockroaches traverse crevices, crawl rapidly in confined spaces, and inspire a soft, legged robot," *Proceedings of the National Academy of Sciences*, vol. 113, no. 8, pp. E950–E957, 2016.

[33] J.-M. Mongeau, B. McRae, A. Jusufi, P. Birkmeyer, A. M. Hoover, R. Fearing, and R. J. Full, "Rapid inversion: Running animals and robots swing like a pendulum under ledges," *PLOS ONE*, vol. 7, no. 6, pp. 1–9, 06 2012.

[34] N. Doshi, B. Goldberg, R. Sahai, N. Jafferis, D. Aukes, R. J. Wood, and J. A. Paulson, "Model driven design for flexure-based microrobots," in *2015 IEEE/RSJ International Conference on Intelligent Robots and Systems*, Sept 2015, pp. 4119–4126.

[35] A. Firouzeh, A. F. Amon-Junior, and J. Paik, "Soft piezoresistive sensor model and characterization with varying design parameters," *Sensors and Actuators A: Physical*, vol. 233, pp. 158 – 168, 2015.

[36] A. Firouzeh and J. Paik, "The Design and Modeling of a Novel Resistive Stretch Sensor With Tunable Sensitivity," *IEEE Sensors Journal*, vol. 15, no. 11, pp. 6390–6398, Nov 2015.

[37] P. Cheng and B. Oelmann, "Joint-angle measurement using accelerometers and gyroscopes-a survey," *IEEE Transactions on Instrumentation and Measurement*, vol. 59, no. 2, pp. 404–414, Feb 2010.

[38] E. A. Peraza-Hernandez, D. J. Hartl, R. J. M. Jr, and D. C. Lagoudas, "Origami-inspired active structures: a synthesis and review," *Smart Materials and Structures*, vol. 23, no. 9, p. 094001, 2014.

[39] X. Sun, S. M. Felton, R. J. Wood, and S. Kim, "Printing angle sensors for foldable robots," in *2015 IEEE/RSJ International Conference on Intelligent Robots and Systems*, Sept 2015, pp. 1725–1731.

[40] J. K. Paik, R. K. Kramer, and R. J. Wood, "Stretchable circuits and sensors for robotic origami," in *2011 IEEE/RSJ International Conference on Intelligent Robots and Systems*, Sept 2011, pp. 414–420.

[41] H. Vandeparre, D. Watson, and S. P. Lacour, "Extremely robust and conformable capacitive pressure sensors based on flexible polyurethane foams and stretchable metallization," *Applied Physics Letters*, vol. 103, no. 20, pp. –, 2013.

[42] R. Samuel, M. O. Benjamin, G. Todd, X. Daniel, R. S. Herbert, and A. A. Iain, "Self-sensing dielectric elastomer actuators in closed-loop operation," *Smart Materials and Structures*, vol. 22, no. 10, p. 104018, 2013.

[43] S. Rosset, B. M. O'Brien, T. Gisby, D. Xu, H. R. Shea, and I. A. Anderson, "Tunable grating with active feedback," vol. 8687, 2013, pp. 86 872F–86 872F–11.

[44] C. Gentile, M. Wallace, T. Avalon, S. Goodman, R. Fuller, and T. Hall, "Angular displacement senso," *US Patent*, no. US5086785 A, 1992.

[45] D. Thuau, C. Ayela, P. Poulin, and I. Dufour, "Highly piezoresistive hybrid mems sensors," *Sensors and Actuators A: Physical*, vol. 209, no. 0, pp. 161 – 168, 2014.

[46] J. Engel, J. Chen, X. Wang, Z. Fan, C. Liu, and D. Jones, "Technology development of integrated multi-modal and flexible tactile skin for robotics applications," vol. 3, pp. 2359–2364 vol.3, Oct 2003.

[47] Y. Mengüç, Y. L. Park, E. Martinez-Villalpando, P. Aubin, M. Zisook, L. Stirling, R. J. Wood, and C. J. Walsh, "Soft wearable motion sensing suit for lower limb biomechanics measurements," in *2013 IEEE International Conference on Robotics and Automation*, May 2013, pp. 5309–5316.

[48] N. Hu, Y. Karube, M. Arai, T. Watanabe, C. Yan, Y. Li, Y. Liu, and H. Fukunaga, "Investigation on sensitivity of a polymer/carbon nanotube composite strain sensor," *Carbon*, vol. 48, no. 3, pp. 680 – 687, 2010.

[49] M. Knite, V. Teteris, A. Kiploka, and J. Kaupuzs, "Polyisoprene-carbon black nanocomposites as tensile strain and pressure sensor materials," *Sensors and Actuators A: Physical*, vol. 110, no. 1–3, pp. 142–149, 2004.

[50] L. Wang, F. Ma, Q. Shi, H. Liu, and X. Wang, "Study on compressive resistance creep and recovery of flexible pressure sensitive material based on carbon black filled silicone rubber composite," *Sensors and Actuators A: Physical*, vol. 165, no. 2, pp. 207 – 215, 2011.

[51] L. Wang and J. Li, "A piezoresistive flounder element based on conductive polymer composite," *Sensors and Actuators A: Physical*, vol. 216, no. 0, pp. 214 – 222, 2014.

[52] J. Vanfleteren, M. Gonzalez, F. Bossuyt, Y.-Y. Hsu, T. Vervust, I. D. Wolf, and M. Jablonski, "Printed circuit board technology inspired stretchable circuits," *MRS Bulletin*, vol. 37, no. 3, pp. 254–260, 003 2012.

[53] J. Song, H. Jiang, Y. Huang, and J. A. Rogers, "Mechanics of stretchable inorganic electronic materials," *Journal of Vacuum Science & Technology A: Vacuum, Surfaces, and Films*, vol. 27, no. 5, pp. 1107–1125, 2009.

[54] T. Yamada, Y. Hayamizu, Y. Yamamoto, Y. Yomogida, A. Izadi-Najafabadi, D. N. Futaba, and K. Hata, "A stretchable carbon nanotube strain sensor for human-motion detection," *Nat Nano*, vol. 6, no. 5, pp. 296–301, 2011.

[55] R. K. Kramer, C. Majidi, R. Sahai, and R. J. Wood, "Soft curvature sensors for joint angle proprioception," in *2011 IEEE/RSJ International Conference on Intelligent Robots and Systems*, Sept 2011, pp. 1919–1926.

[56] B. O'Brien, T. Gisby, and I. A. Anderson, "Stretch sensors for human body motion," in *In SPIE Proeedings*, vol. 9056, 2014, pp. 905 618–905 618–9.

[57] S. Petsch, R. Rix, B. Khatri, S. Schuhladen, P. Müller, R. Zentel, and H. Zappe, "Smart artificial muscle actuators: Liquid crystal elastomers with integrated temperature feedback," *Sensors and Actuators A: Physical*, vol. 231, pp. 44 – 51, 2015, special Issue of the Micromechanics Section of Sensors and Actuators based upon contributions revised from the Technical Digest of the 27th {IEEE} International Conference on {MICRO} {ELECTRO} {MECHANICAL} {SYSTEMS} (MEMS-14; 26–30 January 2014, San Francisco, CA, USA).

[58] S. P. Lacour, J. Jones, S. Wagner, T. Li, and Z. Suo, "Stretchable interconnects for elastic electronic surfaces," *Proceedings of the IEEE*, vol. 93, no. 8, pp. 1459–1467, 2005.

[59] S. Rosset and H. Shea, "Flexible and stretchable electrodes for dielectric elastomer actuators," *Applied Physics A*, vol. 110, no. 2, pp. 281–307, 2013.

[60] U. Tata, C. Hung, C. M. Nguyen, and C. Jung-Chih, "Flexible sputter-deposited carbon strain sensor," *Sensors Journal, IEEE*, vol. 13, no. 2, pp. 444–445, 2013.

[61] M. A. Lacasse, V. Duchaine, and C. Gosselin, "Characterization of the electrical resistance of carbon-black-filled silicone: Application to a flexible and stretchable robot skin," in *2010 IEEE International Conference on Robotics and Automation*, May 2010, pp. 4842–4848.

[62] S. Xiaoping and D. D. L. Chung, "A piezoresistive carbon filament polymer-matrix composite strain sensor," *Smart Materials and Structures*, vol. 5, no. 2, p. 243, 1996.

[63] Y. Wang, A. X. Wang, Y. Wang, M. K. Chyu, and Q.-M. Wang, "Fabrication and characterization of carbon nanotube–polyimide composite based high temperature flexible thin film piezoresistive strain sensor," *Sensors and Actuators A: Physical*, vol. 199, no. 0, pp. 265 – 271, 2013.

[64] A. Ferrreira, J. Rocha, A. Ansón-Casaos, M. Martínez, F. Vaz, and S. Lanceros-Mendez, "Electromechanical performance of poly(vinylidene fluoride)/carbon nanotube composites for strain sensor applications," *Sensors and Actuators A: Physical*, vol. 178, pp. 10 – 16, 2012.

[65] J. R. Bautista-Quijano, F. Avilés, J. O. Aguilar, and A. Tapia, "Strain sensing capabilities of a piezoresistive mwcnt-polysulfone film," *Sensors and Actuators A: Physical*, vol. 159, no. 2, pp. 135–140, 2010.

[66] K. Kure, T. Kanda, K. Suzumori, and S. Wakimoto, "Intelligent fma using flexible displacement sensor with paste injection," in *Proceedings 2006 IEEE International Conference on Robotics and Automation*, May 2006, pp. 1012–1017.

[67] J. M. Engel, J. Chen, L. Chang, and D. Bullen, "Polyurethane rubber all-polymer artificial hair cell sensor," *Microelectromechanical Systems, Journal of*, vol. 15, no. 4, pp. 729–736, 2006.

[68] W. Luheng, D. Tianhuai, and W. Peng, "Effects of conductive phase content on critical pressure of carbon black filled silicone rubber composite," *Sensors and Actuators A: Physical*, vol. 135, no. 2, pp. 587 – 592, 2007.

[69] L. Wang and L. Cheng, "Piezoresistive effect of a carbon nanotube silicone-matrix composite," *Carbon*, vol. 71, no. 0, pp. 319 – 331, 2014.

[70] E. Jonathan, C. Jack, and L. Chang, "Development of polyimide flexible tactile sensor skin," *Journal of Micromechanics and Microengineering*, vol. 13, no. 3, p. 359, 2003.

[71] L. Ball, "Strain gauge," p. US2556132 A, Jun 5, 1951.

[72] A. Firouzeh, M. Salerno, and J. Paik, "Soft pneumatic actuator with adjustable stiffness layers for multi-dof actuation," in *2015 IEEE/RSJ International Conference on Intelligent Robots and Systems*, Sept 2015, pp. 1117–1124.

[73] A. Firouzeh, S. S. M. Salehian, A. Billard, and J. Paik, "An under actuated robotic arm with adjustable stiffness shape memory polymer joints," in *2015 IEEE International Conference on Robotics and Automation (ICRA)*, May 2015, pp. 2536–2543.

[74] A. Firouzeh and J. Paik, "Stiffness control with shape memory polymer in under-actuated robotic origamis," in *IEEE Transaction on Robotics*, 2017.

[75] E. Torres-Jara, K. Gilpin, J. Karges, R. J. Wood, and D. Rus, "Compliant modular shape memory alloy actuators," *Robotics & Automation Magazine, IEEE*, vol. 17, no. 4, pp. 78–87, 2010.

[76] J. D. Madden, "Actuator selection for variable camber foils," pp. 442–448, 2004.

[77] J. Paik, E. Hawkes, and R. Wood, "A novel low-profile shape memory alloy torsional actuator," *Smart Materials and Structures*, vol. 19, no. 12, p. 125014, 2010.

[78] R. Tiwari and E. Garcia, "The state of understanding of ionic polymer metal composite architecture: a review," *Smart Materials and Structures*, vol. 20, no. 8, p. 083001, 2011.

[79] S. Wolf and G. Hirzinger, "A new variable stiffness design: Matching requirements of the next robot generation," in *2008 IEEE International Conference on Robotics and Automation*, May 2008, pp. 1741–1746.

[80] A. Jafari, H. Q. Vu, and F. Iida, "Determinants for stiffness adjustment mechanisms," *Journal of Intelligent & Robotic Systems*, vol. 82, no. 3, pp. 435–454, 2016.

[81] A. Albu-Schaffer, O. Eiberger, M. Grebenstein, S. Haddadin, C. Ott, T. Wimbock, S. Wolf, and G. Hirzinger, "Soft robotics," *IEEE Robotics Automation Magazine*, vol. 15, no. 3, pp. 20–30, September 2008.

[82] Y.-J. Park, J.-G. Lee, S. Jeon, H. Ahn, J. Koh, J. Ryu, M. Cho, and K.-J. Cho, "Dual-stiffness structures with reconfiguring mechanism: Design and investigation," *Journal of Intelligent Material Systems and Structures*, vol. 27, no. 8, pp. 995–1010, 2016.

[83] J. Choi, S. Hong, W. Lee, S. Kang, and M. Kim, "A robot joint with variable stiffness using leaf springs," *IEEE Trananctions on Robotics*, vol. 27, no. 2, pp. 229–238, April 2011.

[84] D. Aukes, B. Heyneman, V. Duchaine, and M. R. Cutkosky, "Varying spring preloads to select grasp strategies in an adaptive hand," in *2011 IEEE/RSJ International Conference on Intelligent Robots and Systems*, Sept 2011, pp. 1373–1379.

[85] B. Vanderborght, A. Albu-Schaeffer, A. Bicchi, E. Burdet, D. Caldwell, R. Carloni, M. Catalano, O. Eiberger, W. Friedl, G. Ganesh, M. Garabini, M. Grebenstein, G. Grioli, S. Haddadin, H. Hoppner, A. Jafari, M. Laffranchi, D. Lefeber, F. Petit, S. Stramigioli, N. Tsagarakis, M. V. Damme, R. V. Ham, L. Visser, and S. Wolf, "Variable impedance actuators: A review," *Robotics and Autonomous Systems*, vol. 61, no. 12, pp. 1601 – 1614, 2013.

[86] M. A. McEvoy and N. Correll, "Thermoplastic variable stiffness composites with embedded, networked sensing, actuation, and control," *Journal of Composite Materials*, vol. 49, no. 15, pp. 1799–1808, 2015.

[87] W. Shan, T. Lu, and C. Majidi, "Soft-matter composites with electrically tunable elastic rigidity," *Smart Materials and Structures*, vol. 22, no. 8, p. 085005, 2013.

[88] L. Hines, V. Arabagi, and M. Sitti, "Shape Memory Polymer-Based Flexure Stiffness Control in a Miniature Flapping-Wing Robot," *IEEE Tranactions on Robotics*, vol. 28, no. 4, pp. 987–990, 2012.

[89] W. Shan, S. Diller, A. Tutcuoglu, and C. Majidi, "Rigidity-tuning conductive elastomer," *Smart Matererials and Structructures*, vol. 24, no. 6, p. 065001, 2015.

[90] Y. Yang, Y. Chen, Y. Wei, and Y. Li, "Novel design and three-dimensional printing of variable stiffness robotic grippers," *Journal of Mechanisms and Robotics*, vol. 8, no. 6, pp. 061 010–061 010–15, 2016.

[91] Y. J. Kim, S. Cheng, S. Kim, and K. Iagnemma, "A novel layer jamming mechanism with tunable stiffness capability for minimally invasive surgery," *IEEE Transactions on Robotics*, vol. 29, no. 4, pp. 1031–1042, Aug 2013.

[92] T. Ranzani, M. Cianchetti, G. Gerboni, I. D. Falco, and A. Menciassi, "A Soft Modular Manipulator for Minimally Invasive Surgery: Design and Characterization of a Single Module," *IEEE Tranactions on Robotics*, vol. 32, no. 1, pp. 187–200, Feb 2016.

[93] A. A. Stanley and A. M. Okamura, "Controllable Surface Haptics via Particle Jamming and Pneumatics," *IEEE Trans. Haptics*, vol. 8, no. 1, pp. 20–30, Jan 2015.

[94] N. G. Cheng, A. Gopinath, L. Wang, K. Iagnemma, and A. E. Hosoi, "Thermally Tunable, Self-Healing Composites for Soft Robotic Applications," *Macromolecular Materials and Engineering*, vol. 299, no. 11, pp. 1279–1284, 2014. [Online]. Available: http://dx.doi.org/10.1002/mame.201400017

[95] W. Wang, H. Rodrigue, and S.-H. Ahn, "Deployable soft composite structures," *Sci. Rep.*, vol. 6, p. 20869, 2016.

[96] J. Shintake, B. Schubert, S. Rosset, H. Shea, and D. Floreano, "Variable stiffness actuator for soft robotics using dielectric elastomer and low-melting-point alloy," in *2015 IEEE/RSJ International Conference on Intelligent Robots and Systems*, Sept 2015, pp. 1097–1102.

[97] I. K. Kuder, A. F. Arrieta, W. E. Raither, and P. Ermanni, "Variable stiffness material and structural concepts for morphing applications," *Progress in Aerospace Sciences*, vol. 63, pp. 33 – 55, 2013.

[98] W. B. Cross, A. H. Kariotis, and F. J. Stimler, "Nitinol characterization study," *NASA CR-1433, 1969*, 1969.

[99] B. E. Schubert and D. Floreano, "Variable stiffness material based on rigid low-melting-point-alloy microstructures embedded in soft poly(dimethylsiloxane) (pdms)," *RSC Advances*, vol. 3, pp. 24 671–24 679, 2013. [Online]. Available: http://dx.doi.org/10.1039/C3RA44412K

[100] M. Manti, V. Cacucciolo, and M. Cianchetti, "Stiffening in soft robotics: A review of the state of the art," *IEEE Robotics Automation Magazine*, vol. 23, no. 3, pp. 93–106, Sept 2016.

[101] M. Follador, M. Cianchetti, and C. Laschi, "Development of the functional unit of a completely soft octopus-like robotic arm," in *2012 4th IEEE RAS EMBS International Conference on Biomedical Robotics and Biomechatronics*, June 2012, pp. 640–645.

[102] L. Huai-Ti, G. L. Gary, and T. Barry, "Goqbot: a caterpillar-inspired soft-bodied rolling robot," *Bioinspiration & Biomimetics*, vol. 6, no. 2, p. 026007, 2011.

[103] J. K. Paik and R. J. Wood, "A bidirectional shape memory alloy folding actuator," *Smart Materials and Structures*, vol. 21, no. 6, p. 065013, 2012.

[104] "Nitinol technical properties," http://jmmedical.com/resources/221/Nitinol-Technical-Properties.html.

[105] B. E. Schubert, "Design, fabrication and testing of angled fiber suspension for electrostatic actuators," Ph.D. dissertation, University of California, Berkeley, 2011.

[106] Z. K. Lu and G. J. Weng, "A self-consistent model for the stress–strain behavior of shape-memory alloy polycrystals," *Acta Materialia*, vol. 46, no. 15, pp. 5423–5433, 1998.

[107] "Smp-technologies," 2016, http://www.smptechno.com/.

[108] K. Takashima, J. Rossiter, and T. Mukai, "Mckibben artificial muscle using shape-memory polymer," *Sensors and Actuators A: Physical*, vol. 164, no. 1–2, pp. 116–124, 2010.

[109] T. Hisaaki, H. Hisashi, Y. Etsuko, and H. Shunichi, "Thermomechanical properties in a thin film of shape memory polymer of polyurethane series," *Smart Materials and Structures*, vol. 5, no. 4, p. 483, 1996.

[110] A. Firouzeh and J. Paik, "Grasp mode and compliance control of an under-actuated origami gripper using adjustable stiffness joints," 2017.

[111] K. C. Galloway, K. P. Becker, B. Phillips, J. Kirby, S. Licht, D. Tchernov, R. J. Wood, and D. F. Gruber, "Soft robotic grippers for biological sampling on deep reefs," *Soft Robotics*, vol. 3, no. 1, pp. 23–33, 2016.

[112] R. Deimel and O. Brock, "A novel type of compliant and underactuated robotic hand for dexterous grasping," *The International Journal of Robotics Research*, vol. 35, no. 1-3, pp. 161–185, 2016.

[113] L. U. Odhner, L. P. Jentoft, M. R. Claffee, N. Corson, Y. Tenzer, R. R. Ma, M. Buehler, R. Kohout, R. D. Howe, and A. M. Dollar, "A compliant, underactuated hand for robust manipulation," *The International Journal of Robotics Research*, vol. 33, no. 5, pp. 736–752, 2014.

[114] D. M. Aukes, B. Heyneman, J. Ulmen, H. Stuart, M. R. Cutkosky, S. Kim, P. Garcia, and A. Edsinger, "Design and testing of a selectively compliant underactuated hand," *The International Journal of Robotics Research*, vol. 33, no. 5, pp. 721–735, 2014.

[115] L. Birglen, T. Lalibert´e, and C. Gosselin, *Underactuated Robotic Hands. (Springer Tracts in Advanced Robotics)*. Springer, 208, vol. 40.

[116] Y. Sun, X. Liang, H. K. Yap, J. Cao, M. H. Ang, and C. H. Yeow, "Force measurement towards the instability theory of soft pneumatic actuators," *IEEE Robotics and Automation Letters*, vol. PP, no. 99, pp. 1–1, 2017.

[117] M. Ciocarlie, F. M. Hicks, R. Holmberg, J. Hawke, M. Schlicht, J. Gee, S. Stanford, and R. Bahadur, "The velo gripper: A versatile single-actuator design for enveloping, parallel and fingertip grasps," *The International Journal of Robotics Research*, vol. 33, no. 5, pp. 753–767, 2014.

[118] R. A. Stavenuiter, L. Birglen, and J. L. Herder, "A planar underactuated grasper with adjustable compliance," *Mechanism and Machine Theory*, pp. –, 2016.

[119] C. Y. Brown and H. H. Asada, "Inter-finger coordination and postural synergies in robot hands via mechanical implementation of principal components analysis," in *2007 IEEE/RSJ International Conference on Intelligent Robots and Systems*, Oct 2007, pp. 2877–2882.

[120] S. Krut, "A force-isotropic underactuated finger," in *Proceedings of the 2005 IEEE International Conference on Robotics and Automation*, April 2005, pp. 2314–2319.

[121] A. Taherifar, A. Alasty, H. Salarieh, and M. Boroushaki, "Path planning for a hyper-redundant manipulator with lockable joints using pso," in *2013 First RSI/ISM International Conference on Robotics and Mechatronics*, pp. 224–229.

[122] M. E. Giannaccini, I. Georgilas, I. Horsfield, B. H. P. M. Peiris, A. Lenz, A. G. Pipe, and S. Dogramadzi, "A variable compliance, soft gripper," *Auto. Robots*, vol. 36, no. 1, pp. 93–107, 2014.

[123] J. Hughes, U. Culha, F. Giardina, F. Guenther, A. Rosendo, and F. Iida, "Soft manipulators and grippers: A review," *Frontiers in Robotics and AI*, vol. 3, p. 69, 2016.

[124] A. Firouzeh and J. Paik, "Soft actuation and sensing toward a wearable device for robot-assisted facial rehabilitation," in *2017 IEEE/RSJ International Conference on Intelligent Robots and Systems*, 2017.

[125] P. Polygerinos, K. C. Galloway, E. Savage, M. Herman, K. O. Donnell, and C. J. Walsh, "Soft robotic glove for hand rehabilitation and task specific training," in *2015 IEEE International Conference on Robotics and Automation*, May 2015, pp. 2913–2919.

[126] D. Jayatilake, T. Isezaki, Y. Teramoto, K. Eguchi, and K. Suzuki, "Robot Assisted Physiotherapy to Support Rehabilitation of Facial Paralysis," *IEEE Transactions on Neural Systems and Rehabilitation Engineering*, vol. 22, no. 3, pp. 644–653, May 2014.

[127] C. J. Nycz, T. Bützer, O. Lambercy, J. Arata, G. S. Fischer, and R. Gassert, "Design and Characterization of a Lightweight and Fully Portable Remote Actuation System for Use With a Hand Exoskeleton," *IEEE Robotics and Automation Letters*, vol. 1, no. 2, pp. 976–983, July 2016.

[128] H. In, B. B. Kang, M. Sin, and K. J. Cho, "Exo-Glove: A Wearable Robot for the Hand with a Soft Tendon Routing System," *IEEE Robotics Automation Magazine*, vol. 22, no. 1, pp. 97–105, March 2015.

[129] M. Wand, C. Schulte, M. Janke, and T. Schultz, "Array-based electromyographic silent speech interface," in *Proceedings of the International Conference on Bio-inspired Systems and Signal Processing*, 2013, pp. 89–96.

[130] L. Bareket, L. Inzelberg, D. Rand, M. David-Pur, D. Rabinovich, B. Brandes, and Y. Hanein, "Temporary-tattoo for long-term high fidelity biopotential recordings," *Scientific Reports*, vol. 6, p. 25727, 2016.

[131] H. Koga, Y. Usuda, M. Matsuno, Y. Ogura, H. Ishii, J. Solis, A. Takanishi, and A. Katsumata, "Development of oral rehabilitation robot for massage therapy," in *2007 6th International Special Topic Conference on Information Technology Applications in Biomedicine*, Nov 2007, pp. 111–114.

[132] N. J. Holland and G. M. Weiner, "Recent developments in Bell's palsy," *British Med. J.*, vol. 329, no. 7465, p. 553, 2004.

[133] C. H. Beurskens and P. G. Heymans, "Positive effects of mime therapy on sequelae of facial paralysis: stiffness, lip mobility, and social and physical aspects of facial disability," *Otology & Neurotology*, vol. 24, no. 4, pp. 677–681, 2003.

[134] I. G. Williamson and T. R. Whelan, "The clinical problem of Bell's palsy: is treatment with steroids effective?" *British J. General Practice*, vol. 46, no. 413, pp. 743–747, 1996.

[135] C. Azra, "Shape memory polymers with controlled time-dependent shape recovery," *PhD thesis*, 2013.

[136] K. L. Feilich and G. V. Lauder, "Passive mechanical models of fish caudal fins: effects of shape and stiffness on self-propulsion," *Bioinspiration & Biomimetics*, vol. 10, no. 3, p. 036002, 2015.

[137] S. Pouya, M. Khodabakhsh, A. Spröwitz, and A. Ijspeert, "Spinal joint compliance and actuation in a simulated bounding quadruped robot," *Autonomous Robots*, vol. 41, no. 2, pp. 437–452, 2017.

Curriculum Vitae

Amir Firouzeh

Email: amir.firouzeh@epfl.ch

Research interests

Soft Robotics
Novel sensors and actuators
Smart material
Compliant and conformant robots with redundant DoFs
Novel manufacturing methods
Adjustable stiffness structures

Education

PhD Robotics and manufacturing 2012-2017
EPFL, Lausanne, Switzerland.
Thesis: Development of essential components for soft wearable technologies.

M.Sc Mechanical Engineering 2009-2012
Sharif University of Technology, Tehran, Iran.
Thesis: Design, modeling and fabrication of a soft robot made of IPMC.

B.Sc Mechanical Engineering 2004-2009
Tehran University, Tehran, Iran.
Thesis: Design of a brake system for an electric car.

PhD research focus

- Studying Robogamis with independently actuated joints as a mobile platform. This research has laid the groundwork for the joint design and some of the components such as the stretchable heaters and the sensors which are essential functional layers in the Robogamis [C3, J7].
- Developing sensors for the joint angles in Robogamis that are compatible with their manufacturing techniques and working conditions [J3, J6].
- Developing mechanically transparent stretchable sensors for monitoring the deformations of soft bodies interacting with the Robogamis [J5].
- Implementing adaptive stiffness layers in soft robots for controlling their mode of operation and overall stiffness [J1-J3, C1-C2].

Publications

Journal papers

[J1] **A. Firouzeh,** J. Paik, “Grasp mode and compliance control of an under-actuated origami gripper using adjustable stiffness joints” IEEE Transaction on Mechatronics (2017)

[J2] **A. Firouzeh,** J. Paik, “An under-actuated origami gripper with adjustable stiffness joints for multiple grasp modes” Smart materials and structures (2017)

[J3] **A. Firouzeh,** M. Salerno, J. Paik, “Stiffness control in under-actuated robotic origamis with shape memory polymer” IEEE Transaction on Robotics (2017)

[J4] M. Salerno, **A. Firouzeh,** J. Paik, “An Origami Robot-based Parallel Platform with Embedded Electro-Magnetic Actuation” ASME mechanisms and robotics (2017)

[J5] **A. Firouzeh,** J. Paik “The design and modeling of a novel resistive stretch sensor with tunable sensitivity”, IEEE Sensors Journal (2015)

[J6] **A. Firouzeh,** AF Amon-Junior, J. Paik “Soft piezoresistive sensor model and characterization with varying design parameters”, Elsevier Sensors and Actuators (2015)

[J7] **A. Firouzeh,** J. Paik “Robogami: a fully integrated low-profile robotic origami”, ASME Journal of Mechanisms and Robotics (2015)

[J8] **A. Firouzeh,** A. Alasty, M. Ozmaian, A. Iraji Zad “IPMC-made deformable ring like robot”, IOP Journal of Smart Materials and structures (2012)

Conference papers

[C1] **A. Firouzeh,** M. Salerno, J. Paik, ”Soft pneumatic actuator with adjustable stiffness layers for Multi-DoF Actuation”, IEEE International Conference on Intelligent Robots and Systems (IROS), Hamburg, Germany, 2015.

[C2] **A. Firouzeh,** SSM Salehian, A Billard, J Paik,” An Under Actuated Robotic Arm with Adjustable Stiffness Shape Memory Polymer Joints”, IEEE International Conference on Robotics and Automation (ICRA), Seattle, USA, 2015.

[C3] **A. Firouzeh,** Y Sun, H Lee, J. Paik, ” Sensor and actuator integrated low-profile robotic origami”, IEEE International Conference on Intelligent Robots and Systems (IROS), Tokyo, Japan, 2013.

[C4] **A. Firouzeh,** A. Alasty, M. Ozmaian,”Motion of deformable ring made of IPMC”, 3rd International Conference on Smart Material and Nanotechnology in Engineering, Shenzhen, China, 2011.

Teaching Experiences

T.A. **Mechanical design principles,** EPFL, Instructor: Prof. J. Paik (Spring 2015).

T.A. **Mechanical product design and development,** EPFL, Instructor: Prof. J. Paik (Fall 2016).

Computer Skills

Matlab
Atmel Studio
Altium designer
Autocad
C++
Labview
Comsol multi physics
Solidworks